First Top Quark Physics with ATLAS - A Prospect

Erik Eise van der Kraaij

First Top Quark Physics with ATLAS - A Prospect

ACADEMISCH PROEFSCHRIFT

ter verkrijging van de graad van doctor
aan de Universiteit van Amsterdam
op gezag van de Rector Magnificus
prof. dr. D.C. van den Boom
ten overstaan van een door het college van promoties
ingestelde commissie,
in het openbaar te verdedigen in de Agnietenkapel
op vrijdag 4 december 2009, te 14:00 uur

door

Erik Eise van der Kraaij

geboren te Kampen

Promotor: Prof.dr. S.C.M. Bentvelsen
Co-promotor: Prof.dr.ir. P.J. de Jong

Faculteit der Natuurwetenschappen, Wiskunde en Informatica

Cover by: Reid, Geleijnse & Van Tol.

ISBN: 978-90-9024764-9
Uitgever: Kraaij, E. van der.
Printed in 2009 by Ipskamp Drukkers, Enschede, The Netherlands.

The work described in this thesis is part of the research program of the 'Nationaal instituut voor subatomaire fysica (Nikhef)' in Amsterdam, the Netherlands. The author was financially supported by the 'Stichting Fundamenteel Onderzoek der Materie (FOM)'.

Contents

Introduction

Most people will remember the periodic system of the elements as they learned it at school. The table, invented in 1869 by Dmitri Mendeleev, has a particular odd shape. The inventor did not know the reason behind the system, but organized all elements in a table by simply ordering the different elements by their observed properties. An important property was the increasing mass of the atoms, at that time the most basic components of an element. The fact that some elements hardly reacted with anything, or that some had very specific electric properties also helped in the ordering.

A great achievement by Mendeleev was the prediction of the existence of several elements as he found gaps of non-observed elements in his classification. It was only later however, at the beginning of the 20$^{\text{th}}$ century, that the ordering of the elements could be explained: first with the discovery of the sub-atomic structure of protons and neutrons in the atomic nucleus (surrounded by an electron cloud) and finally with the development of quantum mechanics.

In the 1960s it was realized that nature goes one level deeper and that protons and neutrons are not so fundamental as was thought; they consist of what were to be called quarks and gluons. In short, the total periodic system could now be replaced by no more than four particles: two quarks, the electron and its partner the neutrino. The interactions between these particles take place by means of so-called messenger particles, such as the photons and the gluons.

The theory describing the classification and interactions of these particles, the Standard Model, took about two decades to take shape. In this period the model gradually consisted of more and more fundamental particles: the two quarks, the electron and the neutrino turned out to each have two heavier brothers. This classification came forth partly by hypothesis, but also partly by unexpected observations. A great success of the Standard Model was the unification of the electromagnetic and the weak nuclear interactions into one, renormalizable, quantum field theory. This theory predicted two messenger particles never observed before, the W and the Z boson. In 1983 these were discovered at CERN. Long awaited, the observation of their existence was of fundamental importance in confirming a crucial aspect of the Standard Model. In 2000, with the observation of the τ-neutrino, the last but one of the particles in the Standard Model was discovered. Only one more particle, the Higgs boson, is still missing.

The exact confirmation of the model was, and still is however, not easy. Large particle colliders are built to accelerate charged particles to speeds as high as possible and to have them collide, either on each other or on fixed targets. The 'debris' flying out of the collisions are particles created as part of the kinetic energy of the accelerated particles is transformed into mass. These debris are analyzed with sophisticated detectors to determine the properties of the particles and their interactions. The final confirmation of the Standard Model is hoped to be established with the most powerful proton-proton collider ever built: the LHC at CERN. Soon to become fully operational, this accelerator will reach energy levels expected to be high enough to find the Higgs boson.

At the same time, the LHC will become a true 'top quark factory'. The top quark is the heaviest of all quarks: its mass is more than 180 times the mass of a proton. Although not a stable particle and not immediately a constituent of matter around us, its large mass gives this particle an important role in all interactions. It was discovered in 1995 at Fermilab in the USA, and its properties are not exactly determined yet. The LHC will produce top quarks at an unprecedented rate enabling measurements more accurate than any experiment is capable of at the moment.

If the Higgs boson is found, all particles of the Standard Model will have been identified. The Standard Model could be the final fundamental theory of particle physics; several known problems however almost certainly exclude this possibility. The energy released in the collisions at the LHC will be at levels never observed before in such controlled environments and might result in the discovery of new particles or interactions, bringing the need of an extension to the Standard Model. Different extensions have already been conceived, such as the theory of extra dimensions or of supersymmetry. The Standard Model is then an effective theory: a low-energy limit of some underlying theory, without being dependent on the details of that theory. On the other hand, if no Higgs boson is found with the LHC, its existence as described by the Standard Model becomes impossible. Several revisions of the Standard Model covering this possibility have also been postulated. In fact, with the open questions remaining and the long list of theorized possible answers, it is often felt nowadays that the time of theoretical predictions should be over and that it is again time for observations and measurements.

In this thesis we set out to prepare ourselves for the first measurements on the top quark with the ATLAS detector, one of the four experiments to study the proton-proton collisions at the LHC. One of the first phases of the measurements will be the calibration of the detector. We have developed an approach for the energy scales calibration of the detector, fine-tuned to the observation of the top quark. Independent from this calibration, we have also set up an analysis to measure the rate of production of top quarks in the first data to be taken.

Thesis layout

In the first chapter the Standard Model is explained; a small study is presented on the Parton Distribution Functions (PDFs) for protons at the LHC. These PDFs are parameterizations of the probability for a constituent of the proton to carry a certain fraction of the proton's momentum. The study discusses the accuracy possible in predicting the rate of production of the top quark with the LHC. In the same chapter also the theory of supersymmetry is summarized. The second chapter discusses the LHC accelerator and the ATLAS detector with all its sub-detectors, while in the third chapter more detail is given on the Inner Detector (ID) of ATLAS: the Semi Conductor Tracker sub-detector is explained, together with the ID cooling system and its commissioning in 2008. Chapter 4 then describes how the signals obtained with the ATLAS detector are used to reconstruct the properties of the particles created in the proton-proton collision. Extra attention is given to the b-tagging algorithms: special tools used for the identification of the b-quark, the second heaviest quark in the Standard Model.

With the signals converted into observables we present in chapter 5 a study on the energy scale calibration of the detector using a kinematic fit based on the constraints of a top quark pair creation. Chapter 6 describes an analysis setup for the measurement of the top quark and the W boson production rates on the first data to be taken. The latter analysis makes use of b-tagging algorithms. Both in chapter 5 and 6 the possibility of using the presented analyses as a further aid to observe signs of supersymmetry is discussed.

Chapter 1

Theoretical background

In this chapter we discuss the theory of the Standard Model and of supersymmetry, specifically the supersymmetric mSUGRA. The chapter covers, among others, those aspects of the theories which are useful as background to the studies presented in this thesis. For a more elaborate introduction we refer the reader to several excellent textbooks, see [1–3].

1.1 The Standard Model

At the moment the Standard Model [4–6] is by far the best theory describing the fundamental building blocks of nature and their interactions. Developed in the sixties and seventies almost all its predictions have been verified in the last decades. It is a relativistic quantum field theory based on symmetries, implying that the physics is invariant under certain transformations. The transformations are described by group theory and the $SU(3) \times SU(2)_L \times U(1)_Y$ group determines the interactions of the Standard Model.

According to Noether's theorem these three symmetries each have an associated conserved charge. For $SU(3)$ the conserved charge is color, which can take one of three values denoted by red, green and blue. The generators of the $SU(3)$ group are the eight gluons which are the carriers of the so-called strong force. The $SU(2)_L \times U(1)_Y$ group is associated with the electroweak part of the Standard Model and the charges under the group are the weak isospin and the weak hypercharge. The generators of the two groups mix and lead to the $W^\pm$ and Z, the carriers of the weak force, and to the photon, the carrier of the electromagnetic force. With these force carriers the Standard Model describes all known fundamental forces in nature, except gravity.

Apart from the force carriers, a further category of particles in the Standard Model consists of the quarks and leptons. These are the building blocks of all matter around us and they appear in three 'families'. The first family contains the up (u) and down (d) quark, plus the electron e^- and the electron-neutrino ν_e. The difference between quarks and leptons is that the quarks carry color charge and are thus sensitive to the strong force.

In nature particles have either integer spin (bosons) and follow Bose-Einstein statistics, or particles have half-integer spin (fermions) and follow Fermi-Dirac statistics. The force carriers are gauge bosons with spin 1, quarks and leptons are fermions with spin $\frac{1}{2}$. A scalar field in the theory generates the particles' masses and by the Higgs mechanism [7–9] results in the only spin 0 particle: the scalar Higgs boson. The mechanism describes the spontaneous breaking of the electroweak symmetry resulting in the observable weak and electromagnetic

	Particles			Spin	Electric charge
Quarks	$(u,d)_L$	$(c,s)_L$	$(t,b)_L$	$(1/2,1/2)$	$(+2/3,-1/3)$
	u_R	c_R	t_R	1/2	+2/3
	d_R	s_R	b_R	1/2	-1/3
Leptons	$(\nu_e,e^-)_L$	$(\nu_\mu,\mu^-)_L$	$(\nu_\tau,\tau^-)_L$	$(1/2,1/2)$	$(0,-1)$
	e_R^-	μ_R^-	τ_R^-	1/2	-1
Gauge bosons	g	(strong)		1	0
	$W^\pm$ and Z	(weak)		1	±1 and 0
	γ	(electro-magnetic)		1	0
Scalar boson	H			0	0

Table 1.1: *The particles of the Standard Model, listed with their spin and electric charges. We note that the quarks carry color charge and thus in fact also come in three different colors.*

force. Although all the measured properties of the W and the Z gauge bosons are consistent with the Higgs mechanism's predictions, one last prediction of the symmetry breaking, that is the existence of the scalar Higgs boson, has yet to be verified.

In Table 1.1 we list all the fundamental particles present in the theory. We note that throughout this thesis the natural units are used, that is $\hbar = c = 1$. The subscript L denotes that the charged weak interaction only applies to left-handed fermions. In the Table it can be seen that the left-handed fermions are described in doublets, while the right-handed fermions appear only in singlets. We note that the W only couples to the left-handed particles, while the Z also couples to right-handed fermions since it is a mix of the $SU(2)_L$ and $U(1)$ generators. This also explains why there is no right-handed neutrino: with no color charge, no weak charge, no electric charge and no mass it is pointless to try and pinpoint a right-handed neutrino. It would not interact and thus cannot 'be'. In the Standard Model the neutrino is massless, yet a few years ago it was established that the neutrino does have a small mass [10,11], leading to the possible existence of a right-handed neutrino. This is one of the clearest hints that although the Standard Model is very accurate up to now, it is not complete.

1.1.1 Quantum Chromodynamics

Quantum Chromodynamics (QCD) is the theory based on the $SU(3)$ symmetry describing the strong interaction between particles carrying color charge. These are the quarks and gluons, also known as partons[1)]. The coupling constant α_s, parameterizing the 'strength' of the force, has the striking feature that it grows at large distances, or in other words, at lower energies. A consequence of this is the confinement of partons: colored particles cannot be free, only bound states of partons into color-neutral particles can be free. A proton for example is the bound state of two up quarks and one down quark. These three are the valence quarks of the proton. Inside the proton quantum fluctuations can lead to the brief existence of gluons and quark-antiquark pairs, also called sea quarks. The bound states are called hadrons and are classified in mesons and baryons, consisting of respectively a quark-antiquark pair and three

[1)] To be correct, 'partons' was the name given to elementary objects observed in deep inelastic scatterings inside the proton, later identified with quarks and gluons.

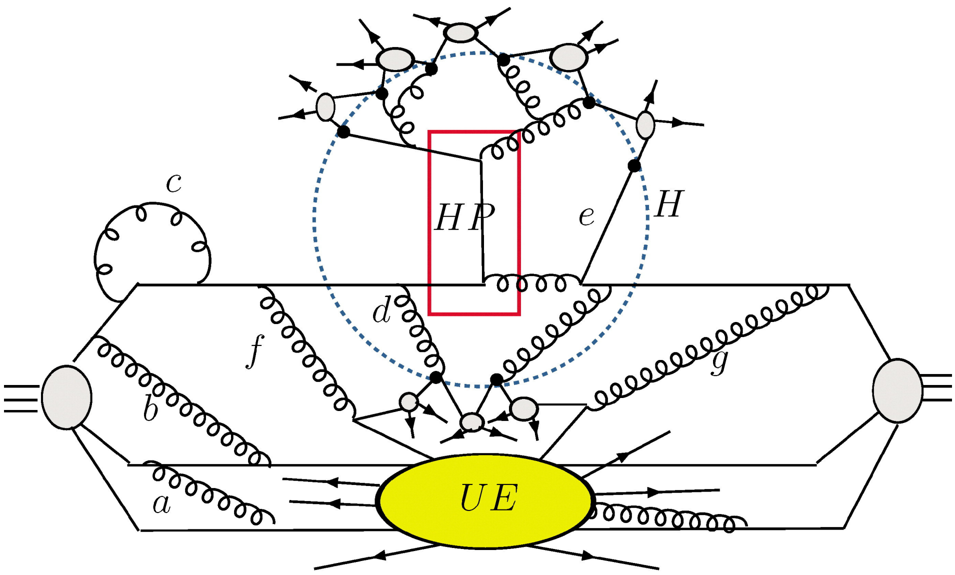

Figure 1.1: *General structure of a hard proton-proton collision. The hard scattering is depicted by the* ***HP*** *(Hard Process) in the rectangular box. The figure is taken from [12].*

valence quarks.

The collision of two protons is thus the interaction of the parton constituents of the protons. The total interaction is extremely complicated and can be visualized as in Fig. 1.1. Left and right the two incoming protons are depicted. We see left the three valence quarks inside the proton exchanging gluons, particle ***a*** and *b*, or even the so-called self-interaction of one quark with gluon *c*. A hard scattering takes place when the energy exchange between two partons from the two protons is high enough to kick each other out of their confinement in the protons, depicted as the ***HP*** (Hard Process) in the rectangular box.

The partons resulting from the hard scattering radiate until the final phase of hadronization takes over. This boundary is depicted with the dotted circle ***H*** in the figure. Intuitively we can see this as follows: the partons lose energy through radiation until the color force becomes strong enough to recombine them back into mesons and baryons. With all the radiation and recombination one parton results in a shower of particles. This is called a jet, see Section 4.3.

With each proton losing a color constituent the remains of the protons are also color charged. Forming an unstable state the total of the remains interacts in the Underlying Event (UE) in mostly soft scatterings, leading to two showers of particles predominantly in the forward directions of the protons. The recombination in the underlying event is not independent of the hard scattering. With the hard scattering carrying color charge the underlying event must be connected to the final state particles of the hard scattering if the total collision is to remain color neutral. This connection can be the exchange of a quark or a gluon, as the particles ***d-g*** we see in the figure, leading to particle production also in the central rapidity regions[2)], partially overlapping with the hard scattering. We note that in the underlying event second hard scatterings can take place.

[2)]That is close to the transverse plane through the interaction point, see Section 2.2.1.

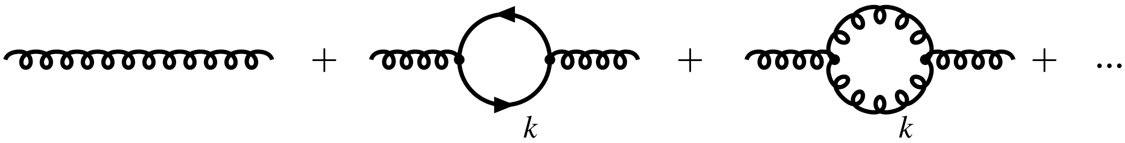

Figure 1.2: *Two diagrams contributing to the self-energy of the gluon propagator. The momentum k of the particle running in the loop can be anything, thus the expression for the loop is an integral $\int_0^\infty dk$.*

Renormalization

In the calculation of physical observables such as cross sections all Feynman diagrams have to be taken into account. This includes loop diagrams such as the one with the gluon c in Fig. 1.1. These self-interactions contribute to the expression of a propagator[3)]. The gluon c for example contributes to the propagator of a fermion. In fact, a propagator is defined by including the sum of all self-interacting diagrams, such as in Figure 1.2. The two right diagrams contribute to the 'self-energy' of the gluon propagator. Yet the expressions for the two diagrams are integrals over the loop momentum $\int_0^\infty dk$ and diverge. And not only do each of the diagrams diverge, the sum also extends to an infinite sum.

A first step in solving this problem is isolating the divergency of each diagram. There are different *regularization* schemes available to do this. The dimensional regularization scheme shifts the integra[illegible]m7e48 7172.6 15460s91 Tf 22.3diaghese

Figure 1.3: *Left: the hard scattering of the quark and gluon as in Fig. 1.1. Right: the same diagram including the emission of a gluon from the incoming quark. The probability for a soft emission grows with smaller momentum k and goes to infinity when $k \to 0$. These divergencies are absorbed by redefining the functions $f_n(x_n, \mu_F)$ as functions of the factorization scale.*

Factorization

The hard process in Fig. 1.1 represents the interaction of a gluon with a quark scattering into a hard gluon and quark. For the measurement of this process' cross section we need to know the momenta of the incoming partons. However, the two are constituents of the protons and their momenta are unknown. At the same time, the outgoing quark and gluon are observed as jets in the detector and distinguishing a jet from a gluon or a quark is difficult.[4] Therefore we typically make inclusive measurements: we cannot measure a partonic cross section such as $\sigma(qg \to qg)$, yet we can measure the hadronic cross section $\sigma(pp \to jj')$ of two jet events. The relation in perturbation theory between the two is given by

$$\sigma_{Hadronic} = \sum_{l,m,j,j'} \int \int dx_1 dx_2 f_i(x_l) f_j(x_m) \sigma^{j,j'}_{Partonic}(x_l, x_m), \tag{1.1}$$

where the sum runs over all possible flavors and species l, m of the incoming partons, and all possible flavors and species j, j' of the outgoing partons. Each of the incoming partons carry a fraction x_l and x_m of their protons momentum and the integral runs over all allowed momentum fractions. The Parton Distribution Function (PDF) $f_n(x_n)$ is the probability that a parton of type n is encountered with momentum fraction x. In the expression of the PDFs we run into trouble.

In Fig. 1.3 we see on the left the hard scattering of the gluon and the quark from Fig. 1.1 drawn again, on the right we see the same scattering including the radiation of gluon d in Fig. 1.1. It turns out that the probability $P_{qq'}$ for the emission of a collinear gluon grows as the momentum k drops. With $k \to 0$ the probability even goes to infinity. The way to deal with this is similar to the renormalization approach. We define a factorization scale μ_F such that the expression for the probability is split into a finite and a divergent part. The factorization theorem states that the last part can be absorbed, such that we remain with finite expressions of $f_n(x_n, \mu_F)$. Similar to the masses in the Standard Model, the PDFs cannot be determined from theory and are to be measured in experiments.

In Figure 1.4 an overview is given for the predictions for several important Standard Model cross sections at $p\overline{p}$ and pp colliders. These cross sections are calculated at next-to-leading order (NLO) in perturbative theory: the exact meaning of this is explained in the next section.

[4] Although identifying jets originating from b-quarks is possible, see Section 4.4.

In the figure we see how the distributions for the Tevatron and for the LHC do not always 'connect'. This is due to the differences between the PDFs of a proton and the PDFs of an anti-proton.

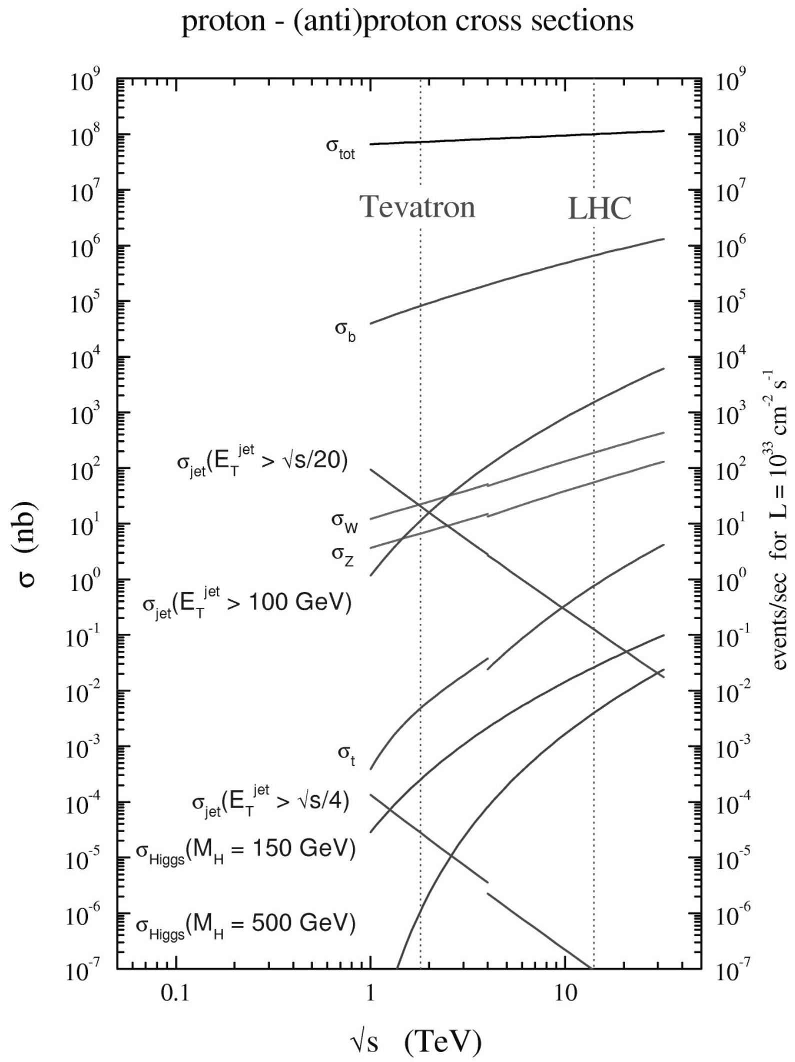

Figure 1.4: *Standard Model cross sections for $p\overline{p}$-collisions (Tevatron) and for pp-collisions (LHC). The Figure is taken from [14].*

1.1.2 Running coupling constant

In this section we discuss the running coupling constant α_s. Before stating the question we want to discuss, we note that the naming is somewhat confusing: a 'constant' which is running is no real constant. Yet this is not the point we want to address in this section. The exact question we want to answer is the following: how can it be that $\alpha_s(\mu_R)$ is often interpreted as the strength of the strong force[5)], varying with the energy scale μ_R used? Is an *observable* such as the strength of the force by definition not supposed to be independent of the renormalization scale?

[5)] Even by the author in this same chapter.

First of all, the fact that the function $\alpha_s(\mu_R)$ is non-constant with varying μ_R tells us that α_s is *not* an observable. The parameter α_s is a value corresponding to the vertex in the Feynman diagrams and depending on the choice of μ_R the contributions from the different Feynman diagrams in an expansion change. In other words, the setup of perturbative QCD with its regularization and renormalization schemes is such that the coupling constant is an expansion parameter. This setup is chosen with the purpose of being able to stay in the perturbative regime: diagrams with N loops are suppressed by powers of α_s^{2N}, and with the choice of $\mu_R^2 \sim Q^2$, where Q^2 is the square of the interaction scale, it turns out that the contributions from the loop diagrams in the expansion are at a minimum, see [1]. The diagram containing no loops is called the tree diagram and is the Leading Order term.

The scale Q^2 denotes the square of the energy level at which the interaction takes place. In electron-positron scattering $e^+e^- \to \gamma \to q\overline{q}$ it is easily set: the interaction scale $Q^2 = s$, where $\sqrt{s}$ is the center-of-mass energy. In some channels the choice is less clear; we come back to this in Section 1.1.3 where we discuss the production of top quark pairs.

To see the 'running of the coupling constant' we start with the Callan-Symanzik equation, which dictates that an observable such as a cross section is to be independent of the renormalization scheme. The equation states, see [1],

$$\left[\mu_R^2 \frac{\partial}{\partial \mu_R^2} + \beta(\alpha_s)\frac{\partial}{\partial \alpha_s}\right] \sigma(\sqrt{s}, \mu_R^2, \alpha_s) = 0, \tag{1.2}$$

which we can read as follows: any direct dependence of the cross section on μ_R should be exactly canceled by the dependence of the coupling constant on μ_R. We note that if we were to perform a calculation for the cross section up to all orders the parameter μ_R would disappear. Yet as we can only go up to a certain order, a value for μ_R has to be chosen. The β function is determined by

$$\beta(\alpha_s) = \mu_R^2 \frac{\partial \alpha_s}{\partial \mu_R^2} \tag{1.3}$$

and to the first order in the perturbative expansion it is given by $\beta(\alpha_s) = -(b_0/4\pi)\alpha_s^2$. The constant $b_0 = 11 - (2/3)n_f$ and is defined with n_f the number of quark flavors considered.[6)] See also [2] for more details. Equation (1.3) can be rewritten and integrated, resulting in

$$\begin{aligned}
\int_{\alpha_s(\mu_0^2)}^{\alpha_s(\mu^2)} \frac{d\alpha_s}{\alpha_s^2} &= -\frac{b_0}{4\pi}\int_{\mu_0^2}^{\mu^2} \frac{d\mu_R^2}{\mu_R^2} \\
\to \quad \left(\frac{1}{\alpha_s(\mu_0^2)} - \frac{1}{\alpha_s(\mu^2)}\right) &= -\frac{b_0}{4\pi}\ln\frac{\mu^2}{\mu_0^2}
\end{aligned} \tag{1.4}$$

From this equation it becomes clear that if α_s has been determined at a certain scale μ_0, it can be extrapolated to any other scale μ. A common approach is the extrapolation from $\alpha_s(\mu_0^2 = m_Z^2)$.

The asymptotic logarithmic behavior of α_s also possesses the possibility of defining the boundary condition *on the asymptote*: with Λ_s the momentum scale at which the coupling constant blows up and setting $\alpha_s \uparrow \infty$ as the scale $\mu_0^2 \downarrow \Lambda_s^2$, we obtain from eq. 1.4:

$$\alpha_s(\mu^2) = \frac{4\pi}{b_0 \ln(\mu^2/\Lambda_s^2)}. \tag{1.5}$$

6) When the interaction scale satisfies $m_c^2 < Q^2 < m_b^2$ only four flavors need to be considered.

Here we see how the coupling becomes larger as the interaction scale decreases. Λ_s is experimentally found to be $\Lambda_s \approx 200$ MeV (its exact value depends on the number of quark flavors n_f considered in the perturbative expansion). Mathematically this simply means that the expansion parameter becomes too large when $\mu^2 \downarrow \Lambda_s^2$ and perturbation theory does not hold anymore. Physically this is often interpreted as the confinement by the strong force.

The expansion parameter α_s becomes an 'observable' only when we first define a common set of conventions. It has become customary to use the coupling after the so-called regularization by modified minimal subtraction ($\overline{\text{MS}}$), with the renormalization scale set at m_Z. The resulting coupling constant is called $\alpha_{s,\overline{MS}}(m_Z^2)$. From measurements of for example the total cross section for e^+e^- annihilation to hadrons, or the transverse momentum distribution of W bosons produced from quark-antiquark annihilation at high-energy $p\overline{p}$ colliders, see [1], the α_s can be determined at different interaction scales. Further on in Section 1.3.2 the running of the coupling constants in the Standard Model and in models including supersymmetry is depicted in Figure 1.13.

1.1.3 Top quark physics

In the Standard Model the top quark was predicted as the weak isospin partner of the observed bottom quark b. In 1995 it was discovered by the CDF and D0 collaborations [15], with a mass nowadays measured to be 173.1 ± 1.3 GeV [16]. This is approximately 35 times larger than the mass of the b quark and 5 orders of magnitude larger than that of the first generation quarks. The classification of the six quarks with increasing masses has led for a long time to the hypothesis of new physics, see for example [17].

In the Standard Model the top quark acquires its mass through the Yukawa coupling to the Higgs field, that is

$$m_t = y_t \frac{v}{\sqrt{2}}, \tag{1.6}$$

where y_t is the strength of the Yukawa coupling between the top quark and the Higgs field and v is the vacuum expectation value of the Higgs field. The latter is fixed by the Fermi coupling constant G_F[7)] and equals $v = (\sqrt{2}G_F)^{-1/2} = 246$ GeV. With y_t close to unity the top quark couples strongly to the Higgs field, or to whatever else might break the electroweak symmetry. It thus plays an important role in the search for and study of the Higgs boson.

Single top quark production

There are several hard scatterings that may lead to the production of top quarks. Through the electroweak force single tops can be produced, accompanied by a W boson (the Wt-channel), or another quark (the s- or t-channel). In Figure 1.5 the three channels are depicted in Feynman diagrams at Leading Order. The NLO cross sections for single top production at the LHC are summarized in Table 1.2. The values for 14 TeV center-of-mass energy are extracted from [18, 19], the values for 10 TeV collisions are calculated at NLO using MCFM [20].

Top quark pair production

Via the strong interaction the top can be produced in pairs. Throughout this thesis we will focus on this channel, also denoted by $t\bar{t}$. In Figure 1.6 we see depicted in Feynman diagrams the

[7)] This constant is again fixed by $G_F = \sqrt{2}g^2/(8m_w^2)$, with g the weak interaction coupling constant and m_W the W boson mass, and can be for example measured in the rate of muon decay $\mu^- \to \nu_\mu e^- \overline{\nu}_e$, see [1].

	$\sqrt{s} = 10$ TeV	$\sqrt{s} = 14$ TeV
t-channel	124.51	246.6
s-channel	6.627	10.65
Wt-channel	32.66	66

Table 1.2: *NLO cross sections (in pb) for single top production at the LHC.*

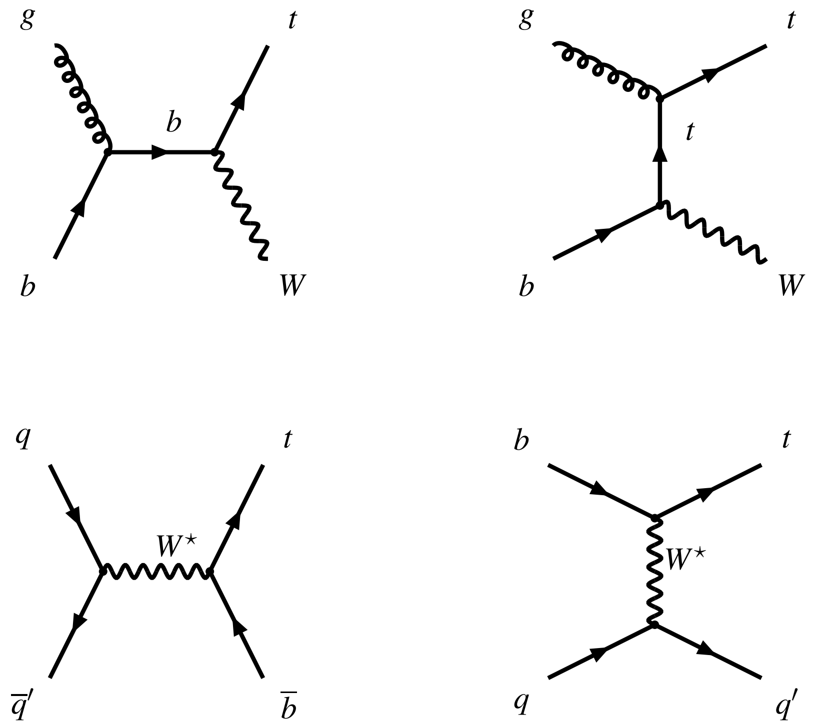

Figure 1.5: *Leading order single top quark production. The upper two diagrams depict the Wt-channel. The s-channel is shown in the lower left and the t-channel in the lower right diagram.*

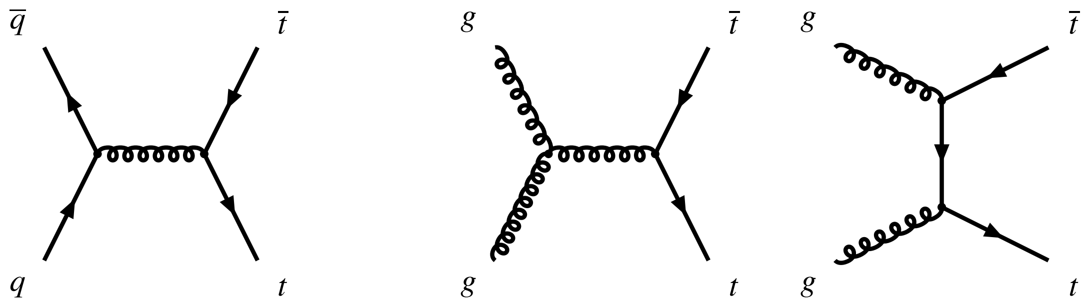

Figure 1.6: *Leading order top quark pair production. Left: quark-antiquark annihilation. Middle and right: gluon fusion, the dominant production channel at the LHC.*

different Leading Order channels for the production of a top quark pair. The total production cross section for the $t\bar{t}$ channel at leading order can be calculated by summing over all possible configuration of the diagrams. Configurations exist with different flavors, colors, spin and momenta for the incoming particles. In short the cross section can be written as:

$$\sigma_{t\bar{t}}\left(\sqrt{s},m_t\right)=\sum_{i,j}\int\int dx_i\ dx_j\ f_i\left(x_i,\mu_F^2\right)f_j\left(x_j,\mu_F^2\right)\times\hat{\sigma}_{t\bar{t}}\left(\sqrt{s},m_t,x_i,x_j,\alpha_s\left(\mu_R^2\right),\mu_F^2\right), \tag{1.7}$$

where the sum runs over all possible flavors and species i,j of the incoming partons. The $\hat{\sigma}_{t\bar{t}}$ is the cross section of the hard scattering process of the partons i and j into a $t\bar{t}$ pair and includes the summation over possible colors and spin. Just as in eq. (1.1) the parton distribution function $f_n(x_n,\mu_F^2)$ is the probability that a parton of type n is encountered with momentum fraction x. An observable should be independent of the factorization scale, yet as we can only perform calculations up to certain order, a μ_F must be set when extrapolating the PDF from the scale at which it has been measured, to the scale at which we are performing our measurements.

As an example, in Fig. 1.7 we set it to the top mass, that is $\mu_F^2=Q^2=(170\text{ GeV})^2$. These distributions are obtained from the CTEQ6.5 PDF set [22]. We see how for all the constituents, the probability increases with smaller x. A simplified calculation of $\sqrt{x_1\cdot x_2}\sqrt{s}\approx x\sqrt{s}=2m_t$ tells us that for the center-of-mass energy present at the Tevatron we need a minimum of $x\sim 0.2$, while at the LHC we need a minimum of $x\sim 0.03$. From the figure we thus understand that the dominant production channel at LHC will be via gluon fusion, while at the Tevatron it is via

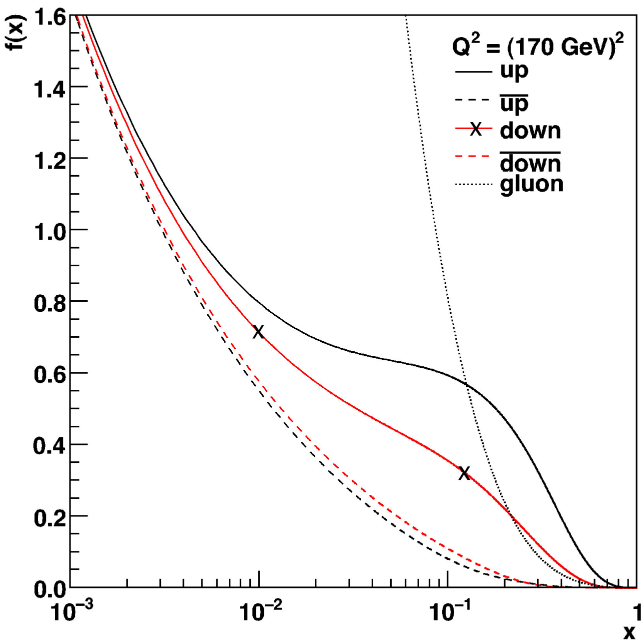

Figure 1.7: *Parton distribution functions for the proton according to the CTEQ6.5 parametrization. We see that the distributions for the up and down quarks are higher than those of the anti-quarks due to the contribution of valence quarks. The gluon distribution can be seen to rapidly increase for lower momentum fraction x. The figure is taken from [21].*

quark-antiquark annihilation. The cross section for the top pair production at the Tevatron and at the LHC was depicted in Fig. 1.4.

The choice of $Q^2 = (170\ \text{GeV})^2$ needs some explanation. In Section 1.1.2 we explained that Q^2 is the square of the interaction scale; from the reasoning followed in that section the first two diagrams in Fig. 1.6 would imply a scale of $Q^2 = 4m_t^2$. Yet for the third diagram, the dominant production channel at the LHC, it is unclear what the interaction scale is. In the end, setting $Q^2 = (170\ \text{GeV})^2$ is solely based on the knowledge that we are investigating the production of the top quark, and thus must be working around the energy level of m_t. In any case, the cross section should be independent of Q^2. In calculations the renormalization scale μ_R is often varied in the range $(0.5Q)^2 < \mu_R^2 < (2.0Q)^2$ to give an estimate of the theoretical uncertainty as a consequence of performing calculations up to finite order, see Section 1.2, where such a study is presented.

Top quark decay

With a mass above the Wb threshold, the top quark decays almost exclusively as $t \rightarrow Wb$. The corresponding branching fraction is larger than 99.8% and with its mass of 173.1 GeV the top quark has a decay width of $\Gamma_t = 1.35$ GeV [23], corresponding to a lifetime of not more than $O(10^{-24})$ s. If we compare this to the time scale governing QCD processes, $1/\Lambda_{QCD} = O(10^{-23})$ s, we see that the top quark will predominantly decay before forming bound states; we can thus describe the decay of a top quark by the decay of a free quark.

With two W bosons in each top pair event and one third of all W bosons decaying into leptons, the top pair decays are categorized in the fully hadronic (only jets), semi-leptonic (one lepton + jets) and fully leptonic events (two leptons + jets). The leptonic decays of the W are spread approximately even over electrons, muons and τ's, resulting in the branching fractions summarized in Fig. 1.8. Throughout this thesis we focus on the semi-leptonic decays with an electron or a muon; these two leptons leave clear signals in the detector and are easy to identify, especially in the busy hadronic environment we can expect in ATLAS. The leptonic decays of the top quarks with τ's are left out, as these particles are more difficult to identify.

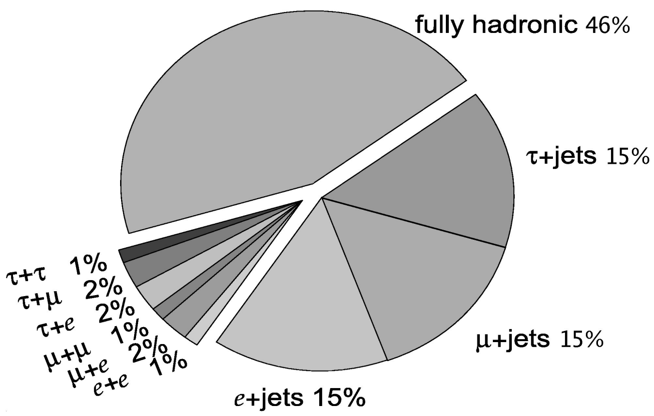

Figure 1.8: *Branching fractions of a top quark pair illustrated in a pie-chart. The pair decay is categorized by the decay of the W boson. The semi-leptonic decays considered throughout this thesis are the channels with one electron or muon +jets. These amount to 30% of all top pair decays.*

1.1.4 The W and the Z boson

The charged W and the neutral Z are the two mediators of the weak interaction. They were discovered in 1983 at the UA1 and UA2 experiments at CERN [24–26] and their properties were extensively studied at LEP from 1989 up to 2000. The current world average for the masses are

$$m_W = 80.398 \pm 0.025 \text{ GeV}, \tag{1.8}$$
$$m_Z = 91.1876 \pm 0.0021 \text{ GeV}. \tag{1.9}$$

These values are obtained from [23]. The accurate measurements will make it possible to use the boson masses for calibration of the ATLAS detector. To this end, the widths are important. These have been measured to be

$$\Gamma_W = 2.141 \pm 0.041 \text{ GeV}, \tag{1.10}$$
$$\Gamma_Z = 2.4952 \pm 0.0023 \text{ GeV}. \tag{1.11}$$

Production and decay

The W and Z bosons can be created as daughter particles of heavier particles in channels such as the top quark decaying into a W and a b-quark, or the Higgs decaying into a ZZ pair[8)]. We note that W's as well as Z's can be produced in pairs, yet we restrict ourselves to the single boson production channels.

The W and Z bosons can also be created directly in the hard interaction by quark-antiquark fusion, see Fig. 1.9. Both bosons need an anti-quark to be produced; at the Tevatron this is present as valence quarks in the anti-proton, at the LHC it is only present as a sea quark. (In Fig. 1.4 on page 8 the distributions therefore do not connect.) The two cross sections have been calculated up to NNLO and for the inclusive production at the LHC are expected to be $\sigma_W = 20.5$ nb and $\sigma_Z = 2.02$ nb at 14 TeV center-of-mass energy, see [27]; this is including the branching ratio into one lepton generation. In this thesis the leptonic decay of the W plays an important role and we restrict ourselves to the decays into an electron plus ν_e or into a muon plus ν_μ. The branching ratios for the W's and Z's are, see [23]:

$$\begin{array}{llll}
W^+ & \rightarrow & l^+\nu & : \quad 10.80 \pm 0.09\% \quad (3\times) \\
 & \rightarrow & hadrons & : \quad 67.60 \pm 0.27\% \\
Z & \rightarrow & l^+l^- & : \quad 3.3658 \pm 0.0023\% \quad (3\times) \\
 & \rightarrow & \nu\bar{\nu} & : \quad 20.00 \pm 0.06\% \\
 & \rightarrow & hadrons & : \quad 69.91 \pm 0.06\%
\end{array}$$

The Z boson production cross section is lower than that of the W boson as the branching ratio in one lepton generation is smaller and as the couplings constants to the fermions are smaller, see [3].

W and Z production with additional partons

For the work in this thesis the W and Z total inclusive production cross sections are not immediately of importance. More important are the cross sections of the W and Z production with at least two additional partons: the radiation of partons as discussed in Section 1.1.1

8) If the Higgs mass is large enough. If not, this channel is heavily suppressed.

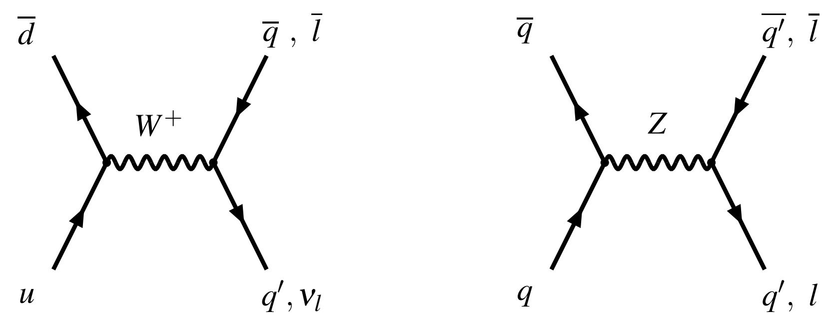

Figure 1.9: *Leading order W (left) and Z (right) production at the LHC.*

can result in additional hard partons, observable as jets, originating from before the hard interaction (Initial State Radiation, ISR) or originating from after the hard interaction (Final State Radiation, FSR).[9)] Together with ISR/FSR the observable signature of these events, called W+jets or Z+jets event, can be similar to the signature of a top quark pair event.

The prediction of the W+jets and Z+jets cross sections is however not trivial. In [28] it is explained how going from calculations at Leading Order to calculations at Next-to-Leading Order improves the results as the renormalization and factorization scale dependence is reduced. Yet at the same time it is shown how the higher order opens new possible production channels, increasing the cross section. From the same article the NLO cross sections for W- and Z+jets events in Table 1.3 are obtained.[10)]

In [29] it is discussed how the prediction for the cross section for Z plus four or more jets has a 50% uncertainty. The reason for this is that in these (Leading Order) predictions the coupling α_s is difficult to determine at all four or more vertices, as the scale Q^2 is unknown. The same reasoning goes for the cross section of W plus four or more jets. The W+$b\bar{b}$ cross section also has a relative large uncertainty. From data taken at the Tevatron the cross section measurement for leptonic decays of W plus associated b-quark production results in 2.74 ± 0.50 pb, while 0.78 pb is expected from Leading Order calculations, see [30]. Studies are ongoing to fully understand this discrepancy, but for now a safe margin of a factor of two is placed on the production cross section of W+$b\bar{b}$ at the LHC.

9) ISR and FSR lead to the same final state and are in principle indistinguishable.
10) The exact definition of a jet as used in the article is similar to what will be used in this thesis.

	$W^+ \to e^+\nu_e$	$Z \to e^+e^-$
+ jj + X	669^{+0}_{-18}	105^{+1}_{-5}
+ $b\bar{b}$ + X	$3.06^{+0.62}_{-0.54}$	$2.28^{+0.32}_{-0.29}$

Table 1.3: *Cross sections (pb) for the production of W- and Z plus two or more jets at the LHC with 14 TeV center-of-mass energy. The table lists the inclusive cross section for the leptonic decay with an electron, and the exclusive cross section for the production including a $b\bar{b}$ pair. The uncertainties are the consequences of renormalization and factorization scale variations $\mu = M_V/2$ to $\mu = 2M_V$, where V stands for either a W or a Z, and $\mu = \mu_R = \mu_F$. In Section 1.2 these variations are explained in detail.*

1.2 PDF uncertainties in the top quark pair and W boson cross sections

In Section 1.1.3 we explained how for the calculation of the top pair cross section PDFs are necessary. There are several PDF parameterizations available for which different techniques are applied, or for which different data sets have been used to extrapolate the functions. In this section we investigate the prediction of the top quark pair and of the W boson cross sections at the LHC with a center-of-mass energy of 14 TeV, focusing on the systematic errors due to the uncertainties known for the PDFs. We investigate two sources of errors: the choice of the μ_R and μ_F scales and the uncertainty on the data used to determine the PDFs.[11)]

The PDFs needed for the simulations of the pp collisions at the LHC are extrapolations of PDFs fitted to data taken at HERA and Tevatron. These extrapolations are obtained using the DGLAP equations, which describe the QCD-evolution of a PDF as function of the factorization scale.[12)] The uncertainty on the experimental data propagates into uncertainties on the free parameters in the PDF fits. Through the DGLAP equations these uncertainties can be extrapolated to the PDFs needed for the LHC. Since 2001 certain PDFs have been extended with an extra functionality of calculating the consequences of these uncertainties. We will be using the MRST2001E [32] and the CTEQ6.1 [33] PDFs.

These two versions consist each of a set of PDFs. In the global fit to data, the authors of both versions use a number of free parameters (n_{group}). For the MRST group this is a total of 15 parameters, for the CTEQ group this is 20 parameters. As to determine an uncertainty on their PDF fits, they use the following approach: for each parameter an upper and lower bound is calculated for which the fit deviates from the best fit by a small amount. In other words, the best fit has a minimized χ^2 and the parameters may deviate such that χ^2 grows by a certain $\Delta\chi^2$, also called the tolerance. The MRST2001E set consists of 31 PDFs: one as a result of the best fit, plus 2×15 for the upper and lower result for each of the 15 free parameters used in the PDF fits. The CTEQ6.1 set with its 20 parameters has 41 different PDFs.

Unfortunately, an appropriate deviation is not easily set. For normal, that is Gaussian errors, the tolerance would be $\Delta\chi^2 = 1$. Yet this criterion depends on the assumption that the statistical and systematic errors are known, which is not the case for the PDFs. By investigating the χ^2 variations per data set used, the CTEQ group has settled with a final tolerance of $\Delta\chi^2 = 100$, see also [34], while the MRST group has settled with $\Delta\chi^2 = 50$.

Ratio of the top pair and W boson cross sections

We calculate the uncertainty on the top pair cross section as a consequence of two methods: the (μ_R, μ_F) scale variations and the PDFs internal parameter variations we just discussed.[13)] Furthermore, we investigate the ratio of the top pair cross section to the W boson cross section, specifically the $\sigma_{W\to leptons}$. With almost all top quarks decaying via $t \to Wb$, the ratio of the two cross sections has the potential of dividing out several systematic errors and could thus serve as a calibration tool at the start up of the LHC. We therefore investigate the consequences the PDF uncertainties have on this observable.

[11)] Another important source of error, which we will not discuss, is the uncertainty on α_s. See for example [31].

[12)] Comparible to the β function in eq.(1.3) describing the evolution of α_s as a function of μ_R.

[13)] An alternative analysis is presented in [35] and a similar investigation for the cross section at the Tevatron is also available, see [36].

1.2.1 Setup of the calculation

For the computation of the cross sections we use the event generator MC@NLO, version 3.2 [37,38]. This Monte Carlo program simulates the pp collision at a 14 TeV center-of-mass energy and calculates Matrix Elements up to Next-to-Leading-Order; in Section 4.2 event generators are discussed in more detail. The different PDFs have been made available in one library, the LHAPDF, while the interface between the event generator and the library is taken care of by LHAGLUE [39].

The event generator can compute the full top pair cross section as a single channel. For the W boson production and subsequent decay, one can choose to either compute the full channel of $W \to 2X$ with $2X$ being leptons or quarks, or the channel with W^+ or W^- going to one of the three lepton families. Although the production rates of W^- and W^+ at the LHC will not be equal, their ratio can accurately be determined. Using the MRST PDFs [31] it is calculated to be

$$\frac{\sigma_{W^-}}{\sigma_{W^+}} = 0.731 \pm 0.005. \tag{1.12}$$

As the branching of the W boson to either of the three leptons is also well known, we have chosen to simply look at the single channel of $W^+ \to \mu^+ + \nu_\mu$. For a good approximation of the full W cross section one can then easily apply the rule $\sigma_W = 16.4\sigma_{W^+\to\mu^++\nu_\mu}$.

The top quark mass - The top pair cross section has a large dependence on the top mass. We investigate this by varying the top mass with ± 2.5 GeV, where the average is set to $m_t = 175.0$ GeV. This was the standard top mass at the time the work was performed.

The QCD scale - Another variable of importance is Λ_5, the scale Λ_s calculated with five flavors in the renormalization equations, see Section 1.1.2. For the CTEQ PDFs it is set to $\Lambda_5 = 0.226$ GeV, for the MRST PDFs it is set to $\Lambda_5 = 0.239$ GeV. [14)]

μ_R and μ_F dependence - For the determination of the dependence on the renormalization and factorization scale we let both scales vary by a factor of two [40]:

$$\mu_i = 0.5M \ , \quad \mu_i = 1.0M \ , \quad \mu_i = 2.0M. \tag{1.13}$$

The mass scale is either $M = m_t$ or $M = m_W$, depending on the channel.

The PDF tolerance range - Both the MRST and the CTEQ set consist of one best fit PDF, plus $2 \times n_{group}$ PDFs, which we will call the $(+)$ and $(-)$ direction of variation $V_i^\pm$, with $0 < i < n_{group}$. We have $n_{mrst} = 15$ and $n_{cteq} = 20$. Any observable X, like the top pair cross section we are studying, has an error defined by

$$\Delta X = \frac{1}{2}\sqrt{\sum_{i=1}^{i=n_{group}} \left(X(V_i^{(+)}) - X(V_i^{(-)})\right)^2}. \tag{1.14}$$

The error on the ratio of cross sections is calculated by first taking the ratio of each of the directions of variation $V_i^\pm$ and then applying the above definition.

[14)] If one lets MC@NLO calculate the Λ_5 value for the MRST PDFs from the LHAPDF library, it amounts to $\Lambda_5 = 0.224$ GeV. Yet in the MC@NLO internal PDF library, the default value for the MRST PDFs is set at $\Lambda_5 = 0.239$ GeV. This difference comes from the fact that the MRST group and the MC@NLO group use a different form of calculation of the strong coupling α_s. Since we are using the MC@NLO routine to compute α_s, the correct setup is with $\Lambda_5 = 0.239$ GeV, independent of the PDF library. The differences can be the result of using different data and different numerical approximations.

1.2.2 Results

In Table 1.4 we state the results for the top pair cross section, where the errors are according to eq. (1.14). In our calculations we let the renormalization scale μ_R and factorization scale μ_F vary independently. The outcome is that the cross sections dependence on μ_R is much higher than its dependence on μ_F. As an illustration we list all results of the CTEQ6.1 with $m_t = 175$ GeV in Table 1.5. In Table 1.4 we have set $\mu_R = \mu_F = \mu$. As for the $(W^+ \to \mu^+ + \nu_\mu)$ process it turns out that, within the range chosen, the cross section is independent of the factorization scale μ_F. In Table 1.6 we state the results for the W cross section.

From a comparison of the $\sigma_{t\bar{t}}$ with the $\sigma_{W^+ \to \mu^+ + \nu_\mu}$ we conclude that there is an anti-correlation between the two cross sections. This is clear from Fig. 1.10 where we see the 41 results of the variations within the PDF tolerance range for the CTEQ6.1 distributed, at $\mu_R = \mu_F = m_t$ and $m_t = 175$ GeV.

With the top quarks being mostly produced by gluon fusion at Leading Order and the W boson being mostly produced by quark fusion, a possible explanation for the anti-correlation between the two cross sections is the following: any variation of a PDF resulting in a higher gluon density also results in a lower quark density. We note that this argument would not hold if we evaluated a PDF $f(x)$ at one value of the momentum fraction x. Yet it does hold for a PDF $f(x)$ integrated over x, and for the results presented here the integral over x is more important, as the production of a W boson or a $t\bar{t}$ pair can occur over a large range of x.[15)]

In Table 1.7 we summarize the results for the top pair cross section divided by the $(W^+ \to \mu^+ + \nu_\mu)$ cross section. The relative error due to the PDF tolerance is larger compared to either of the given cross sections' uncertainties.

Figure 1.10 illustrates the result of the PDF tolerance range at a fixed renormalization and factorization scale. If we look at one specific PDF and vary the scales, we see from Table 1.4 and 1.6 that there is also an anti-correlation in the variation of μ_R. The results show a large dependency of the cross section on the top mass. The variation of ± 2.5 GeV results in a cross section difference of approximately $\mp 7\%$.

To see if the choice of scale variation is justified, we have calculated the top pair cross section as a function of μ_i in the range $0.01 < \mu_i/m_t < 10$. For one single PDF, that is the CTEQ6.1 best fit variation with $m_t = 175$ GeV, this results in the distribution in Fig. 1.11. In [40] a similar distribution is calculated for the cross section at Tevatron. It is explained that going to NLO including Next-to-Leading-Log (NLL)[16)] reduces the scale dependence in the range, justifying the choice of $0.5 < \mu_i/m_t < 2$.

[15)] Gluons and quarks are not the only constituents of a proton, antiquarks are also present. Their presence is the result of gluons splitting in quark-antiquark pairs. As the Leading-Order production of a W boson also requires an antiquark, and as the two cross sections are evaluated at different x values, there are some subtleties in the argument presented here.

[16)] Instead of calculating completely one higher order in the perturbative expansion in α_s, one can estimate the next order by reorganizing the large logarithms L in the expansion, where $L \gg 1$. After this so-called resummation, the most dominant logarithmically enhanced terms to all orders in α_s can be isolated in the Leading-Log term. Expressed in exponential form, the expansion for a cross-section σ reads

$$\sigma \sim e^{(Lg_1(\alpha_s L) + g_2(\alpha_s L) + \alpha_s g_3(\alpha_s L) + \ldots)}, \tag{1.15}$$

where the g_i are functions of $\alpha_s L$. Including only the g_1 term results in the Leading-Log expression, complementing this with the g_2 term results in the NLL, etc...

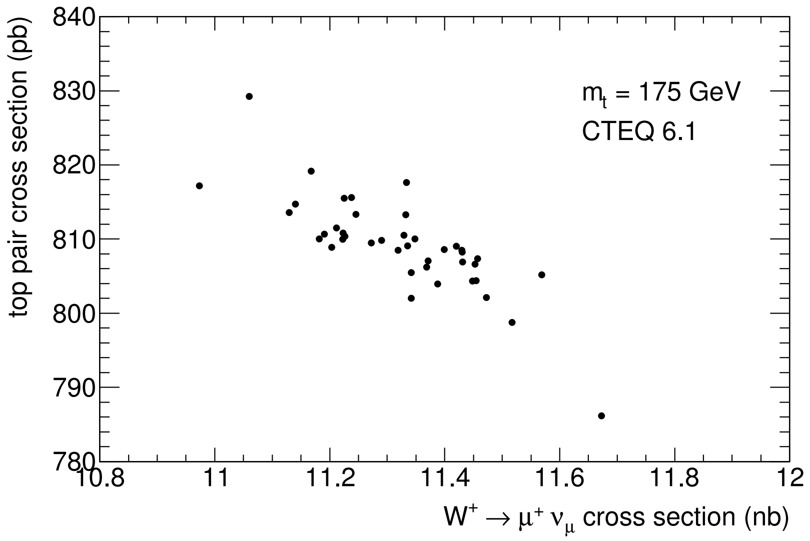

Figure 1.10: *The cross section for top pair production vs the cross section of the* $W^+ \to \mu^+ + \nu_\mu$ *channel, calculated with the 41 variations of the PDFs from CTEQ6.1. An anti-correlation between the two channels is visible.*

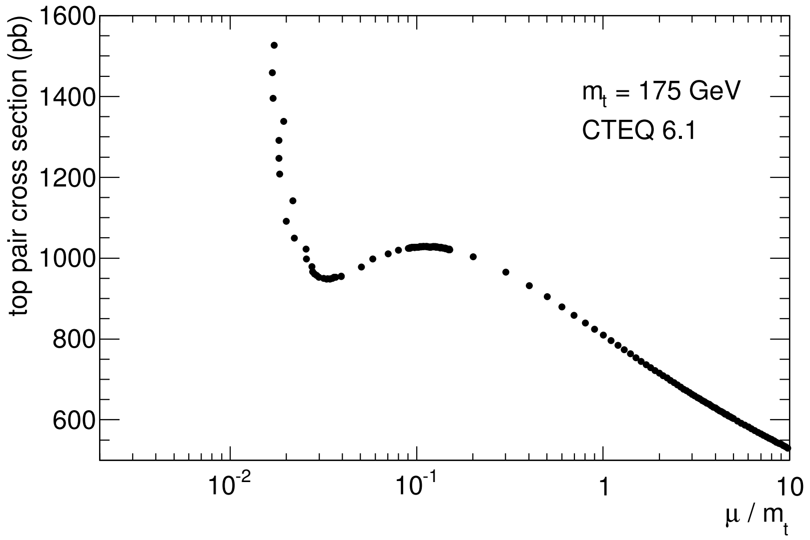

Figure 1.11: *The top pair cross section as a function of the scale* μ*, with* $\mu_R = \mu_F = \mu$*. The calculations are performed at NLO, resulting in a substantial dependence on the scales.*

top mass (GeV)	PDF group	μ/m_t	$\sigma_{t\bar{t}}$ (pb)	$\pm$ error (pb)
172.5	cteq6.1	0.5	967	34 (3.5%)
172.5	cteq6.1	1.0	865	30 (3.5%)
172.5	cteq6.1	2.0	765	28 (3.7%)
172.5	mrst2001	0.5	1000	14 (1.4%)
172.5	mrst2001	1.0	894	12 (1.3%)
172.5	mrst2001	2.0	790	12 (1.5%)
175.0	cteq6.1	0.5	904	32 (3.5%)
175.0	cteq6.1	1.0	809	29 (3.6%)
175.0	cteq6.1	2.0	715	26 (3.6%)
175.0	mrst2001	0.5	935	13 (1.4%)
175.0	mrst2001	1.0	837	12 (1.4%)
175.0	mrst2001	2.0	739	11 (1.5%)
177.5	cteq6.1	0.5	846	31 (3.7%)
177.5	cteq6.1	1.0	758	28 (3.7%)
177.5	cteq6.1	2.0	670	25 (3.7%)
177.5	mrst2001	0.5	875	13 (1.5%)
177.5	mrst2001	1.0	784	11 (1.4%)
177.5	mrst2001	2.0	693	10 (1.4%)

Table 1.4: *Results for the top pair cross section. The most right column is the error due to the PDF tolerance range calculated with eq. (1.14). The renormalization and factorization scales equal* $\mu_R = \mu_F = \mu$.

PDF group	μ_R/m_t	μ_F/m_t	$\sigma_{t\bar{t}}$ (pb)	$\pm$ error (pb)
cteq6.1	0.5	0.5	904	32 (3.6%)
cteq6.1	0.5	1.0	891	32 (3.6%)
cteq6.1	0.5	2.0	885	33 (3.7%)
cteq6.1	1.0	0.5	826	29 (3.5%)
cteq6.1	1.0	1.0	809	29 (3.6%)
cteq6.1	1.0	2.0	797	29 (3.7%)
cteq6.1	2.0	0.5	749	26 (3.5%)
cteq6.1	2.0	1.0	730	26 (3.6%)
cteq6.1	2.0	2.0	715	26 (3.7%)

Table 1.5: *Dependence on both the renormalization and the factorization scales. We only state the top pair cross section for CTEQ6.1 at* $m_t = 175$ *GeV. The most right column is the error due to the PDF tolerance range.*

PDF group	μ/m_W	σ_{W^+} (nb)	$\pm$ error (nb)
cteq6.1	0.5	10.94	.54 (4.9%)
cteq6.1	1.0	11.34	.54 (4.8%)
cteq6.1	2.0	11.66	.56 (4.8%)
mrst2001	0.5	11.06	.23 (2.1%)
mrst2001	1.0	11.40	.23 (2.0%)
mrst2001	2.0	11.71	.24 (2.0%)

Table 1.6: *Results for $\sigma(W^+ \to \mu^+ + \nu_\mu)$. The most right column is the error due to the PDF tolerance range. The renormalization and factorization scales equal $\mu_R = \mu_F = \mu$.*

top mass (GeV)	PDF group	μ/M	Ratio ($\times 10^{-2}$)	$\pm$ error ($\times 10^{-2}$)
172.5	cteq6.1	0.5	8.80	.71 (8.1%)
172.5	cteq6.1	1.0	7.63	.61 (8.0%)
172.5	cteq6.1	2.0	6.56	.54 (8.2%)
172.5	mrst2001	0.5	9.04	.30 (3.3%)
172.5	mrst2001	1.0	7.85	.26 (3.3%)
172.5	mrst2001	2.0	6.75	.23 (3.4%)
175.0	cteq6.1	0.5	8.23	.67 (8.1%)
175.0	cteq6.1	1.0	7.14	.58 (8.1%)
175.0	cteq6.1	2.0	6.13	.51 (8.3%)
175.0	mrst2001	0.5	8.46	.28 (3.3%)
175.0	mrst2001	1.0	7.34	.25 (3.4%)
175.0	mrst2001	2.0	6.31	.22 (3.5%)
177.5	cteq6.1	0.5	7.70	.63 (8.2%)
177.5	cteq6.1	1.0	6.70	.55 (8.2%)
177.5	cteq6.1	2.0	5.74	.48 (8.4%)
177.5	mrst2001	0.5	7.92	.27 (3.4%)
177.5	mrst2001	1.0	6.88	.23 (3.3%)
177.5	mrst2001	2.0	5.91	.20 (3.4%)

Table 1.7: *Results for the ratio of $\sigma(t\bar{t})/\sigma(W^+ \to \mu^+ + \nu_\mu)$, where M is either m_t or m_W. The most right column is the error due to the PDF tolerance range.*

1.2.3 Conclusion

As pointed out earlier the choice of tolerance of the two PDF groups is not trivial. The CTEQ group chose a tolerance twice as large as the MRST group did and we immediately see this translated in a larger error. Besides this discrepancy, we see that the averages for both the top pair and the W cross sections tend to be higher in the MRST calculations. These differences make that in our view the most conservative choice is the outcome with the largest error range, that is the outcome of the CTEQ group. The largest error by far is still due to the variance of renormalization and factorization scale. Combining all errors we come to a final value with $m_t = 175$ GeV of

$$\sigma_{t\bar{t}} = 809^{+95(11.7\%)}_{-94(11.6\%)} \pm 29(3.6\%) \text{ pb.} \tag{1.16}$$

The $^{+95}_{-94}$ is the error due to scale variance and the ± 29 is the consequence of the PDF tolerance range. The latter coincides with the difference between the cross sections of the MRST and of the CTEQ group.

Concerning the ratio of the top pair cross section to the $(W^+ \to \mu^+ + \nu_\mu)$ cross section the conclusion is that as well as for the scale variation as for the PDF tolerance range an anti-correlation is present. The average ratio and its errors are

$$\left(7.1^{+1.09(15\%)}_{-1.01(14\%)} \pm 0.58(8.1\%)\right) \cdot 10^{-2}. \tag{1.17}$$

The $^{+1.09}_{-1.01}$ is the error due to scale variance and the ± 0.58 is the consequence of the PDF tolerance range. Compared to eq.(1.16) the error due to the PDF tolerance has more than doubled to 8.1% and the error due to scale variation has grown with a few percent. The idea that certain systematic uncertainties might diminish in this ratio is clearly not applicable to these two errors.

Going from NLO to NLO+NLL

In [35] a similar analysis is performed including the newest top mass measurement, and including calculations up to NLO+NLL with the new PDF sets CTEQ6.5 [22] and MRST2006nnlo [41]. First, the authors also state the results for the top pair cross section at NLO:

$$\text{CTEQ6.5}: \quad \sigma^{NLO}_{t\bar{t}} = 875^{+102(11.6\%)+30(3.4\%)}_{-100(11.5\%)-29(3.3\%)} \text{ pb, with } m_t = 171 \text{ GeV.} \tag{1.18}$$

Taking into account the dependence of the cross section on the top mass this is in agreement with the result of eq. (1.16). More interesting is the observation of the authors that the renormalization and factorization scales should not be kept equal when going to NLO+NLL: with $\mu_F = \mu_R$ the scale uncertainty reduces to no more than $^{+7\%}_{-5\%}$, yet when the two scales are independent the end result is

$$\text{CTEQ6.5}: \quad \sigma^{NLO+NLL}_{t\bar{t}} = 908^{+82(9.0\%)+30(3.3\%)}_{-85(9.3\%)-29(3.2\%)} \text{ pb.} \tag{1.19}$$

$$\text{MRST2006nnlo}: \quad \sigma^{NLO+NLL}_{t\bar{t}} = 961^{+89(9.2\%)+11(1.1\%)}_{-91(9.4\%)-12(1.2\%)} \text{ pb.} \tag{1.20}$$

Here the two scales are independently varied in the full range of $0.5 < \mu_i/m_t < 2.0$ and the positive/negative errors are calculated at the points (μ_R, μ_F) resulting in the largest positive/negative offset. The results show a significant difference between the CTEQ and the MRST cross sections. As the difference is larger than the uncertainty due to the PDF tolerance range, we can only conclude that the latter is somewhat underestimated.

1.3 Supersymmetry

The Standard Model (SM) describes accurately most of the properties of the fundamental particles observed in nature so far. There are indications however that the model is not complete, the most important of which come from:

- **Gravity.** The fourth fundamental force known in nature is not accounted for in the SM.
- **The neutrino.** In the SM this particle is massless, yet from [10,11] we know this is not the case.
- **Dark matter and dark energy.** The SM describes no more than 4% of all matter and energy present in the universe. The remaining 96% is called dark matter (20%) and dark energy (76%), yet what it consists of is unknown.
- **Unification.** Why is the SM described by the $SU(3) \times SU(2)_L \times U(1)_Y$ group? Is there a larger group in which all three forces can be unified?
- **Unnaturalness.** The scalar Higgs mass m_h is the only 'unprotected' mass in the SM and in the renormalization of m_h unnatural fine-tuning might be necessary.

In Section 1.3.2 we describe some of these problems in more detail. Together with other unanswered questions, these problems make it clear that new physics must lie beyond the Standard Model. Several theories and models have been postulated in the last few decades. In this section we describe only one, that is supersymmetry.

Supersymmetry implies a symmetry between the bosonic and fermionic fields in the Lagrangian. Similar to for example the $SU(2)$ symmetry that exists between the up and down quark, supersymmetry relates bosons to fermions in supermultiplets (or superfields). It is not possible for the Standard Model to be supersymmetric, therefore if the symmetry is applied, it is an extension of the theory and it doubles the particle spectrum as we know it.

The first generation of leptons, denoted in a $SU(2)$ doublet L, is thus related to the doublet of scalar leptons (sleptons) $\widetilde{L}$ in a superfield $\hat{\Phi}$. The scalar partners of the quarks are called squarks and the fermionic partners of the gauge bosons are called gauginos. The fermionic partners of the Higgs bosons are called Higgsinos. As these superparticles have never been observed and thus cannot have the same masses as their Standard Model partners, supersymmetry is thought to be broken. This results in masses too large for the superparticles to have been found yet, but which may become accessible with the LHC.

In the Standard Model lepton and baryon number are conserved by gauge invariance and renormalizability. With supersymmetry these conservations do not hold anymore. Lepton and baryon number can be preserved by demanding conservation of R-parity, which is a discrete multiplicative symmetry and defined by

$$R_p = (-1)^{3B+L+2S}. \tag{1.21}$$

The B is the baryon number, L is the lepton number and S is the spin of a particle. Standard Model particles have $R_p = +1$, whereas the superparticles have $R_p = -1$. This symmetry[17)]

[17)] With n_q the number of quarks and n_l the number of leptons, the baryon and lepton number are simply given by

$$B = \frac{n_q - n_{\overline{q}}}{3} \quad \text{and} \quad L = n_l - n_{\overline{l}}, \tag{1.22}$$

forbids a superparticle to decay into only Standard Model particles. A phenomenological consequence is that superparticles are always produced in pairs, and each superparticle decay must result in one stable superparticle, often called the Lightest Supersymmetric Particle (LSP).

1.3.1 Supersymmetric transformations

Before we discuss the phenomenological aspects of supersymmetry we want to give the reader a brief impression of the theoretical implementation. For a more elaborate introduction we refer the reader to [42–44]. If we start with space-time translation, we remember that for an infinitesimal translation $x'_\mu = x_\mu + \varepsilon_\mu$ we may write for a scalar field $\phi(x)$:

$$U\phi(x)U^{-1} = \phi(x'), \text{ where } \quad U = 1 + i\varepsilon^\mu P_\mu. \tag{1.23}$$

The four operators P_μ are the generators of the transformation. These generate space-time displacements and have the 4-momenta as conserved charge. We can write

$$\phi(x+\varepsilon) \quad = \quad \phi(x) + \delta\phi(x), \tag{1.24}$$

where

$$\delta\phi(x) \quad = \quad i\varepsilon^\mu \left[P_\mu, \phi(x)\right] = \varepsilon^\mu \partial_\mu \phi(x). \tag{1.25}$$

What does the supersymmetric equivalent of the above translation look like? If the supersymmetric operator Q is to translate a boson field into a fermion field as in $Q|\phi\rangle = |\psi\rangle$, the operator itself must carry spinor indices, such as Q_a. It also implies that space-time itself is extended with fermionic degrees of freedom to *superspace*:

$$(x_\mu) \quad \rightarrow \quad (x_\mu, \theta, \overline{\theta}). \tag{1.26}$$

These new dimensions have as components Grassmann numbers which obey anti-commuting rules. For the two numbers θ and η for example we have that

$$\{\theta, \eta\} = 0 \quad \rightarrow \quad \theta\eta = -\eta\theta. \tag{1.27}$$

Thus supersymmetry introduces a new dimension, one that is only defined quantum mechanically and does not possess classical properties, such as continuous extent. The operator for the transformation is given by

$$Q_a \quad = \quad i\frac{\partial}{\partial\theta^a} + \theta^{b\star}(\sigma^\mu)_{ba}\partial_\mu \tag{1.28}$$

and obeys

$$\{Q_a, Q_b^\dagger\} \quad = \quad i(\sigma^\mu)_{ab}\partial_\mu = (\sigma^\mu)_{ab}P_\mu. \tag{1.29}$$

The σ^μ are the three Pauli matrices together with the identity matrix.[18)] We note that more general supersymmetric algebras exist, in which the single generator Q_a is replaced by N generators $Q_a^A(A = 1, 2, ...N)$. Due to phenomenological constraints usually only the $N = 1$ algebra is considered.

It is here that we can grasp the far-reaching effect that supersymmetry has. Looking at eq.(1.29) we see that if we perform two supersymmetric transformations generated by Q we

[18)]Some authors use a different normalization resulting in the anti-commutation rule of eq. (1.29) with a factor 2 on the RHS. Here we have adopted the convention of [42].

get the energy-momentum operator P_μ. This means that we can read the operator Q as the square root of the 4-momentum derivative, just like the Dirac equation can be seen as the square root of the Klein-Gordon equation [42, 45, 46].

Although it is hard to visualize such an extension of our four-dimensional space-time, we can compare this with $i = \sqrt{-1}$. With one simple definition we can extend any real dimension into a complex plane. Superspace is to be understood in a similar way: the space-time coordinates are extended to include *fermionic* degrees of freedom, which are connected to the standard ones by means of transformations generated by Q. The interlock of the operator with space-time derivatives also gives us one of the first hints on how supersymmetry can help bridge the gap to the theory of general relativity and provide a quantum field theory of gravity. In fact, any theory with local supersymmetry must be a theory of gravity. Gravity supermultiplets can thus be constructed containing a spin-2 graviton and a spin-3/2 gravitino, see [43, 44].

1.3.2 Motivation for supersymmetry

The theory of supersymmetry was developed in the seventies[19)], even the extensions of supergravity were already firmly established in 1976 [48, 49]. At the moment the theory is probably the most popular extension of the Standard Model, not only due to its aesthetic appeal, and partly also maybe due to the lack of sound theoretical alternatives, but also due to the possibility of it solving some long standing problems in high energy physics. We will now mention a few of the phenomenological motivations.

Naturalness

One of the most important consequences of supersymmetry is probably the protection of the scalar mass. We can explain this with the diagrams in Fig. 1.12, depicting three contributions to the self-energy of the scalar propagator. With q the momentum of the scalar particle and p and $q-p$ the momenta of the loop particles the three diagrams equal:

$$\Delta_I = A \int d^4p \frac{p^2 + \frac{1}{4}q^2 + m^2}{((p+\frac{1}{2}q)^2 + m^2)((p-\frac{1}{2}q)^2 + m^2)} \tag{1.30}$$

$$\Delta_{II} = -B^2 \int d^4p \frac{p^2 - \frac{1}{4}q^2}{((p+\frac{1}{2}q)^2 + m^2)((p-\frac{1}{2}q)^2 + m^2)} \tag{1.31}$$

$$\Delta_{III} = A^2 \int d^4p \frac{m^2}{(p^2 + m^2)((p-q)^2 + m^2)} \tag{1.32}$$

where m is the scalar Higgs mass. A is the scalar self-coupling and $-B^2$ is the -1 of a fermion loop times the scalar-fermion coupling squared. This symbolic notation is chosen to explain the following: the first two expression Δ_I and Δ_{II} contain a quadratic and a logarithmic divergency. In the Standard Model A can only be the self-coupling of the Higgs, while B is dominated by the top yukawa coupling. the result is $A - B^2 \neq 0$ and we remain with a quadratic divergency. In supersymmetric theories the sum however does cancel, as for each bosonic loop a partner fermionic loop is present. The total sum is always $A - B^2 = 0$ and we remain with only the logarithmic divergencies. The third diagram results in Δ_{III} with only a logarithmic divergency.

[19)]For an excellent overview of the early history of supersymmetry we like to refer the reader to [47].

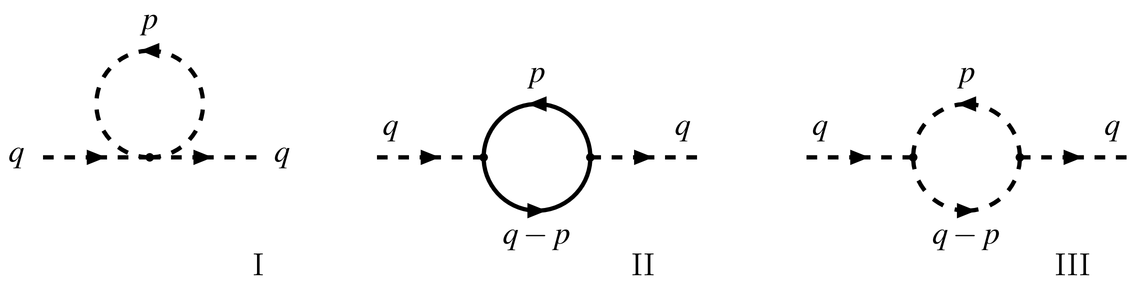

Figure 1.12: *Three contributions to the renormalization of the scalar mass. Solid lines are fermion lines, dashed lines represent scalar fields. The momenta are depicted by p and q.*

The difference between a quadratic and logarithmic divergence becomes more clear if we apply the cut-off scheme to the diagrams above. With the integral going up to a scale Λ we can see by simply counting the powers of p in the integral that

$$\Delta_I \sim -\Delta_{II} \sim \Lambda^2 + m^2 \ln \Lambda. \tag{1.33}$$

Summing all self-interactions in a δm we define the bare mass m_0 such that the physical mass m_h equals

$$m_h^2 = m_0^2 + \delta m^2. \tag{1.34}$$

If new physics lies beyond the Standard Model at say an energy scale of Λ_X we can set $\Lambda = \Lambda_X$, in the case of no new physics the cut-off must be set to the Planck scale at 10^{19} GeV, at which gravity starts to play a role. Thus a quadratic divergency could imply a fine-tuning up to O(10^{38} GeV) for m_h to lie in the expected region of 10^2 GeV [50], while a logarithmic divergency would be of the order of the mass m. This is called the problem of *unnaturalness*.

With exactly an equal amount of fermionic as bosonic fields supersymmetry thus ensures that all the quadratic divergencies from the fermionic loops cancel with those from the bosonic loops; we say that the symmetry protects the scalar mass. In Section 1.1.1 we stated that divergencies are no problem as long as the theory as a whole is proved to be renormalizable. This applies to both quadratic and logarithmic divergencies, so one might wonder what the need is for supersymmetry.

It turns out that the quadratic divergency of the scalar mass is the only quadratic divergency in the Standard Model. In the renormalization of the fermionic mass for example we also have fermionic loops as in diagram II of Fig. 1.12. These are however exactly canceled out, which is subscribed to the chiral symmetry of the theory protecting the fermionic masses. With the gauge bosons protected by gauge symmetry[20)], only the scalar mass goes unprotected. Again, there is nothing ‘wrong’ with this, the Standard Model is renormalizable, yet to many physicists fine-tuning remains too unpleasing.

We mentioned before that supersymmetry must be broken; if the symmetry is to protect the scalar mass, the above implies that the breaking of supersymmetry cannot be at too high an energy level. It is expected to lie at most in the TeV region, bringing it in reach of the LHC.

[20)] Here we neglect the masses of the W and the Z which are a consequence of the spontaneous symmetry breaking of the electro-weak theory.

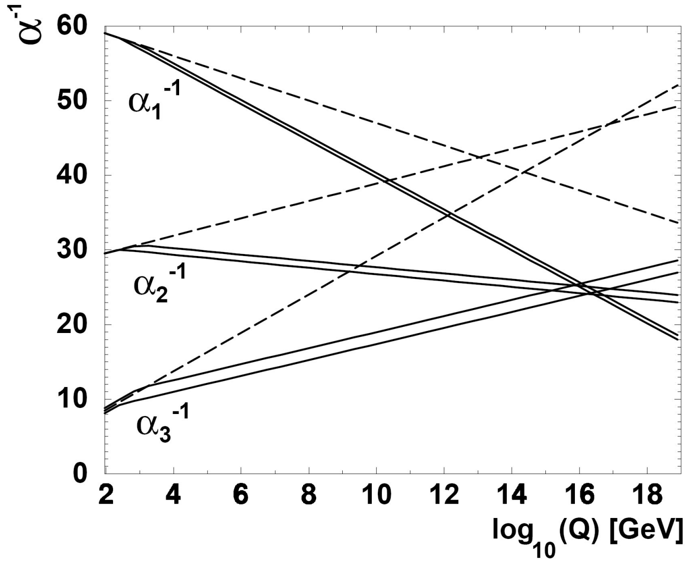

Figure 1.13: *Evolution of the three coupling constants in the Standard Model (dashed lines) and in supersymmetric theories (solid lines). The latter is depicted in case supersymmetry breaking occurs at 250 GeV (lower solid lines) or at 1 TeV (upper solid lines).*

Unification of the coupling constants

Just as the electromagnetic and the weak force are unified in the electro-weak theory, there have been many attempts to unify the three forces in a Grand Unified Theory (GUT). A natural way to do this would be by embedding $SU(3) \times SU(2) \times U(1)$ in a larger symmetry group. This larger symmetry would have to be broken at a higher energy scale, such that by the RGEs we would obtain the coupling constants as we know them.

Turned around, we can try to find the unification scale by evolving the coupling constants up to higher scales. It turns out that with the RGE from only the Standard Model particles this does not work, see [51]. In Fig. 1.13 we can see how the couplings do not unify.[21)] If however new particles exist, such as the supersymmetric partners, the RGEs of the couplings change. In Fig. 1.13 the possible evolution of the couplings is depicted in case the supersymmetry breaking scale lies at 250 GeV or at 1 TeV. We note that there are many different implementations of supersymmetry, and not all result in the same RGEs. This figure merely serves to illustrate the possibility of unification.

As mentioned before, another problem supersymmetry might help solve is the unification of the Standard Model forces with gravity, see [43, 44].

Dark matter

With the Standard Model only up to 4% of all matter and energy in the universe can be accounted for. A total of 20% is only measurable through gravity; it must be non-baryonic and is called the dark matter, see [53]. 76% of the total is called the dark energy, which is thought to cause the measured acceleration of the expansion of the universe, see [43, 44].

[21)] Taken from [52].

Supersymmetric models that obey the R-parity conservation, see eq. (1.21), predict the presence of a stable Lightest Supersymmetric Particle (LSP). If produced under the correct circumstances at the Big Bang this particle could account for all the dark matter in the universe. We come back to this in Section 1.3.4.

1.3.3 Minimal Supersymmetric Standard Model

In the Standard Model one complex Higgs doublet couples to the fermions and gauge bosons. After the electro-weak symmetry breaking three degrees of freedom from the doublet form the masses of the W and Z boson, and we are left with one Higgs particle. Because of the structure of supersymmetric theories (contrary to the SM, supersymmetric models do not allow complex conjugates), two Higgs doublets of opposite hypercharge are needed to generate the masses of the up-type and of the down-type quarks: the H_u with hypercharge $Y = +1/2$ and the H_d with $Y = -1/2$. With again three degrees of freedom forming the gauge boson masses, we are left with five scalar Higgs particles denoted by h^0, H^0, A^0, H^+ and H^-.

Since no superparticles have been observed yet, supersymmetry must be broken if present in nature. There are no phenomenological satisfying theories known with a spontaneous breaking of the symmetry[22)] and the breaking is usually parameterized by introducing mass terms for the superparticles. For more details on the exact parametrization we refer the reader to for example [43, 44], here we only want to mention that by breaking of the supersymmetry, the spontaneous symmetry breaking in the Higgs sector comes naturally.[23)] The ratio of the vacuum expectation values (vevs) of the neutral Higgs components is usually written as

$$\tan\beta = \frac{\langle H_u \rangle}{\langle H_d \rangle} \tag{1.35}$$

and at tree level the mass of the lightest Higgs h^0 is to satisfy $m_{h^0} \leq m_Z|\cos 2\beta|$. This is experimentally excluded. Taking into account large radiative corrections from mainly tops and stops the upper limit can be raised, but it cannot exceed approximately 135 GeV [56]. If the theory is allowed to be extended with extra singlets, see for example [57], this upper limit can be raised further. The model in [57] has an upper limit of 168 GeV, or 195 GeV if several constraints are neglected [58].

Experimental results combined with only Standard Model calculations prefer a Higgs mass around 90 GeV [50]. With the lower bound from LEP set at $m_h = 114.4$ GeV at 95% confidence level [50], supersymmetry might explain its relative large mass; that is of course if it exists. If the Tevatron or the LHC can exclude the full range up to O(200) GeV for the Higgs mass, both supersymmetry and the Standard Model are in trouble.

The particle content

In Table 1.8 we see left the superpartners of the Standard Model fields. The squarks and sleptons are spin-0 particles, the gauginos and Higgsinos are spin-1/2. The L- and R-labeling does *not* refer to the handedness or the chirality of the sparticles, as the sparticles are bosons. The labels merely serve as to indicate the relation with the fermions in Table 1.1. (In an

22) The Fayet-Iliopoulos breaking [54] and the O'Raifeartaigh breaking [55] are examples, yet these are non-compatible with the Standard Model.

23) That is, in large parts of the parametrization phase space. As this is a great benefit of supersymmetry, we restrict our discussion only to models including this property.

	Fields			Mass eigenstates		
Squarks	$(\widetilde{u},\widetilde{d})_L$	$(\widetilde{c},\widetilde{s})_L$	$(\widetilde{t},\widetilde{b})_L$	$\widetilde{u}_L,\widetilde{u}_R$	$\widetilde{c}_L,\widetilde{c}_R$	$\widetilde{t}_1,\widetilde{t}_2$
	$\widetilde{u}_R$	$\widetilde{c}_R$	$\widetilde{t}_R$	$\widetilde{d}_L,\widetilde{d}_R$	$\widetilde{s}_L,\widetilde{s}_R$	$\widetilde{b}_1,\widetilde{b}_2$
	$\widetilde{d}_R$	$\widetilde{s}_R$	$\widetilde{b}_R$			
Sleptons	$(\widetilde{\nu}_e,\widetilde{e})_L$	$(\widetilde{\nu}_\mu,\widetilde{\mu})_L$	$(\widetilde{\nu}_\tau,\widetilde{\tau})_L$	$\widetilde{\nu}_e$	$\widetilde{\nu}_\mu$	$\widetilde{\nu}_\tau$
	$\widetilde{e}_R$	$\widetilde{\mu}_R$	$\widetilde{\tau}_R$	$\widetilde{e}_L,\widetilde{e}_R$	$\widetilde{\mu}_L,\widetilde{\mu}_R$	$\widetilde{\tau}_1,\widetilde{\tau}_2$
Gauginos	$\widetilde{g}$			$\widetilde{g}$		
	$\widetilde{B},\widetilde{W}_1,\widetilde{W}_2,\widetilde{W}_3$			$\widetilde{\chi}^{\pm}_{1,2}$	(Charginos)	
Higgsinos	$\widetilde{H}_u,\widetilde{H}_d$			$\widetilde{\chi}^{0}_{1,2,3,4}$	(Neutralinos)	

Table 1.8: *Left: the supersymmetric partners of the Standard Model particle fields. Right: in the mSUGRA model the mass eigenstates are mixtures of the fields. The L- and R-squarks and the L- and R-sleptons can mix into two states, denoted simply by their increasing mass with 1,2. The mixing is usually negligible in the first two generations. The gauginos and Higgsinos mix into the charginos and neutralinos, except for the gluinos.*

unfortunate terminology the '+'chirality of a fermion in the Standard Model is denoted by 'R' and the '$-$'chirality is denoted by 'L'.) Due to mixing the mass eigenstates of the superfields are combinations of the L- and R-sparticles. The resulting mixing is mainly important for the third generation and the eigenstates are called $\widetilde{t}_{1,2}, \widetilde{b}_{1,2}$ and $\widetilde{\tau}_{1,2}$. We note that the gaugino and Higgsino fields also mix, with an exception for the gluinos. The mass eigenstates are the two charginos $\widetilde{\chi}^{\pm}_{1,2}$ and the four neutralinos $\widetilde{\chi}^{0}_{1,2,3,4}$. The indices $1,2\ldots$ classify the increasing mass.

The Minimal Supersymmetric Standard Model (MSSM) is the supersymmetric extension of the Standard Model with the minimal particle content as listed in Table 1.8 and with R-parity conservation[24)]. The breaking is parameterized and introduces 105 new parameters in addition to the Standard Model ones. This parameterization is a consequence of our ignorance, we do not know how the symmetry truly is broken. Once we understand the supersymmetry breaking the number of parameters will be drastically reduced.

It is usually assumed that the breaking occurs in a hidden sector, where through some weak interaction radiative corrections lead to supersymmetry breaking. There are many of such models, the most popular probably are the gauge mediated symmetry breaking [59] and the gravity mediated symmetry breaking. We restrict ourselves to the latter, that is supergravity. With its promises to unify the Standard Model with gravity and to perhaps identify the dark matter it is one of the most attractive theories.

1.3.4 Minimal supergravity

Simply assuming gravity to be the source of symmetry breaking is of course not enough, we still remain with 105 new free parameters. The approach in dealing with this, is restricting ourselves to certain parts of the phase space by experimental limits and applying certain assumptions. For the minimal supergravity model (mSUGRA) it is assumed that at the GUT scale all scalars, be it squarks, sleptons or Higgs bosons, have a common mass m_0. All the gauginos and higgsinos have a common mass $m_{1/2}$ and all the trilinear Higgs-sfermion-sfermion couplings

[24)] In some models the R-parity conservation is not implemented, see for more information [52].

have a common value A_0, see [43,44]. These restrictions are not completely out of the blue; the common masses are suggested by the fact that gravity is universal and limits on for example the decay of the $\mu \to e+\gamma$ and on CP violation hint in the direction of these constraints, yet we do emphasize that these are but assumptions helping to restrict the total phase space. Altogether there are five free parameters left in mSUGRA, or better four and a half:

$$m_0, \quad m_{1/2}, \quad A_0, \quad \tan\beta \quad \text{and} \quad \text{sgn}(\mu) = \pm, \tag{1.36}$$

where μ is the bilinear coupling between the two Higgs fields. With these parameters and the RGEs all couplings and the entire mass spectrum can be determined. For dedicated studies a few benchmark points have been agreed upon within the ATLAS collaboration, see [60]. Table 1.9 lists five of them.

The effect of the five free parameters on the mSUGRA mass spectrum can be summarized as follows:

- The parameters m_0 and $m_{1/2}$ have the largest impact on the mass spectrum of the superparticles. With an increasing $m_{1/2}$ all mass values increase. With increasing m_0 all squark and slepton masses become larger, while the remaining sparticles are mostly insensitive to the m_0, see [61].
- The reason that the sign of μ is positive in all the benchmark points is that the effect of the sign on the mass spectrum is negligible compared to the other parameters. The parameter space for $\mu < 0$ is also more restricted than for $\mu > 0$ due to the muon anomalous magnetic moment $(g-2)_\mu$ measurements, see for example [62], and due to dark matter constraints: if dark matter is to be an LSP it must consist of a neutral particle, yet for $\mu < 0$ and low $\tan\beta$ the stau becomes the LSP.
- The most important consequence of the A_0 value is for the h^0 mass, which becomes larger as A_0 gets more negative. The Higgs mass can shift by +10 GeV when A_0 goes from +1000 to -1000. A different impact of the A_0 parameter is on the stop mass. For an increasing value of $|A_0|$ the lightest stop mass becomes smaller, especially if $\tan\beta$ is large.
- As for $\tan\beta$ we can say that for larger values the heavy Higgses and the third generation sfermions become lighter; the mass splitting for the sfermions in the third generation also increases resulting in relatively light $\tilde{\tau}_1$ and $\tilde{t}_1$.

The cross section for the total production of supersymmetric particles mostly depends on the masses of the initial pair of superparticles produced, which at the LHC are expected to

Name (Label)	m_0 (GeV)	$m_{1/2}$ (GeV)	A_0 (GeV)	$\tan\beta$	sgn(μ)	σ^{NLO} (pb)
Coannihilation (SU1)	70	350	0	10	+	10.86
Focus Point (SU2)	3550	300	0	10	+	7.18
Bulk (SU3)	100	300	-300	6	+	27.68
Low Mass (SU4)	200	160	-400	10	+	402.19
Funnel (SU6)	320	375	0	50	+	6.07

Table 1.9: *Five of the ATLAS benchmark points in the mSUGRA parameter space. The naming finds its origin mostly in the dark matter constraints (see text for more details). The cross sections listed are at 14 TeV center-of-mass energy.*

be the $\widetilde{g}, \widetilde{u}, \widetilde{d}$ and in some cases the $\widetilde{t}_1$. Especially for larger values of $\tan\beta$ combined with a large value for $|A_0|$ this last channel is more present. In this thesis we only study the SU3 and SU4 benchmark points. For both models the mass of the $\widetilde{t}_1$ lies above the top quark mass and it often decays through a top. Especially in the SU4 model the stop mass is relatively small: $m_{\widetilde{t}_1} = 206$ GeV.

Dark matter constraints

If the neutralino is to be the dark matter constituent, the measurements from WMAP [53] are among the strongest constraints on the mSUGRA parameter space. Over the majority of the phase space the neutralino dark matter is expected to be overproduced relative to the observed dark matter. Therefore models with annihilation of the LSP in the high-density early universe are needed.

Several regions in the parameter space have been identified as suitable. These are classified as the stau coannihilation, the focus point, the bulk and the A-funnel region, see [62,63]. These names are also used to define the benchmark points, see Table 1.9. Figure 1.14 depicts the $(m_{1/2}, m_0)$ plane with $A_0 = 0, \tan\beta = 50$ and $\mu > 0$. The upper left corner of the phase space is ruled out by experimental bounds on the chargino mass, the lower right corner is ruled out as the stau becomes the LSP. The light gray area spanning most of the space in between is favored by measurements on the muon's magnetic moment, while the limit of $m_h = 114$ GeV is drawn by a solid line; the allowed space lies to the right of this boundary.

The Focus point is the narrow band near the upper left corner, while the coannihilation region is the narrow band near the boundary of the stau LSP region. The bulk region is the parameter space with low m_0 and $m_{1/2}$, which in some cases enables the neutralino to annihilate efficiently. The A-funnel region is not visible in this specific parameter space.

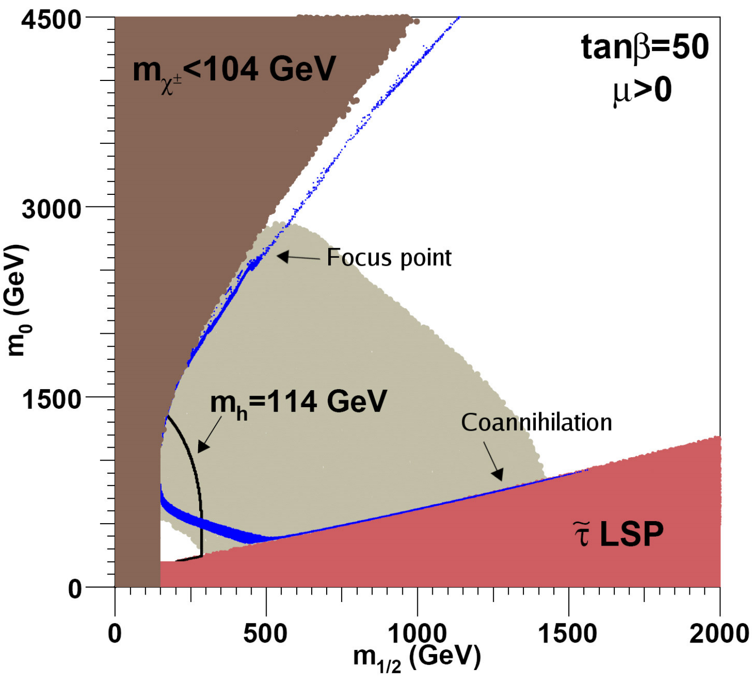

Figure 1.14: *The $(m_{1/2}, m_0)$ phase space in the mSUGRA model with $A_0 = 0$, $\tan\beta = 50$, $\mu > 0$.*

Chapter 2

LHC and the ATLAS detector

CERN is a particle physics laboratory located on the border of Switzerland and France, near Geneva. From 1989 to 2000 it operated LEP, the most powerful lepton accelerator ever built, and from now on CERN's main facility is the LHC, the Large Hadron Collider. Built in the same tunnel as LEP was, 27 km long and between 50 to 100 m under ground, the LHC is now the largest and most energetic hadron collider ever constructed.

2.1 The Large Hadron Collider

The LHC accelerates bunches of protons or heavy ions in both directions along its ring. At four different points the bunches cross and the particles can collide. The LHC will collide protons on protons at a maximum center-of-mass energy of 14 TeV. To reach such energies the particle beams are accelerated in different steps: injected in the Proton Synchrotron Booster (PSB) by the LINAC the beams are accelerated to 1.4 GeV. The Proton Synchrotron (PS) and Super Proton Synchrotron (SPS) increase this energy up to 26 and 450 GeV respectively and inject the particles in the LHC, where each beam is accelerated to 7 TeV.

In Fig. 2.1 we see an overview of the CERN accelerators and the experiments at the four collision points. The ALICE experiment (A Large Ion Collider Experiment) is dedicated to study heavy ion collisions. LHCb is an experiment dedicated to study CP-violation, while CMS

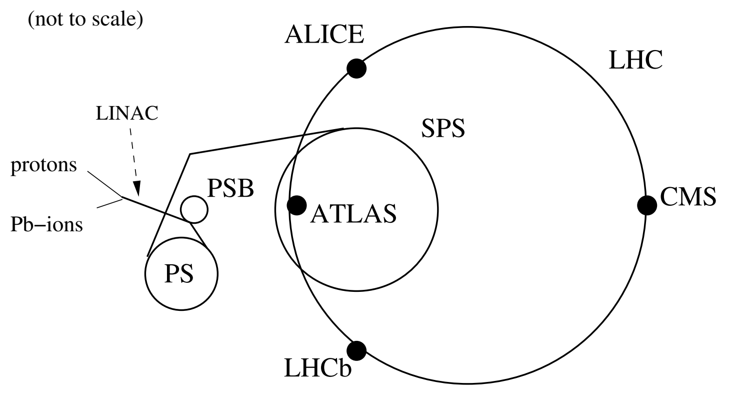

Figure 2.1: *Overview of the CERN accelerators and four experiments.*

(Compact Muon Solenoid) and ATLAS (A Toroidal LHC ApparatuS) are two general purpose detectors.

To reach 7 TeV, the beams are accelerated in the LHC by RF-cavities and their path is bent along the ring by super-conducting dipole magnets providing a 8.36 Tesla magnetic field. The two beam-pipes in the dipole magnets, necessary to circulate the protons in opposite directions, are embedded in one single iron yoke. The super-conducting coils around both beam-pipes are made of copper-clad niobium-titanium cables and carry currents up to 15 kA. The dipoles are cooled by super-fluid Helium, keeping the temperature at 1.9 K. For more technical details on the LHC machine we refer to [64].

The two beams each consist of multiple bunches of protons which cross each other inside the four experiments along the ring. The rate at which hard scatterings take place depends, among other things, on the luminosity $L = fnN^2/A$; f is the revolution frequency, n is the number of bunches in each beam, N is the number of particles in each bunch and A is the cross section of the beam. In the LHC the luminosity will be ramped up to a design level of 10^{34} s^{-1}cm^{-2}. To reach this level, the bunches in LHC will consist of 10^{11} protons and almost 3000 bunches will circulate in each ring. A normal beam life-time is around 10 hours, this is limited by beam losses due to collisions and imperfections. With the high density of particles per bunch each crossing can result in multiple scatterings, resulting in so-called pile-up events. We come back to this shortly.

In the early phase the luminosity will be two or three orders of magnitude lower. On the 10$^{\text{th}}$ of September 2008 the first beams were circulated in the LHC. Unfortunately a bad soldering between two superconducting magnets caused the breakdown of the LHC on September 19$^{\text{th}}$. The commissioning was halted and repairs were made in the winter of 2008/2009. The new turn on of the LHC is now planned for the end of 2009.

During the commissioning phase the number of bunches will be increased in steps to reach the design level; in Table 2.1 we list the first steps as they are planned at the moment with collisions of 10 TeV center-of-mass energy. We see in the table that the number of events per crossing rises. Once the LHC is at design luminosity this will have increased to an average of 23, while the bunch spacing will have decreased to 25 nsec.

Machine parameters	Step 1	Step 2	Step 3	Step 4	...	Design Level
Bunch intensity	$1.0 \cdot 10^{10}$	$1.0 \cdot 10^{10}$	$4.0 \cdot 10^{10}$	$9.0 \cdot 10^{10}$	...	10^{11}
Number of bunches	1	4	43	156	...	2808
Luminosity [s^{-1}cm^{-2}]	$1.1 \cdot 10^{27}$	$4.5 \cdot 10^{27}$	$2.9 \cdot 10^{30}$	$5.4 \cdot 10^{31}$	...	10^{34}
Events/crossing	$<< 1$	$<< 1$	0.36	1.8	...	23

Table 2.1: *The machine parameters for the commissioning phase for the first collisions of 10 TeV center-of-mass energy. Also shown are the parameters at the LHC design level.*

2.1.1 Minimum bias, pile-up and underlying events

Not all collisions at the LHC will be stored for further analysis. With approximately $\sim 10^9$ events per second at design luminosity the amount of data produced if all events were to be stored would simply be too large. A choice has to be made which events might be interesting and worth keeping the data for. In a particle detector this choice is made by a trigger system which looks for signs of interesting collisions. When searching for interesting hard scatterings there are different types of background we can identify:

- **The minimum bias**: Most interactions between two protons are soft scatterings, i.e. the amount of momentum being exchanged between the protons is small. Not only can perturbative QCD not be applied to soft interactions, see Section 1.1.2, but the physics behind these events is also not what the LHC is designed for to analyze. All in all, the ratio of interesting to non-interesting scatterings, including hard interactions, is small. An average, minimum bias, trigger will thus typically be an uninteresting soft event. Such events can affect the analysis when they form pile-up events to hard scattering.

- **Pile-up events**: A higher density of particles in a bunch increases the chance of multiple scatterings per bunch crossing. When an event is triggered it may happen that in the read-out of that event also the scattering products of other collisions are seen. At the same time, the frequency of scatterings will be so high at the design luminosity of the LHC that events from different bunch-crossings can be read-out simultaneously. The background this creates to the interesting decay channel is defined as pile-up events.

- **The underlying event**: Protons are not elementary particles and the hard scattering is the interaction of the gluon and quark constituents of the two protons. The remnants of the two protons fragment and hadronize resulting in more scattering products in the detector. These form the underlying event.

- Another type of background consists of events not originating from bunch-bunch interactions. *Cosmics* for example, are muons created high in the atmosphere by cosmic radiation. One muon crossing the entire ATLAS detector through its interaction point can thus mimic a back-to-back di-muon event. Another example is *beam-gas* events; these are interactions of the beam with the residual gas molecules present in the vacuum of the beam-pipe.

- The last kind of background we mention is “physics background”: any interesting hard scattering which has the same signature as the signal we are looking for, but in fact originating from a different process. This background is different from the others, as it can resemble the signal at the hard scattering level, making it more difficult to find observables to distinguish the signal from the background.

2.2 ATLAS

ATLAS is one of the two general purpose experiments at the LHC and is designed to explore the physics in the TeV region. Although the protons are accelerated to 7 TeV, the center-of-mass energy of the hard scattering will be lower than 14 TeV. The energy available in the collision is $\sqrt{x_1 x_2 s}$, where x_1 and x_2 are the momentum fractions carried by the two partons participating in the hard scattering. Thus with the ATLAS detector, particles with masses up to several TeV can be searched for, such as possible supersymmetric partners of Standard Model particles, see Section 1.3.

ATLAS consists of several layers of detectors, each with the purpose of measuring specific observables. Figure 2.2 shows a cut-away view of ATLAS. Starting from the inside of ATLAS the detector closest to the interaction point is the Inner Detector (ID), a tracking detector

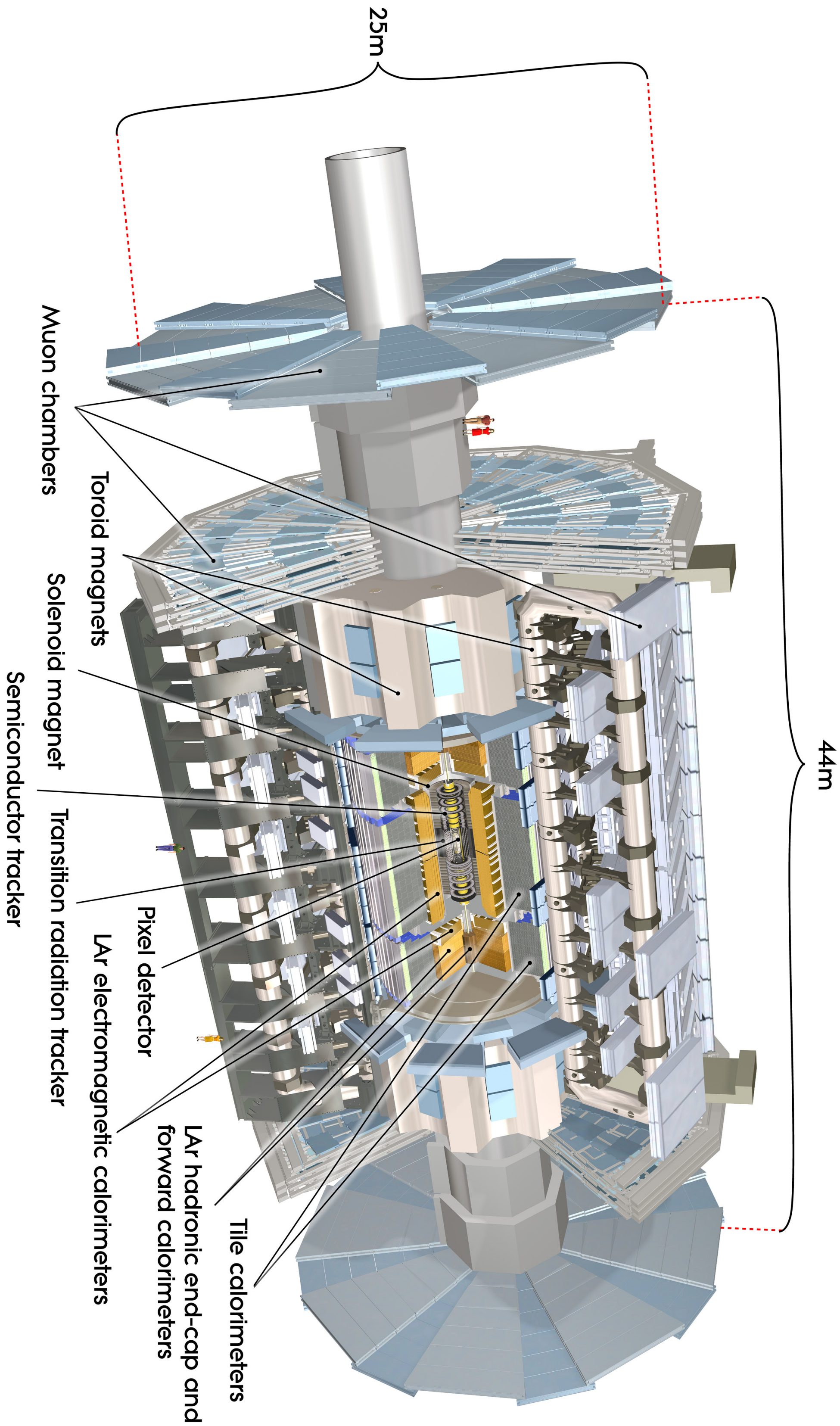

Figure 2.2: *Cut-away view of the ATLAS detector.*

with the purpose of measuring the direction and momenta of charged particles. The momenta can be determined as the particles are deflected by the solenoidal magnet which surrounds the ID; this super-conducting coil generates a field of 2 Tesla oriented along the beam axis. Next in ATLAS are two calorimeters, one to measure the energy from electro-magnetic showers, i.e. the energy from electrons and photons, and second a calorimeter to measure all hadronic energy deposit. The outer layer of ATLAS is the muon spectrometer which measures the momenta of the muons deflected by a toroidal magnetic field. These are, in the Standard Model, the only charged particles able to reach the muon chambers.

The whole detector is built in a cavern along the ring called UX15. On both sides two extra caverns have been built for service tasks, see Fig. 2.3. There is one large area named USA15, located on the outside of the ring, and a smaller area on the inside called US15. The ATLAS control room is located on the surface in building SCX1. We now first define the coordinate system as used in the ATLAS collaboration and then go through all the sub-detectors one by one. We note that a more detailed description of the ATLAS detector is given in [65].

2.2.1 Coordinate system

The coordinates are defined to form a right-handed Cartesian coordinate-system. The z-axis lies parallel to the beam direction at the interaction point and viewed from that point the positive direction for the axis is in the direction towards the LHCb experiment, see Fig. 2.1. The side of ATLAS on the positive z-axis is also referred to as side A, while the opposite side is called side C, and the barrel is B. The positive x-axis points towards the center of the LHC ring and the positive y-axis points upwards. To be correct, the y-axis has a small angle with

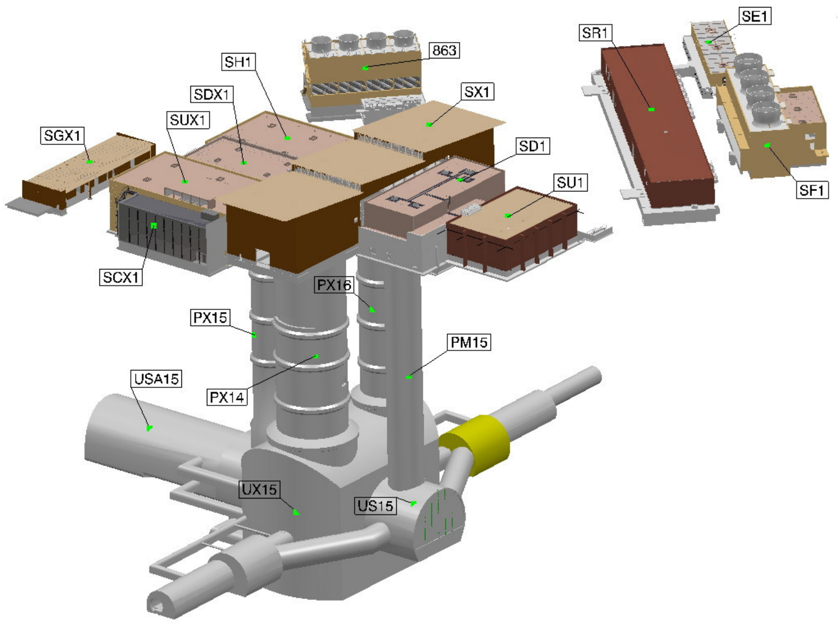

Figure 2.3: *Layout of surface buildings and of access shafts to the ATLAS cavern. The main areas of underground activity are the main cavern (UX15) and the main counting room and service cavern (USA15). The ATLAS control room is in building SCX1 on the surface.*

the vertical (0.704°). Due to geological conditions near Geneva the tunnel was not built in an exactly horizontal plain.

In the ATLAS collaboration an adapted polar coordinate system is used. With the z-axis as described before, a polar coordinate system is defined with an azimuthal angle ϕ with $\phi = 0$ towards the LHC center, in combination with a radial coordinate R and the polar angle θ. This last angle is however replaced by the rapidity

$$y = \frac{1}{2}\ln\frac{E+p_z}{E-p_z} \quad \xrightarrow{m=0} \quad y = -\ln\left[\tan\frac{\theta}{2}\right] \equiv \eta. \tag{2.1}$$

The pseudorapidity η is equal to the rapidity y of a particle if its mass is zero. With the masses of most particles being much smaller than their energies, the pseudorapidity is often used even for massive particles. In this thesis we will be using the pseudorapidity as standard. In other words, whenever the rapidity η is mentioned, the definition of pseudorapidity is used.

The reason for using this transformation of a polar coordinate is the fact that the particle multiplicity distribution in rapidity $(dN/d\eta)$ is basically flat, and the difference in the rapidity of two particles is invariant under Lorentz boosts along the beam axis.

2.3 The Inner Detector

The Inner Detector (ID) is designed to determine to high precision particle momenta and reconstruct the primary and secondary vertices. It covers the track reconstruction up to $|\eta| < 2.5$ and provides electron identification in a momentum region from 0.5 GeV up to 150 GeV, with $|\eta| < 2.0$. The ID is to measure this without interacting too much with the particles themselves, as this complicates their track reconstruction in the ID and their energy measurement in the calorimeters.

The ID itself is composed of three sub-detectors: the silicon pixel detector, the semi conductor tracker (SCT) and the Transition Radiation Tracker (TRT). The first two are both based on semi conductor technology and have a very high spatial resolution, in the order of 10 μm. For the third sub-detector the choice was made for a relatively more lightweight device. The TRT consists of gaseous straw tube elements interleaved with transition radiation material. Although it has a lower spatial resolution than the silicon detectors, it provides many space points enhancing the track reconstruction in the busy environments with up to ~ 1000 particles expected. The TRT is also suitable for electron identification.

2.3.1 Pixel Detector

The pixel detector consists of silicon sensors mounted on a barrel with three cylindrical layers and on six disks. The first barrel layer is located at 50.5 mm of the beam axis, the next two at 88.5 and 122.5 mm. Especially the first layer is of great importance for a good vertex resolution and the performance of the b-quark identification algorithms (b-tagging algorithms); it will however also endure the highest radiation damage rate and its performance will deteriorate after a few years[1)]. On both sides of the barrel the pixel modules are mounted on three disks, these are located at $z =$ 495, 580 and 650 mm, see Fig. 2.4. To compensate for the Lorentz angle the modules on the pixel barrel layers are mounted with an angle of 20° with respect to

[1)]The current plan is to insert a layer even closer to the beam axis (before the current inner layer is too much damaged). For this, the beam pipe is partly removed and replaced by a pipe with pixel modules mounted on its exterior. This could be achieved in a long shut-down of the LHC planned in a winter (not before 2014).

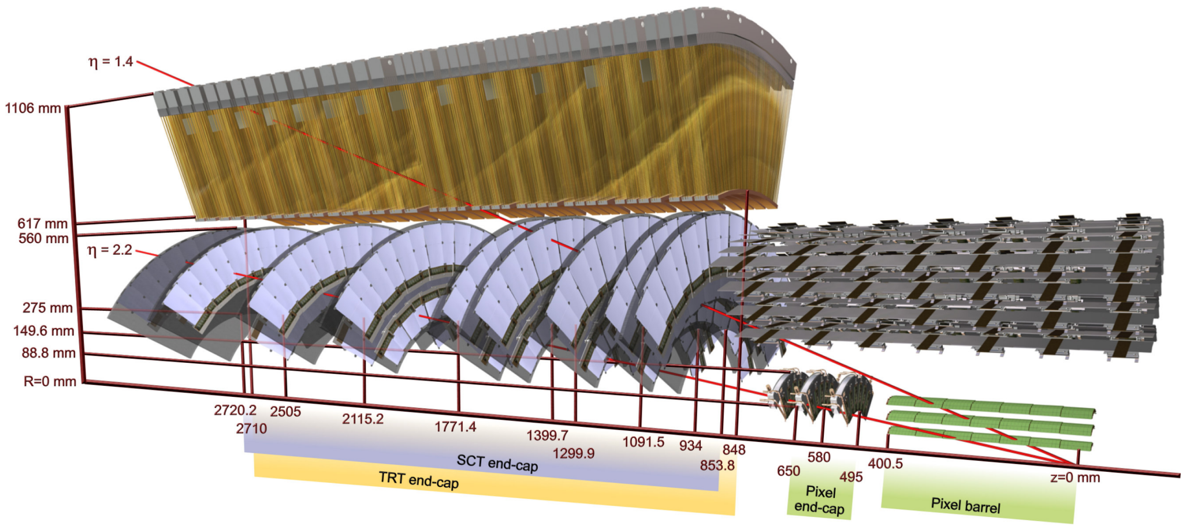

Figure 2.4: *Drawing showing the ID end-caps traversed by two charged tracks, at* $\eta = 1.4$ *and* $\eta = 2.2$*. The track at* $\eta = 1.4$ *traverses successively the beam-pipe, the three barrel pixel layers, four of the SCT disks and approximately 40 straws in the end-cap TRT wheels. In contrast, the end-cap track at* $\eta = 2.2$ *traverses the beam-pipe, only the first barrel pixel layer, two end-cap pixel disks and the last four disks of the end-cap SCT. The coverage of the end-cap TRT does not extend beyond* $|\eta| = 2.0$*. For the SCT disks only the inner and outer modules can be seen, the middle modules are mounted on the other side of the disks.*

the barrel's tangent. In Section 3.1.1 we go into more detail on the working of silicon detectors and we explain the Lorentz angle.

Figure 2.5 shows a schematic view of a barrel module. There are 16 front-end (FE) chips with 2880 electronic channels each, which are bump bonded to the pixel sensor elements. Most pixel sensors have a size of $50 \times 400\ \mu\text{m}^2$, 10% are $50 \times 600\ \mu\text{m}^2$. These larger pixel sensors are to bridge the small gaps between the FE chips. For each pixel sensor which has a charge deposit passing a certain threshold the chip sends the time-over-threshold signal to the Module Control Chip (MCC). With the time-over-threshold signal a more accurate measurement is possible than with a 'hit-or-no-hit' signal: the duration of the signal is proportional to the charge deposited at the pixel sensor. As each traversing ionising particle will deposit some charge on a cluster of pixel sensors, the time-over-threshold signals of the multiple sensors hit enables to locate the center of the cluster.

Each module has one MCC. This communicates with higher levels of the ATLAS Data Acquisition system by optical links. At the same time it controls the power over the individual pixel sensors and is itself powered through the copper on a polyimide flex hybrid circuit. The TMT, that is the Thermal Management Tile, conducts the produced heat to the cooling pipe. To reduce distortions of the material when heating up or cooling down the TMT is decoupled from the module by flexible glue. Each module is also equipped with a temperature sensor, the NTC[2)], as shown in Fig. 2.5.

[2)]Negative Temperature Coefficient

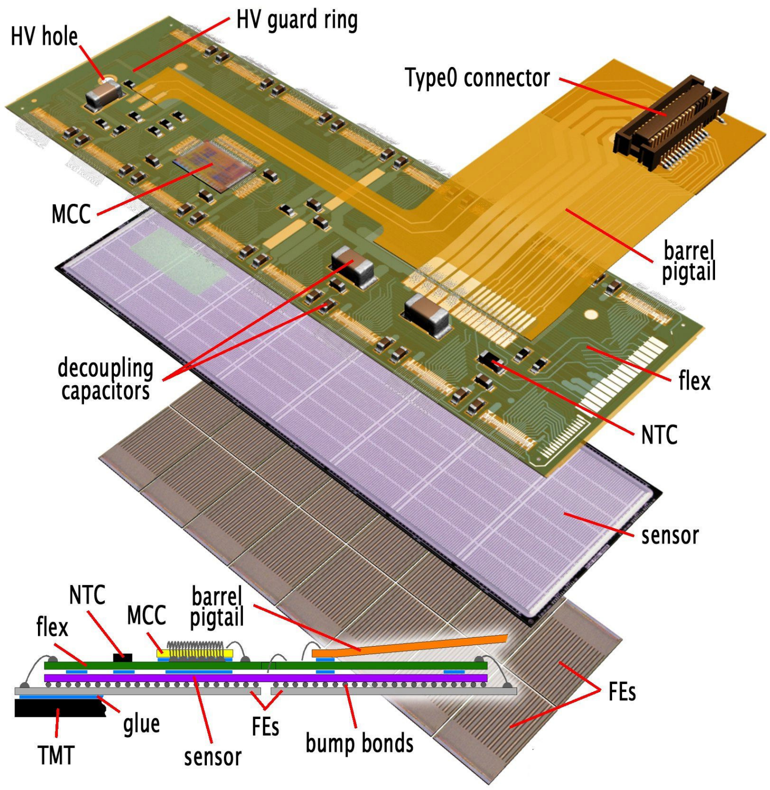

Figure 2.5: *Schematic view of a barrel pixel module. In the plan view we also see the bump bonding of the pixel sensors to the FE chips and the TMT. See text for more details.*

2.3.2 Semi Conductor Tracker

The SCT contributes to the tracking of charged particles by providing four space points in a range of $|\eta| < 2.5$. It consists itself of three sub-parts, one barrel and two end-caps. The barrel consists of four cylindrical layers with its silicon modules mounted such that the strips run parallel to the beam axis. The modules in the barrel have an angle of 11° with respect to the barrel's tangent to compensate for the Lorentz angle and to provide full coverage in the ϕ-direction.

The two end-caps each have nine disks with the modules orientated such that the strips run radially. Each disk can have an inner and outer layer, mounted on the side of the disk facing the interaction point, plus a middle layer on the other side of the disk. This setup ensures there are no gaps between the layers. The exact location of the disks and their occupation in modules are chosen such that any charged particle always hits at least four modules. An impression of this can be seen in Fig. 2.4; to go into more details a separate section is devoted to the SCT, see Section 3.1.

2.3.3 Transition Radiation Tracker

The TRT is the outermost sub-detector in the ID. Its straws (drift tubes) provide many extra space points for the track reconstruction, but with a lower spatial resolution than the SCT or pixel detector. By detecting transition radiation in the TRT, electrons can be identified in the large amount of charged particles produced in the hard scattering.

The TRT consists of cathode straws with radius of four millimeters and length up to 144 cm. They are operated at -1530 V and filled with a gas mixture of 70% Xe, 27% CO_2 and 3% O_2 with 5-10 mbar overpressure. The anodes are 31 μm diameter tungsten wires plated with 0.5-0.7 μm gold and are kept at ground potential. The wires are supported at the straw ends by end-plugs and are directly connected to the front-end electronics. For the barrel straws (with length of 144 cm) the wire is supported near the center by a plastic insert glued to the inside of the wall, isolating both parts and thus reducing the occupancy of each straw. For this, each barrel straw is read out from both ends. However, each long barrel straw is therefore inefficient near its centre over a length of 2 cm. For some straws the wire is even divided in three segments, leaving the middle segment inactive. See [65] for more details.

The straws are bundled in modules: the barrel consists of three layers, each with 32 modules. Figure 2.6 is a schematic view of a part of the ID barrel and depicts how the TRT straws are bundled in triangular shaped modules. This provides a ϕ-coverage without any gaps. The end-cap straws are mounted radially, starting at 63 cm and ending at 103 cm from the beam axis.

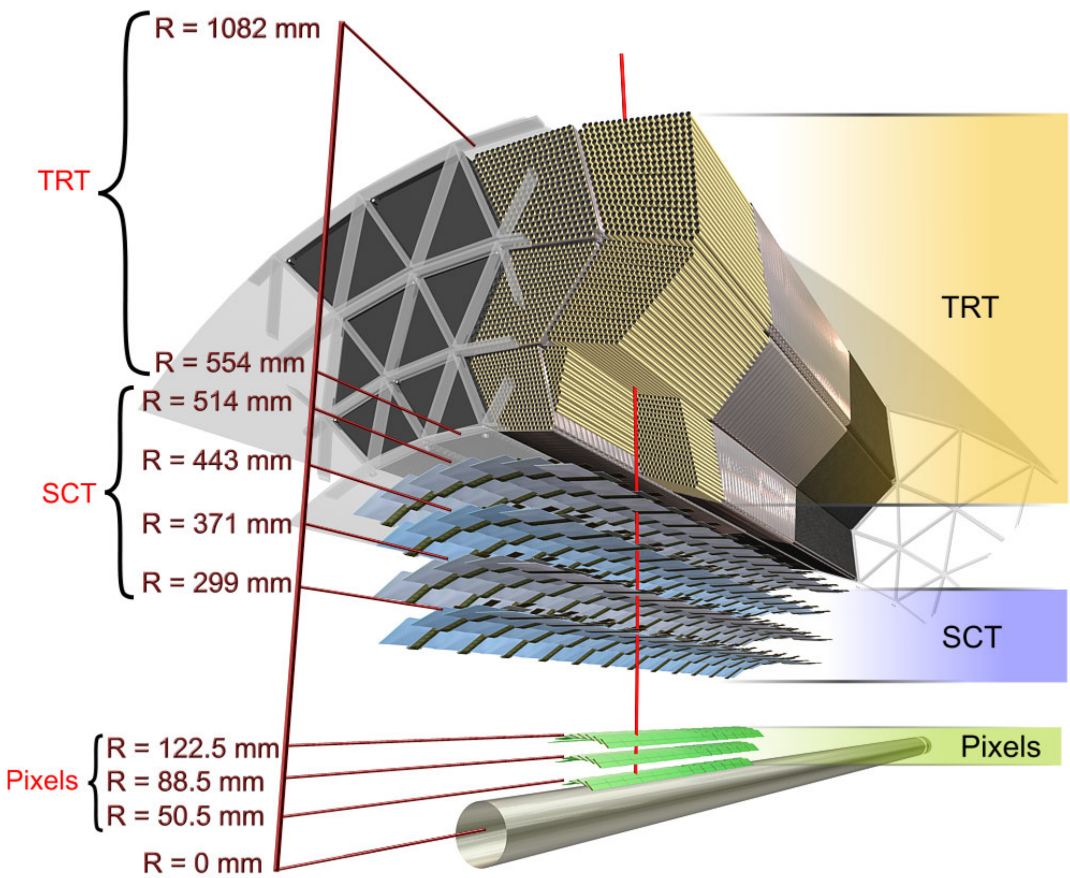

Figure 2.6: *Drawing showing the sensors and structural elements traversed by a charged track in the barrel ID. The track traverses successively the beam-pipe, the three barrel pixel layers, the four SCT layers and approximately 36 axial TRT straws within their triangular support structure.*

The end-caps cover the range of $0.7 < |\eta| < 2.0$, see Fig. 2.4.

A charged particle crossing the TRT will ionize the gas inside the straws. The released electrons drift to the anode wires; the drift time of these released charges in the straw is used to determine the point of closest approach of the charged particle to the wire with a spatial resolution of 170 μm. The TRT will provide typically 30 hits per track, with a maximum of 36, see [66].

The straws are embedded in polypropylene fibers with different indices of refraction. A charged particle will emit transition radiation in the X-ray regime with energy proportional to the Lorentz factor $\gamma = E/m$. The X-rays are efficiently absorbed by the Xenon in the gas in the straws and their energy deposits of several keV can easily be distinguished from the energy deposits from the ionized gas, which are of order 200 eV. The electronics discriminate the signal against two thresholds and can handle both energy deposits simultaneously. As the electron has a small mass, the amount of radiation it emits is clearly larger than that of a heavier particle with the same energy; hence the TRT serves as electron identifier.

To avoid pollution from permeation through the straw walls or through leaks, the straws are operated in a CO_2 envelope. See also Section 3.3 for more information on the environmental conditions of the ID.

2.3.4 Inner Detector material distribution

The material distribution in a detector partly determines its performance. The distribution can be expressed with two important properties, see [23]:

- **The radiation length** X_0 is the mean distance over which a high-energy electron loses all but $1/e$ of its energy by bremsstrahlung. It is also $\frac{7}{9}$ of the mean free path for pair production by a high-energy photon.

- **The nuclear interaction length** λ is the mean free path between inelastic collisions. For a (hypothetical) homogeneous material $\lambda = A/N\rho\sigma$, where A is the atomic weight, N is the Avogadro number, ρ is the density of the material and σ is the cross section of the incoming particle on the nucleus with weight A.

The need for cooling of the pixel detector and the SCT (see Section 3.3), the readout devices and the silicon substrate itself constitute material with significant thickness in terms of radiation length. Figures 2.7(a) and 2.7(c) show the integrated radiation length X_0 traversed by a straight track as a function of $|\eta|$ at the exit of the ID.

In Fig. 2.7(b) and 2.7(d) the material distribution in terms of interaction lengths λ is shown. We see that for the ID it does not exceed 0.7 λ. In Section 2.4 we discuss the calorimeters and we show how their depth amounts up to 10 λ.

A striking feature in Fig. 2.7 is the amount of non-active service and structural material from $|\eta| \sim 0.7$ up to the interface of the barrel and end-cap regions around $|\eta| \sim 1.7$. This includes cooling connections at the end of the SCT and TRT barrels, TRT electrical connections, and SCT and TRT barrel services extending radially out of ATLAS. A large fraction of the service and structural material is external to the active ID envelope, therefore deteriorating the calorimeter resolution but not the tracking performance. Another service contribution is from the pixel services at $2.7 < |\eta| < 3.2$, which leave the detector along the beampipe. Their extended range in $|\eta|$ can clearly be seen: for $|\eta| > 2.8$ the pixel contribution in Fig. 2.7(a) and 2.7(b) can be seen to be almost only cooling and cables in 2.7(c) and 2.7(d).

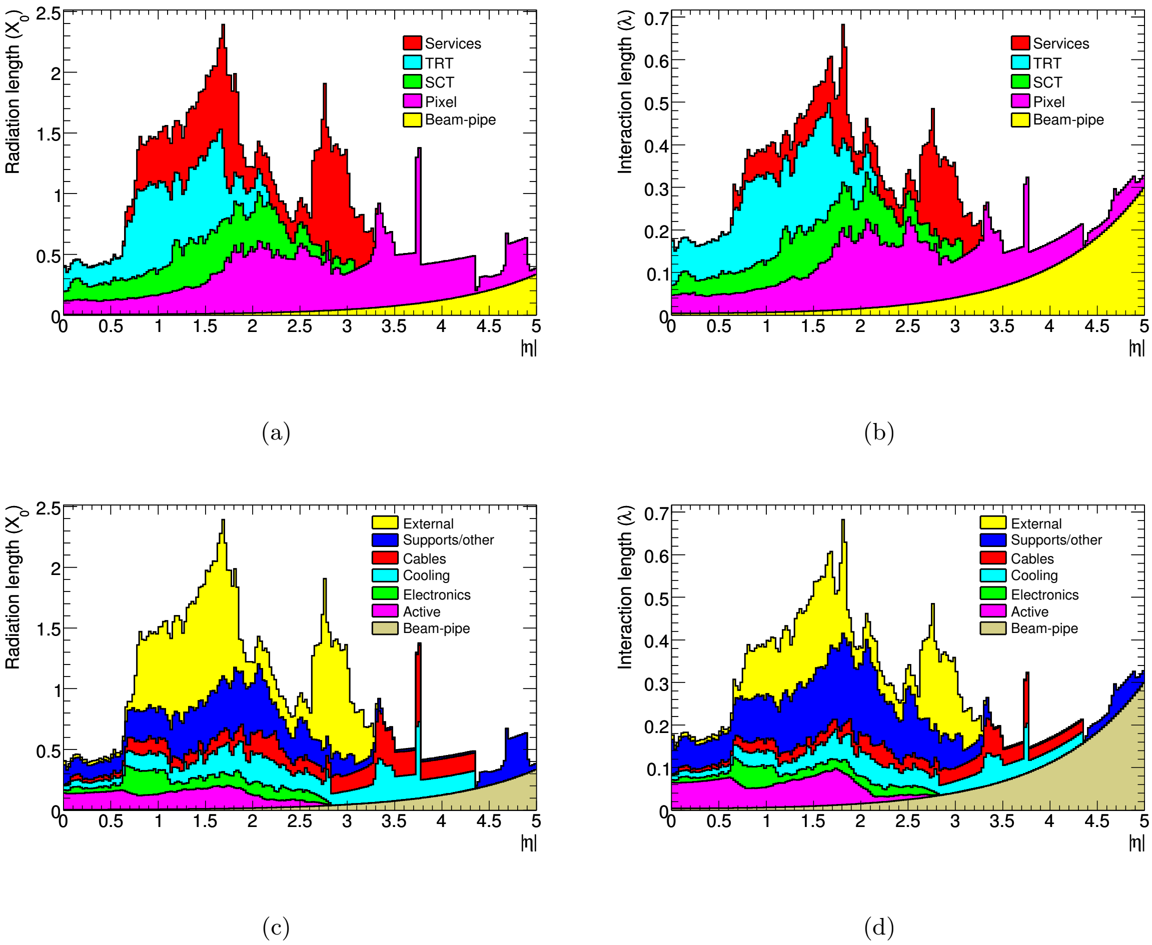

Figure 2.7: *Material distribution (X_0, λ) at the exit of the ID envelope, including the services and thermal enclosures. The distribution is shown as a function of $|\eta|$ and averaged over ϕ. In (a) and (b) the breakdown indicates the contributions of external services and of individual sub-detectors, including services in their active volume. In (c) and (d) the breakdown shows the contributions of different ID components, independent of the sub-detector.*

2.4 The Calorimeters

For the measurement of the particles' energy two different types of calorimeter are used: the electro-magnetic (EM) calorimeter for electrons and photons and the hadronic calorimeter for all strongly interacting particles. In Fig. 2.8 we see that both fully envelop the Inner Detector. Figure 2.9 shows the interaction lengths of all calorimeters. An EM calorimeter must have a high enough X_0 to stop the electrons and photons, yet a low λ to not interfere too much with the hadrons; the EM energy measurement does not depend on λ. In contrast, the hadronic calorimeter's depth must be large enough to stop all hadronic showers *and* prevent punch-throughs in the muon spectrometer. The EM calorimeter material amounts to a maximum of about 1.5 λ, compared to ~ 7.5 λ for the hadronic tile calorimeter, 10 λ for the Hadronic end-cap (HEC), and 10 λ for the forward calorimeter (FCal).

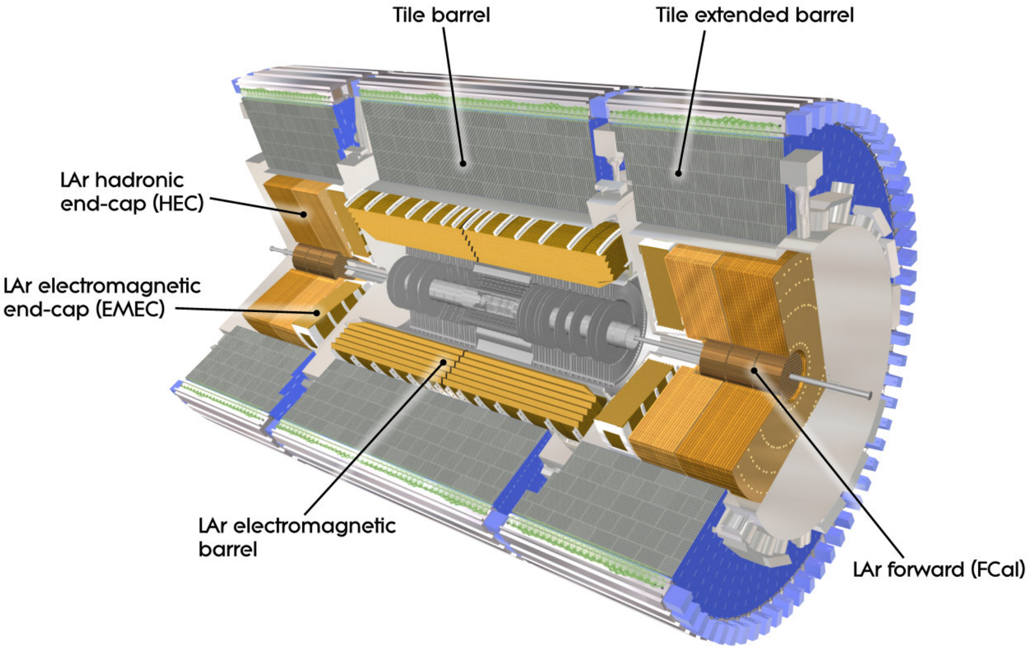

Figure 2.8: *Overview of the Calorimeters. From inside out in we first see an electromagnetic and second a hadronic calorimeter. Services for the Inner Detector and for the cryostat needed to keep the liquid argon in the EM calorimeter cold make that a gap is needed between the middle Tile barrel and the Tile extended barrels.*

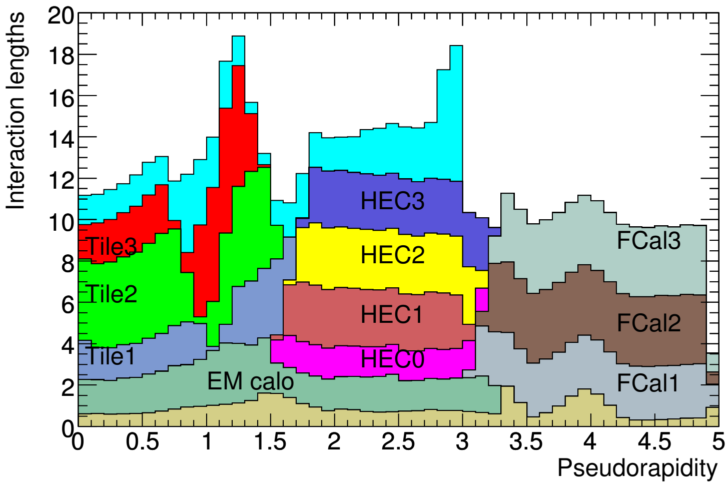

Figure 2.9: *Cumulative amount of material, in units of interaction length, as a function of $|\eta|$. The breakdown starts with the material in front of the electromagnetic calorimeters. We then see the electromagnetic calorimeters themselves, each hadronic compartment, and the total amount at the end of the active calorimetry. Also shown for completeness is the total amount of material in front of the first active layer of the muon spectrometer (up to $|\eta| < 3.0$).*

The calorimeters have been designed to cover the geometrical acceptance as hermetically as possible. The only particle, known so far, to go undetected in the whole of ATLAS is the neutrino. Its presence can however be deduced by 'missing energy' in a certain direction. The longitudinal momentum of the colliding partons is not known, but their transverse momentum is minimal. An unbalanced sum of transverse energy in the event, called E_T^{miss}, can thus be seen as the sum of the p_T of all neutrino's in the event.

The principle of a calorimeter is simple: in a dense *absorber* the incoming particle interacts with the material, creating a shower of charged and neutral particles. The charged particles are measured in the *active medium*. The number of particles counted is ideally proportional to the energy of the original incoming particle. The *sampling fraction* of a calorimeter is the fraction of the energy measured in the active medium to the total energy deposited in the module.[3)]

In the EM calorimeter the showers are a cascade of mostly photons and electron-positron pairs: photons interact with the nuclei in the absorber resulting in the pair production of an electron and a positron[4)]. The charged particles lose energy by ionizing the atoms or by emitting bremsstrahlung, that is radiation as a consequence of acceleration in the EM field of the nuclei or the electrons. The hadrons scatter by strong interactions with the nuclei into showers of lower energy hadrons. We note that in the hadronic calorimeter a shower can be partially electromagnetic. This is mostly due to the many pions produced in the shower, of which the π^0 decays to two photons.

2.4.1 Electromagnetic Calorimeter

The EM calorimeter is a liquid argon based detector and uses lead plus stainless steel as absorber. The charged particles in the shower ionize the argon; the freed charges subsequently drift to electrodes under influence of an electric field applied by high voltage electrodes. The calorimeters are housed in three different cryostat environments cooling the argon down to a liquid state. There is one cryostat for the barrel keeping it at 88 K. To minimize the amount of material the same cryostat is used to cool the solenoidal magnet surrounding the ID to a temperature of 4.5 K. Each end-cap has its own cryostat at a temperature of 88 K containing the entire end-cap *and* the entire forward calorimeter.

The EM calorimeter is made out of modules all built in a similar way, be it for the barrel or the end-cap calorimeter. Only in the Forward Calorimeter (FCal) the modules are different, see Section 2.4.4. Figure 2.10(a) shows the schematics of one barrel module: 1.1-2.2 mm thick lead plates covered with stainless steel are folded in an accordion shape. These are stacked together with a honeycomb structure between the plates, creating gaps of 2-6 mm between the absorbers. Along with the accordion plates, electrodes made out of copper and Kapton in the same shape are installed. These electrodes are used for power supply and for read-out. The space in between the honeycomb structure is filled with the liquid argon.

The accordion shape makes it possible to have a full ϕ coverage without cracks and a fast extraction of the signal at the outside of the detector. The orientation of the modules is not always the same: in the barrel the wave runs in the radial direction, in the end-cap it runs parallel to the beam axis. In both cases the 'amplitude' of the wave is in the ϕ direction. The barrel covers the range of $0 < |\eta| < 1.475$, the two end-caps the range of $1.375 < |\eta| < 3.2$.

3) Another definition, which is just the inverse quantity, is used in TileCal MC data reconstruction [67].

4) If the photon energy is high enough it can also split in a $\mu^+\mu^-$ pair. However $\sigma_{\gamma\to\mu^+\mu^-} \ll \sigma_{\gamma\to e^+e^-}$ as $m_\mu \gg m_e$.

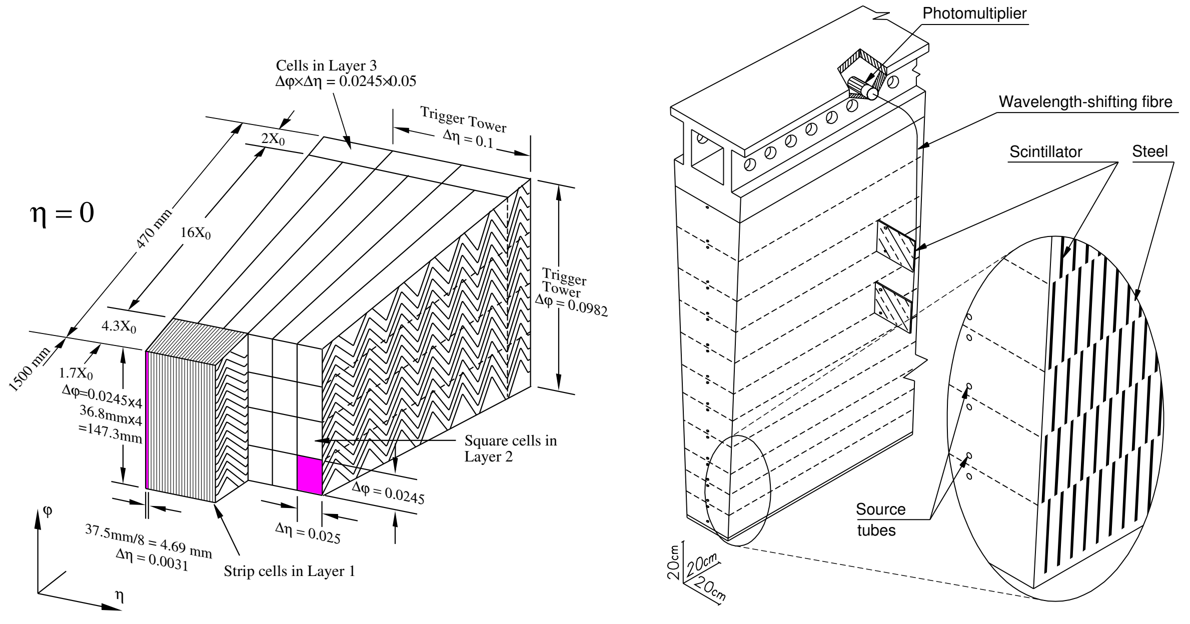

(a) EM barrel calorimeter module (b) Tile calorimeter module

Figure 2.10: *Schematic view of a liquid argon EM calorimeter module (left) and of a Tile calorimeter module (right). See text for more details.*

Between the barrel and each end-cap some space is reserved for cryostat services; electrons reconstructed at $|\eta| \sim 1.4$ are therefore treated with special care, see Section 4.6.1. In the FCal the EM calorimeter is also a liquid argon detector, but differently shaped. It covers the range of $3.1 < |\eta| < 4.9$.

The read-out of the EM calorimeter is segmented with a decreasing granularity at larger radius. The read-out channels of inner segments are thus routed through the outer layers. First, even before the modules described above, the so-called presampler measures the energy loss in the material in front of the EM calorimeter, which can reach up to $\sim 2.5\ X_0$, see Fig. 2.7(a). The presampler covers the range of $0 < |\eta| < 1.8$ and is a single layer of liquid argon with a granularity of $\delta\eta \times \delta\phi = 0.025 \times 0.1$. The modules, as seen in Fig. 2.10(a), consist of three layers with granularities of $\delta\eta \times \delta\phi = 0.003 \times 0.1$, 0.025×0.025 and 0.05×0.025. The first layer with a thickness of 4.3 X_0 is used for γ/π^0 and e/γ separation. The second layer with a thickness of 16 X_0 receives the largest part of the energy deposit, while the third layer (2 X_0) has as purpose to measure the tail of high energy showers and to consequently distinguish electromagnetic from hadronic showers; the hadronic shower has a larger fraction of its energy further 'downstream'.

2.4.2 Hadronic Tile Calorimeter

For the hadronic calorimeter several techniques are used. The barrel parts have scintillator as active medium, while the hadronic end-cap and hadronic FCal are again liquid argon detectors. The barrel hadronic calorimeter uses steel as absorber and consists of three parts, see Fig. 2.8: the 'tile barrel' covers the range of $|\eta| < 1.0$ and the two 'tile extended barrels' on both sides

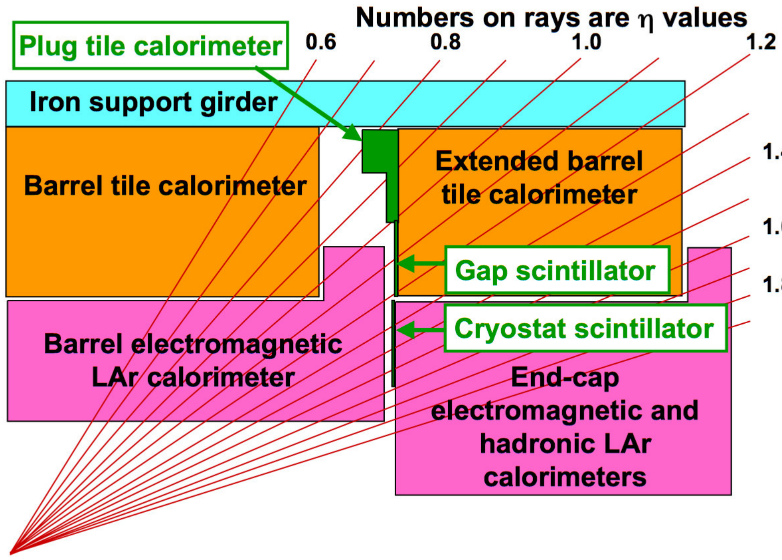

Figure 2.11: *Schematic of the transition region between the barrel and extended barrel tile calorimeter. Additional scintillator elements are installed to provide corrections for energy lost in inactive material (not shown), such as the liquid-argon cryostats and the inner-detector services. The plug tile calorimeter is fully integrated into the extended barrel. The gap and cryostat scintillators are read out together with the other tile-calorimeter channels.*

cover $0.8 < |\eta| < 1.7$. It had to be divided to provide space for cables and services for the inner detector as well as power supplies and services for the barrel liquid argon calorimeter. This 'gap', which is at most 60.0 cm wide, is equipped with a plug tile calorimeter and additional scintillator elements, see Fig. 2.11. This design prevents a pointing gap and results in a full η coverage up to 1.7 by the Tile Calorimeter.

The scintillator in the detector is produced in tiles, hence its name. The unique feature of this hadron calorimeter is the orientation of the tiles; these point radially to the beam line resulting in an excellent ϕ-coverage. The tiles are 3 mm thick and come in different sizes: their radial length varies from 97 to 187 mm, their azimuthal length from 200 to 400 mm. The polystyrene tile produces scintillating light when a charged particle crosses. The material is doped with wavelength-shifting fluors converting the UV to visible light, which is captured in fibers routing it to photomultipliers.

In Fig. 2.10(b) we see the schematics of one module; it is wedge shaped covering 5.625 degrees in azimuth and 64 of these are needed to go round the EM calorimeter. The modules are mounted with a small gap between them of 1.5 mm at the inner radius. The space is needed to route the fibers radially outwards to the top of the module where the photomultipliers (PMTs) are kept inside the steel girder. This girder also provides space for the readout electronics and the flux return for the solenoid field. The fundamental element of the absorber structure consists of a 5 mm thick steel master plate, onto which 4 mm thick steel spacer plates are glued in a staggered fashion to form the pockets in which the scintillator tiles are located. We emphasize that the master plates are placed radially and span the full height of the module as seen in Fig. 2.10(b).

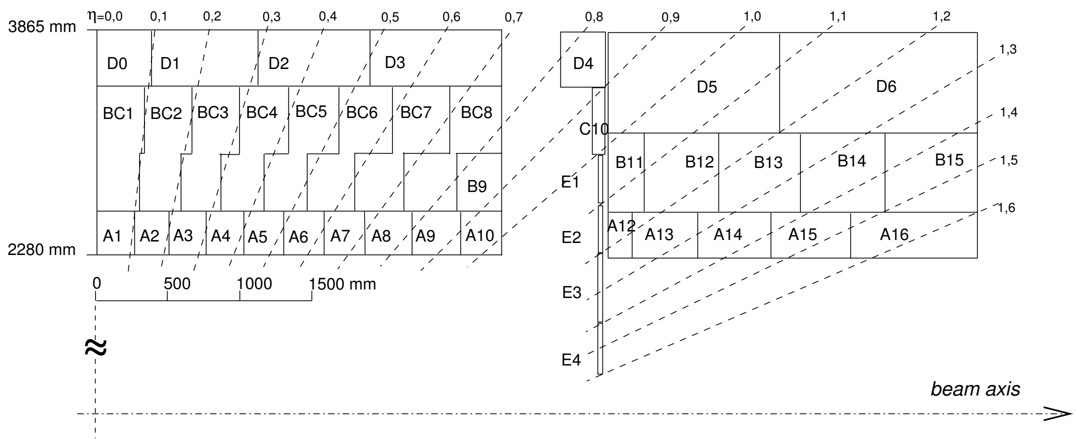

Figure 2.12: *Segmentation in depth and η of the tile calorimeter modules in the central (left) and extended (right) barrels. The bottom of the picture corresponds to the inner radius of the tile calorimeter.*

The light produced in the scintillating material is collected using a wavelength-shifting fiber on each side of the tile. The fibers, which are coupled radially to the tiles along their edges as illustrated in Fig. 2.10(b), are grouped together and coupled to the PMTs. The fiber grouping is used to define a three-dimensional cell structure in such a way as to form three radial sampling depths, approximately 1.5, 4.1 and 1.8 λ thick at $\eta = 0$, see also Fig. 2.9. These cells have dimensions $\Delta\eta \times \Delta\phi = 0.1 \times 0.1$ in the first two layers and 0.2×0.1 in the last layer. The depth and η-segmentation of the barrel and extended barrel modules are shown in Fig. 2.12. The fibers coupled to each edge of the scintillating tiles are read out by two different PMTs; this gives the possibility to average the signal from one tile which might otherwise depend on the impact position of the particle entering the tile. This setup also serves as to provide a redundant read-out link.

2.4.3 End-cap Calorimeter

As mentioned, the EM end-cap calorimeter is similar to the EM barrel. The hadronic end-cap calorimeter (HEC) is also liquid argon based, with copper as absorber and covers the range of $1.5 < |\eta| < 3.2$. It consists of two wheels, the front wheel and the rear wheel, cylindrically shaped with an outer radius of 2030 mm. Each of the four wheels is constructed of 32 identical wedge-shaped modules.

The modules of the front wheels are made of 24 copper plates, each 25 mm thick, plus a 12.5 mm thick front plate. In the rear wheels, the sampling fraction is lower with modules made of 16 copper plates, each 50 mm thick, plus a 25 mm thick front plate. The flat plates are stacked with a honeycomb structure between them. The gaps created this way all have a thickness of 8.5 mm and are filled with the liquid argon and the electrodes. The readout is organized in cells with sizes of $\Delta\eta \times \Delta\phi = 0.1 \times 0.1$ in the region $|\eta| < 2.5$ and 0.2×0.2 for larger values of $|\eta|$. Longitudinally each wheel has two read-out sections. The read-out is segmented in 8 and 16 gaps for the front, and 8 and 8 gaps for the rear wheel. These four segments are named HEC0 up to HEC3 and their contribution in material is shown in Fig. 2.9.[5)]

[5)] A confusing fact in the literature is that HEC1 and HEC2 can also refer to the entire hadronic end-cap wheels. HEC2 can thus be the first read-out segment of the rear wheel, but also the entire rear wheel.

2.4.4 Forward Calorimeter

Each of the two forward calorimeters consists of three wheels. The first is the electromagnetic part (FCal1), the next two together form the hadronic part (FCal2 and FCal3). The FCal, covering the range of $3.1 < |\eta| < 4.9$, is located at approximately 4.7 m from the interaction point and is thus exposed to high particle fluxes. This has resulted in a design with very small liquid argon gaps, which have been obtained by using an electrode structure of small-diameter rods, centered in tubes which are oriented parallel to the beam direction.

The EM wheel of the FCal uses copper as absorber and comprises a total radiation length of 27.6 X_0. The Hadronic part uses Tungsten as absorber and consists of two wheels with radiation lengths of 91.3 and 89.2 X_0. The interaction lengths are respectively 2.7, 3.7 and 3.6 λ, see also Fig. 2.9. The absorbers have longitudinal holes to accommodate the electrodes with the liquid argon in them.

2.5 The Muon Spectrometer

The muon spectrometer in ATLAS is the outermost sub-detector. It consists of precision chambers as well as trigger chambers in a barrel part and in four wheels on each side, of which one wheel is a ‘ring’ radially positioned outside the end-cap toroid. [6] Figures 2.2 and 2.13 show how the spectrometer is built up out of the chambers, taking a large space volume. Its momentum determination performance depends on the toroidal magnetic field which is created by the eight coils of the superconducting barrel toroid magnet and the two end-cap toroid magnets. The magnetic field is on average 0.5 T in the barrel region and 1.0 T in both end-cap regions. Together with the size of the system the magnetic field results in a large bending power. It

[6] The two rings on both sides of ATLAS are not completely installed yet.

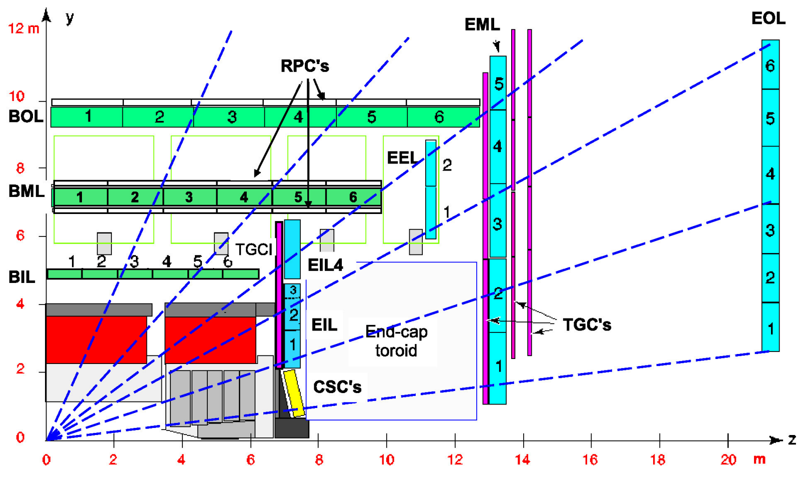

Figure 2.13: *Cross section of the muon system in a (z, r) plane. Infinite-momentum muons would propagate along straight trajectories which are illustrated by the dashed lines and typically traverse three muon stations. We see the three barrel layers, the four wheels and the trigger chambers.*

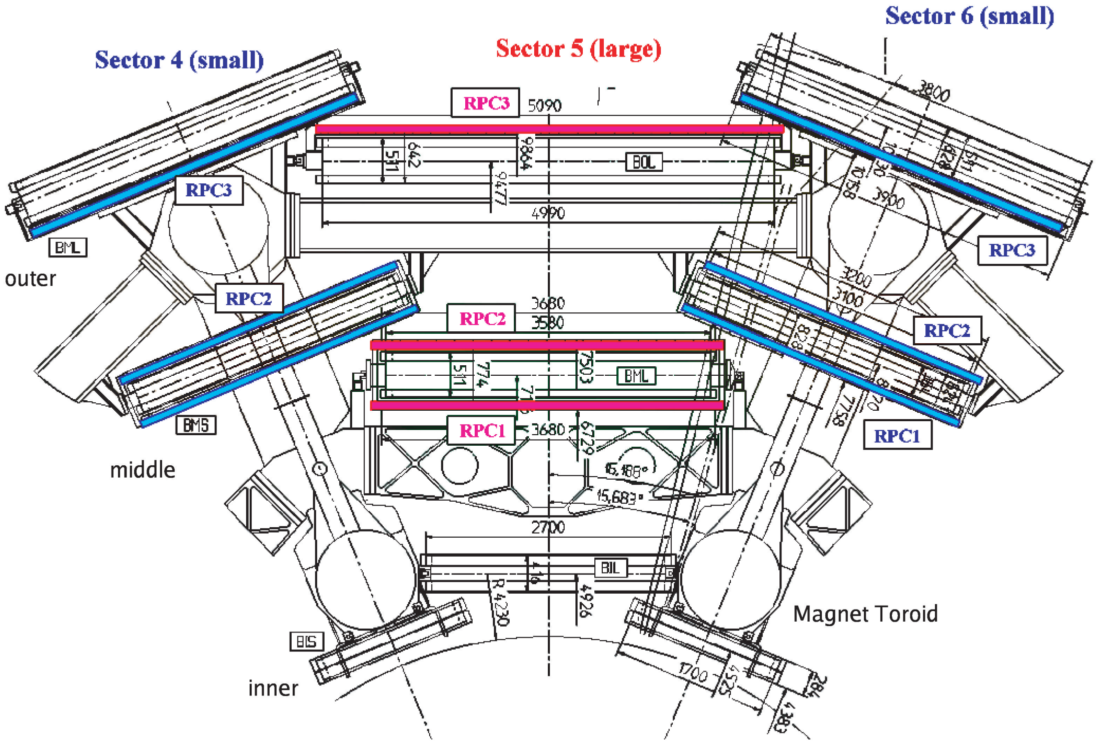

Figure 2.14: *Cross section through the upper part of the barrel, with RPCs marked: they are located on both sides of the middle chambers and on one side of the outer chambers. The barrel consists in total of 16 sectors, alternately with large and small chambers. All dimensions are in mm.*

is however an inhomogeneous field: in the barrel region it varies from 0.15 to 2.5 T and in the end-cap region from 0.2 to 3.5 T. An accurate B-field mapping is necessary to correctly reconstruct the muons' momenta.

The layout of the detector is optimized to provide the best acceptance and resolution, taking into account the inhomogeneous magnetic field and the large size of the apparatus. The spectrometer covers the range of $|\eta| < 2.7$ measuring each muon in three layers of chambers and is designed to reconstruct accurately the momentum and charge of traversing muons with momentum of ~ 3 GeV up to ~ 3 TeV. Fig. 2.14 depicts a cross section through a part of the barrel spectrometer. Two magnet coils can be seen together with nine chambers between and on the coils. The sixteen sectors in the cylindrical barrel have alternately small and large chambers, which results in a small overlap at their edges. This ensures a full coverage in ϕ-space and can be used for relative alignment of the chambers. The precision measurements on the muon's track are performed by the Monitored Drift Tubes (MDTs). The spectrometer also serves as trigger on muons: in the range of $|\eta| < 1.05$ Resistive Plate Chambers (RPCs) are installed, also indicated in Fig. 2.13 and 2.14, and in the range of $1.04 < |\eta| < 2.4$ Thin Gap Chambers (TGCs) are located, see Fig. 2.13.

The barrel has an inner layer at approximately 5.0 m from the beam axis, a middle at 7.5 m and an outer layer at 10 m. The exact radial distance of the chambers varies per sector: the large chambers are closer to the beam axis than the small chambers, see Fig. 2.14. The muon wheels are located at $|z| = 7.4$ m between end-cap calorimeter and end-cap magnet, at $|z| = 10.8$ m forming the ring around the magnet end-cap, and at $|z| = 14$ and 21.5 m, beyond the magnet end-cap. In Fig. 2.13 the wheels are indicated as EIL, EEL, EML and EOL: the end-cap inner large, -extra large, -middle large and -outer large. In the barrel there is a gap between the chambers at $|\eta| \sim 0$ to leave space for cables and services for all the sub-detectors deeper in ATLAS. This gap is at most 2 m between certain chambers: highly energetic muons with straight tracks can go undetected in the spectrometer in a region of $|\eta| < 0.08$ if between large chambers, or in a region of $|\eta| < 0.04$ if between small chambers. These muons can however be measured in the ID and calorimeter.

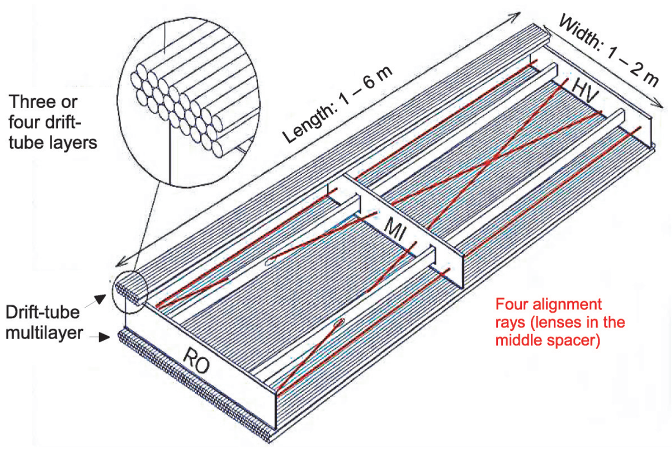

(a) A barrel MDT chamber.

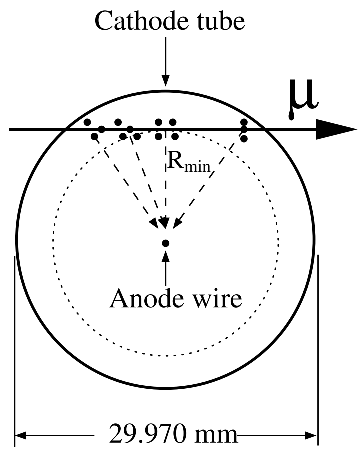

(b) Cross section of a MDT tube

Figure 2.15: *Left: structure of a MDT chamber. An aluminum frame carries two multi-layers of three or four drift tube layers. Four optical alignment rays, two parallel and two diagonal, allow for monitoring of the internal geometry of the chamber. RO and HV designate the location of the readout electronics and high voltage supplies, respectively. Right: cross section of one MDT tube, see text for more information.*

Figure 2.15(a) shows the schematics of one barrel MDT chamber, Fig. 2.15(b) depicts the cross section of one drift tube. It is a 30 mm diameter aluminum tube filled with a gas mixture of Ar (7%) and CO_2 (93%) at an absolute pressure of 3 bar. This gas is ionised when a muon, or any charged particle, passes by. An anode wire operated at 3080 V runs through the tube and collects the charge: the time of arrival of the signal pulse is a measure for the radius of the point of closest approach of the muon's track compared to the wire. The chambers are installed such that the tubes run orthogonal to the beam axis. Within the chamber a hit does not result in a ϕ coordinate.

In the two inner wheels the innermost layer consists of Cathode-Strip Chambers (CSCs). Covering the forward range of $2.0 < |\eta| < 2.7$, see Fig. 2.13, these chambers are more suitable with their higher rate capability and time resolution. The CSCs are multi-wire proportional chambers with cathode planes segmented into strips in orthogonal directions. This allows both coordinates to be measured from the induced charge distribution.

In the track reconstruction, hits in three chambers form a curved path. The sagitta of such a curve is defined as $s = l^2/8r$, where l is the path length in the magnetic field and r the bending radius. The spectrometer momentum resolution design is 10% for a 1 TeV muon. For a muon with no longitudinal momentum this corresponds to a track with sagitta of about 500 μm, to be measured with a resolution of 50 μm, implying that the locations of MDT wires and CSC strips along a muon trajectory must be known to < 30 μm. For this purpose a high-precision optical alignment system monitoring the relative positions among the chambers, *and* their internal deformations is installed. An impression is given in Fig. 2.15(a) for the monitoring of the internal geometry. Together with a track-based alignment with data the position of the chambers can thus accurately be measured.

2.6 The Trigger and Data Acquisition system

At the design luminosity of the LHC in the order of $\sim 10^9$ interactions per second will occur inside the ATLAS detector, generating 1 PB/s of data. As explained in Section 2.1.1 not only is this amount unsustainable for mass storage, many of these events are also not worth storing. The Trigger and Data Acquisition (T/DAQ) system reduces this to ~ 200 events per second, or equivalently to an amount of ~ 300 MB/s for data storage. To achieve this a three-level trigger system is designed for the ATLAS detector.

Figure 2.16 shows an overview of the T/DAQ system. It can roughly be divided in the hardware readout chain and the trigger system. The readout chain starts at the Front-End (FE) electronics on the detector modules which send the data for each bunch crossing to the pipeline memories; we emphasize that at design luminosity each crossing will contain several interactions, which at this point in the data chain are seen as one event. When passing the level 1 (L1) trigger, which only uses reduced-granularity information from the calorimeter and the muon spectrometer, the event data are sent to the Readout Drivers. These RODs align the data in time and forward them to the Readout Buffers (ROBs). The level 2 (L2) trigger requests the data from these large memory buffers. To reduce the amount of data transfer only the information from the Regions Of Interests (RoIs) identified by the L1 trigger is analyzed; the L2 trigger does have access to the full granularity data of these RoIs. If the event passes the L2 trigger, the Event Builder requests the data from the ROBs and forwards the fully assembled event to the Event Filter (EF), the third and last trigger level.

The Data Acquisition system (DAQ) controls the movement of the data down the trigger chain; in addition it also provides for the configuration, control and monitoring of the ATLAS detector during data-taking. We note that the monitoring of the detector hardware (such as gas systems, cooling systems, etc...) is taken care of by the Detector Control System, the DCS. We will now describe the three trigger levels in more details. For a complete description we refer to [65, 68].

2.6.1 Level 1 Trigger

The L1 trigger is a hardware trigger implemented in custom-built electronics. It reduces the event rate from an initial 40 MHz[7)] to about 75 kHz. The flow of the L1 trigger is shown in Fig. 2.17. The trigger decision is taken by the Central Trigger Processor (CTP) and is based on reduced-granularity information from the RPCs and TGCs for a muon trigger and from

7) A bunch crossing of 40 MHz with 23 events per crossing result in the $\sim 10^9$ events/sec mentioned earlier.

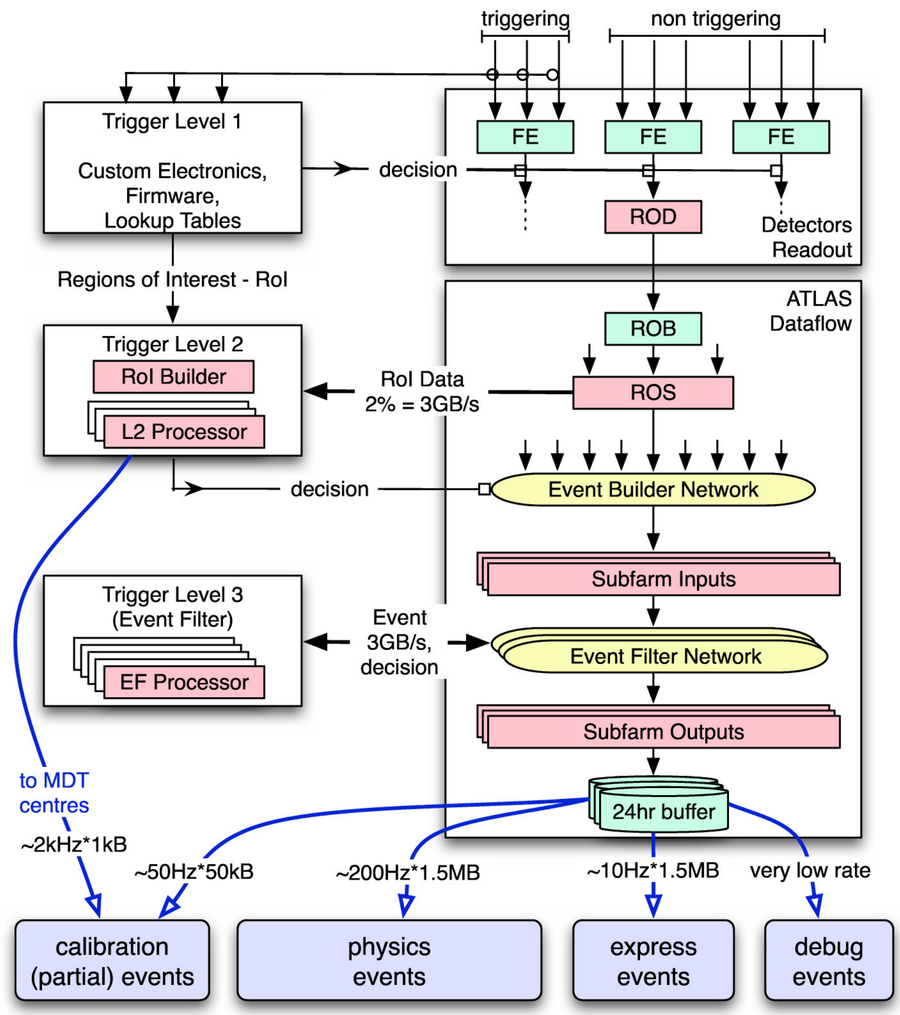

Figure 2.16: *Overview of the Trigger and Data Acquisition system. The right side shows the data collection infrastructure and the left side the different trigger levels. The trigger decision lines show at what level in the data transfer chain the event data are accepted or rejected. At the bottom of the figure different streams are depicted, see text for more details.*

the calorimeters for a trigger on electrons or photons, jets, or τ's decaying into hadrons. With the information from the calorimeter an event can also be triggered on large total transverse energy or large missing transverse energy. The event selection uses inclusive criteria, which in this case means that the objects' p_T or the global energy quantities have to pass a certain threshold. For the electron/photon and τ triggers isolation can also be required: the particle must have a minimum angular separation from any significant energy deposit in the same event.

The L1 muon trigger is implemented in electronics placed on the muon chambers as well as in the USA15 cavern. It receives information from the trigger chambers and searches for

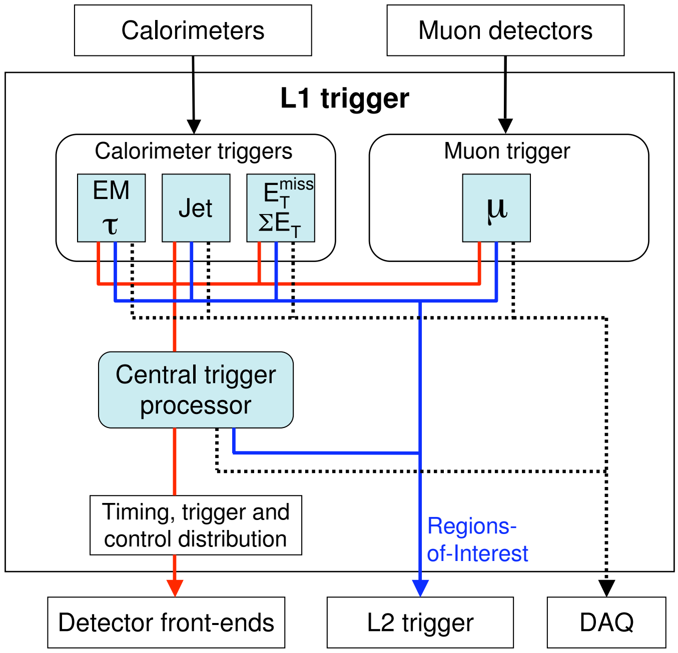

Figure 2.17: *Block diagram of the L1 trigger. The Central Trigger Processor accepts or rejects the event based on information from the calorimeter and muon trigger. If it is accepted the signal is sent to the FE electronics along with a timing stamp, the L2 receives the RoIs and the DAQ handles the data transfer further down the trigger chain.*

patterns of hits consistent with high p_T-muons originating from the interaction point. The only information sent to the CTP is the multiplicities of muons above certain p_T thresholds. The logic provides six independently programmable thresholds.

The L1 calorimeter trigger is also located in the service cavern USA15 and has two subsystems working in parallel: the Cluster Processor (CP) and the Jet/Energy sum Processor (JEP). With no tracking information at this level any electromagnetic energy deposit is simply classified as electron/photon. The CP identifies electron/photon or τ candidates with certain E_T thresholds. The JEP receives jet trigger elements, which are 0.2×0.2 sums in $\Delta\eta \times \Delta\phi$, to identify jets and to produce global sums of scalar and missing transverse energy. Only the multiplicities of each of the different triggered objects and the global energy sums are sent to the CTP.

The Central Trigger Processor receives the multiplicities of all trigger objects and the global energy quantities. This information is compared to a list of items, where a maximum of 256 items can be on the list. Each item can be a combination of conditions: for example, the condition L1_2EM15I demanding two electromagnetic isolated clusters of 15 GeV can be combined in one item with the condition L1_2J45 demanding two jets of 45 GeV. An event is accepted if one or more items are passed. Apart from the trigger conditions the item also has a pre-scaling factor between 1 and 2^{24}. With this factor the amount of events labeled as triggered can be scaled down by randomly choosing among the events that fulfilled the trigger selection.

The trigger decision, together with the 40.08 MHz clock and other signals, is distributed to the detector front-end and readout systems via the Timing, Trigger and Control (TTC) system, using an optical-broadcast network. If the event is accepted by the L1 trigger, the geometric location of trigger objects is sent as RoIs to the L2 trigger. The L1 trigger also identifies the bunch crossing of interest; with a bunch interval of 25 ns this is not a trivial task. For the muon spectrometer, the physical size of the system implies times-of-flight exceeding the bunch-crossing interval. For the calorimeter trigger, a complication is that the width of the calorimeter signals extends over many (typically four) bunch-crossings. While the trigger decision is being formed the data for all detector channels is retained in pipeline memories placed on or near the detector. The L1 latency, which is the time from the proton-proton collision until the L1 trigger decision, is required to be less than 2.5 μs, with a target latency of 2.0 μs, leaving 0.5 μs in case of necessity. About 1 μs of this time is accounted for by cable-propagation delays alone.

2.6.2 High Level Trigger

The High Level Trigger is a software based trigger, running on a PC farm located in USA15. It is subdivided in the L2 trigger and EF, which both have access to the full granularity information of all sub-detectors, but for the L2 only in the RoIs. Better information on energy deposition thus improves the threshold cuts, while track reconstruction in the inner detector significantly enhances the particle identification (for example distinguishing between electrons and photons).

Level 2 Trigger

The L1 trigger sends the RoIs to the L2, which retrieves the full data for those regions from the ROBs; this amounts to about $1-2\%$ of the full data of an event. It has a nominal average processing time of 40 ms and reduces the output rate to around 3 kHz.

The execution of the L2 trigger is organized by the HLT Steering algorithm based on the static configuration information and on the dynamic event data. In simpler words, the Steering algorithm decides which trigger decision step should be run on which of the RoIs that are being reconstructed. At each step in the reconstruction, physics signatures are analyzed and tested against the trigger demands. At each step the event can be rejected, which also stops the data retrieving of other RoIs. This way only for selected events the full data of the RoIs is transfered and the transfer is minimized for rejected events.

The L2 trigger mostly uses inclusive criteria, comparable to the L1 trigger. One exception is the L2 selection for events containing the decay of a B-hadron, which requires the reconstruction of exclusive decays into particles with low momentum.[8)] For this particular trigger decision the L2 algorithm can also access information on the muons in an area larger than the original RoI.

8) By exclusive decays we mean the specific decays of the B-hadron with two muons.

The Event Filter

After passing the L2 trigger, the event builder requests all data from the ROBs and sends the fully assembled event to the EF, which rebuilds the full event using standard ATLAS event reconstruction and analysis applications. On average, one event is processed in four seconds; with a farm of ~ 1500 PCs this reduces the event output to 200 Hz. A full event is approximately 1.5 MB in size. An important part of the event selection is its classification to the ATLAS physics streams, see next section.

At the start-up luminosity of 10^{31} s^{-1}cm^{-2} the event rate is still modest, about 3 orders of magnitude lower than the design level. At this luminosity, low thresholds and loose selections can thus be used for the L1 trigger without running the risk of triggering too many events, while the HLT can be run in pass-through mode.

2.6.3 Trigger menu and data streams

The complete configuration of the ATLAS trigger is called a menu, where a menu consists of different chains. One chain, also called a slice, can for example be the sequence of the L1, L2 and EF trigger selecting two jets. An event is thus accepted if at least one chain is satisfied; the benefit of such a modular setup is that chains can be easily adjusted or replaced. With the luminosity increasing over time, the trigger menu will be continuously adapted as to keep the output rate maintainable.

At the end of the trigger chain the EF classifies the event into one or more physics streams. Events with the same signatures are thus grouped together, simplifying further analysis. It also makes it possible to reprocess events separately for each stream. An event can however also end up in several streams, resulting in duplicate events. The different streams are therefore defined such to have a minimal amount of overlap. A possible configuration at low luminosity is four physics streams: electrons and photons (Egamma-), muons, jet/τ/E_T^{miss} and minimum bias triggers. With such definition the overlap would be less than 10%, see [69]. The minimum bias trigger ensures that some minimum bias events *are* saved; although we defined these as non-interesting scatterings, we do not yet completely understand them. Their expected rate for example at the LHC energy levels has a large uncertainty. Some of these events will be investigated to better understand the background they form.

In addition to the physics streams, there will be three special streams. The so-called express stream is a sub-sample of high-purity signal events from the physics streams used to monitor the quality of the data and the detector. The calibration stream contains events triggered by special calibration triggers. The debug stream is for all the events which caused errors during online running, such as time-outs, crashes, etc... These can then be investigated further.

Chapter 3

The SCT and the ID evaporative cooling system

Nikhef participated extensively in the design and construction of two ATLAS sub-detectors. For the muon spectrometer all BOL chambers, the muon RODS and parts of the DCS were designed or constructed at Nikhef and in Nijmegen. For the ID, 100 inner SCT end-cap modules were produced and the entire end-cap A was assembled in Amsterdam. In this chapter we go into more details on the SCT and its cooling system which is part of the ID evaporative cooling system.

3.1 The SCT end-cap in detail

We discuss the SCT bottom-up: we will first explain how a silicon detector works. Although the modules in the pixel detector have different schematics, they are based on the same principle. We then go into more details on the components of one SCT end-cap module; the barrel and end-caps differ mostly in the size and orientation of their modules. Finally we elaborate on the layout of the modules on an end-cap disk and the assembling of nine disks into one end-cap. For a more detailed description of the design and functioning of the SCT we refer the reader to [70–73].

3.1.1 Basics of silicon strip detectors

Silicon atoms have four valence electrons. In a lattice, these electrons can become conductive electrons if their energies are raised, be it by thermal excitation or by absorption of energy. This energy raise must exceed a certain minimum: the amount needed to jump the energy band gap between the valence and the conductive band. With one conducting electron, the material also gains another conducting ‘hole’: the deficiency left behind by the electron can be filled up by its neighbors. These shifting electrons can be seen as a positive hole moving in the other direction.

Silicon can be doped with impurities to alter its properties. By adding atoms with five valence electrons the result is *n*-type silicon: the fifth electron from the impurity can easily jump in the conducting band of the silicon. Impurities with three valence electrons result in *p*-type material. There the valence electrons of the silicon jump to fill the fourth valence band of the impurity, leaving behind a conducting hole. When a *p*- and *n*-type material have a contact surface, charges start moving: the conducting electrons from the *n*-type material move to the

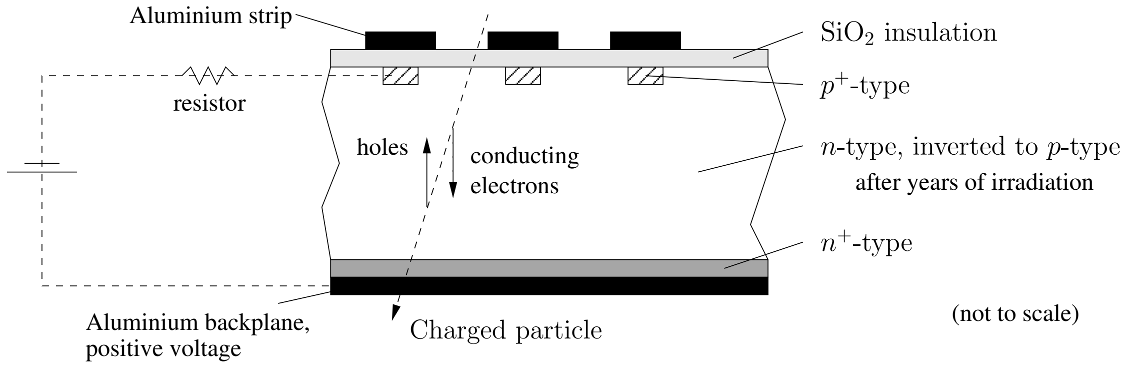

Figure 3.1: *Partial cross section of a silicon strip-sensor. The applied potential depletes the bulk region of its 'free carriers'. The only current measured is the leakage current, caused by electrons freed by thermal energy. Any charged particle passing by releases electrons from the silicon atoms, creating a current in one of the extra-highly doped p^+-strips. The n-type material inverses over time to p-type due to irradiation.*

p-type side, while holes go in the opposite direction. The resulting charge build-up stops any more charge from moving, creating a *depletion* zone.

Figure 3.1 shows the schematic cross section of one SCT silicon sensor. The bulk region is n-type silicon, which is implanted with extra-highly doped p-type strips, so-called p^+-type. The inter-strip distance is $\sim 80\mu$m, while the sensor thickness is $\sim 300\mu$m. The depletion zone between the n- and p-type material is increased to cover the whole silicon bulk by applying a positive voltage to the aluminum backplane, the *bias voltage* V_{bias}. To provide good contact, an extra doped n^+-type material is implanted between the two.

Once the entire silicon bulk region is depleted, all conducting electrons are taken out of the silicon. Only a very minimal leakage current due to thermal excitations runs through the material. A charged particle traversing the SCT can now be accurately detected: it creates electrons and holes along its path, which drift under the influence of the V_{bias} creating a current in one of the strips. Under influence of the magnetic field present in the ID these drifts are deflected, giving rise to the so-called *Lorentz angle*.

The current running through the p^+-strips does not directly go to the read-out chips. First, the charge builds up inside the strip due to a resistor connected to its far end, that is the side not nearest to the hybrid, see Fig. 3.2. This charge build-up induces another charge in the aluminum strips running parallel to the p^+-strips, separated by a SiO_2 insulator, see Fig. 3.1. The benefit of this layout is less noise.

Radiation damage

The high particle flux through the SCT during LHC operation results in radiation damage to the sensors. Two types of radiation can be distinguished: the ionizing radiation caused by all charged particles, and non-ionizing radiation, caused by all particles, but mainly by hadrons. The effects of this last type are dislocation of atoms and nuclear reactions, introducing impurities and in fact altering the doping of the material. The impurities form traps for the charge carriers, increasing the charge collection time and changing the signal efficiency and timing. The impurities also create intermediate levels in the band gap, thereby increasing the

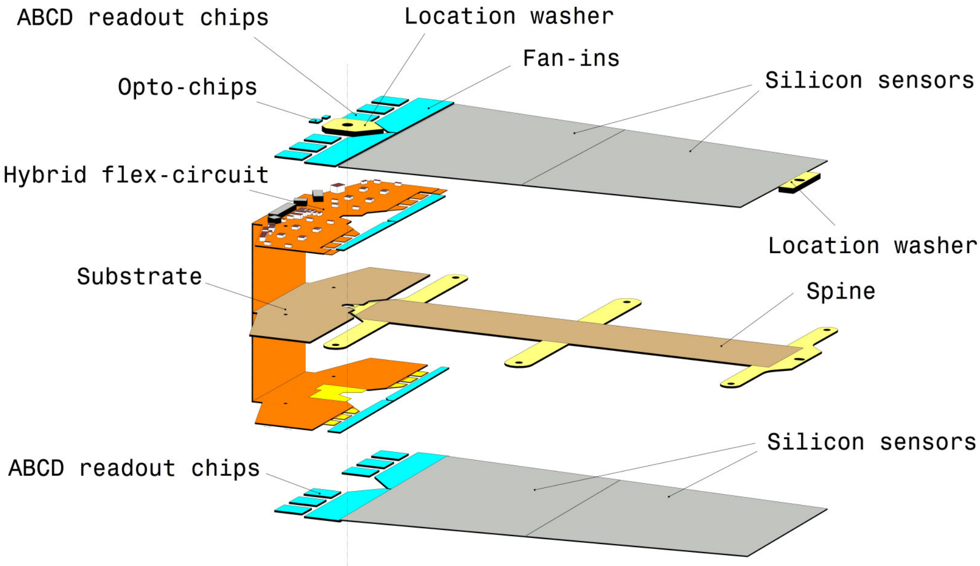

Figure 3.2: *Components of a SCT end-cap module. See Section 3.1.2 for more details on all components.*

leakage current. The ionizing radiation creates trapped holes in the SiO_2. The trapped holes are known as surface and oxide damage. This damage causes charge build-ups, increasing the noise and lowering the signal height.

The dislocations in the material cause it to behave more and more p-type like. This has great consequences for the depletion voltage. The n-type will first become 'less n-doped', decreasing the depletion voltage. After a certain time this process is however so far that the material really is p-type. The junction moves from the p^+-type strips to the n^+-type, see Fig. 3.1, and an increasing depletion voltage must again be applied to keep the silicon bulk entirely depleted. At the start-up in 2009 the V_{bias} will be 150 V; after ten years, the expected life-time of the SCT, it is expected to have increased up to 450 V.

An efficient cooling is of great importance here. The mentioned dislocations can thermally vibrate back into position, a process called 'beneficial annealing'. This is however overshadowed by the 'reverse annealing': a process less well understood, but probably due to the diffusion of the dislocations or impurities and the creation of acceptors (p-type material). This causes the effective doping to increase, be it n- or p-type. Once a p-type material, the reverse annealing speeds up the damage. The annealing can be tempered with decreasing temperature and the SCT will therefore be kept at $-7°$C; any maintenance requiring shutting down the cooling is to be kept to a minimum to prevent more damage.

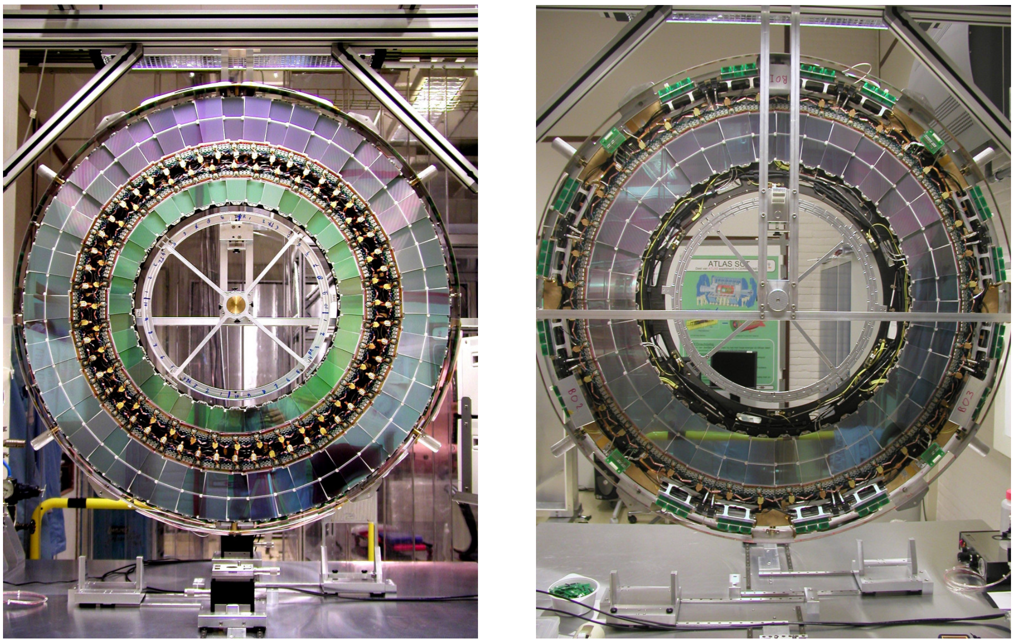

Figure 3.3: *End-cap SCT disk with outer and inner modules (left) on the side of the disk facing the interaction point. The middle modules (right) are mounted on the other side.*

3.1.2 One SCT end-cap module

Each SCT end-cap consists of nine disks, mounted with modules in an inner, middle and/or outer ring. In Fig. 3.3 we see photographs taken of an end-cap disk with all three layers populated. The three layers have modules of different sizes and shapes, yet all modules are built in a similar way. One hundred inner modules were produced at Nikhef, the rest at different locations. Figure 3.2 shows the components of one end-cap module. Each module has two or four sensors glued back-to-back onto a spine at a 40-mrad stereo angle to provide a two-dimensional position measurement. The modules in the inner ring on a disk have one sensor per side, the modules in the two other rings have two sensors per side, which are bonded together.

There are 768 strips per sensor read out by 6 ABCD chips. In total there are thus twelve ABCD chips per module. For the SCT end-caps the inter-strip distance, also called pitch, varies from 57 to 94 μm. For the barrel there is but one type with a pitch of 80 μm. The ABCD chips are mounted on the copper/Kapton hybrid and each is wire-bonded to 128 strips, also called channels, via the glass fan-ins. A chip converts the strip signals into binary output signal and stores the hits for 132 bunch crossings in a pipeline memory, while awaiting a Level 1 trigger signal, see Section 2.6.1. The chips also contain a charge injection circuitry which can be used for calibration. In contrast to the time-over-threshold signal in the pixel detector, the SCT strips in the end thus result in a hit-or-no-hit signal. The resolution of such a signal is $pitch/\sqrt{12} \sim 20$ μm, if only one strip is hit. When more strips are hit the resolution is smaller, see also Section 3.2.3.

On the hybrid two more chips control the optical link between the module and the off-detector system. Each module has one *p-i-n* diode[1)] to receive the Timing, Trigger and Commands (TTC) signals and two VCSELs returning the data from both sides of the modules to the Readout Drivers (RODs). Redundancy links ensure that the TTC can be sent via a neighboring module, and that the data from both sides can be sent through one VCSEL[2)].

The spine with its side-bars not only gives structure to the module, it also electrically connects the sensor backplanes and the bias voltage, see Section 3.1.1, and serves as thermal conductor to transport the heat generated by the bias current in the sensors to the cooling blocks. The cooling blocks are at the same time the mounting blocks; the fixation of the location washers to these blocks is with a precision that is better than 20 μm in the perpendicular direction of the strips, see [74]. Figure 3.4 depicts the fixation of a module and the heat flows from the module to the cooling circuit.

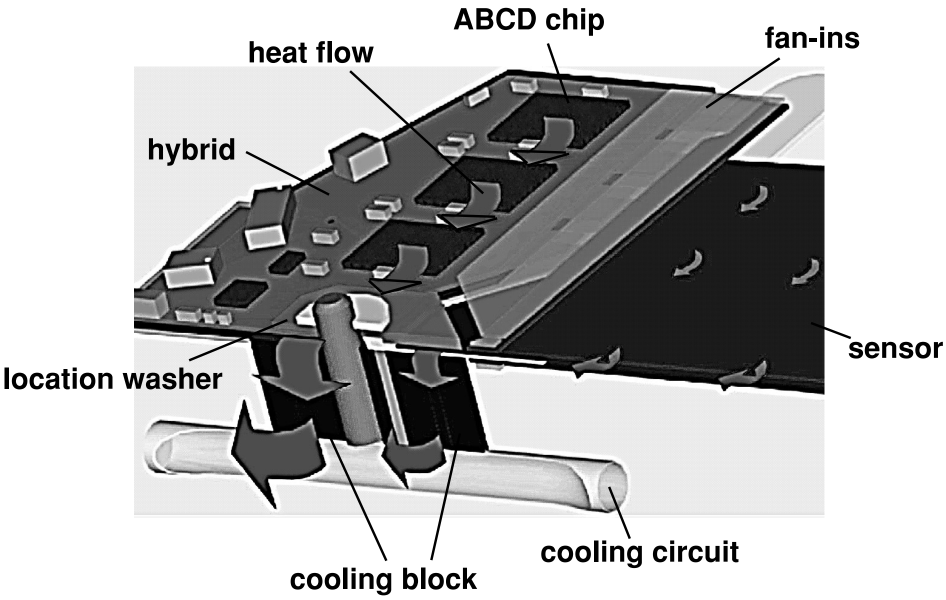

Figure 3.4: *Cross section along the spine of an outer module at the hybrid end, with the fixation of the location washer to the cooling block (see also Fig. 3.2). The arrows indicate the heat flows from three ABCD chips and from the sensor. The flow along the cooling block to the cooling circuit is also depicted. The figure is taken from [75].*

3.1.3 End-cap disk and cylinder design

Figure 3.3 shows photographs of the front (left) and back (right) side of a fully populated disk. Per quadrant the disk has 13 outer, 10 middle and 10 inner modules. One disk is 1.2 cm thick and has an outer radius of 56.7 cm, an inner radius of 26.7 cm and consists of a carbon fiber sandwich with a Korex® honeycomb filling. Various mounting points and holes have been machined on the disk, to facilitate the routing of the cooling circuits, fibers and power

---
1) *p*-doped-intrinsic-*n*-doped semiconductor diode.
2) Vertical Cavity Surface Emitting Laser.

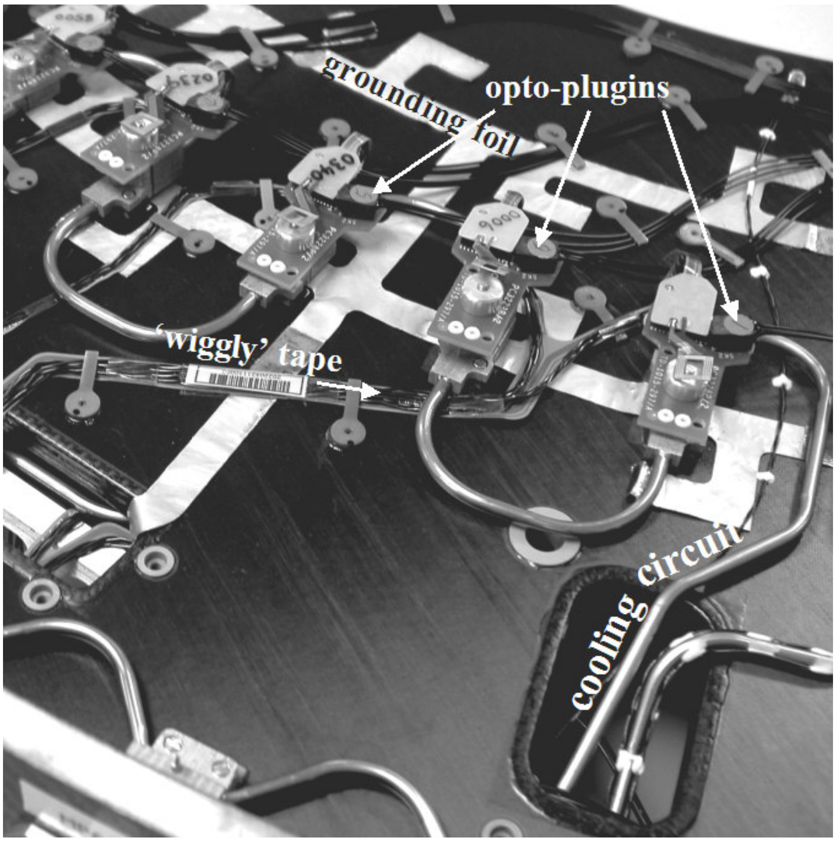

Figure 3.5: *Photograph of a part of one SCT end-cap disk, illustrating the services before the disk is populated with modules. The latter are temporarily replaced by dummy hybrids. Five of these are visible.*

tapes over the disk surface. The front and back side are used, to ensure a full coverage of the (x,y)-plane by the modules[3)] and at the same time have space for their associated services.

In Fig. 3.5 a photograph of a part of one disk is shown illustrating the service cables and pipes. The picture was taken before populating the disk with modules; the functioning of the modules was temporarily simulated with dummy hybrids. All the services reach the disk edge where they are routed along the cylindrical support structure, also called 'the cylinder'. The service components on the disk will now be summarized.

- **The power tapes**, also called 'wiggly' tapes, supply the control signal, the high voltage and the low voltage power to each module. Each wiggly tape can supply power for up to three modules.

- **The opto-harnesses** route all the optical fibers to and from the modules. Two fibers per module are used for the transmission of data and one fiber per module is used to send the timing, trigger and control signals. These three lines are connected to each module by an **opto-plugin**, which converts the optical signals into electrical signals. Each opto-harness can be connected to up to six modules.

[3)] In Figure 3.3 we see how the middle modules cover the radial gap where the front-end electronics and services from the outer and inner modules are located.

- **DCS sensors**, where DCS stands for Detector Control System, are for measuring the temperature and humidity. Up to 30 thermistors are located on one disk and more are attached at various locations throughout the SCT volume.

- **Grounding foils** are located on the front and back sides of all disks to ensure proper grounding connections to all the applied services. All disk elements are linked up to the support structure (see further down), which is connected to common ATLAS ground.

- **The FSI jewels**, where FSI stands for Frequency Scanning Interferometry, are present throughout the SCT. A 'jewel' is the reflecting element in a grid-line interferometer, with which an accurate measurement of a distance can be made. Each section (barrel or end-cap) is equipped with an FSI grid and is thus monitored for any change in shape.

- **The cooling circuits** are highly modular allowing one circuit per disk quadrant. The pipes have a Cu-Ni composition and consist of consecutive S-bends to alleviate the stress caused by thermal expansion. Each circuit is divided in up to three different branches, where the mass flow through each branch is regulated by a capillary located on the outside of the end-cap cylinder.[4)] The modules in one quadrant of a ring are all cooled by the same branch: one main circuit per quadrant feeds up to three circuits for the modules present on the inner, middle and outer ring.

  In Figure 3.6 (left) the schematics of the cooling circuit for the middle modules is given. The right figure shows a photograph of the realization on a disk. As it is the back side, there is but one circuit; the inner and outer modules are mounted on the other side. On a photograph in Fig. 3.8 the capillaries can be seen.

- **The cooling blocks -** For the outer and middle rings both module ends are cooled, whereas for the inner ring, where the modules consist of only two sensors and are thus

[4)]To be exact, the length of the capillary determines the mass flow, see also Section 3.4.2.

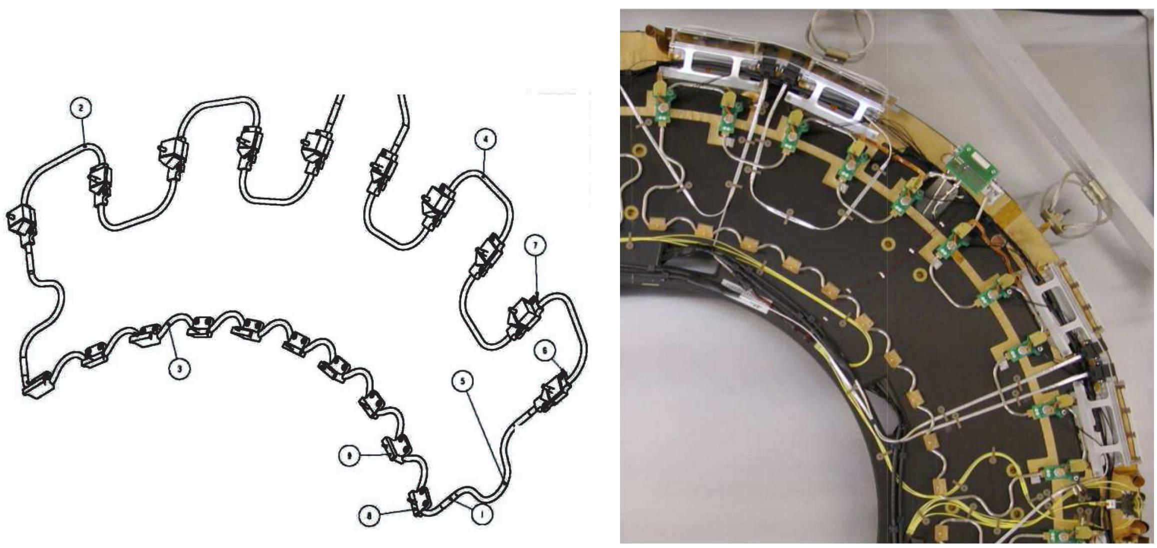

Figure 3.6: *Cooling circuit for middle modules: design (left) and realization on a (prototype) disk (right).*

shorter, only one cooling contact is implemented. The carbon-carbon[5)] cooling blocks are soldered to the pipes and mounted on the disk. The blocks have an aluminum threaded pin over which the module is placed and secured, with a controlled layer of thermal grease (20 μm thick) in between. The largest heat production is in the chips on the hybrid, approximately 0.8 Wcm^{-2} per chip. For the blocks located on the hybrid side of the module a 1 mm split therefore separates the block into two parts: a larger part for cooling the hybrid, and a smaller one making contact with the spine for the removal of heat from the sensor. See also Fig. 3.4.

In Table 3.1 the population of all end-cap disks with either inner, middle or outer modules is listed; both end-caps are identical. Disk 8 needs only a short middle, since having a full middle module would not have any optimizing effect on the η coverage. The outer and inner modules face the interaction point, except for disk 9, which was rotated and was mounted with its outer modules facing away from the interaction point to maximize the η coverage.

Disk	1	2	3	4	5	6	7	8	9	Total
$\|z\|$ (mm)	854	934	1092	1300	1400	1771	2115	2505	2720	
Outers	52	52	52	52	52	52	52	52	52	468
Middles	40	40	40	40	40	40	40	-	-	280
Short middles	-	-	-	-	-	-	-	40	-	40
Inners	-	40	40	40	40	40	-	-	-	200
Total	92	132	132	132	132	132	92	92	52	988

Table 3.1: *The total population of modules on each disk; each quadrant contains exactly one-fourth of the total. The nominal $|z|$ position of the center of each SCT end-cap disk is also listed.*

The nine disks are accurately mounted inside a cylindrical support structure, which itself is supported by a front and rear 'wing', see Fig. 3.7. The front wing is closest to the interaction point. These wings are used to place the end-cap on the TRT rails, allowing the SCT and TRT to share a common axis. Apertures are available on the cylinder to allow connections for the fibers and cables to be made at the patch panels at the disk edge. From these so-called patch panel forward 0 (PPF0s) the disk services are routed along the surface of the cylinder to the rear side, where they are again connected to the service lines connecting the end-cap with the systems in the service caverns, see Fig. 2.3. The entire cylinder is grounded with a copper-polyimide ground sheet that covers the outside of the cylinder surface, see Fig. 3.8.

The on-cylinder service lines are fiber ribbons carrying the optical signals, power tapes and the cooling circuits. At the PPF0s the wiggly tapes from the disks connect to Low Mass Tapes (LMTs), 21 mm wide polyimide power tapes with copper traces. These LMTs have been designed very thin to keep the amount of material as low as possible, which however also means that they have a significant resistance and produce considerable heat. LMTs connecting to modules in the same ϕ-segment of the disks are occupying the same surface position on the

5) a form of graphite with high thermal conductivity in one plane (typically $\sim$ 100 W/m·K) and poorer conductivity out of the plane ($\sim$ 50 W/m·K).

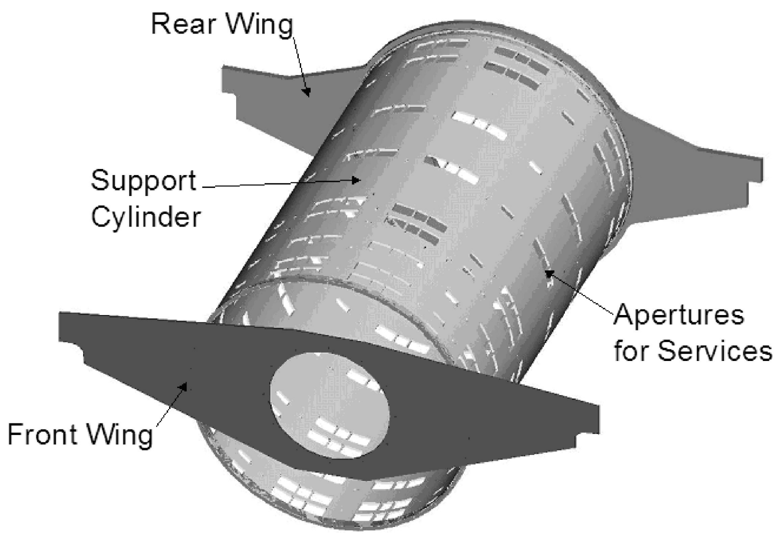

Figure 3.7: *The cylinder support structure. The two wings are used to mount the end-cap on the rails also used by the TRT.*

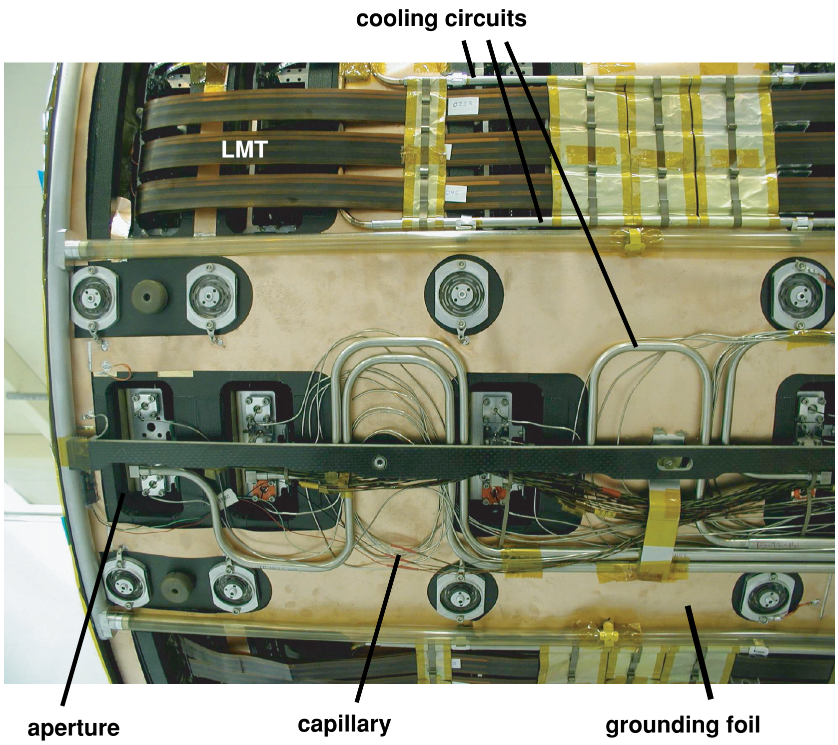

Figure 3.8: *Photograph of a part of the end-cap surface with the on-cylinder services. LMT stacks are visible, cooled by two cooling circuits on either side. More cooling circuits and capillaries are present, which connect to the on-disk services through the aperture.*

cylinder and are stacked together. When powered, the temperature in the center of a stack of LMTs can rise to 50°C, leading to a significant heat load on the detector.

In order to transport this heat away from the detector, dedicated cooling pipes are placed along side the LMTs, with foils wrapped around the LMTs and the cooling pipes to create sufficient thermal contact between the two components. These pipes are fed from the cooling circuits of disk 7,8 and 9, which have additional cooling capacity as they contain less module rings. Each set of three LMT stacks has a pipe on either side: one from disk 9 and one from disk 7 or 8. In case of failure of the cooling circuit on one of these disks, the LMTs are still cooled by the cooling circuit from another disk, preventing the loss of a full azimuthal slice of modules.

Separate capillaries carry the coolant to each circuit inlet. The exhausts from the circuits in one disk quadrant merge at the disk edge, such that all inner, middle and outer modules in one disk quadrant rely on a single cooling line outlet. This means that one leaking circuit can cause an entire disk quadrant to be affected. For end-cap C this is unfortunately the case on disk 9: circuit 186 is leaking and the quadrant with positive y and negative x cannot be operated. (Luckily disk 9 only carries outer modules.) Thirteen outer modules are thus non-functional.

3.2 SCT performance

The Inner Detector is designed to measure the transverse momentum of charged particles with precision better than 30% for tracks with p_T up to 500 GeV, requiring a resolution of ~20 μm in the bending plane [70]. For the track reconstruction the hit efficiency is to be >99%, at least 99% of the channels are to be operational and the noise occupancy per strip[6)] in the SCT is required to be less than $5{\cdot}10^{-4}$. To satisfy this last requirement, the threshold in the ABCD chip above which the signal is interpreted as a hit, needs to be at least 3.3 times higher than the average noise on the strip. With a typical value of the input noise on the silicon strips of $\sim$ 1500 electrons, the threshold setting is thus to be >0.8 fC (4950 electrons). The hit efficiency requirement dictates the threshold to be $<$ 1.3 fC. For comparison: a charged particle passing through the $\sim 300\mu$m thick silicon sensor creates approximately $2.5 \cdot 10^4$ electron-hole pairs, equivalent to a charge deposition of about 4 fC within the silicon.

The performance of the SCT has been monitored all along its production line. First, the individual modules were tested before being sent to the assembly site, i.e. Nikhef for end-cap A. Then during the assembly four main stages of tests can be considered: the end-cap disk (or barrel-layer) assembly, the end-cap cylinder (or entire barrel) assembly, the surface reception tests in building SR1 at CERN and finally the integration in the ATLAS detector in the cavern.

The testing consists of digital and analogue tests: the digital tests check that the redundancy links between modules and the chips bypass links are functional. It also includes a test of the pipeline circuitry. The analogue tests are: the Strobe Delay test, for the correct setting for the delay between the charge injection time and readout time needed for proper calibration, the 3-point-gain and the Response Curve test, see further, and the Trim Range Scan. The latter determines the optimum 'trim setting' for each channel, which compensates for the threshold offset each strip can have with respect to the one signal threshold that is set per ABCD chip. In [73] all tests and test results are discussed in detail, here we summarize the results of the tests performed in 2008 after the SCT was integrated in the ATLAS detector in the cavern.

[6)]Number of hits on a strip as a result of noise divided by the number of times the signal is read out.

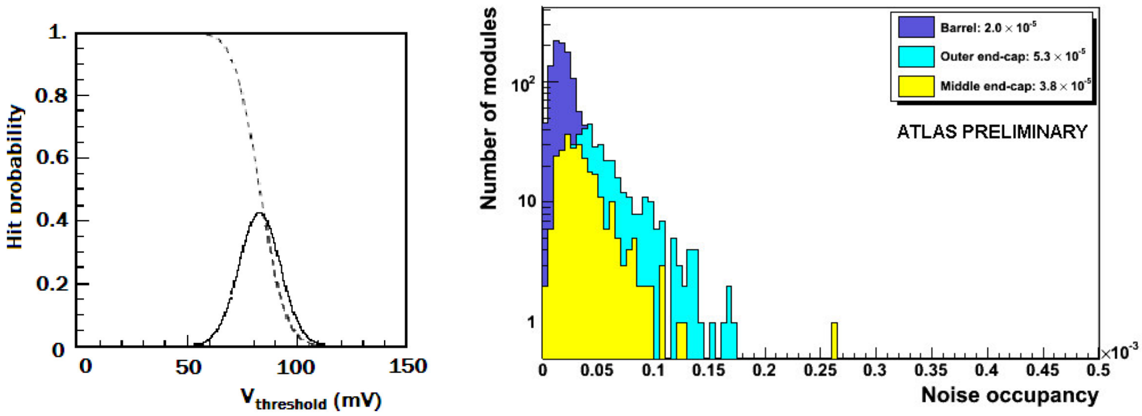

Figure 3.9: *Left: a typical threshold scan with the fitted width of the step function characterizing the output noise. Right: noise occupancy measured in the barrel and end-cap modules.*

3.2.1 Noise and dead channels

An important test is the 3-point-gain with which the input noise, the channel gain and the channel efficiency can be determined.[7)] As mentioned in Section 3.1.2 the ABCD chips on the modules are equipped with a charge injection circuitry which can be used for calibration. For this calibration pulse a step of 10 mV corresponds to an input charge of 1 fC. These pulses can be used to measure the input noise in the so-called gain test: on each channel increasing values of charge are injected and the number of hits for a given number of triggers is measured over a range of threshold.

In Fig. 3.9 (left) we see a typical result for one channel of such a scan. A scan of a (hypothetical) perfect channel with no noise would result in a step function: the hit probability drops from 1.0 to 0.0 when the threshold is varied from low to high values (keeping the injected charge fixed). Due to noise on the channel this step function is smeared and the scan produces an S-curve. The threshold at which 50% of the triggers are measured as hits corresponds to the average channel output for that charge, the width of the smeared step function characterises the output noise.

Repeating this scan with pulses with different input charges results in the 'response curve', the 50%-response-threshold vs the input charge. The 3-point-gain is simply a response curve of three points. The slope of a linear fit to this is the gain, and the input noise is determined by the output noise at 1 fC divided by the gain. The noise is measured in units of ENC: the Equivalent Noise Charge which is defined as the amount of electrons needed to be delivered to the input to produce the noise. In Table 3.2 an overview of the input noise for the different module groups at the different test stages for end-cap A is given. All values are comparable at each stage of testing. For end-cap C and the barrel the results were similar, see also [76].

With the noise temperature coefficients measured to be ~ 5 ENC/°C for the outer and middle modules and ~ 4 ENC/°C for the inner and short-middle modules, the final results in the table are almost within specification: the maximum allowed noise during the initial LHC running is set at 1500 ENC with sensor temperatures ~ -7°C. This upper limit is to ensure

7) The Response Curve test does the same as the 3-point-gain test, with a larger number of injected charges for more accuracy.

that even after radiation damage the noise occupancy does not exceed $5 \cdot 10^{-4}$. In Fig. 3.9 (right) the noise occupancy is depicted, as measured in the cavern in December 2008 at the end of the cosmic muon run[8)]. It is clearly below the specification of 5×10^{-4}. The results in Table 3.2 are only a few percent too high and should be no reason for concern.

With the noise test defective channels (noisy or dead) can be identified, as well as bonding defects (noise too high or low). After comparing the results from the different test stages it can be concluded that there is no significant increase in the number of bad channels. The fraction of defective channels is 0.2% in the SCT barrel and 0.3% in the SCT end-caps, see [73, 77], safely below the specification of 1%.

Test Stage	Outers	Middles	Short Middles	Inners
Disk assembly	1606 ± 51	1527 ± 44	911 ± 25	1066 ± 31
Cylinder assembly	1586 ± 52	1519 ± 45	908 ± 25	1057 ± 33
SR1 reception	1584 ± 77	1534 ± 62	895 ± 38	1055 ± 44
Cavern integration	1608 ± 83	1559 ± 51	911 ± 26	1072 ± 32

Table 3.2: *The mean input noise and spreads (in ENC) of the four module groups for end-cap A during the four main stages of testing. All values have been normalized to a module temperature of* 0° *C.*

3.2.2 Hit efficiency

The hit efficiency is, in simple words, the fraction of hits recorded in a region of a sensor where a charged particle traversed and a hit can be expected. The hit prediction is calculated in the following way: for a reconstructed track in an event the hit (if there is any) located on the SCT barrel or disk under investigation, i.e. the i^{th} layer, is removed. A track refit is then performed excluding this hit and from the parameters of the new track an extrapolation to the i^{th} layer results in the predicted position of a hit on a module.

In order for a hit to be entered into the numerator of the efficiency calculation, it must be found within a certain road width around the predicted hit prediction. The results presented in this section are obtained with the cosmic run data of fall 2008; as most tracks correspond to low momentum cosmic muons the Multiple Coulomb Scatterings (MCS) of the charged particle traversing the detector can cause significant kinks in its trajectory. (This is not the case for the LHC in general.) In order to neglect the effect of these MCS a value of 2 mm was chosen for the road width.

The result obtained this way for the unbiased[9)] hit efficiency is depicted in Fig. 3.10. The horizontal axis is defined as follows: 0.0 is the module side facing the interaction point on the innermost layer of the barrel, or disk of the end-cap; 0.5 is the other side of the same module. 1.0 is again the inner side of the next layer/disk, etc... For this study $5 \cdot 10^4$ cosmic muon tracks were used, taken end 2008. For the barrel plot the selection cuts[10)] reduce the initial $6 \cdot 10^5$ track/silicon intersections by a factor of 0.47. The left figure thus contains around $3 \cdot 10^4$

8) Cosmic muons are muons created in the atmosphere by cosmic radiation and can travel all the way down to the ATLAS detector. End 2008 these muons were analyzed for commissioning and calibration purposes.

9) 'Unbiased' here means that the hit was excluded from the track fitting. The same analysis can be done without excluding the hit on the i^{th} layer, biasing the results.

10) Of which the synchronization of the SCT and TRT read-out timing and the requirement of a $< 40^\circ$ incident angle result in the biggest losses.

entries per layer point. There are however only about $1.7 \cdot 10^4$ entries for the entire end-cap A, as no end-cap triggers were operational yet in the cosmic run of 2008. All tracks are triggered by barrel trigger chambers and the number of entries drops rapidly with the disk number. The results for disk 9 are with approximately 50 entries. Almost all layer hit efficiencies are measured to be within specifications, i.e. greater than 99%. For this data set a preliminary alignment was used, i.e. the barrel was aligned down to the module level, while the end-caps were aligned as a whole to the barrel.

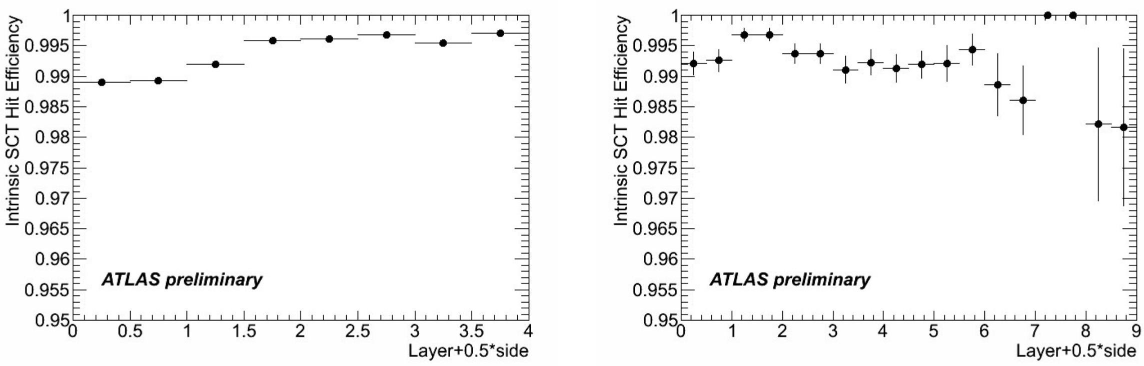

Figure 3.10: *Hit efficiency for each layer of the SCT barrel (left) and each disk of end-cap A (right) from cosmic muon tracks, using a preliminary alignment. Each layer/disk has two sides.*

3.2.3 Alignment and resolution

As the detected cosmic muons originate in the upper atmosphere, the vertical orientation of the end-cap disks makes a direct alignment using these muons more difficult. Therefore, the end-caps are aligned to the barrel. Figure 3.11 depicts the distribution of the hit residuals in the barrel, defined as the measured hit position minus the expected hit position from the track extrapolation, for the nominal and the preliminary aligned geometry[11)]. Compared to the results for a perfect geometry, which are determined from MC results and are shown in the same figure, we can conclude that the alignment is already on a good track.

The SCT detector resolution can be extracted from the width of the SCT hit residual distribution of a given module side after subtracting the track prediction and alignment corrections uncertainties, see [77]. The track uncertainty is however poorly estimated for the case of low momentum particles. Figure 3.12 shows the width of the SCT unbiased residual distribution, for the outer side of the modules in barrel layer 2, as a function of the unbiased track χ^2; this is the track χ^2 minus the contribution of the hit under evaluation.[12)] These modules were chosen to maximize statistics and minimize track errors. The figure depicts the distribution obtained for simulated and for real data. The benefit of showing it as a function of the track χ^2 is that when the χ^2 tends to zero the contribution of low momentum tracks, and thus from track uncertainty, is negligible.

A width of 24 ± 1 μm is obtained for real data for tracks with an unbiased χ^2/ndof of less than 1. This is slightly higher than the 20 ± 2 μm obtained for the simulated data, most likely

[11)] For the alignment the global χ^2 approach was used, see [78].

[12)] The total track χ^2 is simply the sum of $\sum_i \left(\frac{residual_i}{\sigma_i}\right)^2$, where the sum runs over all hits i.

caused by the alignment uncertainties which have not been considered. A width of 20 μm is however *lower* than the theoretical value of 23 μm belonging to barrel module strips with a pitch of 80 μm. These small widths measured are due to the large number of double hits in both the real and simulated data. Approximately one in three of the hits is in fact a double hit, meaning that two neighboring strips are hit. From this one learns that the particle must have passed in between the two, reducing the uncertainty on its exact trajectory. This effectively reduces the resolution of the one-strip hit measurement.

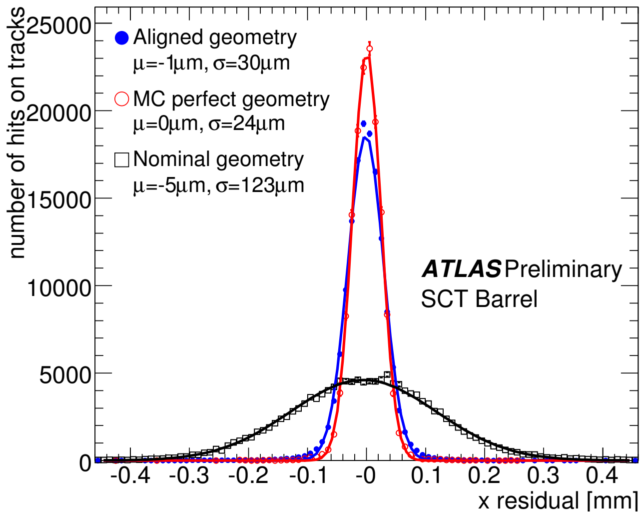

Figure 3.11: *Residual distribution in x (the projection onto the local x coordinate, which is the precision coordinate), integrated over all hits-on-tracks in the SCT barrel for nominal and preliminary aligned geometry. Tracks are required to pass the pixel inner layer.*

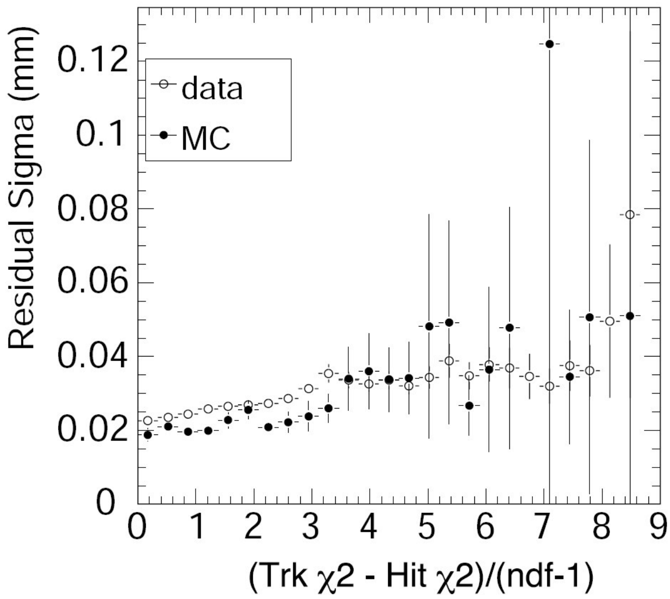

Figure 3.12: *Width of the SCT unbiased residuals (taken from [77]) as a function of the unbiased track χ^2 per number of degrees of freedom, for real and simulated cosmic muon data.*

3.3 The ID evaporative cooling system

For both the pixel and the SCT detector a special cooling system has been designed. Being the closest to the interaction point, these two detectors have the highest particle flux, resulting in radiation damage with a continuous degradation of the bulk silicon material and an increase in the device leakage current. To slow down the reverse annealing of the silicon modules, as explained in Section 3.1.1, the temperature must be kept as low as reasonably possible.

The cooling system installed must not only lower the temperature, it must at the same time remove a large heat load. Each of the modules in the detectors is read out through several front-end (FE) chips. With the heat produced at each FE chip (0.8 Wcm^{-2}) all modules together produce a considerable amount of heat: the SCT barrel produces by itself 22 kW, the two SCT end-caps together produce a similar amount and the total heat production of the pixel detector is around 17 kW. Although these values are only expected after years of irradiation, the capacity of the cooling system installed now must be sufficient to remove this heat load. At the start-up of ATLAS the power consumption of the modules will be almost a factor two lower: it increases over time as sensor currents increase due to the radiation damage, see Section 3.1.1. In Table 3.3 we summarize the power loads in different parts of the ID.

	Number of capillaries per circuit	Number of circuits	Nominal power load per circuit [W]	Subtotal nominal power load [kW]	Nominal mass flow per circuit [g/s]
SCT Barrel	2	44	504	22.2	7.8
SCT EC (3 sectors disk)	3	64	346.5	22.2	5.7
SCT EC (2 sectors disk)	2	8	241.5	1.9	4.5
Pixel Barrel	1	56	220	12.4	4.1
Pixel Discs	1	24	110	2.7	2.1
Pixel service panels	1	8	220	1.8	4.1
TOTAL		204		63.2	

Table 3.3: *Basic parameters and cooling capacity of the cooling circuits.*

A silicon detector can survive longer at lower temperature, yet with the pixel and SCT detector being at the heart of ATLAS the material restriction and the limited space put severe constraints on the possible cooling achievable. An evaporative cooling system has been chosen, to operate at a coolant temperature of -25°C. With the total thermal resistance between the modules and the cooling pipes, this amounts to the SCT and pixel modules operating at around -7°C and 0°C respectively. In this section we go into the details of the ID cooling system. We cannot however cover everything and for a more detailed description we refer the reader to [79, 80].

3.3.1 Evaporative and mono-phase cooling systems

An evaporative system has been chosen over a mono-phase system for several reasons: the higher heat transfer coefficient between the cooling fluid and the cooling pipes, the smaller temperature gradient along the long cooling channels, and the smaller pipe size required for the circuits. An important reason is that extracting heat at a phase change is a more efficient way than using a single phase cooling system, reducing the amount of cooling liquid needed and reducing the sizes of the pipe work.

To give an indication, the specific heat capacity (SHC) of C_3F_8 , the refrigerant used in the cooling system, is 0.794 J/(gK), at 1 bar and +25°C. Its latent heat vaporisation (LHV) is 97.0 J/g at 1.7 bar and −25°C. With a heat load of 63 kW the evaporative system thus needs 0.65 kg/s to keep the detector cooled[13)]. A mono-phase system would need 7.2 kg/s, assuming we tolerate a 10°C increase in temperature[14)]. Not only is such an increase in temperature undesirable, but a factor of ten more coolant would thus be needed.

3.3.2 Coolant choice

There are several reasons for choosing C_3F_8 as the coolant for the system. The saturated n-type fluorocarbon refrigerants C_nF_{2n+2} have many properties needed in ATLAS: they have very good stability against radiation, they are non-flammable, non-toxic and electrically insulators.

Different types of fluorocarbons have been considered and in Table 3.4 we list some important properties of two of them. In the end C_3F_8 was chosen for mainly three reasons: firstly, it gives a lower pressure drop in the vapor phase, as we see in Table 3.4, which allows for a reduced size of the return pipe. Secondly, it has a low saturated vapor temperature at the minimum operating temperature of −25°C, which is still above the atmospheric pressure. This means that there can be no air ingress. And thirdly, it shows the highest heat transfer coefficients.

Refrigerant	Latent Heat $[J/g]$	Vapor volume per cm^3 of liquid $[cm^3]$	Vapor pressure $[bar_a]$
C_4F_{10}	101.1	242.6	0.58
C_3F_8	97.0	71.4	2.46

Table 3.4: *Physical properties of two possible refrigerant candidates, at −15°C.*

A system with CO_2 has also been considered. Such a system has several advantages: the coolant can operate at lower temperatures, there might be less material needed, and CO_2 is a cheaper material than C_3F_8 ; last but not least, it is environmental-friendlier, see [81]. However, due to lack of expertise with such a system and time to develop it, it has not been chosen to be implemented in ATLAS. Especially the higher pressures at which it operates and the exact amount of pipe-work (material) needed for such a system were reasons for concern.

3.3.3 Thermal enclosure

For the detectors to be kept at such low temperatures, they must be contained in a dry environment to prevent condensation occurring on the cold structures. The four different parts of the SCT and the pixel, i.e. the pixel, the SCT barrel and the two SCT end-caps, are therefore all individually isolated by a thermal enclosure flushed with dry nitrogen. The TRT itself is

13) This is lower than the total of 1.1 kg/s in Table 3.3: to be sure to have enough cooling capacity at any time, the total flow is almost twice as large. Hence also the need for heaters, see page 76.

14) Here we assume that the SHC is the same at −25°C as it is at +25°C. The boiling point is at −37°C, so the assumption is not too far off.

split in three individual parts, i.e. the barrel and its two end-caps, and these are flushed with CO_2 as they operate with a gas mixture of CO_2 , O_2 and Xe. To form a barrier between the TRT and the silicon detectors, the gaps in between the sub-detectors are flushed with CO_2 . See Fig. 3.15 for an overview of the seven systems and [80] for more details.

The enclosures of the seven sub-detectors must ensure thermal neutrality and gas isolation between them, all seven thus have an independent temperature and gas control system. With the limited available space the choice was made for active elements: the pixel and SCT are covered with heating foils to ensure thermal neutrality at the boundary between sub-detectors. During normal operation of ATLAS this means that the outside of the SCT is warmed to the temperature of the TRT, i.e. room temperature; the pixel heater pads can stay off. A second role of the heater pads is keeping the pixel and SCT outer temperatures above the dew point of the cavern, when the detector is open and the cooling is running. This is when the pixel heater pads are also needed.

3.4 Cooling system components

The easiest way to understand how the cooling system works is to go step by step through its pressure-enthalpy (PH-) diagram, see Fig. 3.13(a). The part of the system actually in the ID is between point D' and point F'. We will start by explaining the process from point A. From there up to point D the system is located in the USA15 area, see Fig. 2.3. A schematic overview of the lay-out of the cooling system is given in Fig. 3.13(b). The parts going between point D and D' and between point F' and A correspond to the pipes carrying respectively the fluid and the gas to and from the detector.

3.4.1 Off-detector part

The off-detector part consists first of the main cooling plant with the compressors and the condenser located in USA15, and second of the four distribution racks which are located on the gallery at the sides of the ATLAS cavern (UX15). Each rack serves one quadrant of the detector and controls both the inlet pressure and the back pressure of each of the, on average, 51 individual fluid circuits in a quadrant.

Starting at point A, the gas returns from the back pressure regulator and goes to the compressors. At normal operation of ATLAS a maximum of six compressors, working in parallel, compress the gas from 800 mbar absolute at the main return manifold to 17 bar absolute at their outputs. All but two of these compressors run in an ON or OFF mode; the first two (also on UPS[15)]) have a by-pass line, making it possible to fine tune the flow rate and thus tuning the pressure at the compressor inlet manifold to a constant value. We note that in 2008 not more than four compressors ran simultaneously; the maximum of six compressors will only be needed at the end of life of the sub-detectors, when the heat production is at its highest. A seventh compressor will also be installed, such that for maintenance one compressor can be turned off with the cooling system still running.

At point B in the PH-diagram, the fluid is still in a gas form. It is condensed inside a mixed water plate heat exchanger, which has the water circulation inside the heat exchanger regulated to maintain a constant condensation pressure. After the condenser the liquid returns

[15)]Uninterruptible Power Supply. A system ensuring a continues power supply, even in case of failure of the regular supply.

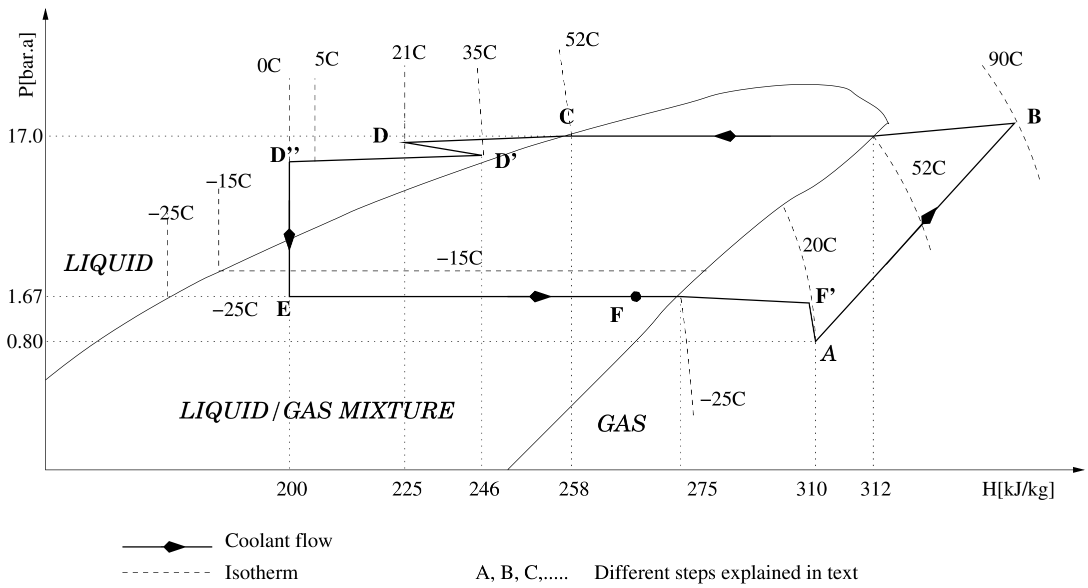

(a) Pressure-enthalpy diagram for the ID cooling system.

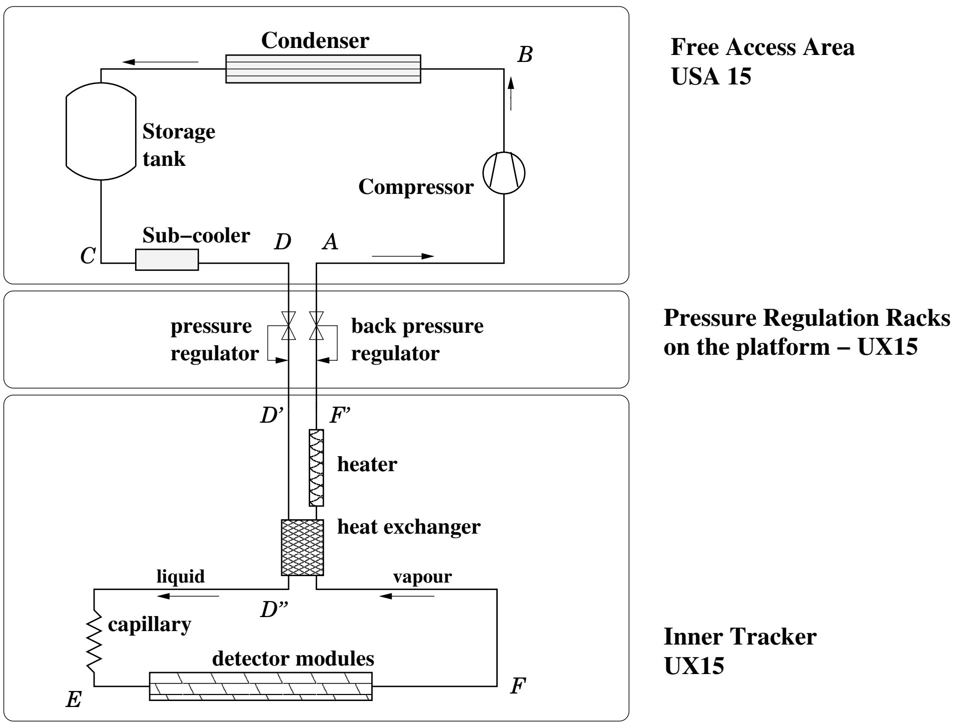

(b) Schematic layout of the ID cooling system.

Figure 3.13: *The process of the cooling liquid given in different steps from A to F' in a P-H diagram and in a schematic layout of the system.*

to the main inlet distribution manifold, passing first through a storage tank and a sub-cooler. This last cooler, also working with mixed water, brings us from point C to point D in the PH-diagram.

Leaving the USA15 area the liquid has a long way to go to reach the detector. Along this passage, which is in total more than 100 m long, the pipes are routed for more than 20 m through a tunnel also used to route power cables to UX15. The heat produced by these cables and the environmental temperature in the tunnel is unknown. After the pressure regulators, see next section, but just before the ID, the pipes are again routed along cables. Altogether it has therefore been assumed that, as a worst case, the liquid could warm up to a temperature of 35°C before reaching the ID, bringing us to point D'. By the end of the year 2008 it was clear that the temperature increase is much less and the liquid arrives at the ID not warmer than 25°C: the last part of the routing just before the ID is also together with the returning cold gas pipes, effectively cooling the incoming warmer liquid pipes.

3.4.2 On-detector part

A schematic view of the on-detector part is given in Fig. 3.14. From the distribution racks on the platforms a total of 204 circuits go into the detector. Each circuit starts with one Pressure Regulator (PR) on one of the racks, which sets the inlet pressure. This can be used for small adjustments of the flow rate through the circuit, but its main purpose is to keep the pressure above the saturation point of the fluid; otherwise vapor formation will lead to a significant reduction of the flow through the capillaries and to a reduced cooling capacity.

Each circuit then consists of several components we will discuss shortly and finally returns to the distribution rack where the Back Pressure Regulator (BPR) controls the outlet pressure. This pressure in fact sets the temperature of the outlet cooling fluid, which can be seen in the PH-diagram of Fig. 3.13(a). Setting a higher/lower pressure means that the point in the diagram where the fluid goes from saturated state to gas state will be higher/lower on the phase-transition line and be at a higher/lower temperature. Obtaining a temperature of −25°C requires therefore an absolute pressure of 1.67 bar for the C_3F_8 cooling fluid.

Heat exchanger Going from point D' to point D" in the PH-diagram there is a temperature drop of the liquid. This happens in the heat exchanger (HEX) where the incoming warm liquid interacts with the outgoing cold gas. The benefit of this component is that a more efficient use of the available enthalpy can be made, and that the outgoing gas is warmer.

The design of the HEX is sub-detector dependent, mainly driven by the available space. The efficiency of a HEX depends on several factors: the fluid mass flow and speed, the fraction of liquid to vapor in the fluid returning from the detector and the orientation of the HEX. This last factor is of importance as the orientation influences the flow and thus the amount of contact between the incoming and outgoing coolant.

Capillary After the heat exchanger the coolant passes the capillaries. The purpose of these is to drop the pressure of the fluid, such that it enters the detector structure in a mixed phase of liquid and gas, with a vapor quality[16)] as low as possible. That is, it must be just in the boiling phase to be as efficient as possible in extracting the heat from the modules.

The flow through the capillaries is the pressure drop we observe in the PH-diagram from point D" to point E. Each circuit can have either one, two or three capillaries, depending on

[16)] A fluid which is pure gas has vapor quality of 1; pure liquid has vapor quality of 0.

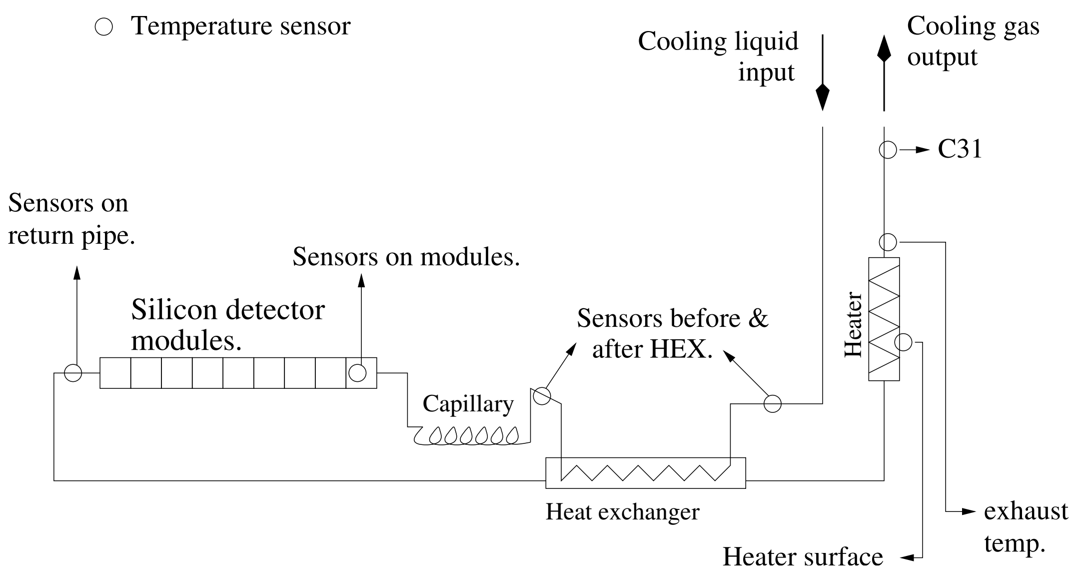

Figure 3.14: *The on-detector part of one cooling circuit. All components and several important temperature sensors are shown.*

the number of branches the circuit splits into. Each capillary is used to set the correct mass flow needed in that specific branch. The required mass flow is branch specific: it depends on the power dissipation along that branch, the efficiency of the circuits HEX and on the vapor quality at the exhaust of the cooling structure. Setting a correct mass flow is achieved by tuning the length and diameter of the capillary. The lengths vary between 1.5m and 6m, the diameters between 0.65mm and 1.00mm; see [79] for all details.

Detector structure Arriving finally at the point where the cooling does what it is designed for, that is taking the heat load from the detector, the fluid goes from point E to point F in the PH-diagram. At point F, this is again after the detector structure, the fluid must not have reached the phase-transition line, since that would imply that it is 100% gas which greatly reduces its cooling capacity.

Heater After the detector structure the fluid passes the HEX again where it absorbs more heat from the incoming liquid. The fluid after the HEX can still be a mixture of liquid and gas, and has a very low temperature. If this were to leave the dry environment of the ID, it would cause condensation along the pipes going back to the distribution racks on the platforms. To prevent this, the coolant is brought to room temperature by a heater, basically an electric coil. This brings it to point F' in the PH-diagram, where it is at room temperature and completely in a gas state.

If the heat load of the detector should suddenly drop or completely disappear for whatever reason, the heater still has the function of bringing the fluid to room temperature. This means that it must be able to react within a reasonable time to changes in the cooling flow and that its maximum power is equal to or greater than the full heat load of the detector branch.

In Fig. 3.14 we can see the location of several temperature sensors at different points in the cooling circuit. These are used to monitor the whole system; some are used to control the heater power such that the temperature of the fluid leaving the detector is around 20°C. The temperature of the heater surface is used for the interlock system: if it rises above 55°C, the current is immediately stopped, independent of the power request. When the temperature drops below the limit, the current is resumed. We note that for some circuits the interlock limit is set higher, see Section 3.5.2.

Change of heater design In the beginning of 2007 during the installation of the heaters, two problems were discovered. First, the location of the control sensor on the heater was found to be not-optimal. Secondly, a combination of moisture and wrong glue used for the connectors on the heater resulted in a short-circuit in a limited number of heaters. This ended in one heater partly melting one connector when testing the installation. To prevent this from happening again the heaters were redesigned. It turned out that exactly around the original location of the control thermocouples on the heater the fluid is coldest. This is probably caused by the narrowing of the pipe. In the new design the narrowing was made less severe, and the regulation thermocouple for the control line was placed after the heater, where the fluid has a more homogeneous temperature. In order to still be able to reach the SCT heaters after installation, these were also placed at a different position than originally planned. Figure 3.15 shows the original location where the SCT heaters were supposed to be placed. In the new design they were moved to the end-flanges, just like the pixel heaters.

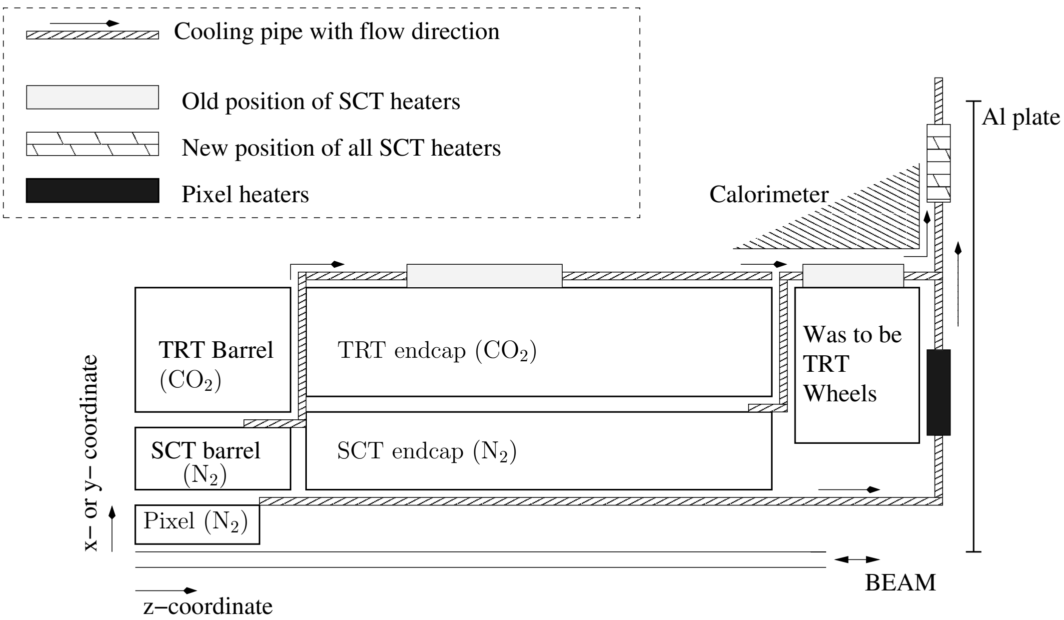

Figure 3.15: *Schematic layout of one quadrant of the ID. The old and new position of the SCT heaters is given. The barrel compartments extend to the other half of the detector: with a mirrored quadrant to the left, we can see the seven different environments. The 'Was to be TRT wheels' indicates space reserved for additional TRT wheels. These never were constructed, and the space is now used for the pipe-work needed to the new SCT heaters.*

The Back Pressure Regulators The pressure drop observed from F' to A in the PH-diagram is the drop over the BPRs which set the pressures at the on-detector side. The pressure of the fluid at the off-detector side of the BPRs is regulated by the operation of the compressors.

For the coolant temperature to be $-25°$C in the detector, the pressure at the inlet-side of the compressors is to be around 800 mbar, see Fig. 3.13(a). Turning on cooling circuits however changes this pressure, with more fluid arriving at the compressors. In Fig. 3.16 the Vapor Return Pressure is shown and we observe the pressure rising as circuits are turned on. From 15:00 up to 17:00 a total of 63 loops is turned on. At 15:28 and at 15:42 the pressure suddenly drops: at both times an extra compressor is turned on. The pressure drop is a consequence of the sucking-effect of the extra compressor. The fact that we do not measure 800 mbar after the turn on of a compressor, is because in 2008 the cooling system was operated at higher temperatures than in final operation.

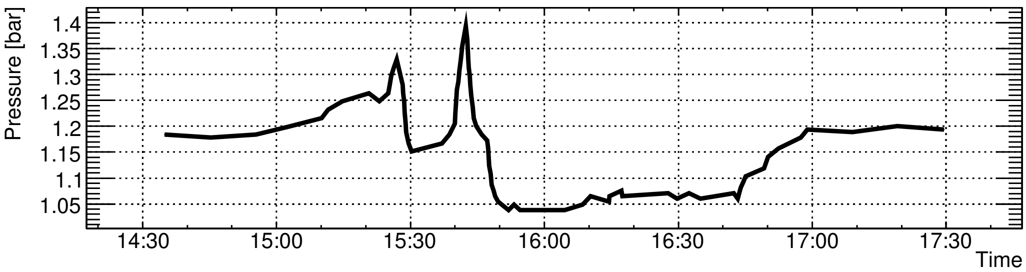

Figure 3.16: *Vapor return pressure during turn on of circuits. At 15:28 and at 15:42 the effect is visible of two compressors turning on.*

Problems with the compressors

On May 1st 2008 a serious failure of the cooling plant occurred, shutting it down for three months. It turned out that three compressors were badly damaged due to slipping of the internal magnetic couplings. Fig. 3.17(a) shows a schematic of one compressor. An electric motor drives the compressor through a magnetic coupling; this type of compressor was chosen because the magnetic coupling makes it possible to have a good isolation of the C_3F_8 gas, reducing leaks and possible contaminations. Due to a still unknown reason the coupling started to slip. The magnet driving the compression came to a halt, while the magnet driven by the electric motor kept turning, creating electric currents heating up the magnets. The system almost certainly ran for more than twelve hours in this condition and came to a halt when the magnets broke to pieces due to the heat.

The manufacturer repaired the compressors and also installed sensors on all compressors counting the number of rotations of the cranks to make sure these run at 1450 RPM; the cranks drive the compression and are magnetically coupled to the electro motor running at 1450 RPM, see again Fig. 3.17(a). The interior damage from the May 1st incident was however such that small parts of the debris might have been transported into the cooling pipes. After investigation only the pipes outside the detector in the USA15 pump room were found to be contaminated, filters protected the pipes further downstream. When taken apart for cleaning the debris was found to be mostly from *another* part of the compressors: apparently the pistons eroded much

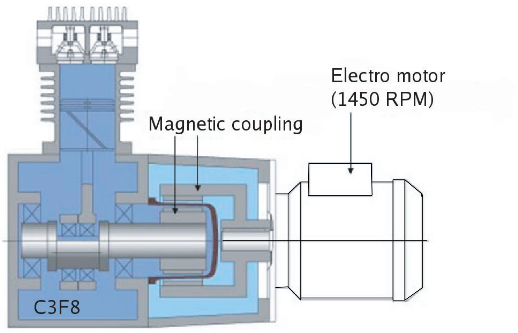

(a) Schematic of the compressor. (Type HAUG, model QTOGX 160/80 LM.)

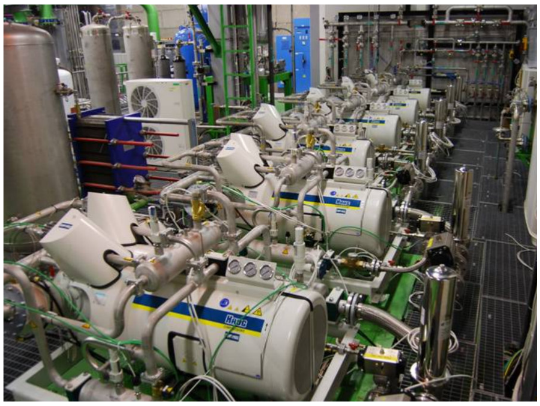

(b) Picture of the compressors in USA15.

Figure 3.17: *Left: In the compressor the electro-motor drives the outer of the two magnets. Through magnetic force this drives the inner magnet, making it possible to have a good isolation of the left part of the compressor containing the* C_3F_8 *. Right: a photograph of the six compressors installed in USA15.*

faster than assumed. Independent of the slipping problem, but also serious, this has lead to the installation of extra filters after the compressors and a more frequent replacement of the piston rings.

Two questions however remain unanswered: what caused the slipping, and why did it occur in three of the five running compressors at the same time?

3.5 Operating the cooling

Once the cooling plant is operational there are basically three controls to be set:

- The PR which is set for groups of circuits. In total there are 18 PRs to be set.
- The BPR which in fact controls the temperature of the cooling fluid in the detector. The BPR is set for 40 groups of circuits.
- The power of the heater of each of the 204 circuits. This is automatically regulated by a standard PLC[17)], which uses the temperature sensors downstream of the heater as a control input.

The operation of the system is straightforward once it is in normal run mode. The PR and BPR are at a certain fixed point, only the heater-power in fact is to be controlled and this is done by the PLC, which is based on a PID algorithm.

PID algorithm A Proportional-Integral-Derivative (PID) algorithm is used to control a certain parameter, such as the temperature of the cooling fluid, by measuring it and changing

[17)]Programmable Logic Controller

the setting of the heater current to reach a certain operational point. It does so by calculating the needed correction based on three different measurements of the coolant temperature: the absolute offset (the Proportional value), the integrated offset over time (the Integral value) and the rate at which the offset is changing (the Derivative value). The correction is a weighted sum of the three values and must be tuned to achieve a smooth transit to the set-point.

In our case, each circuit temperature is to be controlled by adjusting the power of the heater. Parameters to be fine-tuned are the proportional weights of the three measurement values and the set-point. A set of parameters can easily lead to (too big) overshoots. For example, if the temperature is too low, the power request will heat the fluid, but with such an amount that the temperature may become too high. If a wrong set of parameters is chosen, these overshoots will never get smaller, or worse, they will get bigger. The trick is to find that set of parameters which stabilizes the temperature as smooth as possible.

Most of the heaters have now been fine-tuned, however some still have problems with regulation. These problems are not immediately caused by wrong PID parameters and have to be dealt with in other ways. We go more into details on this in section 3.5.2.

3.5.1 Turning on and off the circuits

The cooling process shown in Fig. 3.13(a) operates during a standard stable run. The turning on and off of the circuits are however processes causing large temperature fluctuations themselves. Once LHC and ATLAS are operational and running normally, the cooling system will be turned on and off only once a year. In 2008 we were still in the commissioning phase. We will now discuss the turn on and off process of the circuits and with it the problems that were encountered during that time.

In Table 3.5 the different states a circuit can be in are given. As we mentioned, only the BPR, the PR and the heater-power are to be controlled.

Turning on

Turning on a circuit is a matter of setting the BPR and PR to the desired set-points and of opening the PR valve. We can go directly from any state, be it the LOCKED, OFF or STANDBY state, to the ON state. We note that only when a circuit is in ON state can the pixel or SCT modules on that circuit be powered. Whenever the state changes from ON to something else, the modules are also immediately powered off.

State	PR valve	BPR valve	Heaters
ON	Open & pressure set	Open & regulating to set-point	On & controlled by PLC
STANDBY	Closed	Open & regulating to set-point	On & controlled by PLC
OFF	Closed	Open & line is sucked vacuum	On & controlled by PLC
LOCKED	Closed	Open & line is sucked vacuum	Off

Table 3.5: *Different states of the cooling circuits.*

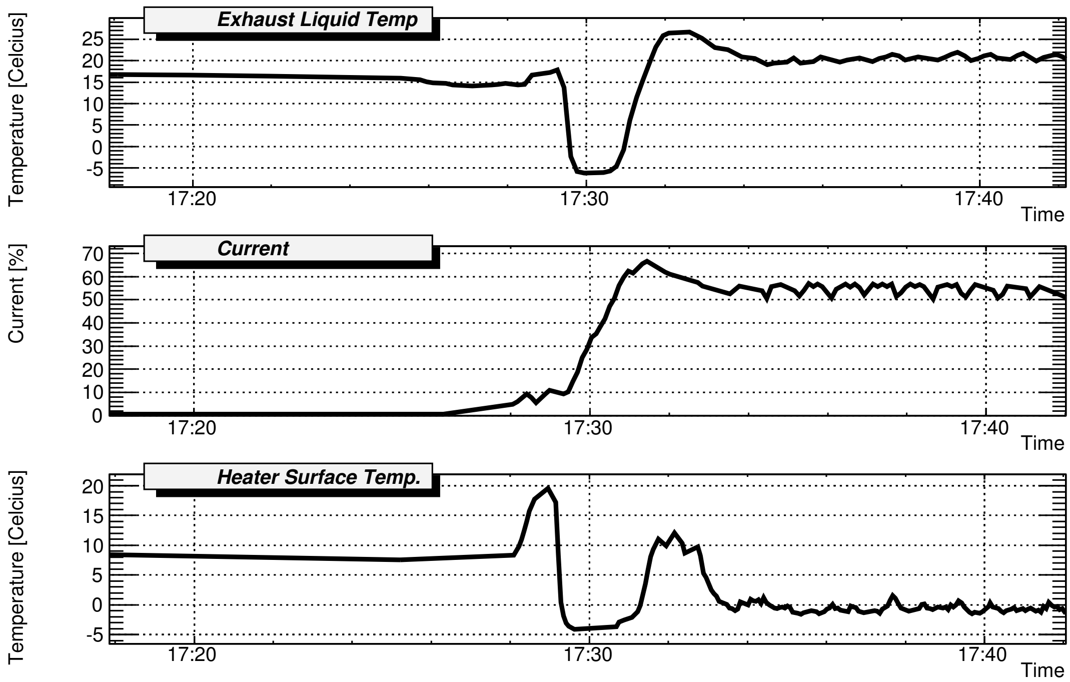

Figure 3.18: *Heater sensors for a well-behaving loop (#126); at 17:28 the circuit is set to ON. The power request is adjusted to the fluctuations of the exhaust temperature, until a stable state is reached. See text for more details.*

Figure 3.18 depicts the heater sensors for a circuit being turned to ON state. In the top plot we observe how the temperature of the exhaust liquid is slowly dropping before 17:28. This is due to neighboring circuits being turned on and lowering their surrounding temperature. At 17:28 the command to turn to ON is sent and the heater current in the second plot starts to rise initially with a few percent[18)]. The exhaust temperature, which is the control temperature to be stabilized by the PLC at 20°C, does not drop immediately, only at 17:30 it suddenly goes down by 20°C: it takes a few minutes for the liquid to fill the pipes. At this point the heater current goes up, until 17:32 when the exhaust liquid temperature is too high and the current is turned down a few percent. At 17:35 the circuit is finally stable. In the third plot the heater temperature is depicted and we observe how this fluctuates: first it rises, as there is a (small) current, but no fluid flowing yet. Once the flow starts passing, it goes down to -4°C. At 17:32 it has gone up again due to the too high current and at 17:35 it is stable at -1°C.

Turning off

When going to STANDBY, the PR valve of a circuit is closed. The coolant flow comes to a halt and the pressure at the on-detector side of the PR will slowly drop until it reaches the same value as at the BPR. The pipes are thus *kept full*, and the PLC can still run a current through the heater.

This is the reason that the intermediate STANDBY state is needed when shutting down: if

[18)]Throughout this section the heater current is given in percentages of its nominal 100%. The PLC regulates the current by turning on/off a power source of 110 V.

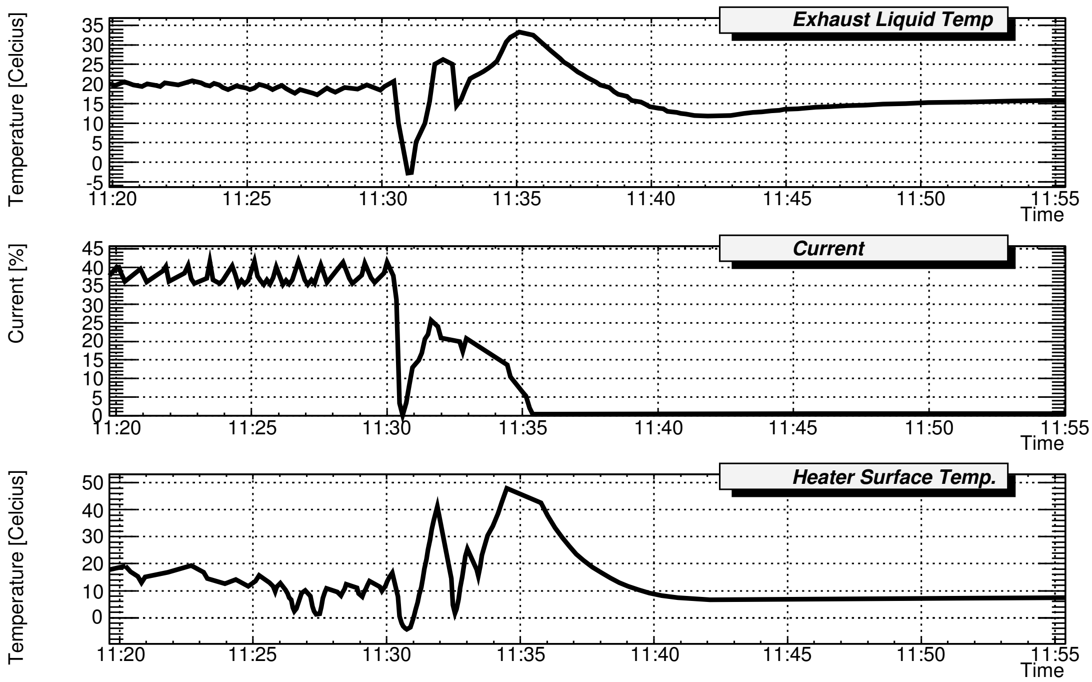

Figure 3.19: *Heater sensors for a well-behaving loop (#126); at 11:30 the circuit is set to STANDBY. The power request is adjusted to the fluctuations of the exhaust temperature, until a stable state is reached. See text for more details.*

a circuit is turned immediately from ON to OFF, the line is sucked vacuum at the BPR causing it to turn very cold; the P-H diagram of Fig. 3.13(a) shows how a lower BPR corresponds to a lower temperature. During the sucking the temperature of the coolant goes below $-25°$C, although of course at the same time the amount of liquid decreases, effectively decreasing the cooling capacity. Not only can the steep temperature gradient be dangerous for the detector, also the minimum temperatures reached can cause damage to the modules.

In these three states, the ON, STANDBY and OFF state, the heater is still on and its power is under control of the PLC. It is only when the circuit has stabilized again, visible by steady temperatures and no power over the heater, that the circuit is set to LOCKED: the heater is secured in an off-state. Figure 3.19 depicts the heater sensors during a standard turn to STANDBY. At 11:30 the circuit is put into STANDBY and with this command the PLC also sets the current to 1%. This is however too extreme and the exhaust liquid temperature drops more than 22°C. The heater current is resumed until 11:32 when the exhaust liquid temperature shoots over the 20°C and the heater temperature itself goes up to 40°C. This last value is still below the interlock level of 55°C. The heater current fluctuates until 11:35, and these fluctuations are immediately seen in the temperatures. At 11:35 the current stops as the exhaust temperature gets too high and these start dropping again. The exhaust temperature goes to 12.5°C at 11:42, not low enough to resume the heater current, and then stabilizes around 15°C.

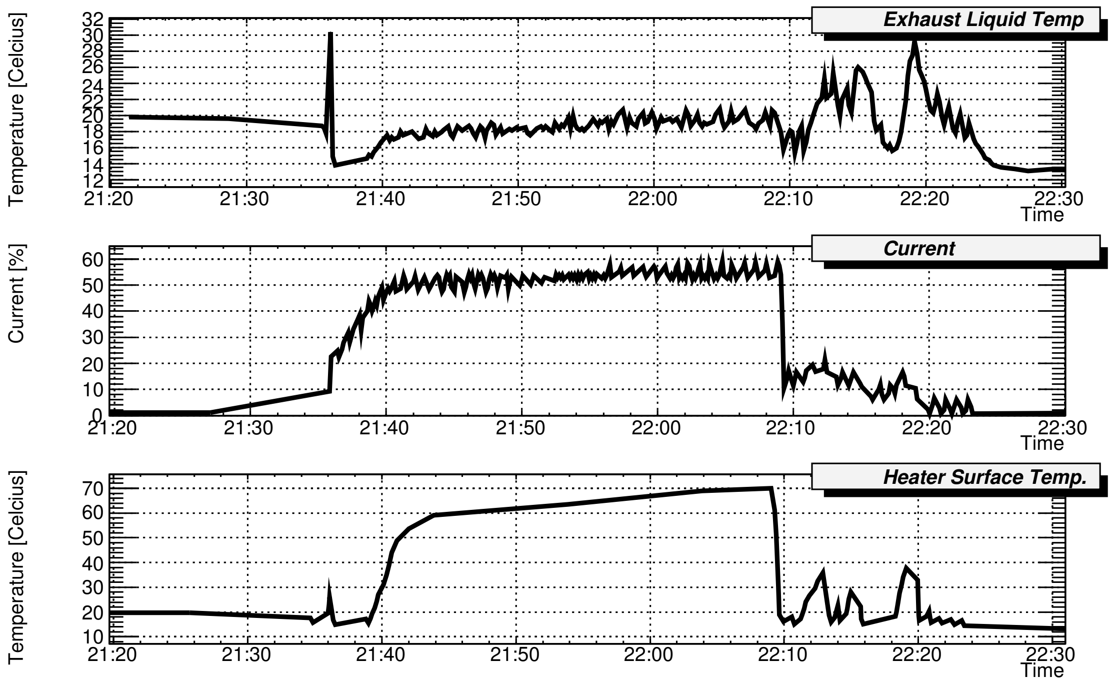

Figure 3.20: *Heater sensors for a problematic loop (#50) with temperature readout at the wrong location; at 21:35 the circuit is turned ON, but no stable setting is found. At 22:09 the circuit is set to STANDBY. See text for more details.*

3.5.2 Loops with problematic heater control

The turn on and shut down shown in Fig. 3.18 and 3.19 are both of circuit 126, a loop with no problems. Some circuits have turned out to be difficult to regulate. Due to different geometries of the circuits the flow through the 204 heaters is not always the same and the orientation of the heaters turns out to have a significant impact. During the first operation of the pixel cooling circuits in April 2008 it was seen that the pixel heaters were unstable (for approximately 30 loops) in the bottom half of the detector. For the SCT a similar problem exists for some circuits in the bottom half of the detector. All in all, we can distinguish two different problems we will discuss here.

Temperature regulation problem - temperature readout at the wrong location

It turns out that for some circuits the position of the control temperature sensor is too close to the heater itself. At that location, the mixture is not homogeneous enough and the temperature is not a correct measurement of the fluid's overall temperature. The control sensor for several pixel heaters is placed in the bend of the circuit, which happens to be a cold spot due to the dynamics of the flow. In Fig. 3.20 we see consequently how the temperature cannot be stabilized: at 21:35 the circuit is turned on. The exhaust temperature stays below 20°C, while the heater temperature almost goes up to 70°C. [19] The exhaust temperature however stays low, simply because the sensor is reading at a cold spot, and at the same time the current

[19] For these pixel circuits the interlock limit has been changed: the temperature limit is set to 80°C.

and heater temperature keep rising. At 22:09 the loop is turned to STANDBY again. For circuits with these problems a different method is now in use for regulation of the heaters: the temperature is read out further downstream by the so-called C31 sensors (50 to 100 cm downstream), which give a more correct measurement of the liquid temperature, see also Fig. 3.14.

In the SCT there are no circuits with a similar design as the bended ones in the pixel detector. Still, some circuits do have the drawback that the position of the control sensor directly after the heater is not perfect, i.e. even after the re-designing, see section 3.4.2. Especially the circuits again in the bottom part of the SCT have this problem. For these the control has not been moved to the C31 sensors: a stable regulation is recovered by lowering the control temperature to 17°C *and* by setting the PR to lower values, thus reducing the mass flow. For two SCT barrel circuits this does not recover the regulation, as these also suffer from the next problem we will discuss.

Temperature regulation problem - Interlock problem

When the heater is on, a current runs through a coil which runs around the fluid pipe. In Fig. 3.21 a schematic is drawn which shows how this creates a front somewhere along the heater where the liquid/gas mixture goes to a 100% pure gas. The gas after this front is heated even further by the current and being now in a single phase, its temperature rises.

For many circuits this single phase heating creates a problem. If the control sensor measuring the heater body temperature is behind the phase front, its readout can easily trigger the interlock and stop the current. Figure 3.22 shows the heater sensors for a circuit which has been turned on, but cannot find a stable current. First, just before 21:40 the loop is turned to ON. At 21:45 a stable exhaust temperature seems to be found, but the power request does go up slowly to 60%, probably to compensate for the small fluctuations of the exhaust temperature just below the 20°C. The heater temperature however is very high and at 22:14 hits the 55°C, thus triggering the interlock; this briefly cuts the current at 22:14, until the temperature is below 55°C again. The power request at the same time goes up due to the current being cut and not providing enough heat. After this, the current fluctuates due to the interlock being hit all the time, and with it the temperatures. The power request keeps rising until at 22:45 it reached 90%. To prevent this from getting even worse, the loop is turned to STANDBY manually.

There are several solutions to this problem: first, the limit for the heater body temperature can be raised such that the interlock is not fired. The heater will find a stable point, but the drawback is that this means running the system with several very hot heaters in the detector.

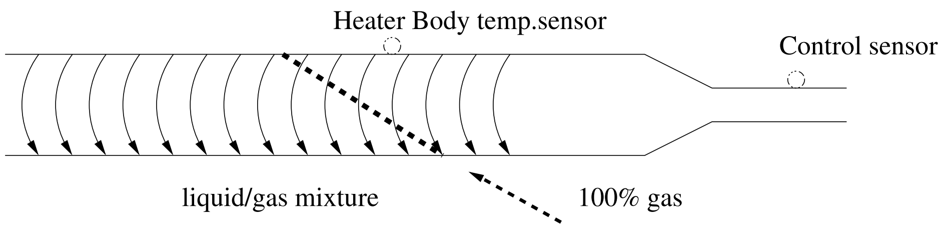

Figure 3.21: *Schematic of a heater. The coil lines are given by the arrows, the front between liquid/gas mixture and 100% gas is shown by the dotted line.*

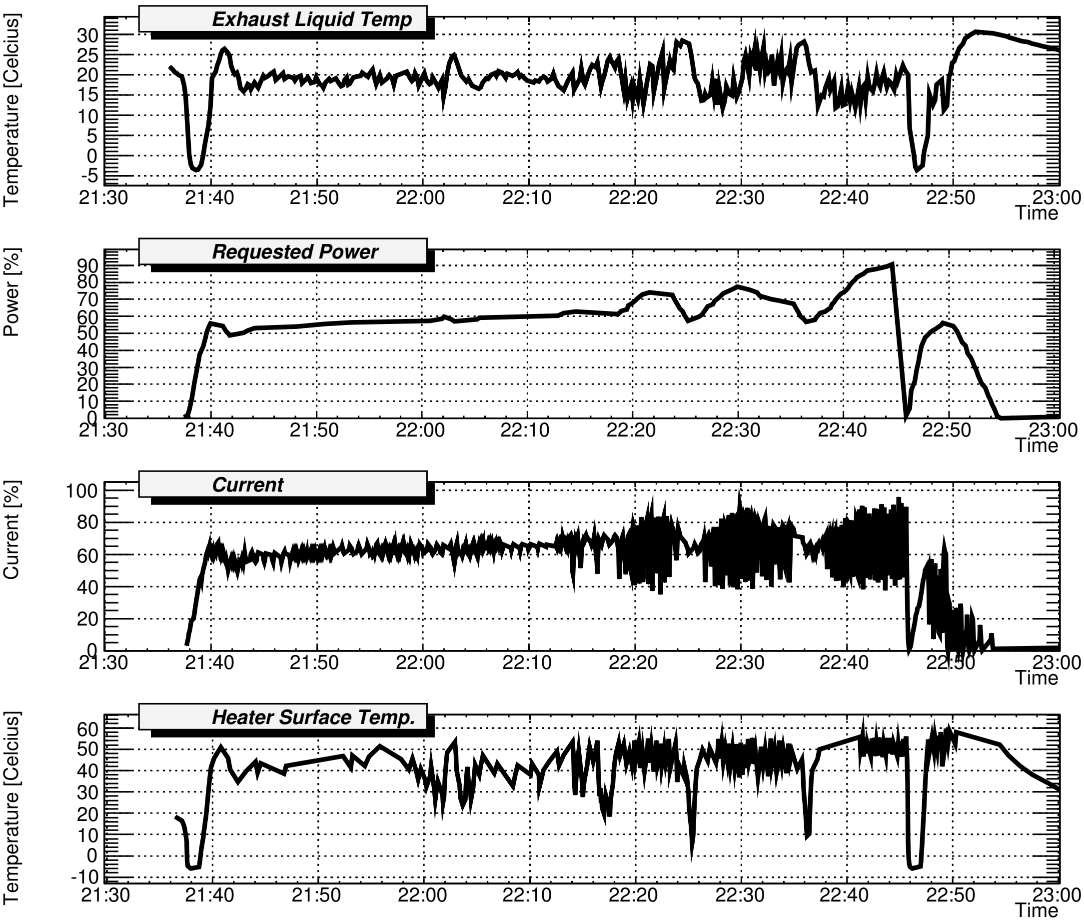

Figure 3.22: *Heater sensors for a problematic circuit (#149) hitting the surface temperature interlock when turned on. No stable run can be found and the circuit is turned to STANDBY at 22:45. See text for more details.*

Another solution is turning on the modules on that circuit immediately when the cooling circuit is turned on. The heat load of the modules means that the heater power request does not have to be too high and a stable running of the circuit can be found, as can be seen in Fig. 3.23. At 23:00 the coolant flow starts and the temperatures drops, the modules are turned on at this same time. The power request goes up and overshoots, just as we observed in Fig.3.18. In this overshoot the heater temperature hits the 55°C limit twice at 23:06 and 23:07 and the current is cut at those times. This does not cause any problem. A few minutes later the exhaust temperature is at a stable value and the heater is still safely below the interlock limit. Around 23:40 when it is clear that it stays stable, the loop is turned to STANDBY again.

Although this last problem has made the operation of the cooling more difficult during the commissioning phase in 2008, it is believed to be temporary. (Approximately 5 loops are still affected by this problem.) In the commissioning phase the cooling was operated at a back-pressure set to around 3 bar. This 'warm' running was chosen as a safe way to test the system. During normal operation of ATLAS, the back-pressure will be lowered to around 1.3 bar and the system will be much colder. This will solve the interlock problem: during tests on several

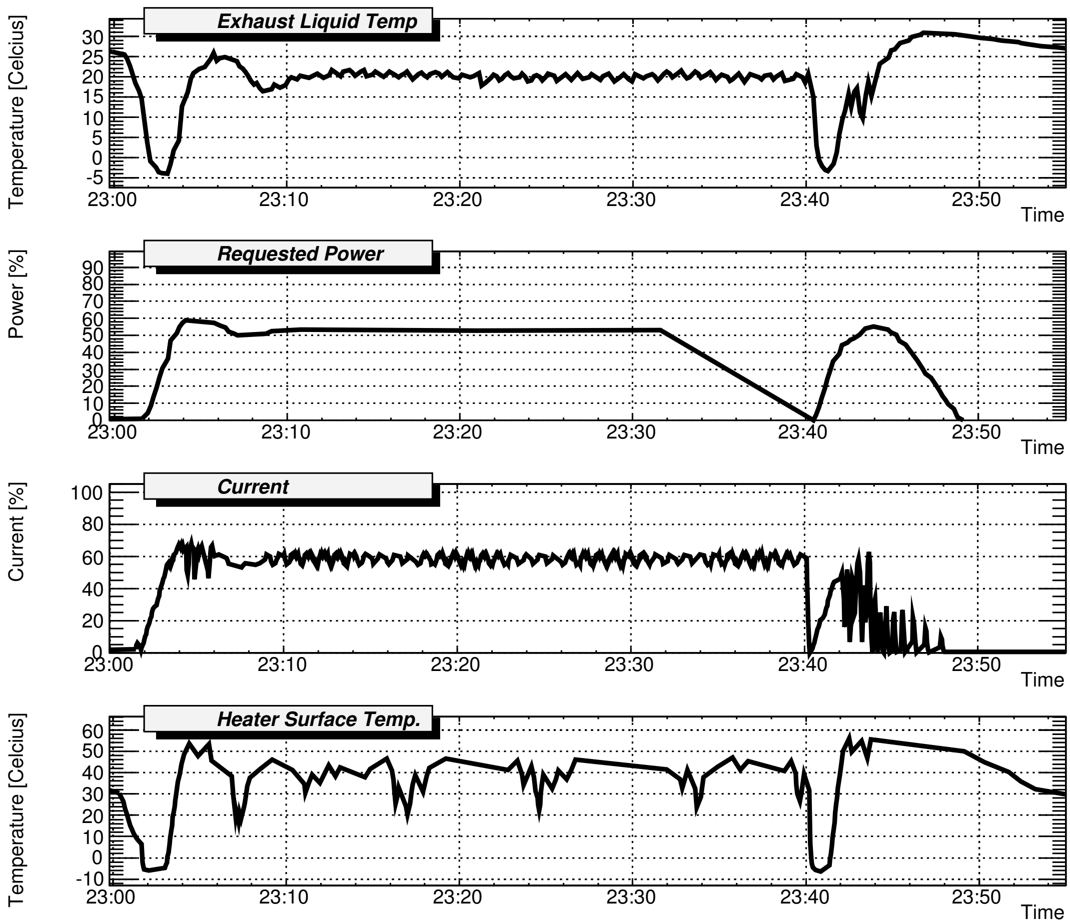

Figure 3.23: *Heater sensors for the same circuit as in Fig. 3.22. The difference is that at 23:00 the modules are also turned on. At 23:40 the circuit is again turned to standby.*

heaters it was found that the front as visualized in Fig. 3.21 moves to the left or right when the back-pressure is raised or lowered respectively. With the interlock sensor on the mixture side of the front, the problem disappears.

Chapter 4

Event simulation and reconstruction

In this chapter we give an overview of the software packages used to perform the event reconstruction and selection. We first discuss the software framework and briefly present the Monte Carlo (MC) generators used to simulate events. We then go into more details on the jet reconstruction and b-quark identification (b-tagging) algorithms. We also discuss the measurement of the Missing Transverse Energy ($\not\!\!E_T$) and finally we summarize the different object definitions and selections we will be using in our analyses.

4.1 ATHENA framework

The software package used is a flexible modular framework called ATHENA [82], which is derived from the GAUDI framework [83] developed for the LHCb experiment. With its modular design it can be applied to different types of events, be it proton-proton collisions in ATLAS or single particles such as cosmic muons traversing the detector. The framework is also designed such that it can be used for analysis of actually recorded events, or of simulations thereof. Simulated events are created with Monte Carlo generators and are used to study the performance of the detector and to validate the reconstruction algorithms.

The framework ensures that the algorithms requested by the user are run in the correct order. For this, the output of an algorithm is written to a common place in memory called the 'transient event data store', from where the next algorithm can retrieve it and process it further. The output can also be written to disk; in case the needed input for an algorithm is not present in the event store, the framework ensures that the data is read from disk. This setup makes it possible to run the complete chain of algorithms in one single job, or to only perform a certain part of the chain in a smaller job.

Event simulation

At the time of writing no collisions have been recorded yet in ATLAS. For a preliminary physics analysis we therefore need first to create events with MC generators and simulate the detector's response. In Section 4.2 we go deeper into the MC generators. For the detector's response the simulated passage of the created particles through the detector is handled by the GEANT4 toolkit [84]. This handles the interaction of the particles with the magnetic field and with the detector material, causing for example multiple scattering, energy loss, and much more. The toolkit also simulates the response of all sub-detectors and their sensors: a particle traversing a sensitive element such as a silicon sensor can create a 'hit'. The consequences of

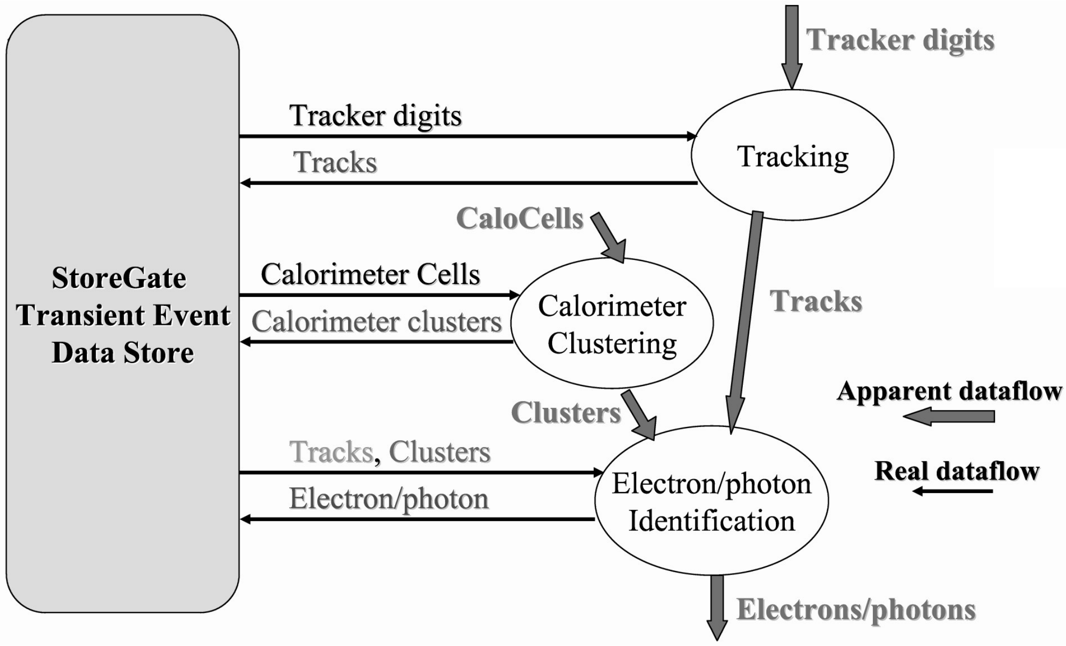

Figure 4.1: *An example of an ATHENA algorithm chain for the reconstruction of electrons/photons. The balloons are algorithms each performing a specific task. The algorithms retrieve their information from the transient event data store, where they also store their output. This is then used by the following algorithms in the chain. The Tracker Digits and the Calorimeter Cells can be simulated or real data.*

a hit, such as the drift of the charges in a silicon module and the response of the electronics is simulated. This final step is called the digitization.

We note that for the simulation of the detector's response there are several algorithm packages available. The most detailed is called the 'full simulation', which is the most accurate, but also the most time-consuming in processing. The least detailed simulation is called Atlfast; although less accurate it is still useful for many analyses and makes it possible to simulate events in far less cpu-time. For some specific studies it can be useful to combine the full and fast simulation: AtlfastII contains the full simulation of the Inner Detector, the fast simulation of the calorimeter and either the full or fast simulation for the muon spectrometer.

In this thesis, all samples analyzed are processed with the full simulation unless stated otherwise.

Event reconstruction

With either a simulated or a truly recorded event, the next step in the analysis chain is the event reconstruction. This requires various algorithms to perform the pattern recognition, track fitting, energy measurement, and much more. A detailed output of the reconstruction is written to an event summary data (ESD) file, a less detailed summary is written to an analysis object data (AOD) file. In case of a simulated event these samples also contain 'truth' information, that is information from the event simulation which can be used to study the quality of the reconstruction. As a last step, the samples can be analyzed either within the ATHENA framework or using ROOT [85] to perform physics analysis.

Figure 4.1 shows an example of an algorithm chain in ATHENA performing the reconstruction of an electron or photon candidate. Parts of the information stored in the transient event data store are written to the data set files, more in the ESD than in the AOD. This gives the possibility to rerun the ATHENA chain, if for example some calibration constants are changed. Whether the candidate is finally labeled as an electron or a photon depends on the object definition used in each specific physics analysis. In Section 4.6 we state the definitions we will be using in our analysis.

4.2 Event generators

In Section 1.1.1 we discussed how in the collision of two protons the hard scattering is an interaction of the quark and/or gluon constituents. In the simulation of events both the hard scattering and the underlying event are taken into account. The physical concept that makes such simulations possible is factorization, the ability to isolate separate independent phases of the overall collision. These phases are dominated by different dynamics, and the most appropriate techniques can be applied to describe each of them separately. For a detailed review on event generation we refer to [12]. In this section we only discuss the simulation of the hard scattering.

For the creation of events with Monte Carlo programs we can distinguish two steps: the first is the selection of the partons from the protons according to the PDFs and the calculation of their interaction. This is the calculation of the Matrix Element (ME) for a certain process with an MC generator. The second step is the parton showering used to simulate initial and final state radiation (ISR and FSR) on the calculated process. We will take the simulation of $t\bar{t}$ events to illustrate some of the possible techniques available for MC generators.

Figure 4.2 shows a hard scattering of two gluons producing a $t\bar{t}$ pair. We note that this is but one example, there are more processes with a top pair as outcome. The ME of this diagram is calculated at Leading Order (LO) and is made visible here in black, while additional FSR is created by a parton showering algorithm, visible in gray. In Chapter 6 we will be analyzing the $t\bar{t}$ AcerMC [86, 87] samples, which are created as this example. For the AcerMC samples the Pythia [88] parton showering is used.

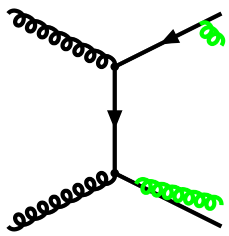

Figure 4.2: *Example of $t\bar{t}$ production at Leading Order (black) combined with parton showering (gray).*

Parton showering is known to be a good approximation for the radiation of extra partons in the soft and collinear limit only. If we want to incorporate $t\bar{t}$ events with extra hard jets it is therefore more accurate to use next-to-leading order (NLO) matrix elements. These do not only take into account the exact calculation for radiation of an extra gluon or quark, they also incorporate the effect of virtual corrections. In Figure 4.3 the two left diagrams are examples of NLO $t\bar{t}$ production, with again parton showering applied. MC@NLO [37, 38] is a MC generator based on this method; for the MC@NLO samples analyzed in this thesis the Herwig program [89, 90] is used for subsequent parton showering.

However, when quantum amplitudes of the matrix elements up to NLO are summed, interference contributions may be positive, negative or zero. To compensate for this, some events from MC@NLO are generated having negative weights. Typically about 13% of all generated events in the MC@NLO samples used in this thesis have negative weight.

A problem which arises when combining parton showering with matrix elements up to NLO is double counting. In Figure 4.3 the most right diagram is a LO $t\bar{t}$ production, which after parton showering has the same topology as the middle diagram. Some sort of subtraction or veto is needed to compensate for this. In MC@NLO the double countings are avoided using analytic expressions for the first shower emissions.

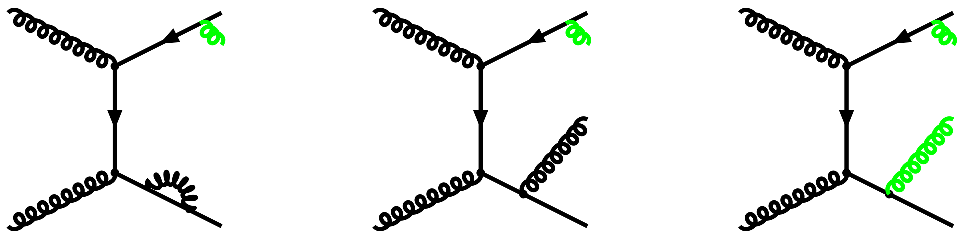

Figure 4.3: *The two left diagrams are examples of next-to-leading order $t\bar{t}$ production (black) combined with parton showering (gray). The most right diagram illustrates a $t\bar{t}$ production at LO with the same topology after the parton showering as the diagram in the middle, which is produced at NLO. Several techniques are available to prevent such double countings; see text for more details.*

For $t\bar{t}$ events with more and more extra partons the matrix elements of order α_s^N (with large N) are, at the moment, too difficult to calculate. The Alpgen program [91] can calculate the ME for $t\bar{t}$ events with up to 6 extra partons, at Leading Order. Compensating analytically for the overlap between jets created at ME level or at parton showering level becomes more difficult (with the ME calculated up to Leading Order only). A solution for this problem is the division of the phase space: the parton showering after the ME calculation is only used for soft and collinear radiation. If the parton showering does create an extra hard parton the event is rejected.

In more technical details: after the parton showering a jet algorithm is applied and the reconstructed jet of the showered partons is matched to the original ME partons. If no match is found, the assumption is that the jet is a consequence of hard ISR/FSR and is rejected. This specific technique is called the MLM matching.[1)] Another procedure to divide the phase space is the CKKW matching, see [92]. Figure 4.4 depicts a few examples of $t\bar{t}$ events with up to two extra jets. In the lower right diagram the gray gluon is created by the parton showering. The jet this creates cannot be matched to a parton generated at the ME level and the event is rejected. This prevents a double counting of the lower left diagram.

[1)]Free parameters in the MLM procedure are the minimum p_T of the parton and the minimum angular distance $\Delta R = \sqrt{\Delta\phi^2 + \Delta\eta^2}$ between two partons, for an event to be generated by the matrix element. The parameters are set at $p_T = 20$ GeV and $\Delta R = 0.7$ in ATLAS studies.

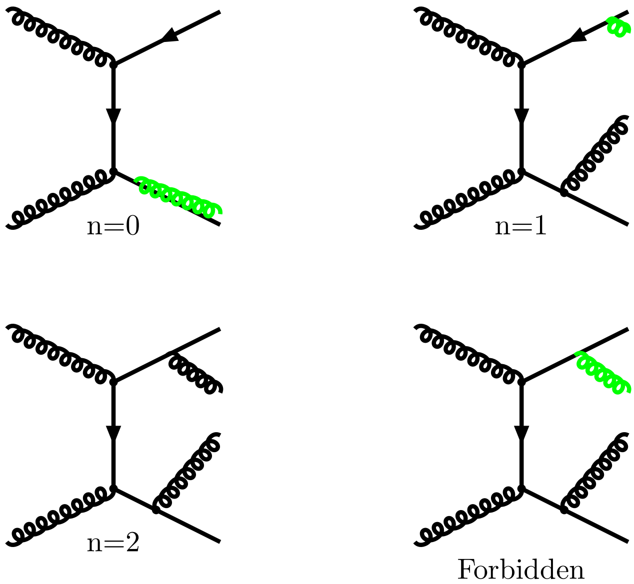

Figure 4.4: *Approximation of higher order $t\bar{t}$ production by combining tree level matrix elements (black) with parton showering (gray). To prevent double counting as in the two lower diagrams, the parton showering is restricted to only provide soft and collinear radiation.*

With different techniques available for event generation the difference between the predictions from several MC generators can be used for a study of the systematic uncertainty of the generators. A study on the prediction for the $t\bar{t}$ + n-jet spectrum from different MC generators is given in [93]; their conclusion is that Alpgen and AcerMC predict a slightly higher jet multiplicity per event than MC@NLO. We come back to this in Section 6.2.3.

4.3 Jet algorithms

A parton that has participated in a hard scattering hadronizes into a jet which can contain up to ~ 10 particles. A jet definition is a set of rules to cluster particles that "belong together", ideally (but impossibly) originating from a single parton, or at least corresponding to the distribution of partons before hadronization. In the busy environment we can expect at ATLAS this is far from trivial. We can reduce the problem at first to two questions: which particles get put together into a common jet? And how does one combine their momenta? The last question is nowadays mostly solved with the direct four-momenta sum (E-scheme), although other schemes have been used, see for example [94].

In this section we discuss the first question: which particles to put together? A jet leaves tracks from its charged constituents in the Inner Detector and deposits most of its energy in the calorimeter, where each incoming particle creates a shower of charged and neutral particles. Although studies are underway to gain information from the tracks in the ID, see [95], most jet algorithms only work with the information from the calorimeters. We will discuss step by step how this information is put together into a jet.

4.3.1 Algorithm requirements

Based on the study from Ref. [96] a set of basic rules has been assembled in ATLAS for the jet reconstruction. The most important requirements are:

- **Infrared safe -** The presence or absence of additional soft particles between two particles belonging to the same jet should not affect the recombination scheme. Generally, any soft particles not coming from the fragmentation of a hard scattered parton should not affect the number of jets produced.

- **Collinear safe -** A jet should be reconstructed independent of whether a certain amount of transverse momentum is carried by one particle, or a particle is split into two collinear particles.

- **Detector independence -** The reconstructed jet and its kinematic variables should not depend on the detector characteristics, i.e. all detector-specific signal characteristics and inefficiencies must be calibrated out or corrected as much as possible.

- **Order independence -** The algorithm should behave equally at the parton, particle and detector level.

The last two criteria for detector and order independence are the most difficult and are for now only approximately correct for most algorithms. The first two criteria must be satisfied however by all algorithms. Yet we will see later that this is also not always the case.

4.3.2 Calorimeter activity reconstruction

The calorimeters in ATLAS have about 200,000 individual cells of various sizes and with different readout systems, see Section 2.4. Before a jet finding algorithm can be applied to decide which particles to put together, the cell signals have to be converted into larger signal objects with physically meaningful four-momenta. Two different object definitions are available in ATLAS, the *calorimeter tower signals* and the *topological cell clusters*.

Figure 4.5 depicts an overview of the three jet reconstruction sequences available with these two calorimeter objects. For the tower signals there is one sequence; the cell clusters can however be dealt with in two ways, which differ in the point at which the hadronic energy calibration is performed. We come back to this in Section 4.3.4, we first give the definition of the tower signals and the cell clusters.

Calorimeter tower signals

For the tower signals the cells are projected onto a fixed grid in pseudorapidity (η) and azimuth (ϕ). The tower bin size is $\Delta\eta \times \Delta\phi = 0.1 \times 0.1$ in the whole acceptance region of the calorimeters, i.e. in $|\eta| < 5$ and $-\pi < \phi < \pi$ with $100 \times 64 = 6.400$ towers in total. Projective calorimeter cells which completely fit inside a tower contribute their total signal, as reconstructed on a basic electromagnetic energy scale[2)], to the tower signal. Non-projective cells and projective cells larger than the tower bin size contribute a fraction of their signal to several towers, depending on the overlap fraction of the cell area with the towers. The cell signals are on the basic electromagnetic energy scale; the tower signal as a sum of (possibly weighted) cell signals is thus at the same energy scale.

[2)]The raw signal from the ATLAS calorimeters. See [95] for more details.

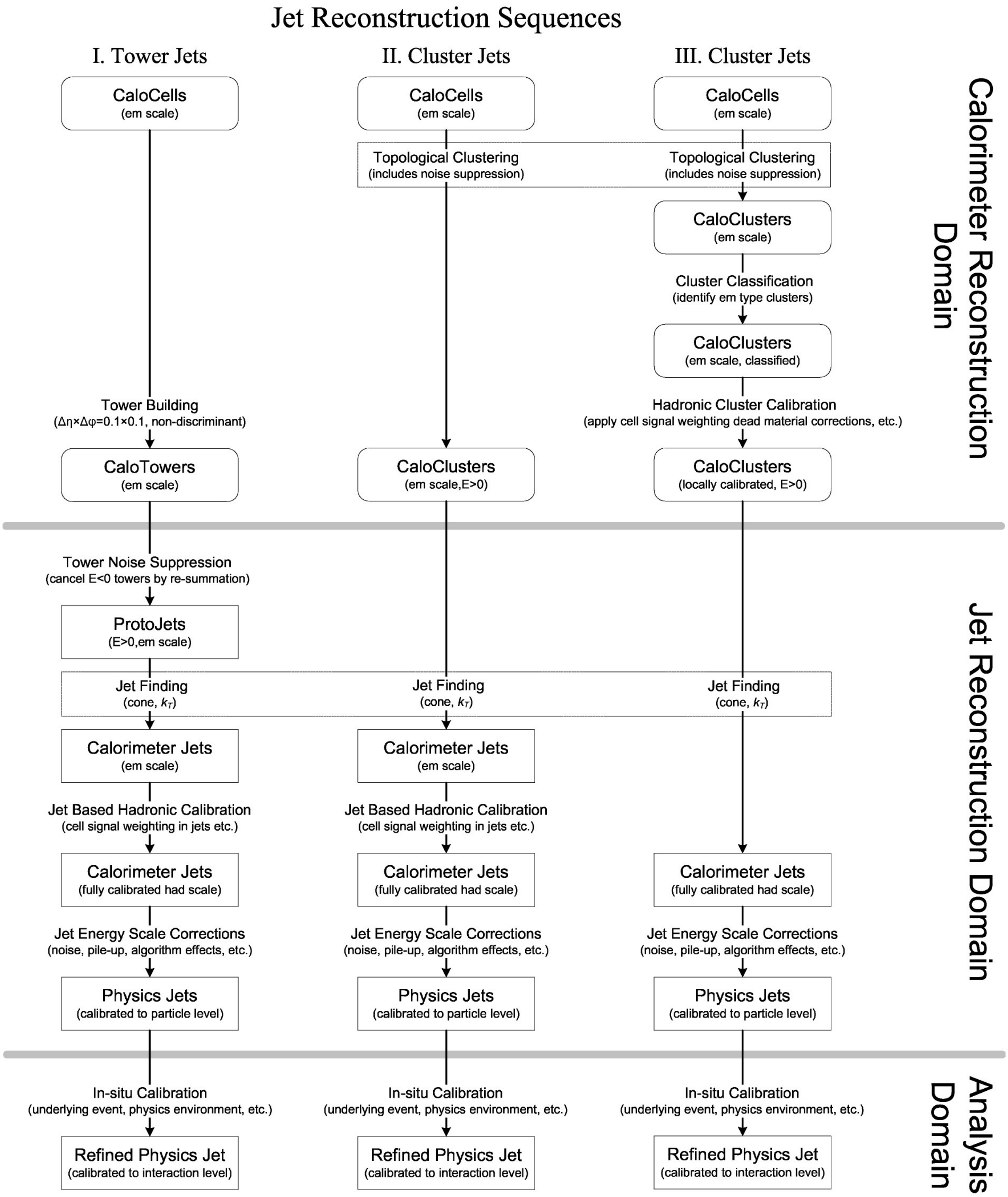

Figure 4.5: *Schematic overview of three jet reconstruction sequences: from calorimeter towers (left), from uncalibrated (center) and from calibrated (right) cell clusters. The most notable difference is the location of the hadronic calibration. The classification in three software domains is also visible.*

Topological cell clusters

A topological cell cluster is a representation of the three-dimensional "energy blob" left by the shower of each particle entering the calorimeter. Starting with a seed cell with a high signal-to-noise ratio, or signal significance $\Gamma = E_{cell}/\sigma_{noise,cell}$ above a level $|\Gamma| > 4$ all directly neighboring cells are collected. The neighbors of these neighbors are again collected if the cell has $|\Gamma| > 2$ and finally a third neighbor is added if the cell has $|\Gamma| > 0$. After the initial clusters are formed, they are analyzed for local signal maxima by a splitting algorithm and split between those maxima if any are found. This set of threshold is referred to as 4/2/0. We note that the absolute values of Γ in these cuts are taken with a specific reason: due to noise the cells can be readout with negative values. The idea is that by taking the absolute value the contributions from cells with positive noise are canceled by those from negative noise. This is especially important for the contributions in the second and third neighbor-layer.

At first the clusters are formed using the basic electromagnetic energy scale of the calorimeter cells. These can directly be transferred to the jet finding algorithms, as in Sequence II in Fig. 4.5, or they can be calibrated to a local hadronic energy scale[3)] as in Sequence III. For this last calibration the clusters are first classified as electromagnetic, hadronic, or noise, based on their location and shape. After that, cell signals inside hadronic clusters are weighted with functions depending on cluster location, energy, and the cell signal density. Then, a correction for energy losses in inactive materials close to or inside the cluster is applied. Finally, a correction for signal losses due to the clustering itself (out-of-cluster correction) is applied.

4.3.3 Jet finders

The tower signals and cell clusters are fed to the jet finding algorithms as massless pseudo-particles. Their directions are fixed by the bin center in the (η,ϕ) grid for each tower, or they are reconstructed from the energy-weighted center for the cluster. The most commonly used algorithms in ATLAS are a seeded fixed cone finder, based on [96], and the k_{T} algorithm [94,97].

Fixed cone jet finders

The algorithm starts by ordering all input objects in decreasing order in transverse momentum. The object with the highest p_T serves as a seed if its transverse momentum lies above a certain threshold (1 GeV in ATLAS). All objects which then lie within a cone in η and ϕ with $\sqrt{\Delta\eta^2+\Delta\phi^2} < R_{cone}$ are combined with the seed into a new object; R_{cone} is the fixed cone radius and is most commonly 0.4 for narrow jets or 0.7 for wide jets in ATLAS. If the direction of the new object does not coincide with the previous direction of the jet, objects are (re-)collected in the new cone and the previous steps are repeated. This stops when the direction of the four-momenta sum does not change anymore and the jet is subsequently called stable. The following step is to take the next seed from the input list, from which a new jet is formed with the same procedure. This stops when no more seeds are available. At this point the created jets can overlap, that is share constituents. This problem is solved by the split-and-merge step: jets which share constituents with more than a certain fraction f of the p_T of the less energetic jet are merged. If they share less than the fraction f they are split. In ATLAS the fraction is set at 0.5.

[3)]In Section 2.4 the electromagnetic and hadronic showering in jets is discussed. The two differ in the fraction of the particles' energy being measured by the calorimeter; thus two calibration schemes are needed.

We note that this algorithm is in fact not completely infrared safe. For events with only a few jets this has almost no impact on observables and the cone algorithm performs as good or even better than the k_{T} algorithm. We come back to this in Section 4.3.5. Complex events with many jets do however suffer from this IR unsafety, see [95]. Recently the Seedless Infrared Safe cone algorithm SISCone [98] has been developed and it is anticipated that this will be available for the first experimental collisions.

Sequential recombination jet algorithms

The sequential recombination jet algorithms are different implementations of one algorithm. Here we describe the standard implementation as used in ATLAS, the k_{T} algorithm [97].

Starting with a list of objects, be it a tower signal or a cell cluster, or even a parton if analyzing at for example the truth level, we do:

1. For each object i we define $d_i = p^n_{T,i}$ where $n = 2$ for the k_{T} algorithm. For each pair (i, j) of objects with $i \neq j$ we define
$$d_{ij} = \min(p^n_{T,i}, p^n_{T,j}) \frac{\Delta\eta^2_{ij} + \Delta\phi^2_{ij}}{R^2}, \tag{4.1}$$
where R is a free variable. This distance parameter allows some control on the size of the jets and is set at 0.4 for narrow jets and 0.6 for wide jets in ATLAS.

2. Find the minimum of all the d_i and d_{ij} and label it d_{min}.

3. If d_{min} is a d_{ij}, remove the objects i and j from the list and replace them with a new object k, which is given by the four-momentum sum of i and j.

4. If d_{min} is a d_i, the object i is considered to be a jet by itself and removed from the list.

5. If the list of objects is not empty, go back to step 1.

When the algorithm has terminated, each object we started with is either part of a jet or is a jet itself. We note that this algorithm is infrared and collinear safe. A recently developed implementation of the algorithm is a similar recombination scheme, yet with $n = -2$. This 'anti k_{T} algorithm' [99] has the benefit that the jet boundary is resilient with respect to soft radiation, but flexible with respect to hard radiation. The algorithm thus behaves conically, yet does not suffer from the infrared unsafety. Very likely, the anti k_{T} algorithm will be the ATLAS default in future analyses.

4.3.4 Jet calibration

In Figure 4.5 we saw that for the tower signals there is one reconstruction sequence, while for the cell clusters there are two. These differ in the point at which the hadronic energy calibration is performed. The raw signals from the calorimeters are namely at first on a basic electromagnetic energy scale and the cells containing hadronic energy depositions therefore have to be recalibrated. Tower signals remain at the EM scale, only after the jet finding algorithm is an hadronic calibration performed. Cell clusters can be immediately calibrated to hadronic level (Sequence III in the overview), or can remain at the EM scale and the hadronic calibration is again performed only after the jet finding algorithm (Sequence II in the

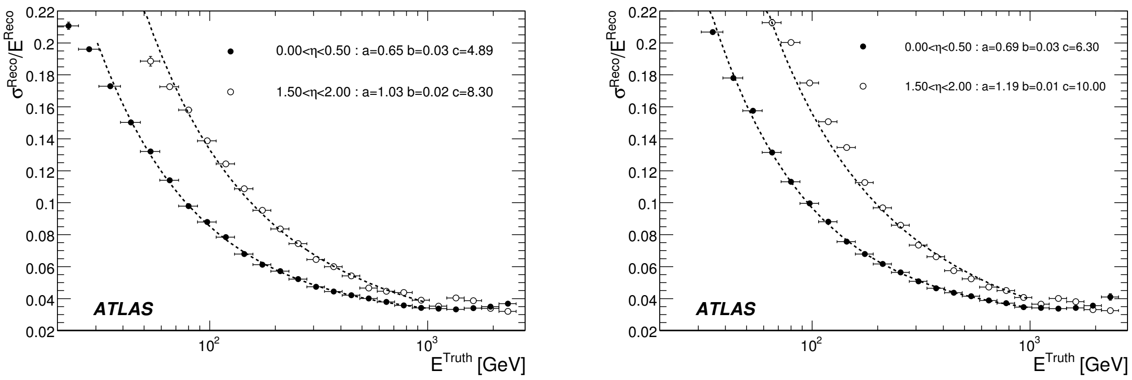

Figure 4.6: *The energy resolution of reconstructed jets in a di-jet sample, as a function of the energy. Left is the result for cone jets ($R_{cone} = 0.7$), right for k_T jets ($R = 0.6$). The resolution is measured in two rapidity regions. The smooth curve corresponds to a fit done with the function given in Eq. 4.2.*

overview). The final step we see in the 'Jet reconstruction Domain' in the overview figure is the Jet Energy Scale Corrections resulting in Physics jets. Those include corrections for residual non-linearities in the jet response due to algorithm effects, like missing energy from the jet, or adding energy not belonging to the jet in the clustering procedure.

In this thesis we only use jets reconstructed as in sequence I and II. The cell signal weighting in the jets (after the jet finding algorithm) is the application of the *H1 calibration scheme*. The basic idea behind this scheme is that low signal densities in calorimeter cells indicate a hadronic signal and thus need a signal weight for compensation of the order of the electron/pion signal ratio, while high signal densities are more likely generated by electromagnetic showers and therefore do not need additional signal weighting.

The in-situ calibration depicted in the 'Analysis domain' of the overview brings the jet energy to the original parton energy. This can (mostly) only be addressed in the context of a specific physics analysis, of which the study in Chapter 5 is an example.

4.3.5 Reconstruction performance

In [95, 100] the performance of the different jet finder algorithms is studied. Here we only highlight a few of the results mentioned. First we consider the resolution $\sigma(E_{rec})/E_{rec}$ of the reconstructed energy of the jet[4)]. The dependence of the resolution on the energy is shown in Fig. 4.6 for the cone (left) and for the k_T algorithm (right) applied to a sample of di-jet events. The fit to the data is done with a function encompassing three contributions, given by

$$\frac{\sigma}{E} = \frac{a}{\sqrt{E(\mathrm{GeV})}} + b + \frac{c}{E}. \tag{4.2}$$

The first term with the fit parameter a is due to the statistical fluctuations in the energy

[4)] For a resolution measurement the reconstructed energy must be compared to an energy value it was 'supposed to be'. For this we *do not* use the quark energy; we use the energy the jet algorithm measures at particle level. This definition for the "truth" energy is used throughout this section.

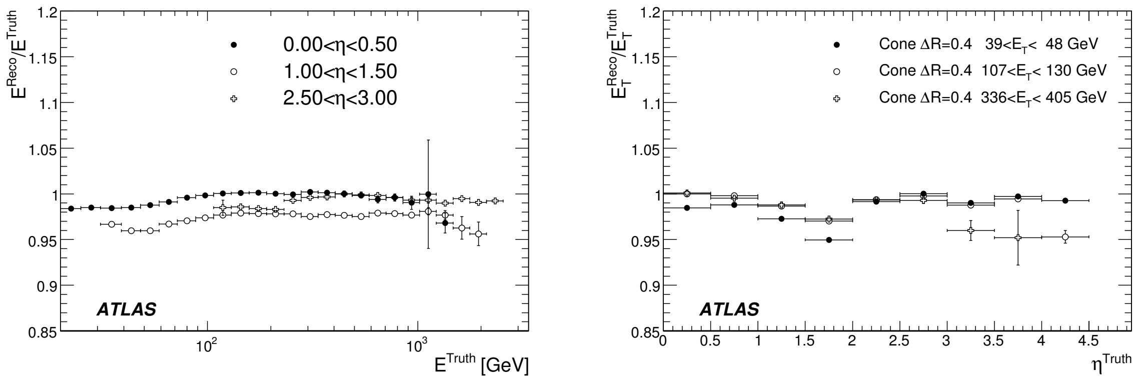

Figure 4.7: *The E^{reco}/E^{truth} as a function of the true jet energy for three rapidity regions (left), and the E_T^{reco}/E_T^{truth} as function of the rapidity for three E_T bins (right). These results are obtained with the cone jet algorithm ($R_{cone} = 0.4$) applied to $t\bar{t}$ events.*

depositions. The second term b is a constant; this is the consequence of the calorimeter non-compensation and the detector non-uniformities. The last term in the resolution function is the noise c. From the results in Fig. 4.6 we conclude that the cone algorithm performs better; especially in the central region the resolution of the k_{T} algorithm is worse at low energies. The latter also shows a larger noise value.

In [100] the studies show further that no significant difference is measured when comparing the calibrated and uncalibrated topological clusters. A difference is found when comparing clusters with towers: the noise term is lower when clusters are used.

Results on $t\bar{t}$ events

The jet reconstruction performance on $t\bar{t}$ events has also briefly been studied in Ref. [100]. The results in Fig. 4.7 are obtained using events generated with MC@NLO with the same jet finder as we have used in the analyses in this thesis, that is the ATLAS cone algorithm ($R_{cone} = 0.4$). We see the E^{reco}/E^{truth} dependence on the jet energy in three rapidity regions (left) and its dependence on the rapidity in three energy bins (right).

From the left figure we can conclude that the energy measurements improve at higher energies. In the right figure we notice at first the dip at $|\eta| \sim 1.5$, which corresponds with the gap between the barrel and the end-cap calorimeter, see Section 2.4. The intermediate range of $1.00 < |\eta| < 1.50$ is stated explicitly in the left figure to show the quality of the measurement in the gap region. The reconstruction in the gaps remains difficult, despite the extra calibration steps made (in all jet algorithms) in this region. We further notice that the jets' transverse energies in the lowest E_T bin are reconstructed worse than those in the higher E_T bins, that is at low rapidity. At higher rapidities the opposite is the case. This reflects the fact that the energy increases with η at fixed E_T and that E^{reco}/E^{truth} improves with increasing energy.

These performance studies however only reflect the reconstruction up to the particle content of the jets, we must assume that the comparison of the jet energies to the quark energies is worse. If a systematic uncertainty for the jet energy scale of better than 1% is desired, see [95], in-situ calibrations for dedicated measurements are necessary.

4.4 B-tag algorithms

In this section we go into the details of the identification of jets originating from b-quarks, which will be needed for the analysis in Chapter 6. There are several algorithms used in ATLAS, we will not discuss all of them. For all details on b-tagging and a full coverage of all algorithms we refer to [101].

The decay of a b-quark is different from that of the light quarks. The most important property of the b-quark is that the B-meson or baryon it hadronizes to has a relatively long lifetime, typically of the order of 1.5 ps ($c\tau_B \sim 450\mu m$). If a B-hadron is produced with a significant boost γ, its flight distance can be significantly enhanced. With a good reconstruction tracks can be reconstructed as not pointing to the primary vertex, or a secondary vertex can be found. Almost all b-quarks decay to a c-quark.[5)] A semi-leptonic decay of $b \to c\ l\nu$ leaves its signature with a soft lepton and missing energy. With the relatively long charm lifetime τ_c a tertiary vertex can sometimes be reconstructed, although since $\tau_c < \tau_b$ the third vertex is often mixed with the secondary.[6)] A further important property is the relative large mass of 5 GeV or more of the B-hadrons, giving the decay products typically larger opening angles and transverse momenta relative to the jet direction than those of light quark jets.

With these properties we can divide the available taggers in two categories: the spatial taggers, using the long life time and displaced vertex, and the soft-lepton taggers, which look for typical signatures of the lepton produced in the semi-leptonic decays. We will only discuss the first category. For the soft-lepton taggers we refer to [103] and [104].

4.4.1 Impact parameters

With the displaced decay point of a B-hadron the reconstructed tracks are (ideally) not pointing to the primary vertex. To quantify this, the two *impact parameters* of the tracks are used:

- The transverse impact parameter d_0: the distance of closest approach of the track to the primary vertex, measured in the $r-\phi$ plane.
- The longitudinal impact parameter z_0: the z coordinate of the track at the point of closest approach in the $r-\phi$ plane.

Tracks in a b-jet will have on average larger impact parameters than tracks in a light quark jet. To emphasize that the secondary vertex must lie along the flight path of the hadron, the impact parameters are signed: positive if the track crosses the jet axis in front of the primary vertex and negative if it crosses it behind. Tracks from the primary vertex will have a random impact parameter sign due to detector resolution, while tracks from the secondary vertex will have more often a positive impact parameter sign.

Not all tracks in a jet are considered in b-tagging. A set of selection criteria is implemented to only use well measured tracks, to reject fake tracks and to reject tracks from long lived particles:

- All tracks are taken into account within a distance of $\Delta R < 0.4$ to the jet axis, where ΔR is defined by $\Delta R = \sqrt{\Delta\phi^2 + \Delta\eta^2}$ and thus represents the distance in ϕ and η space to the jet axis, independent of the jet reconstruction algorithm and/or cone-size. The

5) The simplest model of a B-meson or B-baryon decay assumes the b-quark is entirely undisturbed by the accompanying lighter quarks. We note that this "spectator model" is only an approximation, see [102].

6) Examples of charmed hadrons are the $D^{\pm}$ with a life-time of $c\tau = 312\mu m$, and the D^0 with $c\tau = 123\mu m$.

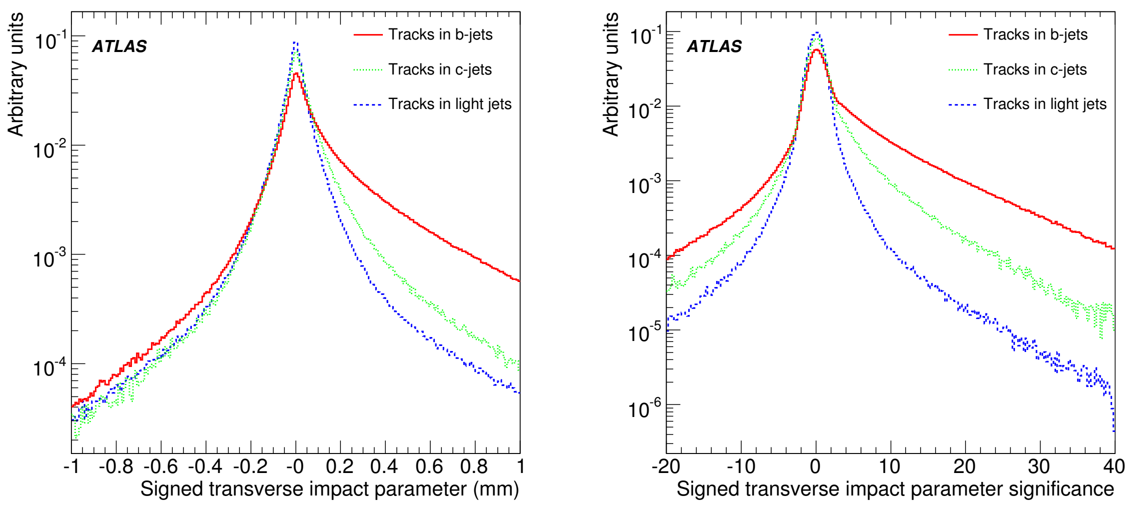

(a) The signed transverse impact parameter.

(b) The signed transverse impact parameter significance d_0/σ_{d_0}.

Figure 4.8: *Distributions for the transverse impact parameter for tracks in b-, c- and light quark jets. The tracks were selected from $t\bar{t}$ events, see text for details on the selection cuts.*

tracks must have a $p_T > 1$ GeV and at least seven hits are required, be it pixel or SCT hits. For these tracks the impact parameters at the perigee must satisfy $|d_0| < 1$ mm and $|z_0 - z_{pv}|\sin\theta < 1.5$ mm. z_{pv} is the longitudinal location of the primary vertex. The pixel detector must have at least a hit in its innermost layer, the *b*-layer, and one extra hit.

- From the selected tracks all possible two-track pairs are formed. Only tracks which do not come too close to the primary vertex are used, that is tracks with $L_{3D}/\sigma_{L_{3D}} > 2$, where L_{3D} is the three dimensional distance between the primary vertex and the point of closest approach of the track to this vertex, and $\sigma_{L_{3D}}$ the error on this parameter. With the secondary vertex finder, see section 4.4.2, all pairs are rejected that are likely to come from K_s or Λ decays, or from photon conversion. The location of the vertex is compared to the location of the innermost pixel layers to cut out secondary interactions in material.

Figure 4.8 depicts the transverse impact parameter distribution for the tracks remaining after these selections from a sample of $t\bar{t}$ events. Figure 4.8(a) shows the distribution for the signed d_0 for different types of jets; to give more weight to correctly measured tracks Figure 4.8(b) shows the significance distribution d_0/σ_{d_0}.

For this study jets are labeled as a b-jet if a b-quark in the MC truth information is found with a $p_T > 5$ GeV and a distance of no more than $\Delta R = 0.3$ to the jet direction. If this hypothesis fails the same is tried with c-quarks and finally with τ leptons. If all fail, the jet is labeled a light quark jet. The resolution $\sigma_{d_0}(p_T, \eta)$ is the width of a Gaussian fitted to the difference between the measured and the true impact parameter in different bins of (p_T, η).

The discriminating power of the impact parameters for b- and other jets is used in several taggers. The IP1D algorithm relies on only the longitudinal impact parameter z_0. The IP2D relies on the transverse impact parameter d_0 and the IP3D uses a two-dimensional distribution of the longitudinal and transverse impact parameter. In section 4.4.3 we go more into the details of the algorithms' formalism.

4.4.2 Secondary vertex finders

To find a possible secondary vertex, all two-track pairs formed earlier are combined in a single vertex, using an iterative procedure to remove the worst track until the χ^2 of the vertex fit is satisfactory. The secondary vertex tagging algorithms use three properties of this vertex to calculate a b-jet likelihood:

- The invariant mass of all the tracks in the vertex.
- The ratio of the energy sum of all the tracks in the vertex to the energy sum of all tracks in the jet.
- The number of two-track pairs.

Figure 4.9 shows the distributions for these three variables obtained from $t\bar{t}$ events. We emphasize that these results are obtained after the track selection mentioned in Section 4.4.1, as is the case with all further results discussed in this chapter on b-tagging performance. These distributions have been taken from [105] and we refer to this note for more details.

The available secondary vertex taggers use these properties in different ways: the SV1 uses a 2D distribution of the first two variables and a 1D distribution of the last variable. The SV2 tagger relies on one overall 3D distribution of all three observables. We explain how these properties are combined to give a b-jet likelihood in the next section.

The SV1 and SV2 methods result in one secondary vertex. As mentioned, almost all b-quarks decay through a c-quark and some have a tertiary vertex. A new algorithm, JetFitter, uses this property by always looking for two decay vertices. It finds a line along which the primary, secondary and tertiary vertex are best fitted. For more details we refer to [105].

4.4.3 The b-jet likelihood method

The formalism for most of the b-taggers is identical. For some variable S_i, which could be for example one of the impact parameters or one of the secondary vertex variables mentioned above, a probability density function (pdf) $b(S_i)$ and $u(S_i)$ is defined for the b- and light quark jet hypotheses respectively. As mentioned, some taggers also use two- and three-dimensional distributions. Any track or vertex thus gets a weight defined by $b(S_i)/u(S_i)$, which can be combined into one jet weight ω_{jet} by the definition

$$\omega_{jet} = \sum_{j=1}^{N_C} \left(\sum_{i=1}^{N_T^j} \ln \omega_i^j \right) = \sum_{j=1}^{N_C} \left(\sum_{i=1}^{N_T^j} \ln \frac{b^j(S_i)}{u^j(S_i)} \right). \tag{4.3}$$

where the sum runs over the selected N_T^j tracks in each *category* j: the tracks are divided into N_C categories with dedicated pdfs. In the b-tagging algorithms used so far in ATLAS two categories exist, i.e. $N_C = 2$: the *Shared* tracks (tracks with shared hits) and the complementary subset of tracks called *Good* tracks. The distributions of the weights $b(S_i)/u(S_i)$ for tracks with

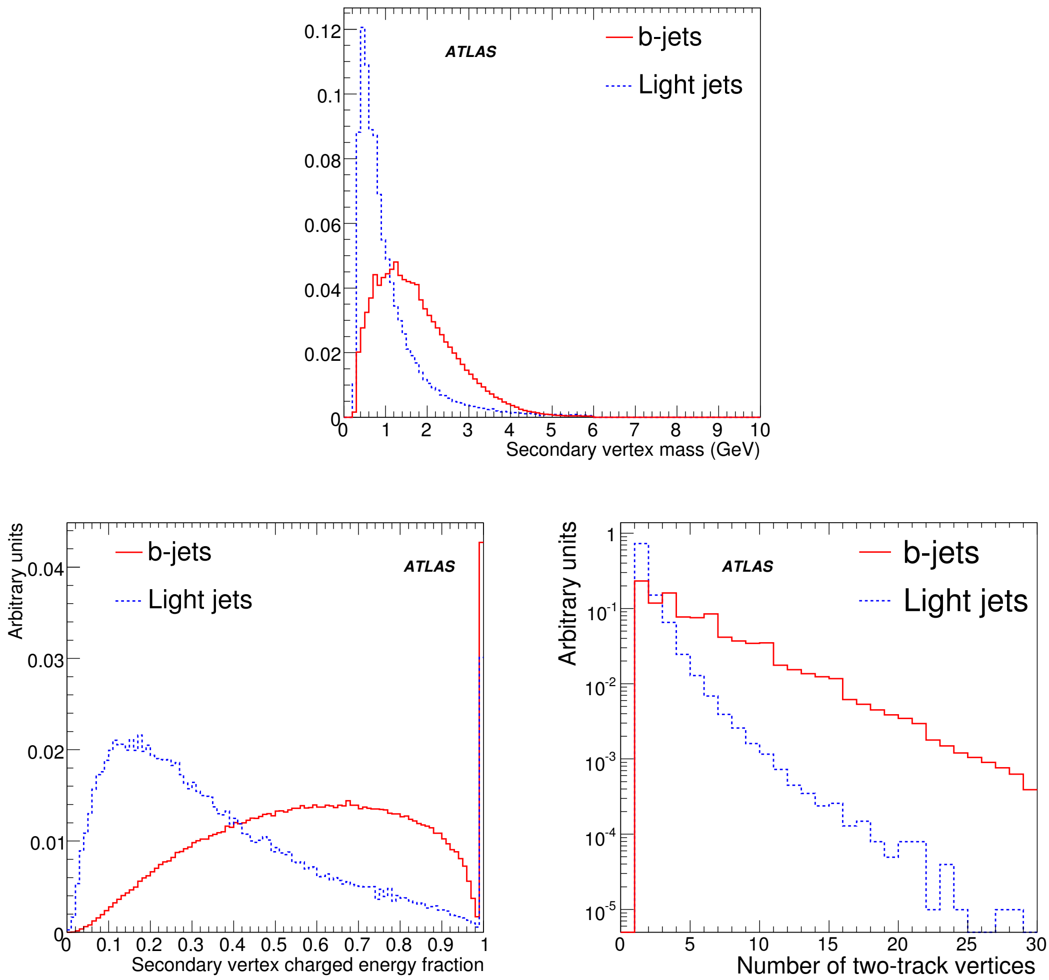

Figure 4.9: *The three properties used in SV taggers for b- and light quark jets: vertex invariant mass (up), ratio of energy in vertex and in jet (left) and the number of two-track pairs used (right); all results are obtained from $t\bar{t}$ events. See Section 4.4.2 for more details.*

shared hits is thus different than the distributions for so-called Good tracks. See [101] for more details.

The jet weight is the final variable of the algorithm: if a jet has a weight above a certain pre-defined cut value it is labeled as a b-jet. Each choice of a cut value has a probability of rightly tagging a b-jet, but also a probability of mis-tagging a light quark jet. The efficiencies vary with the algorithms. The best results are from taggers which combine weights as we can observe in Fig. 4.10, which shows the distributions for the IP2D and the combined IP3D+SV1 taggers.

Taggers for first data

For now the probability density functions $b(S)$ and $u(S)$ used in the different taggers must come from MC studies, which results in the problem for the first data to come from ATLAS that

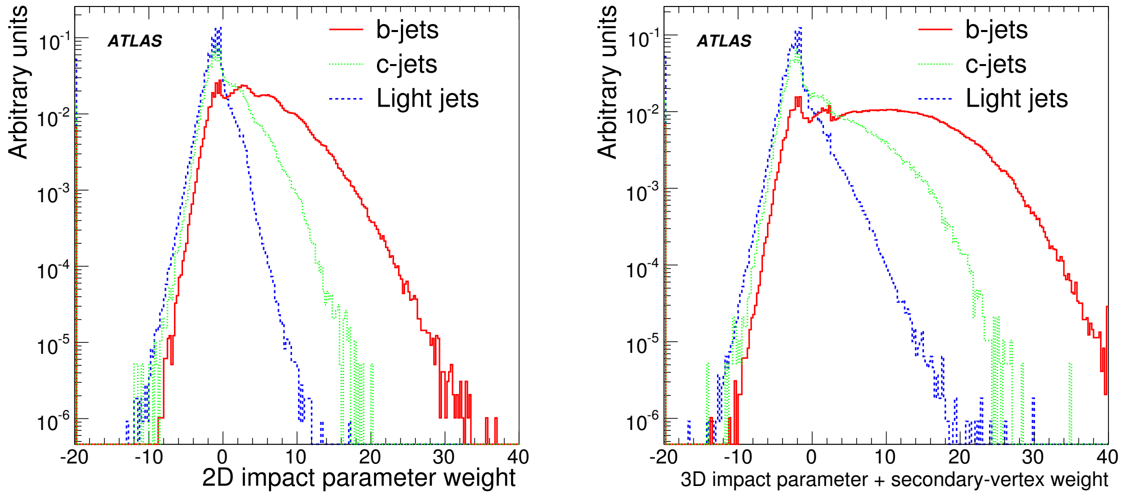

Figure 4.10: *The weight distributions for the IP2D tagger (left) and for the IP3D+SV1 (right), for b-, c- and light quark jets; all results are obtained from $t\bar{t}$ events.*

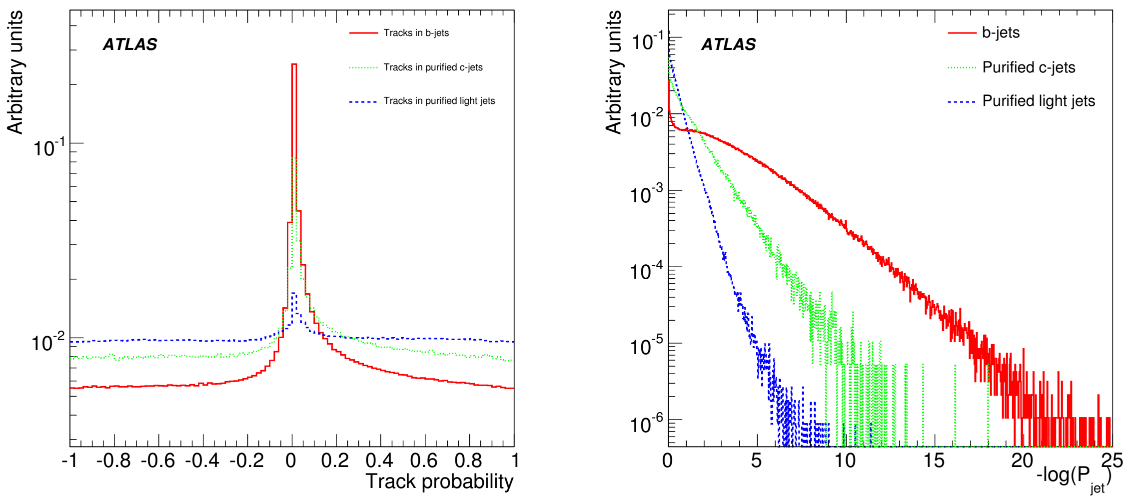

(a) Individual track probability $P_i \times \mathrm{Sign}(d_0^i)$.

(b) Jet probability: $-\log_{10} P_{jet}$.

Figure 4.11: *Distributions of the probability of compatibility with the primary vertex for individual tracks (left plot) and for all tracks in the jet (right plot) as defined for JetProb. The cases of b-quark (plain), c-quark (dashed) and light quark jets (dotted line) are shown. A purified sample of light quark jets means that within a cone of size $\Delta R = 0.8$ around the jet direction no b- or c-quark may be present, nor a τ lepton. A similar reasoning goes for the purified c-jets; all results are obtained from $t\bar{t}$ events.*

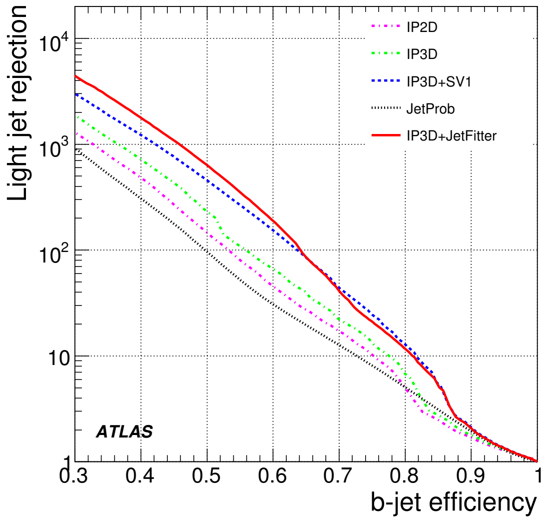

Figure 4.12: *Rejection of light quark jets versus the b-tagging efficiency for different tagging algorithms; all results are obtained from $t\bar{t}$ events.*

these might not accurately simulate the behavior of the detector. More simpler but robuster taggers have been developed for the start-up phase of ATLAS. For the vertexing algorithms, SV0 is an example. This algorithm tags a jet as a b-jet simply if the B-hadron flight distance significance calculated from the secondary vertex position exceeds some cut value.

The recommended tagger for the start-up phase is the JetProb algorithm, see [101]. This calculates for each selected track i the probability P_i that it originated in the primary vertex by comparing its signed IP significance $d_0^i/\sigma_{d_0}^i$ to a resolution function R for prompt tracks:

$$P_i = \int_{-\infty}^{-|d_0^i/\sigma_{d_0}^i|} R(x)dx, \tag{4.4}$$

where x is the signed IP significance. The probability of the tracks in a jet can then be combined into a jet probability P_{jet}. The benefit of this algorithm is that the resolution function R can be measured in data using the negative side of the signed IP distribution, which will have little contribution from heavy-flavor particles. This makes it possible to have an early commissioning of the algorithm with the first data. In Fig. 4.11(a) the probability for individual tracks P_i is shown; in Fig. 4.11(b) we show the $-\log_{10} P_{jet}$ distributions for different types of jets. We emphasize that a $P_{jet} \sim 1$ implies a high probability for all tracks in the jet to originate in the primary vertex.

A drawback of this algorithm is that it performs worse than the other, more advanced, algorithms. Figure 4.12 depicts the light quark jet rejection, i.e. $1/\varepsilon_{light}$, versus the b-jet efficiency: a rejection of 30 is expected for a b-tagging efficiency of 60%. For comparison, the ultimate JetFitter algorithm has a rejection of 200. Yet the latter is only the case if the pdfs are correct; due to possible mis-alignments in the commissioning phase of ATLAS, the performance of the JetProb is more trustworthy.

Figure 4.12 serves mainly to illustrate the differences between the taggers, the absolute values of the rejection and tagging efficiency namely also depend on the jet p_T and η. Figure

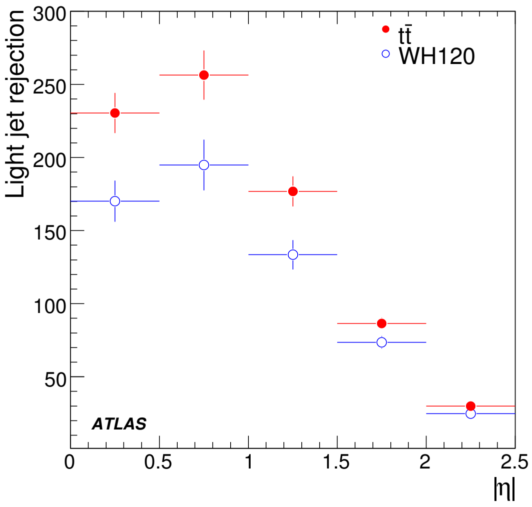

(a) Jets with $30 < p_T < 45$ GeV.

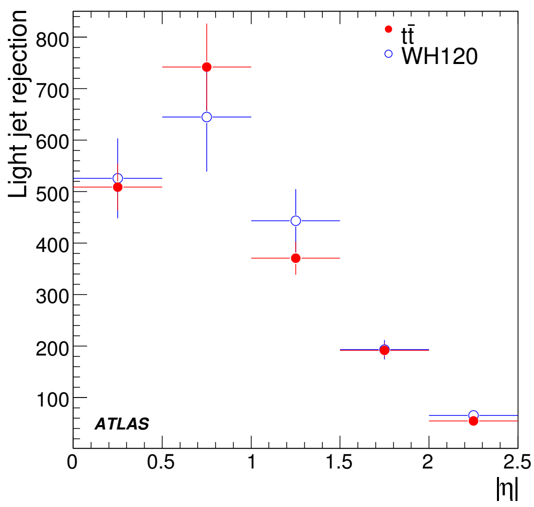

(b) Jets with $60 < p_T < 100$ GeV.

Figure 4.13: *The light quark jet rejection (purified jet sample) as a function of the jet η. The IP3D+SV1 tagging algorithm is used on two different samples: jets from $t\bar{t}$ events and from WH ($m_H = 120$ GeV) events. The cut on the algorithm weight varies from bin to bin, such that the b-tagging efficiency remains at 60%.*

4.13 depicts the rejection as a function of the jet η for two p_T bins. These results are obtained on $t\bar{t}$ events, and on WH ($m_H = 120$ GeV) events. We observe that in the higher p_T bin the rejection increases, while at the same time the best rejection is achieved on jets around $\eta \sim 0.7$. The shapes of the different distributions are mostly similar, yet the absolute rejection is lower for the jets from the WH events. This is attributed to the large binning in p_T (on average the jets in the WH sample have lower p_T), but also among others to the fact that different MC generators have been used: MC@NLO+HERWIG for the $t\bar{t}$ events, PYTHIA for the WH. We refer to [101] for more details on this matter.

4.5 Measurement of the missing transverse energy

In the Standard Model the only particle which goes undetected through ATLAS is the neutrino. Its presence can be derived by measuring the missing transverse energy $\not{E}_T$: for events with only one neutrino the $\not{E}_T$ is equal to the p_T of the missing particle.[7)] Complications start when multiple neutrinos are present, there is no way of deriving the different p_T's from one $\not{E}_T$ measurement. New (unknown) particles might also go undetected, such as the LSP in supersymmetry models, see Section 1.3. In other words, an accurate measurement of the $\not{E}_T$ is needed to fully reconstruct the event and might lead to a good signature for new physics.

There are two algorithms in ATLAS to determine the $\not{E}_T$. The Object-based algorithm starts from the reconstructed, calibrated and classified objects in the event, taking also into

[7)]This is of course assuming a hypothetical detector covering perfectly the entire (η,ϕ) plane.

account the deposits outside these objects. The Cell-based algorithm starts from the energy deposits in calorimeter cells; this procedure is expected to be robust from initial data taking on and is therefore used throughout this thesis.

The calorimeter is designed such that it covers as much as possible of the (ϕ, η)-plane. If we were to have a perfect sphere-coverage we could also measure the energy in the longitudinal direction. Yet the beam-pipe entrances make this impossible; with most of the underlying event disappearing through these pipes we can therefore not say anything about the longitudinal energy present in the hard-scattering and we are restricted to a transverse energy measurement.

With some gaps between the different sub-detectors, a finite detector resolution and possible dead or noisy readout channels we also produce fake $\not{E}_T$. The largest contributions of fake $\not{E}_T$ are, in random order:

- **Noise -** The electronic noise alone in the ~ 200k readout channels in the calorimeters contribute about 13 GeV to the width of the $\not{E}_T$ distribution, that is before the noise suppression in the measurement of the '$\not{E}_T$ calorimeter contribution' (see further).
- **Missed and fake muons -** Muons can sometimes escape detection, especially in the gap regions of the muon spectrometer. Fake muons can be caused for example by high p_T jet punch-throughs from the calorimeter to the muon spectrometer.
- **Jet leakage -** This is jet energy which is not deposited in the calorimeter, but for example in the muon spectrometer (without faking a muon) or in the cryostat. For this last possibility the reconstruction algorithms have compensations, but the large fluctuations in these deposits can still cause fake $\not{E}_T$.
- **Mismeasured jets -** Due to mis-calibration of jets, or because of jets passing through the gaps in the calorimeter. Although the measured jet energies are compensated for this, the resolution in these areas is worse.

Most of these contributions can be kept to a minimum by a good selection and calibration of calorimeter cells, which we discuss in the following section. Fake muons are kept to a minimum by using information from the Inner Detector (ID), missed muons are however more difficult to compensate for.

4.5.1 Cell-based reconstruction

The Cell-based $\not{E}_T$ algorithm uses information from all sub-detectors. It encompasses contributions from energy deposits in the calorimeters, from measured muons in the muon spectrometer and the ID, and corrections for energy loss in the cryostat. The component in the x and y direction are thus given by:

$$\not{E}_{x,y}^{Final} = \not{E}_{x,y}^{Muon} + \not{E}_{x,y}^{Cryo} + \not{E}_{x,y}^{Calo}. \tag{4.5}$$

The $\not{E}_T$ muon contribution The $\not{E}_{x,y}^{Muon}$ is calculated from all muons measured in the rapidity range $|\eta| < 2.7$, that is $\not{E}_{x,y}^{Muon} = -\sum E_{x,y}$. To reduce the amount of fake muons the muon is to be matched to a track in the ID. With the ID covering the range up to $|\eta| < 2.5$, muons with $2.5 < |\eta| < 2.7$ are free of this requirement.

The resolution of the muon spectrometer is of such good quality that the fake $\not{E}_T$ mostly has contributions from entirely missed muons, or jet punch-throughs which reach the spectrometer. Missed muons could be accounted for with information from the ID and calorimeter, yet this is not yet implemented in ATLAS. As a final note we mention that the energy muons loose in the calorimeter is taken into account elsewhere, that is in the $\not{E}_T$ calorimeter term.

The $\not{E}_T$ cryostat contribution The cryostat between the LAr barrel electromagnetic calorimeter and the TileCal is thick enough for hadronic showers to loose non-negligible amounts of energy, see Section 2.4. The $\not{E}_T$ reconstruction recovers this loss of energy in the cryostat using the correlation of energies between the last layer of the LAr calorimeter and the first layer of the hadronic calorimeter. A similar correction for the end-cap cryostats is applied, see also [106].

The $\not{E}_T$ calorimeter contribution This is the most difficult term in the $\not{E}_T$ calculation. The first step is to reduce the calorimeter noise, for which two possibilities exist. One is to select only cells with energy depositions above a certain threshold. This selection is still being refined. A better solution for now is the use of topological cell clusters. In Section 4.3.2 we explained how these are formed by clustering neighboring cells if these have a high enough signal-to-noise ratio. The set of threshold 4/2/0 used is optimized to suppress noise, while keeping the single pion efficiency as high as possible, see [106]. Thus we have:

$$\not{E}_{x,y}^{Calo} \sim -\sum_{\text{TopoCells}} E_{x,y}. \tag{4.6}$$

For the best results the cells first however have to be calibrated to account for the different depositions we get from different particles.

The calorimeter cell calibration

The first step in the calibration is based on the energy density inside the cell. Electromagnetic showers tend to have higher densities as compared to hadronic showers. For this 'global calibration' two schemes exist: the H1-like, see Section 4.3.4, and the Local-Hadronic[8)] calibration. This last scheme uses further information related to the shape and depth of the shower to classify a topological cluster.

The next step in the calibration improves the $\not{E}_T$ measurement by associating each cell with a reconstructed high p_T-object. As each cell can be part of multiple objects, such as an electron *and* a jet, the association is performed in a chosen order: electrons, photons, muons, hadronically decaying τ's, b-jets and light jets. If a cell is not associated to any object only the previously mentioned global calibration is applied, but it is still used in the measurement of the $\not{E}_T$. Studies have shown the importance of these cells: when excluding them from the measurement, the mean $\not{E}_T$ shifts by about 1 GeV and the resolution worsens by 25%, see [106].

The calibration steps taken in the reconstruction of the objects are redone for each of the cells in the $\not{E}_T$ measurement. Some of these steps are however excluded. In the jet reconstruction for example an overall scale factor is applied to correct for (among other things) out-of-cluster effects. This correction must not be applied for the $\not{E}_T$, as the contribution of cells outside the clusters already accounts for it. The final 'refined' contribution of the calorimeter term to the $\not{E}_T$ in eq.(4.5) is now

$$\not{E}_{x,y}^{Calo} = -(\not{E}_{x,y}^{RefElec} + \not{E}_{x,y}^{RefMuon} + \not{E}_{x,y}^{RefTau} + \not{E}_{x,y}^{RefBjets} + \not{E}_{x,y}^{RefJets} + \not{E}_{x,y}^{RefOut}). \tag{4.7}$$

8) Although the name seems to imply the opposite, this scheme is classified in the $\not{E}_T$ reconstruction as a 'global calibration' scheme.

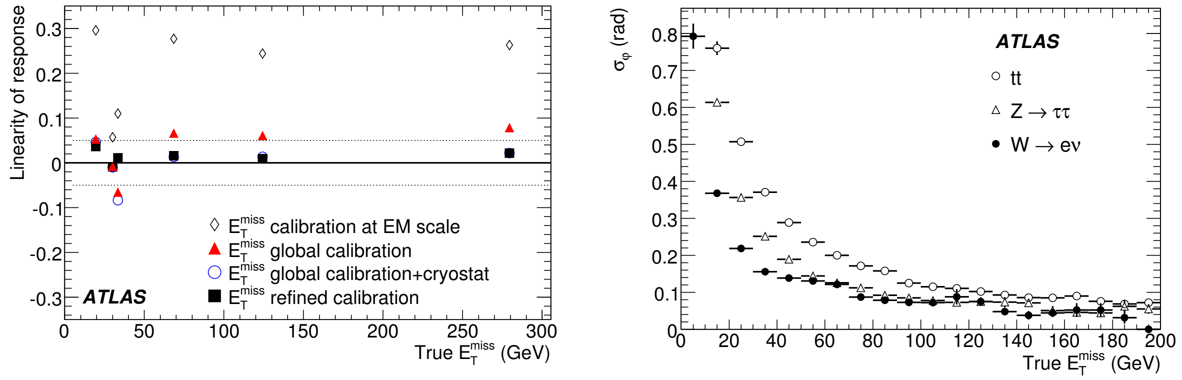

Figure 4.14: *Left: the $\not\!\!E_T$ linearity, given by $(\not\!\!E_T{}^{\text{True}} - \not\!\!E_T)/\not\!\!E_T{}^{\text{True}}$, as a function of the true $\not\!\!E_T$. The results at $\not\!\!E_T{}^{\text{True}} \sim 20$ GeV are from $Z \to \tau\tau$ events, those at ~ 35 GeV are from $W \to e\nu$* and *$W \to \mu\nu$, those at 68 GeV from semi-leptonic $t\bar{t}$ events, those at 124 GeV from supersymmetric Higgs $A \to \tau\tau$ with $m_A = 800$ GeV and those at 280 GeV from events containing supersymmetric particles at a mass scale of 1 TeV. Right: resolution of the $\not\!\!E_T$ measurement in the ϕ-direction for three different physics processes.*

Each term is the sum of the calibrated cells inside a specific object. With $\not\!\!E_{x,y}^{RefOut}$ the sum of all cells not associated to any of the other objects, all calorimeter cells are taken into account. With this definition of the calorimeter term the total missing transverse energy in eq.(4.5), $\not\!\!E_T{}^{Final}$, is referred to as the 'refined final' $\not\!\!E_T$, or in short $\not\!\!E_T{}^{RefFinal}$.

4.5.2 Reconstruction performance

In [106] the performance of the $\not\!\!E_T$ reconstruction is discussed in detail. We again highlight the more important results. We will be using the definition of the $\not\!\!E_T$ linearity, given by $(\not\!\!E_T{}^{\text{True}} - \not\!\!E_T)/\not\!\!E_T{}^{\text{True}}$, and the total transverse energy in the calorimeters, which is the *scalar* sum of E_T of all topological cells that constitute the topological clusters:

$$\Sigma E_T = \sum_{\text{TopoCells}} E_T. \tag{4.8}$$

Figure 4.14(a) shows the $\not\!\!E_T$ linearity as a function of $\not\!\!E_T{}^{\text{True}}$, defined from the sum of all stable and non-interacting particles in the final state (such as neutrinos, LSPs in supersymmetric models, etc...). Clearly the $\not\!\!E_T$ with all cells still at electromagnetic scale has a high offset of $\sim 30\%$. Only the results around 35 GeV are lower: these are obtained from $W \to e\nu$ and $W \to \mu\nu$ with low hadronic activity. The global calibration improves this and together with the cryostat corrections the linearity is $\sim 1\%$. The refined calibration does not result in much better results for the linearity, it does however greatly improve the resolution.

The results for the $\not\!\!E_T$ resolution for different events samples are depicted in Figure 4.15 as functions of the total transverse energy ΣE_T. The left figure shows a smaller range for the Z and W decays, the right figure shows processes with higher values for the total transverse energy. Fitting the results with a function $\sigma = a \cdot \sqrt{\Sigma E_T}$, the parameter a varies between 0.53 and 0.57. This is where the refined calibration is important: for the W decays the parameter is reduced

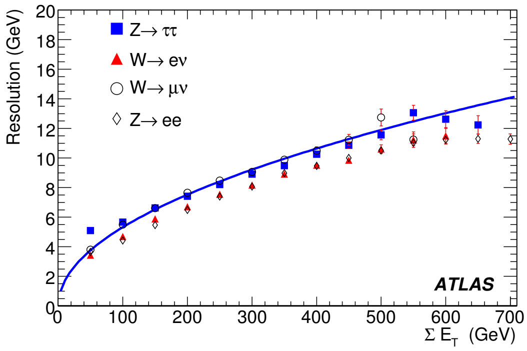

(a) The fit function is given by $\sigma = 0.53\sqrt{\Sigma E_T}$.

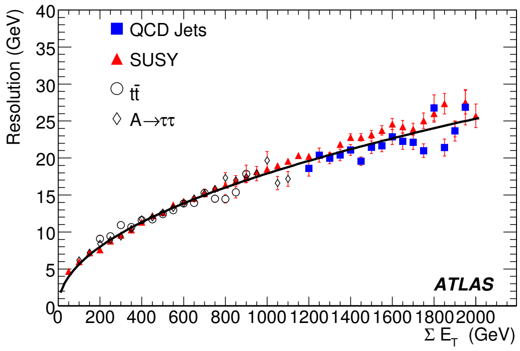

(b) The fit function is given by $\sigma = 0.57\sqrt{\Sigma E_T}$. The $A \to \tau\tau$ events are with $150 < m_A < 800$ GeV.

Figure 4.15: *The $\not{E}_T$ resolution as a function of the total transverse energy in the calorimeter ΣE_T. The curves are the fits of $\sigma = a \cdot \sqrt{\Sigma E_T}$ to the $Z \to \tau\tau$ results (left) and to the $A \to \tau\tau$ events (right).*

by $\sim 80\%$ with respect to the global calibration with the cryostat corrections applied. The fitted function accounts only for statistical fluctuations in the $\not{E}_T$ measurement. Deviations to the fit can be found mostly for low values of ΣE_T where the noise contributes relatively more, and for high values of ΣE_T where the constant term in the resolution of the calorimetric energy measurement dominates.

The accuracy of the $\not{E}_T$ direction measurement is also studied. In Figure 4.14(b) we show the ϕ-resolution as a function of the true $\not{E}_T$, measured for three different event samples. The leptonic decay of the W has the best results, which can be explained by the low hadronic activity in the event. For $t\bar{t}$ events the resolution is about a factor 2 larger. Overall it is clear that the accuracy rapidly increases for higher values of the true $\not{E}_T$.

To study the dependence on energy flowing longitudinally around the beam-pipe, the $\not{E}_T$ resolution is measured with and without the forward calorimeters (FCAL) included. In $Z \to \tau\tau$ events the $\not{E}_T$ resolution is respectively 7.8 and 10.1 GeV, see [106], showing the importance of the FCAL in the regions with high values of η.

4.6 Object definition & selection for the analyses in this thesis

In the Chapters 5 and 6 we present two studies, performed on two different samples. The first study is performed on samples with 14 TeV center-of-mass energy, the second on samples with 10 TeV center-of-mass energy. The reconstruction of the first is performed with ATHENA v.12, while for the latter ATHENA v.14 is used.

With the changes in the reconstruction between these two versions, the best performing object definitions also changed. We present here the definitions as used for the v.14 samples, and if needed we state what is different for the v.12 samples.

4.6.1 Lepton trigger and selection

In the hadronic environments created in pp collisions isolated high p_T charged leptons such as electrons and muons are clear and clean objects. Their reconstruction is not only of importance for the offline physics analysis performed on the events, it can also be used in the trigger step for an early selection on certain channels. In the analysis on the v.12 samples we have not implemented a trigger selection, only in our second analysis on v.14 samples do we demand the EF_e25i_medium1 to have passed when an electron is reconstructed in the event, or the EF_mu20 trigger when a muon is reconstructed. See also Section 2.6.

The uncertainties on the efficiencies of the lepton trigger and of the lepton reconstruction are expected to be $< 1\%$ for the first 100 pb^{-1}, see [29]. With the efficiencies of order $80-90\%$, this translates in an uncertainty on the predicted number of selected events of $\sim 1\%$.

Electrons

Electron candidates are reconstructed by the `egamma` algorithm, see also [107]. For the candidate to be accepted as a good electron it must pass the following cuts:

- The object must pass the `medium` cuts provided by the algorithm: a set of requirements based on both the shower shape properties in different compartments of the calorimeter and on variables combining inner detector and calorimeter information.
- The object must have a pseudo-rapidity of $|\eta| < 2.5$. If an electron candidate is found in the calorimeter crack region $1.37 < |\eta| < 1.52$ it is dismissed as a good electron. See also Section 2.4.1.
- It must have a transverse momentum $p_T > 20$ GeV.
- It should be isolated. Therefore an isolation cut of $E_T < 6$ GeV is applied, by which we mean that the sum of additional transverse energy in a cone with radius $\Delta R = 0.2$ around the electron axis is required to be less than 6 GeV.

For the v.12 samples some cuts are different:

- The previously mentioned `medium` set of requirements are defined as the `isEM` set and contains less calorimeter isolation requirements.
- The crack region is defined as $1.35 < |\eta| < 1.57$. Just as for the v.12 samples, electron candidates in this region are vetoed.
- The isolation cut is dependent on the electron p_T. It can be summarized as $E_{T,\Delta R=0.40}/p_T < 0.20$, and $E_{T,\Delta R=0.20}/p_T < 0.12$.

Muons

Muon candidates are reconstructed by the STACO [108] algorithm. A good muon must pass the following cuts:

- It should pass the `best match` cuts provided by the algorithm. This implies it is defined from the best match combination of the muon chambers and the ID information.
- The candidate must have a pseudo-rapidity of $|\eta| < 2.5$.

- It must have a transverse momentum $p_T > 20$ GeV.
- It should be isolated. The isolation cut is $E_T < 6$ GeV in a cone with radius $\Delta R = 0.1$.

For the v.12 samples the muon selection is again different. For these samples the muons are reconstructed by the MUID [109] algorithm and the isolation cut of $E_T < 6$ GeV is for a cone with radius of $\Delta R = 0.2$.

4.6.2 Jets and missing transverse energy

Jet candidates are reconstructed by the ATLAS cone algorithm, see Section 4.3.3, on topological cell clusters in the v.12 samples and on tower signals in the v.14 samples. In the v.14 samples the jet is required to be isolated from electrons: if an electron candidate has passed all cuts previously mentioned and lies within a distance of $\Delta R = 0.20$ of a jet candidate, the *jet* is rejected. For the v.12 samples this last isolation cut is more severe: if an electron or a muon candidate lies within a distance of $\Delta R = 0.40$ of a jet candidate, the jet is rejected. For the two analyses presented in this thesis we apply different cuts on the transverse momentum, see either Section 5.1 or 6.1.2.

For the missing transverse energy $\not{E}_T$ we use the standard ATLAS variable ${\not{E}_T}^{RefFinal}$, with a cut of $\not{E}_T > 20$ GeV unless stated otherwise.

Chapter 5

Energy scale calibration using a kinematic fit

A well determined scale of the energy of jets and scale of the missing transverse energy are of crucial importance for many analyses, notably the searches for new physics like supersymmetry. In the ATLAS collaboration, several techniques based on QCD multi-jet, γ/Z+jets and top quark pair events are studied for the (light) quark jet energy scale calibration [110, 111], while W+jets and Z+jets events are studied for the missing transverse energy ($\not{E}_T$) scale, see [112]. In addition, in this last reference an analysis on the in situ measurement of the $\not{E}_T$ in top quark pair events is described, where a measurement of its scale is proposed using a kinematic fit. In this chapter we describe the kinematic fit in detail and perform several systematic studies. The possibility of applying b-quark tagging, see Section 4.4, is not used in this analysis.

5.1 Introduction

We focus on a measurement of the jet energy and missing transverse energy scale using a semi-leptonic $t\bar{t}$ event sample with integrated luminosity of $L = 160$ pb^{-1} at a center-of-mass energy of 14 TeV. This study shows the possibilities for first data energy scale calibration, although recently it became clear that the first runs of the LHC are planned at a center-of-mass energy of 7 TeV. In this work, based on Monte Carlo (MC) events, a value of the top quark mass of 175 GeV is used and for the studies of systematic effects we use an uncertainty on the mass of 2.5 GeV. This was the default top mass at the time the work was performed, before the new measurement of $m_t = 173.1 \pm 1.3$ GeV was available. In [111, 112] it is shown that with a 14 TeV sample of $L = 100$ pb^{-1} the jet energy scale can be measured to the level of a few percent, while the $\not{E}_T$ scale can be measured to the level of $\sim 10\%$. Assuming the worst (the studies might be wrong, the detector might have problems,. . .), we prepare for large deviations ($\pm$ 20%) of (missing) energy scales.

We have to be clear about which jet energy scale (JES) we set out to measure. Figure 4.5 on page 93 depicts the steps needed before the final "Refined Physics Jet (calibrated to interaction level)" is reached in the jet reconstruction. In Section 4.3 we did not discuss the last step, we only discussed the jet reconstruction and calibration up to the particle level. The last step in the figure brings us from the particle level, i.e. the jet constituents, to the interaction level, i.e. the hard scattering of the protons, by using known physics scales; the step is depicted in the figure as the Analysis Domain and is the domain of studies on QCD or γ/Z+jets events such as in [110], or on $t\bar{t}$ such as in [111]. We will use a fit with kinematic constraints to optimize this last step to obtain the hard scattering quantities. Many of the other studies result in jet calibration functions depending on the jet direction η and transverse momentum p_T. We do not set out to obtain such parton correction functions; in fact, we will apply a p_T-dependent MC based parton correction before starting the kinematic fitting. The jet energy scale we measure with this fit is no more than one number: an overall scale indicating whether on average the jet energies, independent of their flavor, are well calibrated. The $\not{E}_T$ scale is obviously correlated with the overall JES, hence a careful analysis of their dependence is needed.

Kinematic fitting is a technique that exploits the constraints in reconstructed events. Top quarks mostly decay to a b-quark and a W boson. In semi-leptonic $t\bar{t}$ events one W boson decays leptonically and one hadronically. The measurable final state, ignoring QCD radiation and neutrinos from b-decays for the moment, consists of a charged lepton and four jets (of which two are b-jets) and $\not{E}_T$ from the escaping neutrino. By requiring the decay products of the leptonically decaying W to yield the W mass of 80.4 GeV, two solutions for the longitudinal momentum p_z^ν of the neutrino can be obtained. The other mass constraints, imposed by the kinematics of the two top quarks and the hadronically decaying W boson, can be used to find the correct permutation of jet assignments to their parent particle and the correct p_z^ν.

The HitFit program, developed at the D0 experiment, see [113], is designed for this kinematic fitting of semi-leptonic $t\bar{t}$ events. In short, HitFit takes the measured transverse momenta of the six decay-particles and adjusts (or obtains) their 4-momenta using mass constraints. For our analysis we have to perform several kinematic fits with different constraints, imposing the need of a flexible fit-program. We developed a modified version of the HitFit package. With the goal of calibrating the energy scales, in the implementation of the HitFit program in our studies only the energies of the four jets are fitted, while their production angles are kept at their originally measured values. The jet angular resolutions are implemented via the mass constraints in the fit; in the next section these are discussed in more detail. Also, the leptonic energy scale is assumed to be well measured and is fixed throughout this work. We kept the HitFit interface and the handling of permutations, but we replaced the original fitting algorithm by a new χ^2-definition and use the MINUIT package [114, 115] for minimization.

For the study in this chapter we use fully simulated MC@NLO $t\bar{t}$ sample, reconstructed with ATHENA version 12.0.6. This sample contains no events with both top quarks decaying hadronically, but all other decays modes are present. For background events we use a consistent set of W+jets samples generated by Alpgen (with only leptonic W decays), where matrix elements are used to calculate QCD radiation leading to between two and five hard jets. The cross sections are respectively $\sigma_{t\bar{t}} = 461$ pb and $\sigma_W = 789$ pb, taking into account filters[1)] and the above mentioned branching ratios. These are the only samples we study in this chapter, hence no systematic uncertainties from MC predictions will be presented, nor the effect of QCD events.[2)] After the overlap removal and object definition from Section 4.6, we use the following pre-selection:

- Exactly one lepton (electron or muon) with $p_T > 20$ GeV.
- At least 4 jets with $p_T > 20$ GeV, of which at least 3 jets with $p_T > 40$ GeV.
- Missing transverse energy $\not{E}_T > 20$ GeV.

[1)] The W+jets Alpgen sample is filtered for events with at least three reconstructed jets with $p_T > 20$ GeV.

[2)] According to [116] the expected number of QCD events is to be of the order of the number of W+jets events, i.e. after the event selection listed in this section.

Outline of the chapter

In Section 5.2 we discuss the fitting strategy of the modified HitFit. Section 5.3 presents the results of the $\not{E}_T$ scale measurement using a 'scanning method': a scan of the χ^2 function from the kinematic fit is performed over samples with pre-adjusted $\not{E}_T$ scale. As it turns out, the sensitivity of this scan to the *JES* is so large that this has to be measured first, and independently from the $\not{E}_T$ scale. Thus in Section 5.4 the *JES* is determined using a scan over samples with pre-defined jet energy scales. In Section 5.5 an alternative and powerful estimator of the $\not{E}_T$ scale is studied: the transverse momentum difference between the two top quarks reconstructed using the kinematic fit. The possibility of measuring the top quark mass is discussed in Section 5.6 and in Section 5.7 we propose an 'analysis-chain' for early data to determine the energy scales and to check the consistency of the used top quark mass. Finally the conclusion is given in Section 5.8 and in Section 5.9 we study the possibility to use the kinematic fit to distinguish supersymmetry events from Standard Model events.

5.2 Kinematic fit for semi-leptonic $t\bar{t}$ events

With four jets and no use of b-tagging there are 12 possible permutations for assigning the jets to their underlying quark in a semi-leptonic decay of a top quark pair (see also Fig. 5.1). For the reconstruction of the neutrino we assume $p_T^\nu = \not{E}_T$ and obtain the longitudinal component p_z^ν from the leptonic W mass requirement: $m_{lep.W} = 80.4$ GeV. As stated in Section 1.1.4 the world average for the W mass is $m_W = 80.398 \pm 0.025$ GeV. In cases where energy fluctuations lead to solutions with imaginary numbers, that is when the transverse mass $m_{l\nu}^T$ of the lepton/neutrino system is larger than the W boson mass, only the real part is used for p_z^ν. We remark that it is also possible to obtain p_z^ν from the decay products of the leptonic top by requiring that the neutrino solution together with the lepton and b-quark jet combine to the top mass, but in general this turns out to lead to slightly worse results.

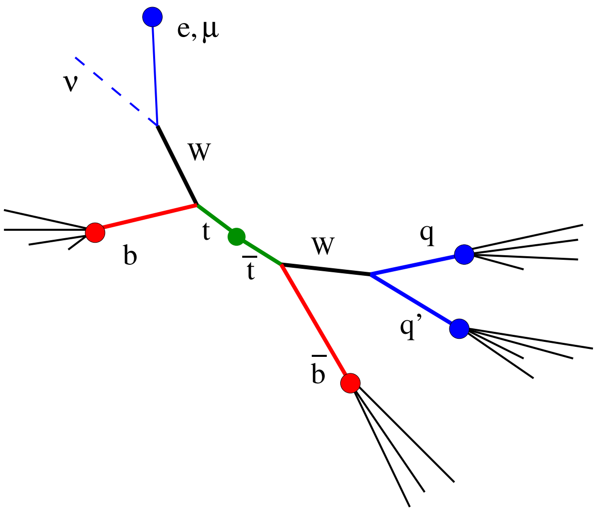

Figure 5.1: *Semi-leptonic top quark pair decay. The 'leptonic' top is the top quark decaying into a b-quark and a 'leptonic' W, which is the leptonically decaying W. The 'hadronic' top is the top quark decaying into a W that subsequently decays into two light quarks/jets. The corresponding b-quarks are named leptonic and hadronic b-quark respectively.*

Finally, the procedure leads to two solutions for the neutrino p_z^ν for each of the 12 permutations, hence effectively 24 permutations for each event. The candidate for the correct permutation is selected by keeping only the permutation with the lowest value of the χ^2 of the fit that will be described below. In events with five or more jets, only the four jets with highest p_T are used. Obviously, in these events, but also in events with exactly four reconstructed jets there is no guarantee that the measured jets correspond to the partons of the hard interaction.

Before applying the minimization procedure the masses of all jets are adjusted. This is a standard application in the HitFit program: in each permutation the mass of a jet is set to either zero or to 5 GeV for a light or a b-jet, according to the labeling of the jet in that permutation. The 3-momentum is not altered in this step.

The χ^2 function will now be discussed term by term. The entire function is defined as:

$$\chi^2 = \sum_{i=1,4}\left(\frac{\alpha_i p_T^i - p_T^i}{\sigma(p_T^i)}\right)^2 \tag{5.1}$$

$$+\left(\frac{\sqrt[4]{\prod_i \alpha_i} - 1}{\sigma_{jes}}\right)^2 \tag{5.2}$$

$$+\left(\frac{m_{had.W} - 80.4}{\sigma_{m_{had.W}}}\right)^2 + \left(\frac{m_{lep.W} - 80.4}{\sigma_{m_{lep.W}}}\right)^2 \tag{5.3}$$

$$+\left(\frac{m_{lep.Top} - m_{had.Top}}{\sigma_{m_{lep.T}}}\right)^2 + \left(\frac{m_{had.Top} - M_{top}}{\sigma_{m_{had.T}}}\right)^2 \tag{5.4}$$

The jet χ^2-terms

The first terms in the χ^2, see equation-line 5.1, allow to absorb fluctuations due to the resolution of the jet energy measurement.

The transverse momenta p_T^i represent the corrected jet momenta based on the measured momenta, $p_{T,reco}^i$. The correction function is obtained from MC events by parameterizing the relation between the measured $p_{T,reco}^i$ of the jet and the $p_{T,true}^i$ of the parton using a polynomial shape.[3)] This is illustrated for b-quark jets in Fig. 5.2 (left), where the ratio of the reconstructed jet p_T to the true quark p_T is fitted as a function of the reconstructed jet p_T. The parameterization results in the function $f(p_{T,reco}^i)$ defined as

$$f(p_{T,reco}^i) \equiv \frac{p_{T,reco}^i}{p_{T,true}^i} = a\cdot(p_{T,reco}^i)^3 + b\cdot(p_{T,reco}^i)^2 + c\cdot p_{T,reco}^i + d, \tag{5.5}$$

where the variables a,b,c,d are given in Table 5.1 separately for light- and for b-quark jets. The functions are applied to the jet 3-momenta vector such that the directions of the jets are not altered:

$$\overrightarrow{p}^i = f^{-1}(p_{T,reco}^i)\,\overrightarrow{p}^i_{reco}, \tag{5.6}$$

where $\overrightarrow{p}^i$ is the momentum of jet i, of which the transverse component is finally used in the χ^2 function.

[3)]First a matching study is performed to identify jets as (possibly) originating from one of the four hard partons in the top decay, where a distinction is made between the b-quarks and the light quarks from the hadronic W. The measured jets are matched to their corresponding hard partons by requiring $\Delta R < 0.2$, where $\Delta R = \sqrt{\Delta\phi^2 + \Delta\eta^2}$.

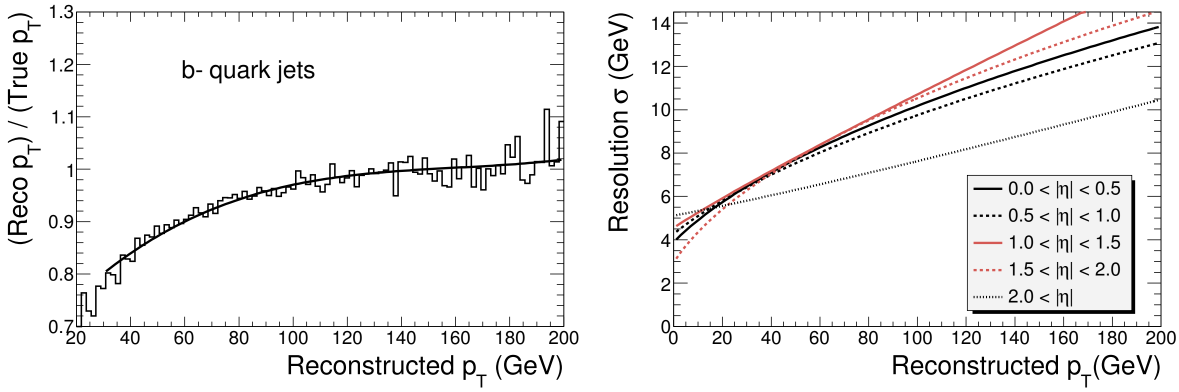

Figure 5.2: *Left: calibration of the parton correction for the heavy jets. Right: the jet p_T resolution as function of the transverse momentum, for five η regions. See text for more details.*

The resolutions $\sigma(p_T^i)$ are parameterized as functions of the transverse momentum and are determined separately for five η regions. The resolution function parameters are obtained in the following way. First, distributions of the transverse momentum difference between jet and corresponding parton for various bins in transverse momentum are fitted with Gaussian shapes. Then, the squared widths of these Gaussians, again as function of the transverse momentum are fitted with a second order polynomial. The functions are thus given by

$$\sigma(p_T^i) \quad = \quad \sqrt{A^2(p_T^i)^2 + B^2 p_T^i + C^2}. \tag{5.7}$$

The resulting functions are depicted in Fig. 5.2 (right) and are given by the parameters in Table 5.2. From the distributions in the figure it becomes clear that the resolutions are worst in the regions nearest to the gap region, that is for $1.0 < |\eta| < 1.5$ and $1.5 < |\eta| < 2.0$. The best resolution is obtained in the most forward region, i.e. with $2.0 < |\eta|$.[4] These observations are in agreement with the results in Section 4.3.5 and [100].

The parameters α_i in equation-line (5.1) are free fit parameters and are preferably equal to unity; their purpose is to absorb fluctuations due to the resolution of the jet energy measurement, and are *not* related to the overall jet energy scale. For this we have the 'correlation term' to which we come back shortly. The parameters α_i are applied to the jet 3-momenta vector such that the directions of the jets are not altered. When adjusting the jet momenta the missing transverse energy is also changed, such that the total transverse momentum in the event, K_T remains constant. The quantity K_T is obtained from the vectorial sum over the leading four jets, the lepton and missing energy:

$$K_T = \sum_{i=1,4} \vec{p}_T^{\,jet\ i} + \vec{p}_T^{\,lepton} + \vec{\not{E}}_T. \tag{5.8}$$

[4]This is because jets in the forward region have very high momentum and, as the shapes of most of the distributions in Fig. 5.2 (right) show, a higher momentum jet has a relative better resolution. Explained with an example: assuming the jet direction is perfectly measured, $\sigma(p_T)/p_T = \sigma(p)/p$. A jet with $\eta = 0$ and $p_T = 40$ GeV has $\sigma(p)/p = 0.18$, see the figure. A jet with $\eta = 2.3$ and $p_T = 40$ GeV has $\sigma(p)/p = 0.15$. That is a better resolution in p_T, but with $p = 200$ GeV for the forward jet the resolution can be compared to the resolution of a jet with $\eta = 0$ and $p = 200$ GeV, i.e. with $\sigma(p)/p = 0.07$.

	a (GeV^{-3})	b (GeV^{-2})	c (GeV^{-1})	d
light jets	$6.07 \cdot 10^{-9}$	$-5.25 \cdot 10^{-6}$	$1.67 \cdot 10^{-3}$	0.889
b-quark jets	$7.54 \cdot 10^{-8}$	$-3.62 \cdot 10^{-5}$	$6.07 \cdot 10^{-3}$	0.650

Table 5.1: *Parameters for the parton correction function eq. (5.5), for light and b-jets.*

	A	B ($\mathrm{GeV}^{1/2}$)	C (GeV)
$0.0 < \mid \eta \mid < 0.5$	0.00	0.94	3.9
$0.5 < \mid \eta \mid < 1.0$	0.00	0.88	4.3
$1.0 < \mid \eta \mid < 1.5$	0.05	0.81	4.6
$1.5 < \mid \eta \mid < 2.0$	0.00	1.01	3.0
$2.0 < \mid \eta \mid$	0.03	0.47	5.1

Table 5.2: *Parameters for the resolution function eq. (5.7), for five $|\eta|$ regions.*

The correlation term

The term in equation-line (5.2) is related to the overall jet energy scale. The idea behind this term is that the four α's enable to absorb fluctuations of the individual jet energy measurements, while the event's overall jet energy scale (which is the quartic root of the product of the four α's) is kept close to unity.

The 'uncertainty' $\sigma_{jes} = 0.01$ in equation-line (5.2) is estimated empirically from the requirement that the magnitude of the correlation term is comparable with other terms in the total χ^2 as appropriate. We can interpret this resolution as follows: the combination of a semi-leptonic $t\bar{t}$ hypothesis with all the jet and mass resolutions in the χ^2, results in an overall jet energy scale resolution to the percent level.[5)] Although a one-to-one correlation is not correct, at first order the σ_{jes} indicates the sensitivity to the overall jet energy scale.

In general this term leads to relatively stable fits. When scanning over samples with pre-defined jet energy scales in Section 5.4, this term is necessary to prevent the absorption of the pre-defined energy scale by the four α's.

The mass constraints

The constraints in equation-line (5.3) and (5.4) are added as penalty terms to the full χ^2. It should be noted that the term related to the constraint from the leptonic W mass only contributes to the χ^2 when the equation $m_{lep.W} = 80.4$ GeV has solutions with imaginary numbers for the neutrino's longitudinal momentum.

The resolutions used in these terms, the σ_m's, are a combination of the physical mass width of the parent particles and the resolution of the corresponding reconstructed objects. Only the resolution of the jet angles contribute to these σ_m's: the resolution of jet energies is already accounted for in the jet terms and should not be invoked again in these terms. The σ_m's are obtained using MC events by replacing the measured energy of the jets by the true energy of the corresponding partons using events with no or negligible final state radiation. For this purpose we select events by requiring the (true) invariant mass of the two light partons and

[5)]This is assuming the correct jet permutation is selected, and excluding any systematic uncertainties such as different MC generator results.

the hadronic b-quark to be larger than 174.5 GeV. The same selection has been applied to the invariant mass of the true lepton, the true neutrino and the leptonic b-quark. To obtain a correct resolution for the leptonic top mass, the neutrino p_z^ν is calculated by requiring the two reconstructed top masses to be equal. If we were to use the solution for p_z^ν with the standard approach of requiring the leptonic W mass to be 80.4 GeV, the error on the $\not{E}_T$, which results in an error on the p_z^ν, would propagate twice into the resolution on the leptonic top mass: once in the p_x^ν and p_y^ν, and once in the p_z^ν.[6)]

In Figure 5.3 the four mass distributions are depicted, including the results of the Gaussian fits. The fitted means do not exactly correspond to the true masses of the particles, implying that on average the opening angles between the partons are different from the opening angles between jets: a fitted mass lower than the true mass effectively means that the jets are closer together than the partons. We neglect these small discrepancies and keep the 'true' values of 80.4 and 175 GeV in the fit for respectively the W and the top mass. The resolutions are:

$$\begin{aligned} \sigma_{m_{lep.W}} &= 9.3 \text{ GeV} \\ \sigma_{m_{had.W}} &= 4.2 \text{ GeV} \\ \sigma_{m_{lep.T}} &= 4.2 \text{ GeV} \\ \sigma_{m_{had.T}} &= 3.2 \text{ GeV}. \end{aligned} \tag{5.9}$$

[6)] Even more correct perhaps, would be to calculate the neutrino p_z^ν by requiring the leptonic top mass to be 175 GeV. In the approach we have adopted the resolution on the hadronic top mass propagates partly into the resolution on the leptonic top. This effect is however smaller than the double counting of the $\not{E}_T$ error.

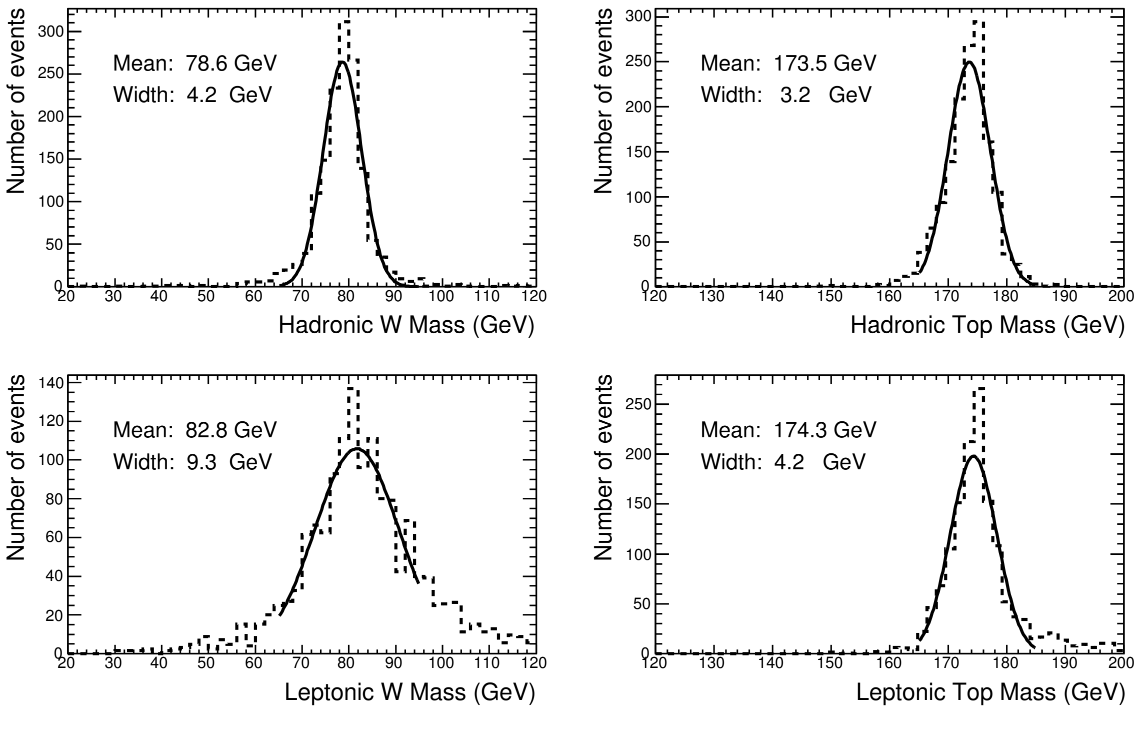

Figure 5.3: *Mass distributions for (clockwise, starting with the upper left): the hadronic W, the hadronic top, the leptonic top and the leptonic W. The dashed distributions are the events selected, including FSR suppression, see text for the exact details. The Gaussian fit results are depicted by the solid lines, with the mean and width given for each mass distribution.*

The degrees of freedom - To determine the number of degrees of freedom n_d in the χ^2 function, we count the contributions to n_d first in eq. (5.1) and (5.2), then in eq. (5.3) and (5.4):

- The four jet parameters α_i are constrained by the corresponding χ^2 terms, and they are additionally constrained by the correlation term. Thus, with a total of 5 terms for 4 parameters and ignoring the correlation between the jet terms and the correlation term, we have a contribution to n_d of $5-4=1$. When the jet terms and the correlation term are fully correlated this contribution reduces to 0.
- In total we have four mass constraints. The term with the leptonic W mass constraint is used to get a solution for p_z^ν. This leads to $4-1=3$ more degrees of freedom. However, we get two solutions for p_z^ν. The correct solution has to be determined by (partially) using the information from the final three mass constraints, which at most 'eats' one more constraint. In the latter case we have a contribution to n_d of $4-2=2$.

Hence, we find a minimum for the number of degrees of freedom at $n_d=2$ and a maximum at $n_d=4$. When discussing the χ^2 probability of the kinematic fit in Fig. 5.4 in the following section we show that $n_d=3$ is a reasonable value.

5.2.1 Performance on matched $t\bar{t}$ events

To study the performance of the kinematic fit we use a selection of events that fulfill the $t\bar{t}$ hypothesis without significant QCD radiation. In these events, which have four jets, the measured jets are matched to their corresponding hard partons by requiring $\Delta R < 0.2$, where ΔR is defined by $\Delta R = \sqrt{\Delta\phi^2 + \Delta\eta^2}$ and represents the distance between jets in ϕ and η space. We refer to these events as *matched* events. The contribution of events with significant final state radiation (FSR) is further reduced by requiring the appropriate combination of partons' (and leptons') true momenta to yield the top mass within 1 GeV and the W mass within 2 GeV,

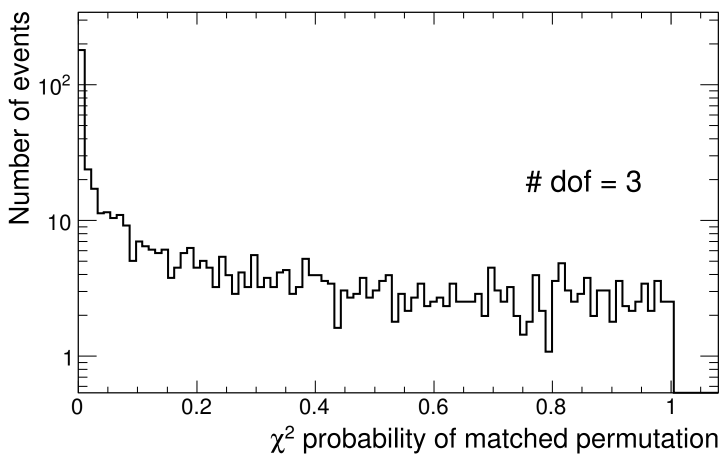

Figure 5.4: *The χ^2 probability distribution of the kinematic fit for the selected events, for the permutation with all four jets correctly matched to the four partons. FSR suppression is applied by requiring the reconstructed top mass and W mass to be within 1 and 2 GeV of the true values; see text for more details.*

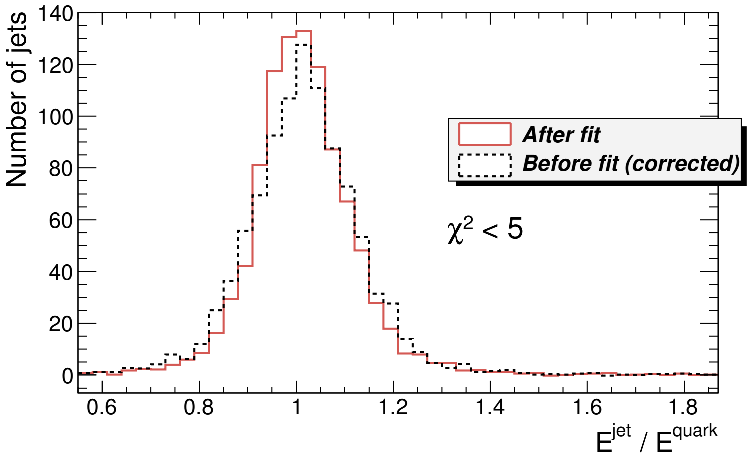

Figure 5.5: *For matched events with additional FSR suppression, the fitted jet energy divided by the corresponding true parton energy together with the original result (corrected, before the fit), after a requirement of $\chi^2 < 5$. Little or no improvement is visible as result of the fit.*

both for the hadronic and leptonic top. It should be emphasized that this Section describes the results of a study restricted to matched events, while this restriction is not used by other studies described in this note, unless specified otherwise.

The result of this selection is as follows: of the $73.2 \cdot 10^3$ events [7] in the sample $10.9 \cdot 10^3$ events pass the standard requirements of Section 5.1, of which 565 events have four matched partons, as defined above.[8] Figure 5.4 shows the χ^2 probability of the kinematic fit for the selected events, assuming 3 degrees of freedom, for the permutation with all four jets correctly matched to the four partons. The distribution peaks around zero, implying that even for the correct permutation of the four jets a significant number of events is poorly reconstructed. In this case either the jet energies, the lepton energy or direction, or the missing transverse energy is poorly measured. At higher probability values, the distribution is essentially flat as expected for purely Gaussian detector resolution. In retrospect, the flat distribution confirms that $n_d = 3$ is a reasonable value. For matched events we find that the correct jet combination has the lowest χ^2 value in about 2/3 of the events.

In Figure 5.5 the distribution of the fitted jet energy divided by the corresponding true parton energy is displayed, for the jets before and after the fit; the first do have the parton correction function applied. When extremely 'clean' events are considered by requiring $\chi^2 < 5$ a little to no improvement is visible.[9] This indicates that the fit could not further improve the overall *JES* for these particular events. As we will see later, the fit over all events is however sensitive to overall jet energy scale offsets. Hence we interpret Fig. 5.5 as confirming the correctness of the parton correction of eq. (5.5). We observe similar behavior of the missing transverse energy resolution. However, as will be shown in the next section, for events with high values of χ^2, the $\not{E}_T$ (fitted and original) resolution degrades, implying that by cutting on χ^2 one selects well measured events.

[7] This is from exactly 10^5 unweighted MC@NLO events, equivalent to an integrated luminosity of 160 pb^{-1}. As stated before, the sample contains no all-hadronic decays.

[8] Without the requirements for FSR suppression we would have ~ 1900 matched events.

[9] The requirement of $\chi^2 < 5$ reduces the sample of 565 events to 246 events.

5.3 The $\not\!\!E_T$ scale from the scanning method

In this section we describe the extraction of the $\not\!\!E_T$ scale based on a scan of the χ^2 function, starting with a brief intermezzo to clarify the additional requirements that will be used in this procedure. Similar to the overall *JES* that we set out to measure, we emphasize that it is the overall $\not\!\!E_T$ scale we try to establish, not its resolution or the amount of fake $\not\!\!E_T$.

The analysis described in this chapter turns out to perform best when the background from W+jets and especially from poorly measured $t\bar{t}$ events is small. Therefore, tight requirements are introduced that are established empirically. The distribution of χ^2 after the kinematic fit is depicted in Fig. 5.6 (left) for $t\bar{t}$ and W+jets events. Also shown is the distribution for the matched $t\bar{t}$ events. The distribution for $t\bar{t}$ peaks at low values of χ^2 and then falls rapidly, but exhibits a long tail. In contrast, for the W+jets events the peak at low values is much less pronounced. The difference between signal and background appears even more dramatic when the $\log_{10}(\chi^2)$ is considered as in Fig. 5.6 (right), where the lowest values of $\log_{10}(\chi^2)$ are dominantly populated by $t\bar{t}$ events.

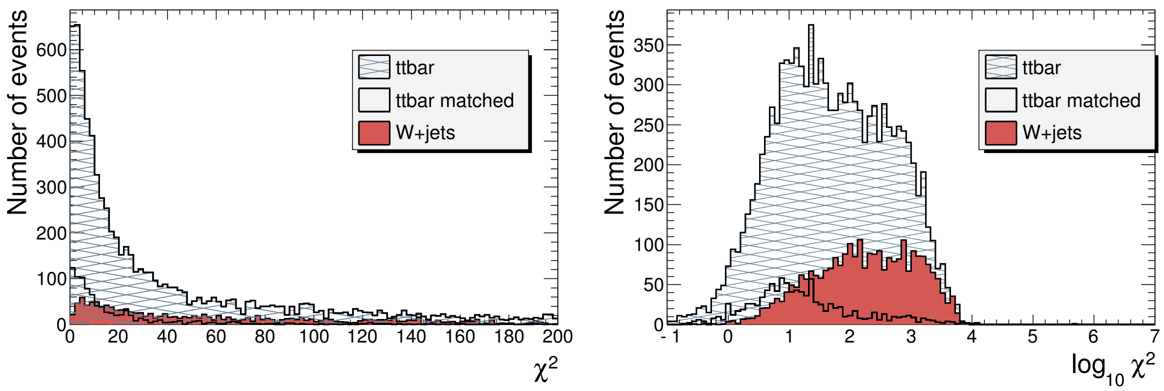

Figure 5.6: *The distribution of the best permutation χ^2 of the kinematic fit for $t\bar{t}$ (all and matched) and W+jets events. The standard selection requirements of Section 5.1 are used. Left, the distribution of χ^2 is depicted, right the distribution of* $\log_{10}(\chi^2)$.

About 50% of the matched events are removed when cutting on $\chi^2 = 10$; this appears to be a reasonable trade off between statistics and event quality. Cutting on χ^2 suppresses events in which the $\not\!\!E_T$ is (relatively) poorly reconstructed, which is confirmed by the distributions of 'fake $\not\!\!E_T$' shown in Fig. 5.7. Fake $\not\!\!E_T$ is defined as the difference between the $\not\!\!E_T$ after the fit and the true missing transverse momentum. These distributions indicate that for events with $\chi^2 < 10$, the $\not\!\!E_T$ resolution is significantly better than for events at higher values of χ^2. Moreover, at high values of fake $\not\!\!E_T$ (larger than 30 GeV), in the tails of the distribution, there are substantially less events with $\chi^2 < 10$.

Figure 5.8 (left) shows the $\not\!\!E_T$ distribution for $t\bar{t}$ and W+jets events with the standard selection requirements of Section 5.1. At this stage, the ratio of signal (S) and background (B_W) events is $\frac{S}{B_W} = 4.0$. The right plot shows the same distributions after rejecting events with $\chi^2 > 10$ and a $m_{lep.W} > 80.7$ GeV, leading to $\frac{S}{B_W} = 13.4$.

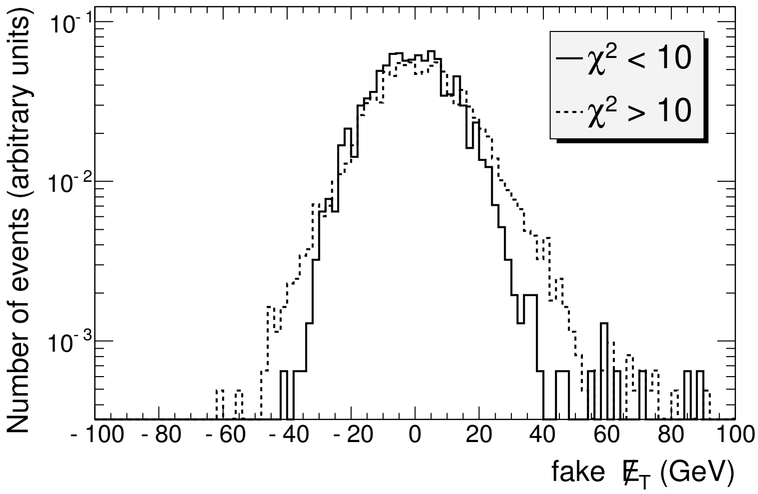

Figure 5.7: *The fake $\not\!\!E_T$ for $t\bar{t}$ events, i.e. the difference between the $\not\!\!E_T$ after the fit and its true value. The distribution is shown for events with $\chi^2 < 10$ and for events with $\chi^2 > 10$. The distributions are normalized.*

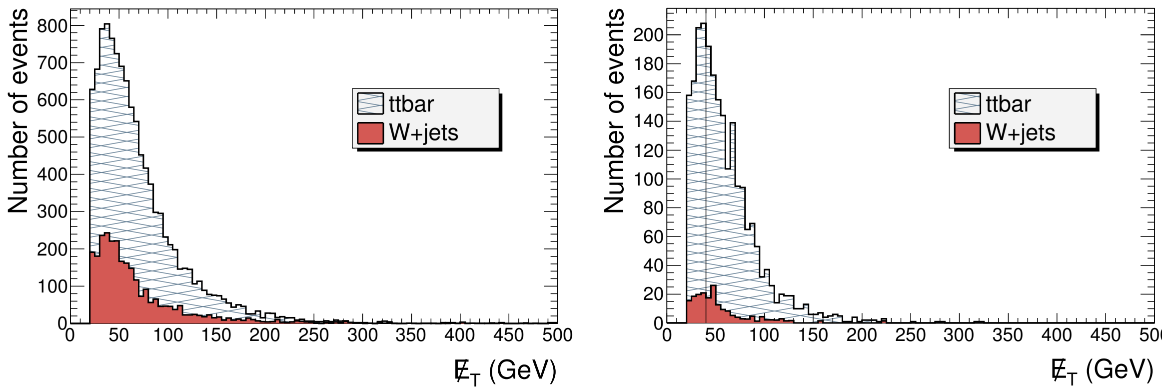

Figure 5.8: *The distribution of $\not\!\!E_T$ for $t\bar{t}$ and W+jets events with standard selection requirements of Section 5.1 (left) and after rejecting events with $\chi^2 > 10$ and a $m_{lep.W} > 80.7$ GeV (right). The cut value of the 'additional requirement' (see text) at $\not\!\!E_T = 40$ GeV is also indicated.*

In the following we only consider the results after the next **additional requirements**:

- The fit must have converged and the best permutation must have a $\chi^2 < 10$.
- The reconstructed leptonic W mass must be $m_{lep.W} < 80.7$ GeV, or in other words the solution for p_z^ν is real.
- Before starting the fit procedure we require $\not\!\!E_T > 40$ GeV. This has no significant effect on $\frac{S}{B_W}$, but is introduced to reject QCD background (though, not present in this MC study).

5.3.1 The scanning method

To determine the scale of the missing transverse energy, the $\not{E}_T$ scale, we use a χ^2-scan running over a hypothetical $\not{E}_T$ scale over a large range in small steps, called 'scan-points'. At each scan-point, first the new $\not{E}_T$ scale is implemented in a straightforward way by just multiplying the original $\not{E}_T$ value by the $\not{E}_T$ scale factor, which gives a new value of the overall transverse momentum, K_T. Then, the events are fitted to determine the event permutation with the lowest value of χ^2 (corresponding to the best fit of the four jet parameters α_i). The event for a particular scan-point is kept if it fulfills the additional requirements discussed on page 121. The statistical uncertainties from the typically 1500 events are correlated between scan-points. However, some events can fulfill the additional requirements for a particular scan-point while for another point, the event is rejected. This leads to uncorrelated statistical fluctuations at different scan-points. The size of these uncorrelated uncertainties is typically 0.5%, obtained from the statistical uncertainty of the number of events at a certain scan-point which do not contribute to the neighboring scan-points.

To optimize the sensitivity of the analysis a readjusted definition of the χ^2 is used: first, the events are weighted with their χ^2 probability P. That is, at each scan-point the average value $\overline{\chi}^2 = \Sigma_i P_i \chi_i^2 / \Sigma_i P_i$ of all selected events (or better their best permutation) is obtained. By taking the average value, the technical problem of having different statistics at each scan-point is solved. Second, to facilitate absolute comparisons of different scans, at each scan-point the average $\overline{\chi}^2$ is scaled by the number of events in the point with the lowest average value: we refer to this quantity as χ^2_w, the *weighted* χ^2.

Figure 5.9 (left) shows the results of a scan of the $\not{E}_T$ scale in steps of 0.05. The top quark mass is fixed to a value of $M_{top} = 175$ GeV. The contribution of $t\bar{t}$ events and that of W+jets background events are shown separately. In order to determine the position of the minimum

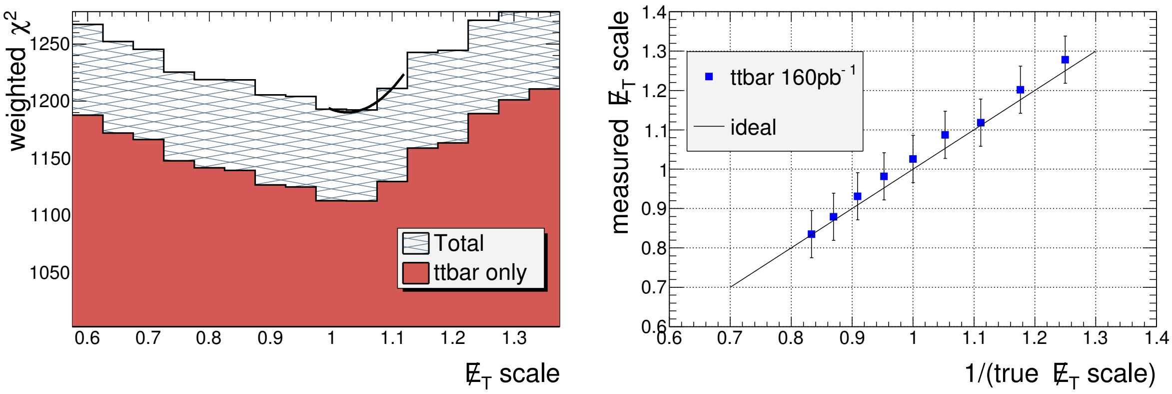

Figure 5.9: *Left: distribution of the weighted χ^2 for a scan of the $\not{E}_T$ scale, for the 'Total' sample (i.e. $t\bar{t}$ and W+jets events) and for $t\bar{t}$ events only. The uncorrelated statistical uncertainty between the points is at the level of 0.5%. The best value for the $\not{E}_T$ scale is determined by fitting a parabolic function. Right: results for the best values of the $\not{E}_T$ scale determined with the scan applied to samples with adapted true $\not{E}_T$ scales. (For a sample with e.g. adapted true $\not{E}_T$ scale=0.8 the expected result is 1/0.8=1.25.) The same sample is used in each point. The uncertainties are obtained from the fluctuation in the results on sub-samples (see text).*

in this distribution a parabolic fit is applied around the scan-point with the lowest value of χ^2_w, leading to a $\not\!\!E_T$ scale $= 1.03$. A statistical uncertainty of ± 0.06 is obtained from the fluctuations on results from scans on subsamples of the sample used: the total sample is divided in four subsamples and from the resulting distribution of the scales the uncertainty is extracted as the $RMS/\sqrt{4-1}$. This method is applied throughout this work.[10)]

The contribution of background events is modest due to the strong requirements on the missing transverse energy $\not\!\!E_T > 40$ GeV and $\chi^2 < 10$. We repeated the procedure without including the background events and find a minimum again at $\not\!\!E_T$ scale $= 1.03$, in agreement with the nominal result.

We continue our study by preparing various event samples with adapted true $\not\!\!E_T$ scales and repeating for each sample the scanning procedure. For this we ignore the W background events. Figure 5.9 (right) shows the fitted result versus the expected result: for a sample with for example an adapted true $\not\!\!E_T$ scale $= 0.8$ the expected result is $1/0.8 = 1.25$. The figure illustrates that the kinematic fitting procedure behaves reasonably linear, even for relatively large deviations. A realistic scenario would be to iterate the scanning procedure, starting each iteration with the $\not\!\!E_T$ scale from the previous iteration.

The variation of the weighted χ^2 in Fig. 5.9 (left) as a function of the $\not\!\!E_T$ scale is relatively small. The stability of this method against possible systematic effects, notably the jet energy scale and the top quark mass, are therefore the key issues now. These issues are addressed in the following two paragraphs.

5.3.2 Sensitivity to the top quark mass

The top quark mass as used in the constraints of the kinematic fit is varied by its uncertainty of 2.5 GeV and the scan procedure is repeated. Table 5.3 lists the results for $\not\!\!E_T$ scale separately for various values of M_{top}. The results show a large variation of -12% of the $\not\!\!E_T$ scale for the

scanned quantity	fixed quantity
$\not\!\!E_T$ scale $= 1.04$	$M_{top} = 177.5$
$\not\!\!E_T$ scale $= 1.03$	$M_{top} = 175.0$
$\not\!\!E_T$ scale $= 0.91$	$M_{top} = 172.5$

Table 5.3: *Summary of the results of the kinematic fitting procedure for 1-dimensional scans of the $\not\!\!E_T$ scale with various values of M_{top}.*

-2.5 GeV variation of the top mass. Although the world average of the top quark mass is known to ± 1.3 GeV, this large correlation can affect our results. With the sensitivity to the jet energy discussed in the next section it will become clear how we can solve this problem. We already note that in Section 5.7.1 we will discuss the possibility of simultaneous offsets in the top mass value expectation, the jet energy scale and the $\not\!\!E_T$ scale.

5.3.3 Sensitivity to the jet energy scale

The light quark jet energy scale may eventually be measured to the 1% level using the mass of the W boson, this method is discussed in [111]. The b-jet energy scale is the most problem-

[10)] As a check the uncertainty was also obtained by applying the analysis to several different samples of 10^5 events. The results were similar.

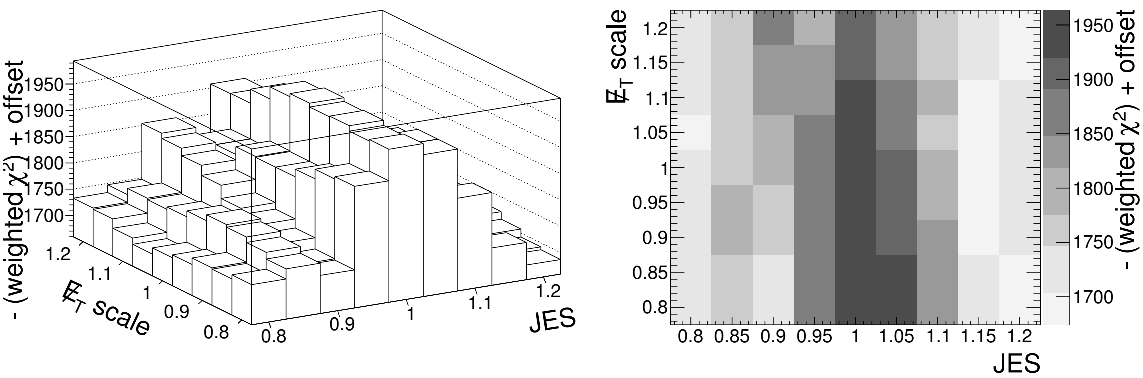

Figure 5.10: *Left: a lego plot of $-\chi^2_w$+offset for hypothetical JES and $\not\!\!E_T$ scale values (scan-points). The value of χ^2_w is inverted and an offset is added to make the minimum visible (as maximum). Right: a gray-scale plot of the same quantities as in the left plot. The darkness of the squares indicate the magnitude as shown in the legend.*

atic since it is difficult to measure with the first data. To study the overall jet energy scale uncertainties, we use a two dimensional scan running over a hypothetical jet energy scale and $\not\!\!E_T$ scale around unity in steps of 0.05.

At each scan-point, first the new $\not\!\!E_T$ scale is applied: the $\not\!\!E_T$ value is multiplied with the new $\not\!\!E_T$ scale factor leading to a new value of the K_T. Then the new jet energy scale is implemented while keeping this value of K_T constant, as described when discussing eq. (5.8). Moreover, the corresponding scaled transverse jet energy resolution, $\sigma(p^i_T)$ is always evaluated at its nominal value; otherwise the minimization of the χ^2 function is artificially forced to prefer higher values of the *JES* scale.[11] The result is graphically displayed in Fig. 5.10 (left) as a lego plot for $-\chi^2_w$ +offset; for visibility it is necessary to 'invert' χ^2_w and an offset is added to ensure positive bin values, needed for technical reasons, in order to see the lego-towers around the minimum value (as maximum). Figure 5.10 (right) shows the same result using a gray-scale index. When we look at slices of constant *JES*, we observe that the χ^2_w value as function of the $\not\!\!E_T$ scale has no unique minimum except for the slice with $JES = 1.0$. For a variation of 5% of the *JES* (a realistic offset of the *JES* that can be expected in the first data sample), the effect on the $\not\!\!E_T$ scale is dramatic and no minimum can be found. The conclusion for early data is that we first need to know the correct overall *JES*; if the overall *JES* is too far off, the 2D scan is useless for the $\not\!\!E_T$ scale determination.

However, the results for the *JES* are spectacular: the minimum of χ^2_w as function of $\not\!\!E_T$ scale remains close to unity for any value (or slice) of $\not\!\!E_T$ scale. At the minimum value of χ^2_w, we find $JES = 1.01 \pm 0.02$ and $\not\!\!E_T$ scale$= 1.03 \pm 0.06$ both close to unity as expected. This suggests that it is possible to extract the *JES* without the necessity to know the $\not\!\!E_T$ scale in advance, which is the topic of the next Section.

[11] The easiest way to see this, is with an example: take a jet measured with $p_T = 100$ GeV, which is also the correct value corresponding to the parton p_T. If we did not evaluate the $\sigma(p_T)$ at its nominal value, a positive offset in the scan of the *JES* of a factor of 1.2 results in a χ^2-term for this jet of $(\frac{-20}{\sigma(120)})^2$. A negative offset of a factor of 0.8 results in $(\frac{+20}{\sigma(80)})^2$ (assuming the fit finds the true value back.) The latter is always larger as $\sigma(p_T)$ decreases with decreasing p_T. Thus a positive offset would be favored over a negative offset in a *JES* scan.

5.4 Determination of the jet energy scale

In the previous section, using a two dimensional scan, we have observed that the *JES* can be determined independently from the $\not\!\!E_T$ scale, implying that the *JES* can be determined from a one dimensional scan as is done for the following studies.

We use the same scanning procedure as explained earlier and scan the χ^2_w as a function of the *JES* from 0.84 tot 1.16 in steps of 0.02. The result is displayed graphically in Fig 5.11 (left). A parabola is fit around the minimum and leads to $JES = 1.01 \pm 0.02$. The uncertainty of 0.02 is again obtained from the statistical fluctuations on results from scans on subsamples. When the W+jets background is ignored, the result does not significantly change.

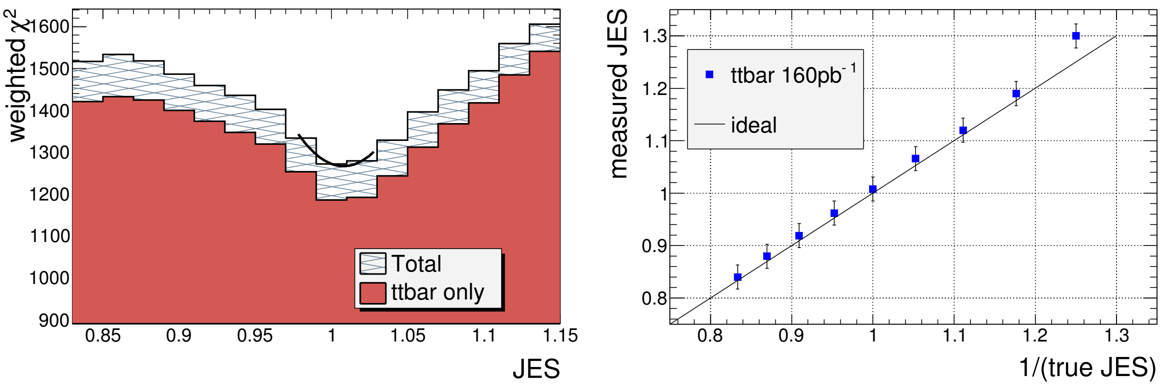

Figure 5.11: *Left: distribution of the weighted χ^2 for a scan of the JES for a fixed top mass at 175 GeV, including $t\bar{t}$ and W+jets events indicated as 'Total'. The contribution of $t\bar{t}$ events only is shown separately. The uncorrelated statistical uncertainty between the points is at the level of 0.5%. Right: the JES scanning results as a function of the expected value, true $1/JES$. A line that represents unity is drawn to guide the eye.*

We have prepared several mis-calibrated $t\bar{t}$ samples (thus ignoring W+jets background) by using a true *JES* in the range between 0.8 and 1.2 and we repeated the scanning procedure. Note that the jet energy and $\not\!\!E_T$ selection cuts are applied after a mis-calibration of the true *JES*, leading to a different event sample than for the nominal case. As can be seen in Fig. 5.11 (right), the procedure behaves linearly and we developed a method to determine the overall *JES* within 2% statistical accuracy. There are several systematic uncertainties which can influence these results. We now study the dependence on the $\not\!\!E_T$ scale and the top mass.

5.4.1 Sensitivity to the $\not\!\!E_T$ scale and top quark mass

Systematic effects may arise from an unknown $\not\!\!E_T$ scale and from the top quark mass. To quantify the first uncertainty we vary the $\not\!\!E_T$ scale by ± 0.2; the resulting variation of the *JES* is small, as listed in Table 5.4. The mass of the top quark is varied by its uncertainty of 2.5 GeV; the results for the *JES*, see Table 5.4, are offset by 0.02 with respect to the nominal result. We conclude that the *JES* can be determined using the scanning procedure to the level of 2% statistically and 2% systematically.

scanned quantity	varied (true) quantity
$JES = 1.007$	(nominal)
$JES = 1.012$	$\not{E}_T$ scale $= 0.8$
$JES = 1.001$	$\not{E}_T$ scale $= 1.2$
$JES = 1.025$	$M_{top} = 177.5$ GeV
$JES = 0.998$	$M_{top} = 172.5$ GeV

Table 5.4: *Summary of results of the kinematic fitting procedure for 1-dimensional scans of the JES for various values of the true $\not{E}_T$ scale and top quark mass; background events are excluded in these measurements. The statistical uncertainty on the fitted JES equals 2%.*

We note here that we did not study the effect of QCD events, if present, nor the effect of the underlying event or pile-up. The first can contaminate the sample, 'blurring' the accuracy of the scan. The latter two event types can make it more difficult to establish the correct permutation, with the same result as QCD events, but it can also affect the measured energy of the jets and the measured $\not{E}_T$. We see in Table 5.4 that a mis-measured $\not{E}_T$ is not of great importance, and an overall mis-measured JES is what we aim to measure, yet the total effect of any underlying event is unknown and should be kept in mind for further study.

With the overall JES measured, the next task is to determine the $\not{E}_T$ scale in a different way than presented in the previous section, since the χ^2 scanning method to obtain the $\not{E}_T$ scale is too correlated to the JES scan.

5.5 The $\not{E}_T$ scale from the top pair ΔP_T

The observable we have constructed to determine the $\not{E}_T$ scale is the measured transverse momentum difference of the two top quarks:

$$\Delta P_T = p_T^{lep} - p_T^{had}, \tag{5.10}$$

where p_T^{lep} is the combined transverse momentum of the measured charged lepton, the $\not{E}_T$ and one b-jet, while p_T^{had} is the momentum of the jets of the hadronic W and the other b-jet. The assignment of the jets is obtained from the permutation with the lowest χ^2.

Figure 5.12 shows the distribution of ΔP_T for $t\bar{t}$ events and W+jets events selected, with the additional requirements of page 121 still applied. A Gaussian shape is fitted to the distribution with a mean of -2.58 ± 1.15 GeV and a width of 24.0 ± 1.8 GeV. When the fit is only applied to $t\bar{t}$ events the mean changes to -2.4 GeV, indicating that the W+jets background can safely be ignored for this initial study.

To study the sensitivity of ΔP_T to the true $\not{E}_T$ scale, several event samples with adapted scale are used; the mean of the distributions versus true $1/\not{E}_T$ scale are shown in Fig. 5.13. A line fitted through the results is also shown. The line with a slope of -37 GeV can be used as calibration curve to obtain the $\not{E}_T$ scale from the ΔP_T distribution with a statistical uncertainty of $\sigma(\text{mean})/\text{slope} = 1.15/36.9 = 0.03$.

The mean of the ΔP_T distribution is clearly not zero. Two effects can play a role in this offset: first, the selection requirements of Section 5.1 cause only the more energetic jets to be selected; the p_T requirement for the jets is higher than the p_T requirement on the lepton and the $\not{E}_T$, biasing the transverse momentum of the reconstructed hadronic top quark. A second effect might be the parton corrections discussed in Section 5.2, where we observe that the corrections can easily amount to an increase in the jet p_T of $0\% - 20\%$ (for jets with $p_T < 100$ GeV). The K_T is altered with these corrections: in the standard HitFit settings the parton corrections are

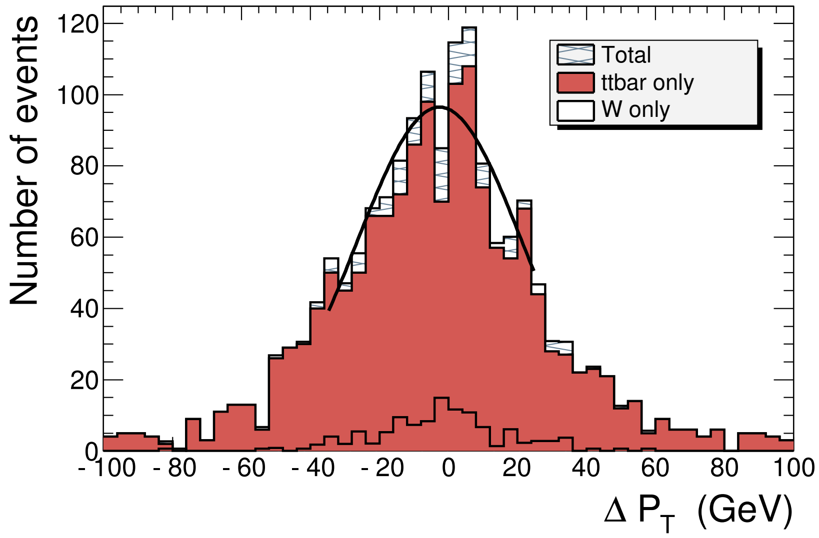

Figure 5.12: *The distribution of the measured momentum difference between the two top quarks ΔP_T, for $t\bar{t}$ and W+jets events. The assignment of the jets is obtained from the permutation with the lowest χ^2. The standard selection requirements of Section 5.1 are used, plus the additional requirements of page 121. A Gaussian is fitted to the Total distribution, of which the mean, and its uncertainty, are used in the next figure.*

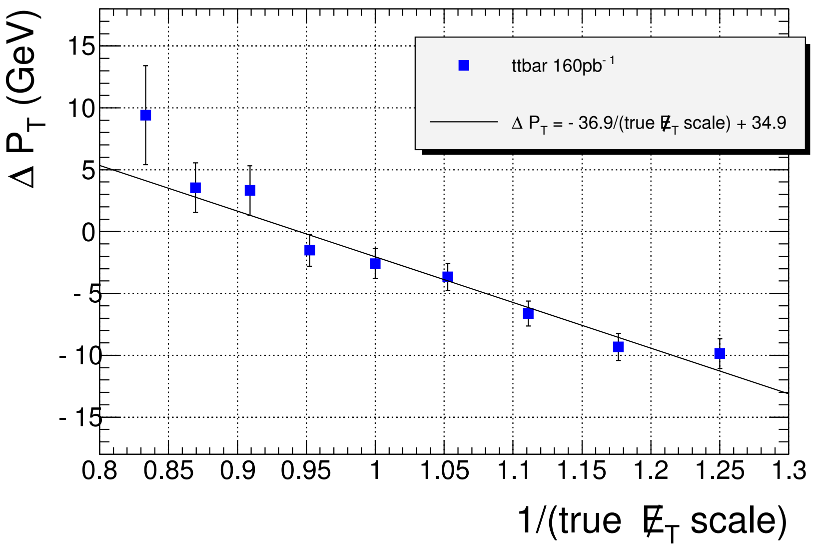

Figure 5.13: *The mean of the distribution of ΔP_T as function of the true $1/\not{E}_T$ scale. A line is fitted through the results.*

not propagated into a change of the missing transverse energy, with the hypothesis that the parton corrections take into account out-of-cone jet energy depositions. As these depositions have already been taken into account in the original calculation of the $\not{E}_T$, there is no need for $\not{E}_T$-corrections. However if the difference between the jet and the parton energy is not only an out-of-cone effect, $\not{E}_T$-corrections might be needed, but not on a one-to-one basis.

An interesting study would be to find the exact cause for the need of the parton correction and its relation with the $\not{E}_T$. The offset of the ΔP_T is however not an immediate problem. The bias in Figure 5.13 can be compensated for; as this introduces a dependence on MC prediction, the bias does introduce an extra systematic uncertainty in our results.

5.5.1 Sensitivity to the *JES* and top quark mass

The mean of the ΔP_T distribution is sensitive to the *JES*, but less dramatically than the scanning method. For example, for a true *JES* of 0.88 and 1.12, the mean changes from the nominal -2.4 GeV (excl. background) to -0.8 GeV and -2.2 GeV respectively. Note that both results shift the mean to higher values. When these mean values are used to extract the $\not{E}_T$ scale, the offset is of the order of 5%. This suggests to first use the scanning method to determine the *JES* and then use the ΔP_T method extract the $\not{E}_T$ scale.

The sensitivity on the mass of the top quarks is estimated by changing M_{top} to 172.5 GeV and 177.5 GeV respectively, which leads to mean values of -3.1 GeV and -2.4 GeV and thus affects the $\not{E}_T$ scale at the 2% level. Hence, the ΔP_T turns out to be relatively stable against systematic variations of the top quark mass. However, the top quark mass also affects the *JES* measurement (see Table 5.4) and thus indirectly has impact on the $\not{E}_T$ scale determination. The systematic variation of the $\not{E}_T$ scale from this combined effect is at most 3%.[12)] With the new, more accurate, world average of the top quark mass this variation can only be smaller.

5.6 A special case study: the top mass distribution

A complete measurement of the top quark mass, simultaneously with the energy scales is beyond the scope of this work, but a first step towards such an analysis is investigated in this Section.

We assume that the jet energy scale and missing energy scales are well known, either from the analyses previously presented in this chapter, or from any other analysis. This allows us to introduce the top mass M_{top} as an extra free parameter in the fit, see also eq. (5.4). As in the previous studies, b-tagging is not included. The result is shown in Fig. 5.14 for events that fulfill the additional requirements from page 121. In the distribution the events are weighted with the χ^2 probability P, defined with 2 degrees of freedom.[13)] The background from W+jets events is comfortably small. To describe the peak of the distribution, we use a Gaussian shape as shown in the figure. The mean of the shape is 174.2 ± 0.75 GeV and the width amounts to 10.2 ± 1.2 GeV. The result is consistent with the input value of 175 GeV.

A dedicated study of the measurement of the top quark mass is presented in [117], where the width of the mass peak is optimized and b-tagging is included. The result of that study for the width of the top mass distribution is comparable to our result.

[12)] A variation of the *JES* with $\pm 12\%$ results in a 5% variation in the $\not{E}_T$ scale; with a systematic uncertainty of 2% as determined in Table 5.4, we can thus expect a $\not{E}_T$ scale variation of 1%.

[13)] Which is different from the function P in Fig. 5.4 with 3 degrees of freedom; the extra free parameter M_{top} 'costs' one degree of freedom.

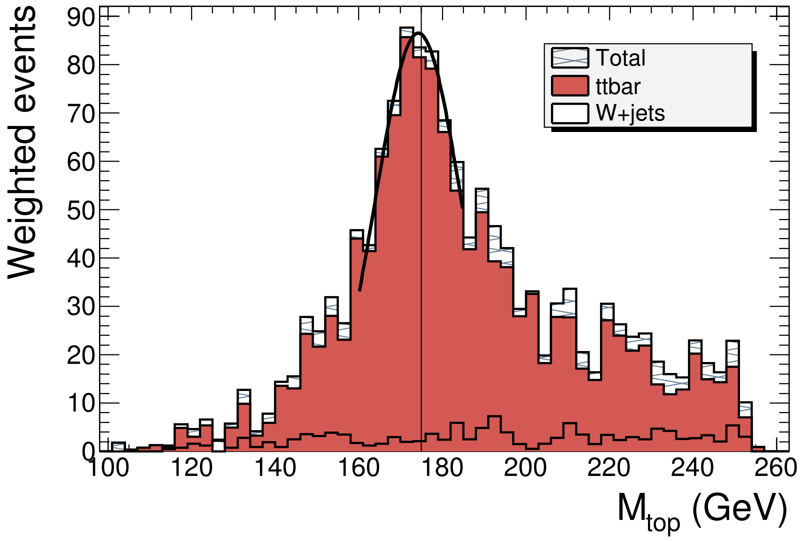

Figure 5.14: *The distribution of the fitted mass for the* W+*jets background, for* $t\bar{t}$ *events and for the total sample. The events are weighted with the* χ^2 *probability. The event selection includes the additional requirements from page 121. A Gaussian shape fitted to the 'Total' distribution is shown.*

5.7 Outline of the analysis using early data

Earlier in this chapter we have presented the 'scanning method' and the 'ΔP_T method' to extract the $\not{E}_T$ scale. The first turns out to be too sensitive to the JES, while the second results in a statistical uncertainty of 3% on a sample with a luminosity of 160 pb^{-1}; the systematic uncertainty is also estimated to be 3%. These methods depend on the knowledge of the JES, but in addition we have demonstrated that we can extract the JES to the level of 2% statistically. The largest systematic effect on the JES turned out to be the variation of 2% when the top quark mass is varied by 2.5 GeV. In this Section we describe the analysis to be performed on early data.

The first steps will be to establish jet energy corrections to the parton level with studies on γ/Z+jets events, see [110]. Assuming that the JES and $\not{E}_T$ scale are subsequently unknown to the level of at most 20%, we propose the following analysis.

1. The JES can be fitted using the scanning procedure to the level of 2% (statistically). This we have demonstrated also if the initial $\not{E}_T$ scale is offset by factors as large as 20%.

2. Now, the JES is known and consecutively the $\not{E}_T$ scale can be determined with the ΔP_T method to 3%. A check can be performed with the scanning method.

3. It may be necessary to repeat the first two steps a few times. Finally, the direct fit of the top quark mass should be made to check whether the used top quark mass is consistent with early data.

We have checked the proposed 'analysis-chain' on several $t\bar{t}$ event samples with modified energy scales and we observed that the input values are indeed successfully recovered. An example will now be described.

5.7.1 A realistic case study

We go through the details of one 'extreme case': we have prepared an event sample with a modified jet energy scale $1/JES = 1.11$ and a modified $\not{E}_T$ scale: $1/\not{E}_T$ scale $= 1.25$. Furthermore, we assume a $M_{top} = 172.5$ GeV in the kinematic fit constraints, although the sample is generated with a top mass of 175 GeV. The background W+jets events are included in this analysis.

Several iterations are needed to come to a stable result; the runs are summarized in Table 5.5. In run 1 the JES scan results in $JES = 1.12 \pm 0.02$. When multiplied with the true JES of 0.9 this leads to an effective result of 1.01±0.02. Using this measured value of the JES, the ΔP_T method in run 2 gives $\not{E}_T$ scale $= 1.30 \pm 0.03$, which leads to an effective $\not{E}_T$ scale of 1.04±0.03. As the calibration curve in Fig. 5.13 is not accurate in the lower and higher regions, we reiterate this method in run 3 with the newest value for $\not{E}_T$ scale; the effective result is 1.00 ± 0.03 for the $\not{E}_T$ scale. In run 4 the JES is again measured, resulting in 1.00 ± 0.02, which finally gives a value of 1.01 ± 0.03 for the $\not{E}_T$ scale in run 5. In these last two runs the energy scales hardly change, and we can conclude that a stable result is found. In run 6 the last step of the analysis chain is performed to measure the top quark mass, with a result of 174.1 ± 0.71 GeV.

These measurements show that the energy scales are correctly recovered and that the wrong input value for the top quark has almost no effect. Since the input values for the energy scales in run 6 coincide again with the 'true' values, the result for the top quark mass measurement is comparable to the measurement in Fig. 5.14. An offset of 2.5 GeV of the top quark mass is thus measurable in this case. If the fitting procedure is to be used for top quark mass measurements, more study is however needed to exactly quantify the correlation of the mass measurement with the energy scale determination, and to determine the accuracy with which the mass can be measured.

run	input JES	input $\not{E}_T$ scale	measured quantity	result	effective result
1	0.90	0.80	JES	1.12 ± 0.02	1.01 ± 0.02
2	1.01	0.80	$\not{E}_T$ scale	1.30 ± 0.03	1.04 ± 0.03
3	1.01	1.04	$\not{E}_T$ scale	0.96 ± 0.03	1.00 ± 0.03
4	1.01	1.00	JES	0.99 ± 0.02	1.00 ± 0.02
5	1.00	1.00	$\not{E}_T$ scale	1.01 ± 0.03	1.01 ± 0.03
6	1.00	1.01	M_{top}/GeV	174.1 ± 0.71	174.1 ± 0.71

Table 5.5: *Results of several steps of the analysis for the scenario true $JES = 0.9$ and true $\not{E}_T$ scale $= 0.8$ with $M_{top} = 172.5$ GeV in the kinematic fitting procedure. See text for more details.*

5.8 Conclusion and outlook

We presented the first results of a constrained kinematic fitting procedure on a semi-leptonic $t\bar{t}$ event sample of 160 pb^{-1}. As we aim for an analysis on early data, the possibility of applying b-tagging has not been used in this analysis. We focus on the measurement of the overall jet energy scale and the missing transverse energy scale.

Two methods to measure the scale of the $\not{E}_T$ are investigated: a scan of the χ^2 obtained from the kinematic fit as a function of the $\not{E}_T$ scale, and the ΔP_T method that is based on the momentum difference between the reconstructed top quarks. It turns out however that the $\not{E}_T$ scale can only be determined precisely when the overall JES is measured first. It is demonstrated that the JES can be accurately measured with a scanning procedure, and that consecutively, the $\not{E}_T$ scale can be best determined using the ΔP_T method. Preliminary studies show that a measurement of the top mass could be possible, but further study is needed to explore the correlations with the energy scale determinations.

For a follow up of this study we suggest the study of more systematic uncertainties. Especially the uncertainty on the MC prediction for the parton correction functions and for the offset in the calibration curve to obtain the $\not{E}_T$ scale from the ΔP_T distribution needs to be studied. Also the uncertainty due to the presence of more background events such as QCD events, or the underlying event or pile-up should be studied. The latter two event types are present ‘throughout’ the detector, thus possibly affecting both the missing transverse energy and the jet energy measurements.

5.9 Supersymmetric scenarios

In this section we study the possibility to use the kinematic fit as a further method, apart from kinematic cuts, to distinguish supersymmetry events from Standard Model $t\bar{t}$ events. In the experimental signature with one lepton in the final state, plus jets and missing transverse energy, the largest background to the supersymmetry signal events is expected to be $t\bar{t}$ and W+jets events, see [60], and the kinematic fitter could be used as a discriminating tool. To focus on the possibilities with early data we study the SU3 (bulk) and SU4 (low mass) models, see Section 1.3.4, with a data set corresponding to an integrated luminosity of 160 pb^{-1}.

5.9.1 Event selection

The MC samples used for the Standard Model channels are the same as mentioned earlier in this chapter, that is the W+jets and the $t\bar{t}$ samples. For the supersymmetry events we analyze the SU3 and SU4 samples generated with Isajet [118] plus HERWIG. All were reconstructed with ATHENA version 12.0.6. For the event selection requirements we use two different sets: the requirements as mentioned in Section 5.1, which we refer to as the 'top-cuts', and a set as defined in the study of [60], which we will refer to as the 'susy-cuts':

- Missing transverse energy $\not{E}_T > 100$ GeV.
- Exactly one isolated electron or muon with $p_T > 20$ GeV; no trigger selection.
- At least four jets with $p_T > 50$ GeV, of which at least one jet with $p_T > 100$ GeV.
- A transverse W boson mass $M_T > 100$ GeV. M_T is reconstructed from the lepton and the $\not{E}_T$ and, assuming the lepton to be massless, is defined by

$$M_T = \sqrt{2(p_T^{lep}\not{E}_T - \overrightarrow{p}_T^{lep} \cdot \overrightarrow{\not{E}_T})}. \tag{5.11}$$

These 'susy-cuts' requirements increase the signal to background ratio. In Table 5.6 the numbers of events selected from a sample of 160 pb^{-1} are listed after applying the top- or susy-cuts. For the latter the results with and without the $M_T > 100$ GeV requirement are given.

	W+jets	$t\bar{t}$	SU3	SU4
top-cuts	27×10^2	1.1×10^4	4.2×10^2	6.7×10^3
susy-cuts (excl. M_T cut)	1.0×10^2	6.0×10^2	2.2×10^2	1.8×10^3
susy-cuts (incl. M_T cut)	0.1×10^2	0.7×10^2	1.3×10^2	0.9×10^3

Table 5.6: *Number of events selected from the standard model samples W+jets and $t\bar{t}$, and from the supersymmetric scenario models SU3(bulk) and SU4(low mass), all normalized to an integrated luminosity of 160* pb^{-1}. *Two sets of selection requirements are used: the low energy 'top-cuts', see Section 5.1, and the 'susy-cuts', see text in present section. For the latter we state the results with and without the requirement on the transverse mass M_T.*

5.9.2 Best permutation χ^2

The setup of the minimization package and the χ^2 is as described in Section 5.2. We fit the events to the $t\bar{t}$ hypothesis. All mass constraints are implemented, the leptonic W mass constraint is used to calculate the p_z^ν and we only consider the permutation with the lowest χ^2. Since we were previously interested in the $t\bar{t}$ events we only considered the results if the fit had converged, had a $\chi^2 < 10$ and had a $m_{lep.W} < 80.7$ GeV. These three demands we leave out for the study in this section since we are interested in the supersymmetry events, which should not be fitable to a $t\bar{t}$ hypothesis.

In Figure 5.15 we present the χ^2 distributions for the different samples. The upper plot depicts the results with the top-cuts, the bottom left and right plots show the results with the susy-cuts, where the $M_T > 100$ GeV requirement is excluded and included respectively. We emphasize that the distributions are *non*-cumulative and that in the two lower plots the SU4 results have been scaled down by a factor of 3, to show more details on the remaining samples. With the top-cuts we observe that a large fraction of the $t\bar{t}$ events has $\log(\chi^2) \sim 1$, while at the same time there is a background of $t\bar{t}$ events which has $\log(\chi^2)$ up to ~ 3. This difference becomes more clear when we look at the results in the lower left figure with the susy-cuts, excluding the M_T cut: only a small fraction of the $t\bar{t}$ sample is correctly fitted and most of the $t\bar{t}$ events have a $\log(\chi^2) > 2$. From the difference between the lower left and right figure we conclude that the transverse mass requirement removes all $t\bar{t}$ events which were still 'correctly' fitted, with $\log(\chi^2) < 2$, and thus greatly reduces the $t\bar{t}$ and W+jets contributions.

From Fig. 5.4 and 5.6 we learn that of the matched $t\bar{t}$ events only a few have $\log(\chi^2) > 2$. It turns out that none of the $t\bar{t}$ events remaining after the susy-cuts have all four jets matched to the original partons. The conclusion we draw is that for these events either the lepton, the missing transverse energy or one of the jets is poorly reconstructed.

These results illustrate a major problem that occurs when analyzing $t\bar{t}$ as background to supersymmetry events: with the susy-cuts, be it with or without the M_T cut, a considerable amount of $t\bar{t}$ events remains in the selected sample[14)], and these events are difficult to tag as $t\bar{t}$. Comparing the $\log(\chi^2)$ distributions for the $t\bar{t}$ and the two supersymmetry samples it is difficult to use the χ^2 as a discriminating tool: removing all events with $\log(\chi^2) < 3$ does for example increase the signal to background ratio, yet if supersymmetry is to manifest itself in real data taken with ATLAS, the shape of the cumulative distribution of the χ^2 cannot be used. Both the $t\bar{t}$ and the supersymmetry samples have distributions peaking around $\log(\chi^2) \sim 3$, and the tail of a χ^2 is not a reliable observable to consider.

5.9.3 The fitted masses

We can gain more information by looking at the masses of the reconstructed top and W's. In Fig. 5.16 we show the distributions for the fitted hadronic top quark mass (upper plots) and the fitted hadronic W mass (bottom plots). The leptonic masses are correlated with these observables and we leave these out of consideration. In the figure we see left the cumulative results for a sample of 160 pb^{-1} with the supersymmetry SU3 sample included after the top-cuts. The right two plots are the results with SU4 included. Clearly with the top-cuts a large fraction of the selected $t\bar{t}$ events can be fitted to the expected values for the masses. The SU3

[14)] Although after the requirement of $M_T > 100$ GeV the ratio of supersymmetry events to $t\bar{t}$ events looks overwhelming, we emphasize that the SU3 and SU4 scenarios have relative high cross sections. Other supersymmetric models must be kept in mind and the remaining $t\bar{t}$ events after the susy-cuts are thus definitely non-negligible.

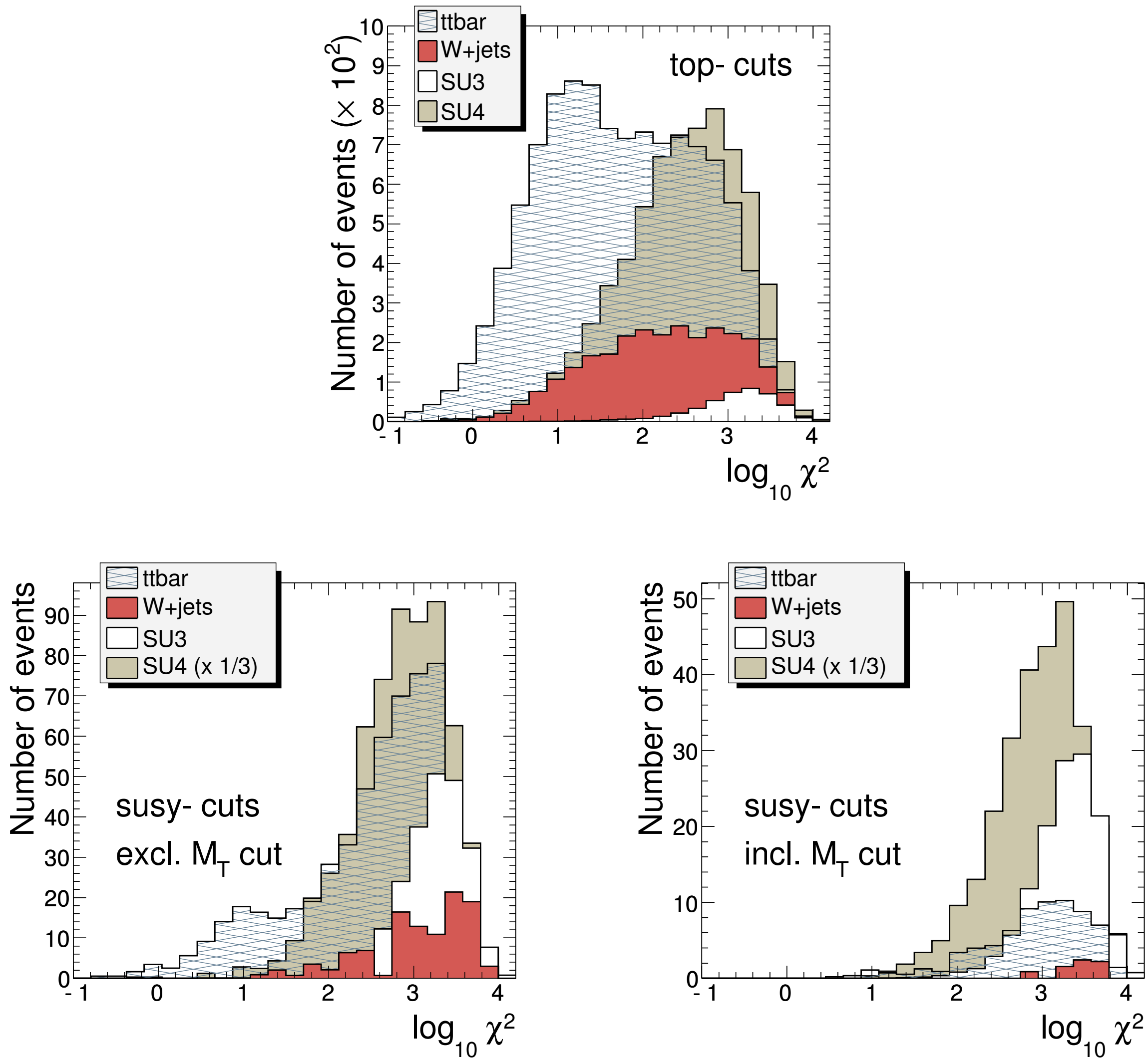

Figure 5.15: *The non-cumulative distributions of χ^2 for W+jets, $t\bar{t}$, SU3 and SU4 events for a sample of 160* pb^{-1}. *The upper results are with the top-cuts; the distributions for the W+jets and $t\bar{t}$ channels are equal to those in Fig. 5.6. Bottom left is with the susy-cuts excluding the $M_T > 100$ GeV requirement and bottom right is with the susy-cuts including this requirement. The distribution for SU4 in the two bottom plots has been scaled down by a factor of 3, to show more details on the remaining samples.*

contribution is almost too small to see, while the number of SU4 events is more substantial. Although not immediately clear from the plots, the results show that the supersymmetry events tend to have higher masses.

In Figure 5.17 we show the same results, with the susy-cuts applied, *excluding* the requirement of $M_T > 100$ GeV. This last cut reduces the number of events too much; we therefore leave it out to be able to better analyze the difference between the Standard Model and the supersymmetry events in a qualitative way. In the distribution for the top quark mass of the

$t\bar{t}$ sample we now observe a small peak at ~ 175 GeV on top of a broad $t\bar{t}$ background distribution. The SU3 events have a high mass, which we see reflected in their high χ^2 in Fig. 5.15. We also note that for SU3 events the distribution for the top mass is narrower and peaks around ~ 260 GeV. The supersymmetry events from the SU4 sample behave differently, in fact the distribution for these events resembles the $t\bar{t}$ background; their presence is however most pronounced from the large number of events. The results for the hadronic W mass are less pronounced, yet we see similar results: on average the SU3 events have a higher W mass and the distribution for the W mass for the SU4 events resembles that of the $t\bar{t}$ background. The high masses in the supersymmetry events are an indirect measurement of the mass of the pair of supersymmetric particles produced in the proton-proton interaction. This supersymmetry mass scale is related to the effective mass M_{eff} defined by

$$M_{\text{eff}} = \sum_{i=1}^{4} p_T^{jet,i} + p_T^{lep} + \not{E}_T, \tag{5.12}$$

see also [60]. In Fig. 5.18 the distributions for the fitted hadronic top mass vs the M_{eff} are depicted.

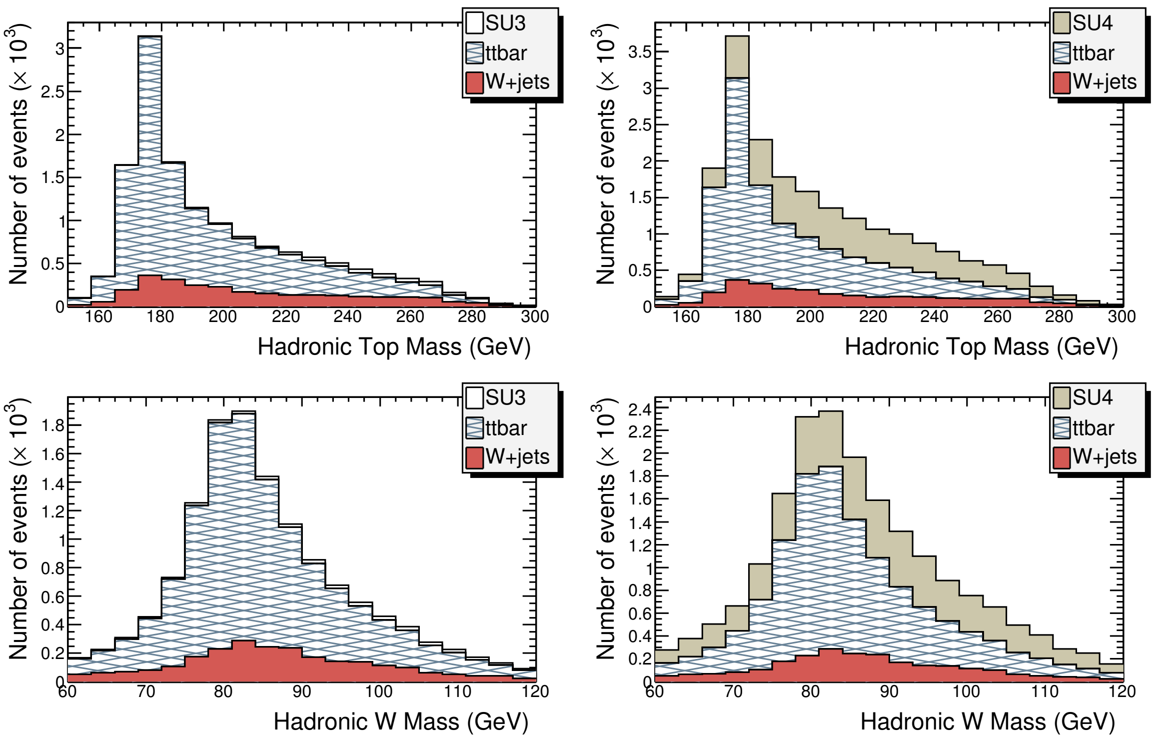

Figure 5.16: *Results for the fitted hadronic top mass (two top plots) and the fitted hadronic W mass (two bottom plots). Left are the distribution gained from a 160 pb*$^{-1}$ *sample after the top-cuts including the SU3 sample. Right are the same results including the SU4 sample.*

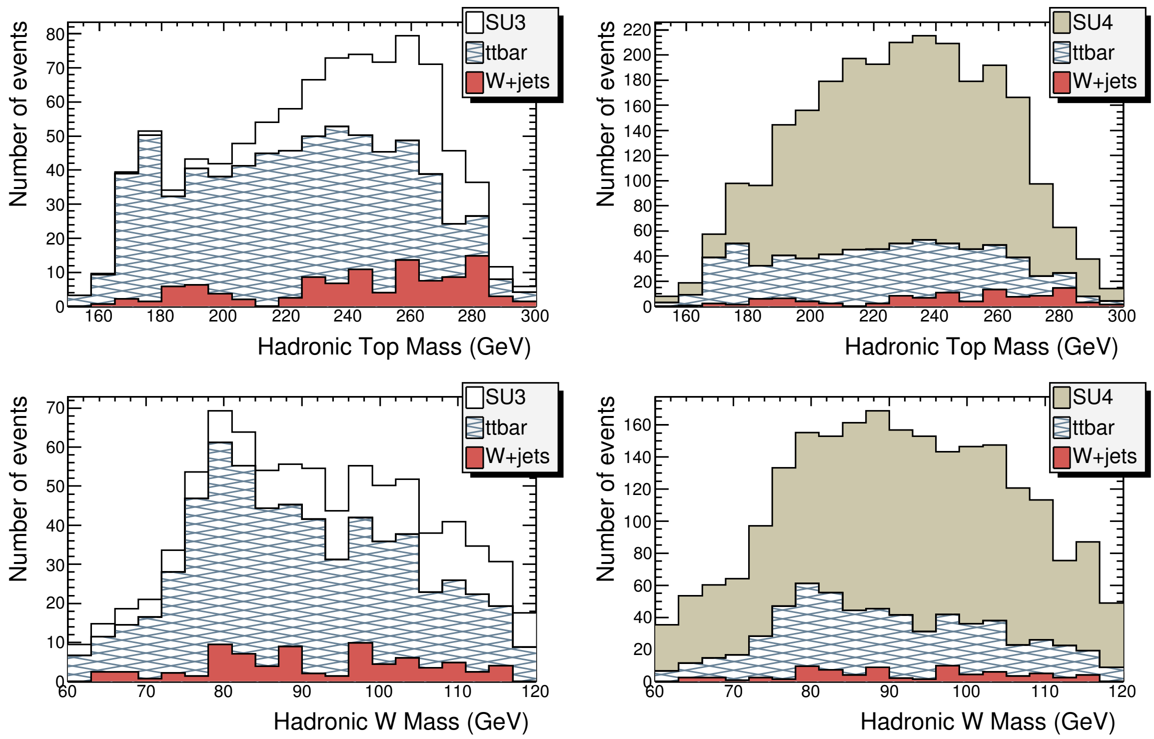

Figure 5.17: *Results for the fitted hadronic top mass (two top plots) and the fitted hadronic W mass (two bottom plots). Left are the distribution gained from a 160 pb^{-1} sample after the susy-cuts including the SU3 sample. Right are the same results including the SU4 sample.*

5.9.4 Conclusion

The conclusion we draw from these results is that the kinematic fit can be used to isolate a few remaining $t\bar{t}$ events which can be reconstructed, although these are also removed if the requirement of $M_T > 100$ GeV is used. A substantial background from the Standard Model events however remains after the susy-cuts. Isolating these is more difficult, yet with the mass constraints applied we can gain extra information: the expected mass distributions from the $t\bar{t}$ background are lower than those from the supersymmetry samples, especially those with high supersymmetry mass scale. This last conclusion does not alter when the requirement of $M_T > 100$ GeV is included.

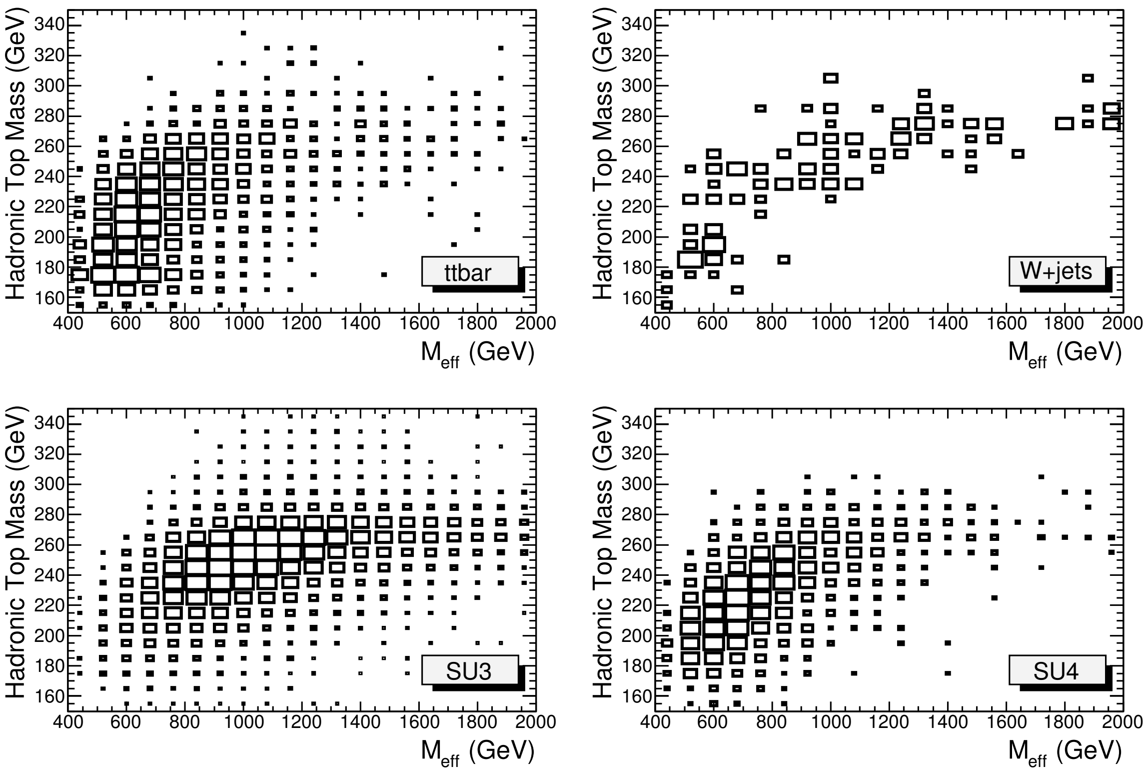

Figure 5.18: *The fitted hadronic top mass vs the M_{eff} for the four different samples analyzed. A correlation between the two observables is visible, and with M_{eff} relating to the M_{susy} scale the fitted top mass can thus give an indication of the M_{susy} scale of possible supersymmetric scenarios.*

Chapter 6

Top quark and W boson production cross section measurement

Most studies look into top quark pair events with at least four jets [116], as a semi-leptonic top quark pair decay leads to at least four partons. For the determination of the $t\bar{t}$ cross section we may gain more information by also measuring the number of top events with less than four reconstructed jets, since jets can be missed due to losses through the beam pipe or detector cracks, or due to mis-reconstruction, p_T requirements, etc... In this chapter we discuss such a method, making use of b-tagging algorithms, see Section 4.4. An accurate measurement of the $t\bar{t}$ cross section is important for the searches for new physics beyond the Standard Model, such as supersymmetry.

First, we explain the setup of the analysis and discuss all significant systematic uncertainties. Second, we apply the analysis to a sample with unknown cross sections of the different channels, and to a small sample of events with integrated luminosity of 50 pb^{-1}, to determine the possibilities with the first data to be taken with ATLAS. Finally we discuss the implication of supersymmetric scenarios and their effect on the analysis results.

6.1 The analysis setup

The purpose of this analysis is to measure the contribution of top quark pair and W boson production to events with 'low' jet multiplicities, that is events with four or less jets. Defining the $t\bar{t}$ channel as the signal channel, the main backgrounds are QCD multi-jets, W+jets, and single top events.[1)] With a b-tagger we can perform a counting measurement in which we count the number of events with one, two or three jets tagged. Since the top quark pair events have a different b-jet multiplicity than the background channels, the combination of the number of events tagged one, two or three times contains information on the amount of top quark pair events in the sample. We set as a goal to perform the analysis on first data with 50 pb^{-1} of integrated luminosity. It is widely assumed that due to imperfect alignment and calibration of the detector the b-tagging efficiency cannot be predicted from MC samples, see [101], and thus also needs to be determined.

For the events that contain exactly two jets, which we shall refer to as the two-jet sample, the number of events with one or two jets tagged can be determined. The number of zero tagged

1) See Sections 1.1.3 and 1.1.4. QCD multi-jet events are hard scatterings of $pp \to Xj$, with $X = 2,3,\ldots$ and are also simply called QCD events.

jets is completely correlated with these two measurements. For events that contain three or four jets we can determine the number of events with one, two or three tags. In total we thus perform eight measurements on our entire sample. There are not many events containing four jets in a data sample of $L = 50$ pb^{-1}, and we therefore also perform this analysis on only the total of the two- and three-jet samples.

With the eight numbers extracted from the data we can solve the five unknowns in our analysis, i.e. the number of $t\bar{t}$ events in the two-, three- and four-jet samples, and the two different b-tagging efficiencies: the efficiency for b-jets and the efficiency for light quark jets. For this last variable we must be careful as to what we call a light quark jet. In this analysis only the b-jets in top decays are categorized as b-jets. *All other jets* are categorized as light quark jets. This implies, however, that the light quark jets from W+jets events do not have the same composition as the light quark jets from top quark pair events: the latter have a substantial amount of s- and c-quarks coming from the hadronically decaying W. As the jets in the W+jets events are all initial state radiation (ISR) and/or final state radiation (FSR), see Section 1.1.4, these mostly originate from gluons or u- and d-quarks. We will measure the b-tagging efficiency on light quark jets in top events, but not in W events. The small contribution from $W+b\bar{b}$ events complicates this definition; we come back to this in section 6.1.4.

The standard b-tagging algorithm in ATLAS is the IP3D+SV1, a combined weight method mentioned in section 4.4. For the first data this is not suitable, for the same reason as mentioned before: the detector performance will not exactly be known, and a reliable calibration of the IP3D+SV1 b-tagger will take time. For the first data the JetProb algorithm is recommended, see Section 4.4.3. We have therefore used the IP3D+SV1 b-tagger for our study on the reliability of our analysis, and JetProb to show the feasibility of the analysis on first data.

6.1.1 Likelihood functions

To solve the five unknowns, i.e. the b-tagging efficiency on the b-jets (ε_b), the b-tagging efficiency on the light quark jets content of the top sample (ε_l^{top}) and the number of $t\bar{t}$ events in the two-, three- and four-jet samples, called $N_{2j}^{top}, N_{3j}^{top}$ and N_{4j}^{top}, we use RooFit [119] for the minimization of a negative log-likelihood (NLL), defined as follows:

$$-\ln L = -\ln \prod_{x,n} P(N_{nj}^{x\ tag,meas}, N_{nj}^{x\ tag}) \equiv -\ln \prod_{x,n} \frac{e^{-N_{nj}^{x\ tag}} \left(N_{nj}^{x\ tag}\right)^{N_{nj}^{x\ tag,meas}}}{N_{nj}^{x\ tag,meas}!}, \tag{6.1}$$

where $P(N_{nj}^{x\ tag,meas}, N_{nj}^{x\ tag})$ is the Poisson Likelihood of measuring $N_{nj}^{x\ tag,meas}$, that is the number of events with x jets b-tagged in the n-jet sample, when $N_{nj}^{x\ tag}$ events are expected.

For the expected numbers of tagged jets in the NLL we have to make some assumptions to keep the number of unknowns reasonable. We will explain these assumptions by discussing the expected numbers of tagged jets in the two-jet sample as an example: with N_{2j}^{1tag} and N_{2j}^{2tag} denoting the expected numbers of events with one and two jets tagged, we can write:

$$\begin{aligned} N_{2j}^{1tag} &= \varepsilon_1^W N_{2j}^W + \varepsilon_1^{top} N_{2j}^{top} && (6.2)\\ N_{2j}^{2tag} &= \varepsilon_2^W N_{2j}^W + \varepsilon_2^{top} N_{2j}^{top} && (6.3)\\ \text{with}\quad \varepsilon_1^W &= 2\varepsilon_l^W(1-\varepsilon_l^W) && (6.4)\\ \varepsilon_2^W &= (\varepsilon_l^W)^2. && (6.5) \end{aligned}$$

In the equations above we assume there are only two 'types of events': W events and top events. The assumption here is that single top events will be $t\bar{t}$ -like in their b-jet content, hence we sum up the contributions of both the single top and the top quark pair channels in events with exactly two jets to N_{2j}^{top}. The contribution to the number of W events with two jets, N_{2j}^{W}, comes of course from the W+jets events containing two jets. Other background channels, such as QCD multi-jets, might however also contribute to this number. The assumption is that QCD events have few b-jets and will be 'W+jets' like; we note that we do not analyze QCD events in this chapter and we will not check this last assumption.

We previously stated that we define all jets which are not b-jets as light quark jets. In eq. (6.4) and (6.5) the probability for having one or two jets tagged in a W+jets event, ε_1^W and ε_2^W, only depends on one variable ε_l^W. This b-tagging efficiency on the light quark jets content of the W+jets events is *not* a free variable in the fit and is to be measured elsewhere, see section 6.1.4.

For the contribution from the top events in eq. (6.2) and (6.3) we define the probabilities ε_1^{top} and ε_2^{top}

$$
\begin{aligned}
\varepsilon_1^{top} &= 2\varepsilon_l^{top}(1-\varepsilon_l^{top})R_{2j}^{0\ bJet} \\
&\quad + \left(\varepsilon_b\left(1-\varepsilon_l^{top}\right)+\varepsilon_l^{top}\left(1-\varepsilon_b\right)\right)R_{2j}^{1\ bJet} \\
&\quad +2\varepsilon_b(1-\varepsilon_b)R_{2j}^{2\ bJet} &\quad (6.6)\\
\varepsilon_2^{top} &= (\varepsilon_l^{top})^2 R_{2j}^{0\ bJet} + \varepsilon_b\varepsilon_l^{top}R_{2j}^{1\ bJet} + \varepsilon_b^2 R_{2j}^{2\ bJet}. &\quad (6.7)
\end{aligned}
$$

The b-tagging efficiency on the light quark jets content of the top sample ε_l^{top} is a free variable in the fit, together with the b-tagging efficiency on b-jets, ε_b. Due to c-jets in the top sample, $\varepsilon_l^{top} \neq \varepsilon_l^W$. A two-jet event can contain zero, one or two reconstructed b-jets, even before the b-tagging procedure. The probabilities for these three scenarios are given by $R_{2j}^{i\ bJet}$, with $i = 0,1,2$. These three probabilities are the fractions of events in the total $t\bar{t}$ two-jet sample with truly zero, one or two of the b-jets reconstructed and have to be determined by MC studies.

The exact sets of functions giving the expected numbers of tagged jets in the three- and four-jet sample are given in Appendix A. Only one more assumption is made for these last two samples: there are no events with three or more b-jets. In other words, we assume that the sum of the three fractions $R_{nj}^{i\ bJet}$ with $i = 0,1,2$ is equal to one in any jet multiplicity n. ISR and FSR can lead to more b-quarks in the event, yet the high uncertainty on their production rate has led us to keep our model simply based on the presence of two b-quarks in a $t\bar{t}$ event at Leading Order.

6.1.2 Trigger and Event Selection

For the event selection we have performed the standard event selection foreseen for early top quark pair analysis in the ATLAS collaboration [116]. Using the object definitions as mentioned in Section 4.6 the requirements are:

- Missing transverse energy $\not{E}_T > 20$ GeV.
- Exactly one isolated lepton, be it electron or muon, with $p_T > 20$ GeV. At the same time, the Event Filter trigger EF_e25i_medium1 must have passed if the lepton is an electron, or the trigger EF_mu20 must have passed if it is a muon.
- Jets must have a transverse momentum of $p_T > 40$ GeV. Events with two, three or four jets are accepted.

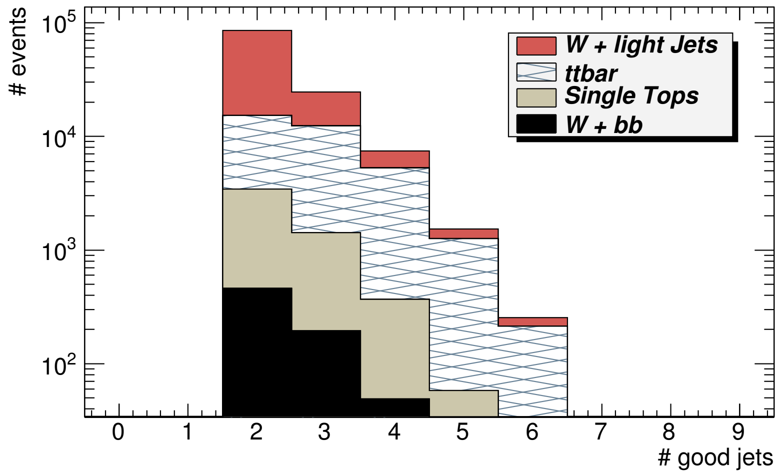

Figure 6.1: *Cumulative jet multiplicity after selecting one lepton (electron or muon) with $p_T > 20$ GeV and missing transverse energy of $\not{E}_T > 20$ GeV. A good jet is defined by $p_T > 40$ GeV. The distribution is normalized to an integrated luminosity of* 500 pb^{-1}*, and for the $t\bar{t}$ sample the events generated with MC@NLO are used.*

MC samples used

We have analyzed MC samples for pp collisions at a center-of-mass energy of 10 TeV. Throughout this chapter we refer to this data set as the MC08 data set.[2)] In Fig. 6.1 the jet multiplicity after the other selection requirements is depicted for the samples used in this chapter, that is:

- $t\bar{t}$ generated with MC@NLO, in combination with the Herwig showering algorithm, or $t\bar{t}$ generated with AcerMC, in combination with the Pythia showering algorithm. Both samples only contain the di-leptonic and semi-leptonic decays of the top quark pair, i.e. there are no all-hadronic $t\bar{t}$ decays. The cross sections, including the branching ratios, are $\sigma_{MC@NLO} = 217$ pb and $\sigma_{AcerMC} = 218$ pb. In Fig. 6.1 the MC@NLO sample is used.

- W+jets, generated with the Alpgen program, with zero up to five partons. The total cross section amounts to 48.5 nb.

- $W+b\bar{b}$, generated with the Alpgen program, with zero up to three additional partons. The total cross section amounts to 17.9 pb.

- Single top, generated with AcerMC. The Wt- (no all-hadronic decays) and the t-channel (only leptonic decays) are used. No s-channel sample was produced. The cross sections, including the branching ratios, are respectively $\sigma_{Wt} = 14.3$ pb and $\sigma_t = 43.2$ pb.

The quoted cross sections are to near-NNLO[3)]. That is, first a cross section is given by the generator: at NLO for the $t\bar{t}$ events generated with MC@NLO, and at Leading Order for the

[2)]The naming refers to the year 2008 in which all samples were generated and reconstructed.

[3)]The near-NNLO is based on the NLO completed with several corrections, see [120]. It is an approximation of the NNLO.

single top, the W boson and the AcerMC $t\bar{t}$ samples. Then, for all cross sections a correction factor (the K-factor) is subsequently applied to correct them to near-NNLO calculations. See also [27, 121].

From Fig. 6.1 it is clear that the W+jets events dominate in the two-jet sample, while in the four-jet sample the largest contribution is from $t\bar{t}$ events. The ratio of $(W+b\bar{b})/(W+$light jets) is approximately 0.01 for all jet multiplicities.

6.1.3 Fraction of b-jets in top quark pair events

The fractions $R_{nj}^{i\ bJet}$, with $i = 0, 1, 2$ and $n = 2, 3, 4$ are the expected fractions of top quark pair events with truly zero, one or two of the b-jets reconstructed (but before b-tagging is applied), in the two-, three- and four-jet samples. For the determination of these fractions from the MC samples the reconstructed jets have to be identified as coming from either one of the b-quarks. We emphasize that we do not take into account b-quarks originating from ISR or FSR.

The approach we have adopted for the matching is the following: first the momentum vector of the two b-quarks is extracted from the MC generator information. Second, the direction of each b-quark is compared to the directions of all reconstructed jets passing the selection requirements. A reconstructed jet is defined to be originating from a b-quark, if the opening angle $\Delta R = \sqrt{\Delta\phi^2 + \Delta\eta^2}$ between the jet and the b-quark is less than 0.2. Finally the number of matched b-quarks in each event is counted. In this final step it can happen that the two b-quarks in the event are matched to the same reconstructed jet. In this case, the event is labeled as having one b-quark reconstructed.

In Table 6.1 we list the fractions extracted from the total semi-leptonic $t\bar{t}$ sample available (MC@NLO sample), with an equivalent of 1665 pb^{-1} of integrated luminosity. We also list the fractions for samples with mis-calibrated jet energy scale (JES), i.e. the JES with an offset of either + or −10%.

$t\bar{t}$	$R_{2j}^{0\ bJet}$	$R_{2j}^{1\ bJet}$	$R_{2j}^{2\ bJet}$	$R_{3j}^{0\ bJet}$	$R_{3j}^{1\ bJet}$	$R_{3j}^{2\ bJet}$	$R_{4j}^{0\ bJet}$	$R_{4j}^{1\ bJet}$	$R_{4j}^{2\ bJet}$
$JES = 0.9$	15.6	59.0	25.3	6.80	43.7	49.5	3.75	35.0	61.2
$JES = 1.0$	15.4	59.2	25.4	6.75	43.1	50.2	3.65	33.7	62.6
$JES = 1.1$	15.3	58.8	25.9	6.57	42.9	50.5	3.75	33.0	63.2
Stat.error	±0.2	±0.4	±0.3	±0.1	±0.3	±0.4	±0.2	±0.5	±0.6

Table 6.1: *The $R_{2j}^{i\ bJet}$ fractions with correct and mis-calibrated JES, extracted from the semi-leptonic $t\bar{t}$ sample, given in percentages. A factor JES = 1.1 means that the jet energy is scaled 10% too high and thus more jets pass the selection cut.*

There is a small influence of the JES on the number of matched b-jets. In Section 6.2.1 we study the systematic uncertainty as a consequence of different $R_{nj}^{i\ bJet}$ fractions; in Section 6.2.2 we study the consequences of mis-calibrated energy scales.

A last difficulty, which we however cannot quantify, is the possibility that a jet is not matched to a b-quark, even though it follows the hadronization of one of the initial b-quarks. In the approach adopted in the calculation of the fractions $R_{nj}^{i\ bJet}$ this jet is counted as a light quark jet. Although this could affect the analysis, we note that as the jet is poorly reconstructed (its direction is off compared to the initial b-quark's direction), the performance of the b-tagging algorithm will probably also be far from ideal.

Fraction of b-jets in AcerMC top quark pair events

For the systematic uncertainty study we will also analyze the effect of using a different $t\bar{t}$ generator: AcerMC. In Table 6.2 the fractions for both samples are summarized and we observe that in the MC@NLO sample on average the events have more b-jets reconstructed. The difference between the two samples is definitely non-negligible. In [93, 122] the different

	$R_{2j}^{0\ bJet}$	$R_{2j}^{1\ bJet}$	$R_{2j}^{2\ bJet}$	$R_{3j}^{0\ bJet}$	$R_{3j}^{1\ bJet}$	$R_{3j}^{2\ bJet}$	$R_{4j}^{0\ bJet}$	$R_{4j}^{1\ bJet}$	$R_{4j}^{2\ bJet}$
MC@NLO	15.4	59.2	25.4	6.75	43.1	50.2	3.65	33.7	62.6
AcerMC	17.5	60.4	22.1	8.16	45.4	46.5	6.00	37.8	56.2

Table 6.2: *The $R_{nj}^{i\ bJet}$ fractions for MC@NLO and AcerMC samples for $n = 2,3,4$ and $i = 0,1,2$. The differences between the two samples are larger than the statistical errors, which are of the order of the errors listed in Table 6.1.*

showering programs used for the two samples are shown to cause a discrepancy in the event jet multiplicity. We will use the difference between the sets of $R_{nj}^{i\ bJet}$ fractions to study the effective systematic uncertainty in Section 6.2.1.

Fraction of b-jets in single top events

The NLO cross sections for the different single top production channels at the LHC are summarized in Table 1.2 on page 11. The s-channel results at LO in two b-quarks, the two other channels can only result in two b-quarks at NLO. By analyzing the MC generator information in the events, we can extract the $R_{nj}^{i\ bJet}$ fractions for the selected single top events. As we stated in Section 6.1.2 there are no s-channel simulations from AcerMC available at center-of-mass energy of 10 TeV.

From the available single top samples we extract the fractions as summarized in Table 6.3. It is clear that less b-jets are reconstructed in single top events than in $t\bar{t}$ events. There are however far less single top events than $t\bar{t}$ events, making the differences between the $R_{nj}^{i\ bJet}$ for the single top sample and the $R_{nj}^{i\ bJet}$ for the $t\bar{t}$ sample less relevant. We will quantify this in Section 6.1.5.

single top	$R_{2j}^{0\ bJet}$	$R_{2j}^{1\ bJet}$	$R_{2j}^{2\ bJet}$	$R_{3j}^{0\ bJet}$	$R_{3j}^{1\ bJet}$	$R_{3j}^{2\ bJet}$	$R_{4j}^{0\ bJet}$	$R_{4j}^{1\ bJet}$	$R_{4j}^{2\ bJet}$
t-channel	15.4	72.7	11.9	10.5	56.6	32.9	10.0	44.8	45.2
Wt-channel	25.1	69.9	5.00	14.1	68.9	17.0	12.3	53.5	34.2
Total	18.9	71.6	9.50	11.7	60.0	28.3	10.6	47.2	42.2
	$\pm$0.8	$\pm$1.5	$\pm$0.6	$\pm$0.9	$\pm$2.1	$\pm$1.4	$\pm$1.8	$\pm$3.9	$\pm$3.7

Table 6.3: *The $R_{nj}^{i\ bJet}$ fractions extracted from the available single top samples for $n = 2,3,4$ and $i = 0,1,2$, given in percentages.*

6.1.4 Extracting the b-tagging efficiency for W+jets from Z+jets events

Figure 6.2 depicts the ε_l^W distribution for the W+jets samples with two, three and four jets. Above is the result of the IP3D+SV1 b-tagger, below of the JetProb b-tagger. The efficiencies for the three samples are similar in most of the b-tagger weight ranges. In our analysis we will use a weighted average of the ε_l^W for the two- and three jet sample. This choice was made for two reasons: first, to have the same ε_l^W-distribution in the analyses including and excluding the four-jet sample. Second, the average was taken to prevent ending up with an efficiency on the three jet sample based on too few events.

The small differences visible in each plot of Fig. 6.2 between the efficiencies for the three samples are negligible: the differences are of the order of the statistical uncertainty on the

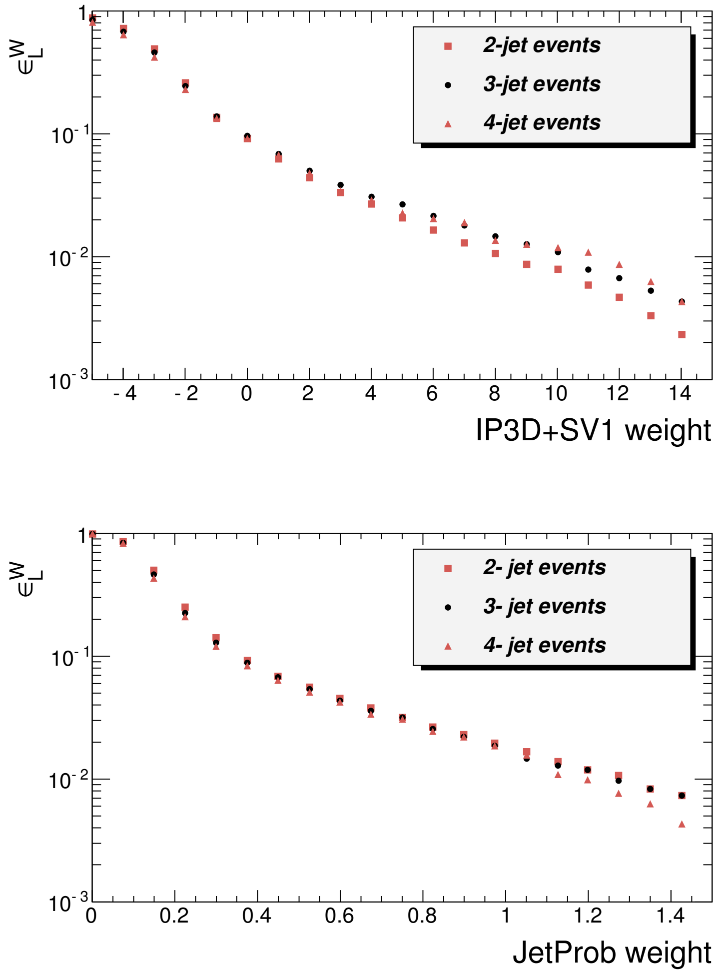

Figure 6.2: *The ε_l^W for the two-, three- and four-jet sample as extracted from the MC generator information of the W+jets samples, after the event selection requirements of Section 6.1.2. All available W+jets events are used, including W+$b\bar{b}$, corresponding to approximately $L =$* 150 pb^{-1}. *Above are the distributions for the IP3D+SV1 b-tagger, below for the JetProb b-tagger.*

efficiencies (not depicted in the figures).

The b-tagging efficiency ε_l^W is an input to the analysis in this chapter; it must be measured on the data before the analysis can be performed. As stated before, we have labeled all jets in the W+jets sample as 'light quark jets', including those from $W+b\bar{b}$ events. For this latter contamination of our light quark jet sample not to be a problem in the determination of ε_l^W, we must measure the b-tagging efficiency on a sample of events with a jet content resembling that of the expected W+jets sample. The approach we have adopted is to measure ε_l^W from Z+jets events, i.e. events with exactly *two leptons*.

With a leptonic decay of either bosons the jets present in a W- or Z+jets event are all ISR and/or FSR. If the contamination from additional b-jets is also similar in the two samples, a clean sample of Z+jets events could thus be used to measure the b-tagging efficiency ε_l^W. From Section 1.1.4 we already know that this is not exactly the case: the ratio of $Z+b\bar{b}$ to Z+jets is approximately four times larger than the ratio $W+b\bar{b}$ to W+jets.

We now explain how the efficiency can be extracted from the first 50 pb^{-1} of data, selecting Z+jets events with two leptons.

Two-lepton event selection

To show that the b-tagging efficiency is similar on W- and Z-events, we analyze the 10 TeV center-of-mass energy Z+light quark jets samples. We emphasize that we do not study any $Z+b\bar{b}$ events. To select the two-lepton Z-events to be as similar as possible to the one-lepton W-events in our analysis, the $\not{E}_T$ requirement is simply replaced by an extra lepton. That is, events are selected with exactly two electrons or two muons, with $p_T > 20$ GeV; no selection on charges, and no $\not{E}_T$ requirement.[4)] To prevent biases introduced by the trigger, the same trigger is used on the Z-events.

With a two-lepton selection, the sample consists mostly of Z+jets and $t\bar{t}$ events, see [123].

[4)]This one-to-one replacement is not entirely correct. First, the acceptances of the leptons and of the neutrino are not the same. Second, the p_T distribution of the neutrino is not the same as that of the electron or muon in a W decay.

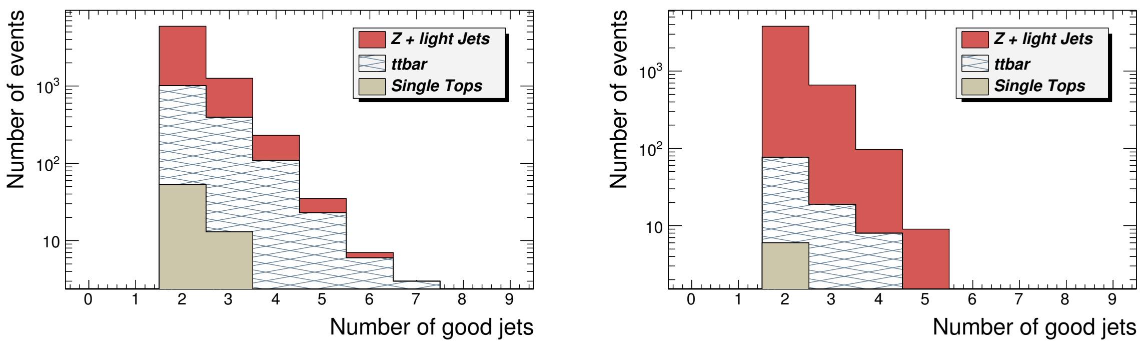

(a) Two leptons with $p_T > 20$ GeV, no $\not{E}_T$ cut.

(b) Same as (a), with an extra requirement of $|M_{ll} - M_Z| < 5.0$ GeV.

Figure 6.3: *Jet multiplicity for events with* <u>*exactly two leptons*</u> *in a sample of* 500 pb^{-1}. *See text for details on event selection.*

In Fig.6.3(a) the cumulative jet multiplicity is depicted after our two-lepton requirements for the Z+jets, $t\bar{t}$ and single top samples of 500 pb^{-1}. The contribution from top events can be reduced with an extra requirement of $|M_{ll} - M_Z| < 5.0$ GeV, where M_{ll} is the invariant mass of the two leptons. Figure 6.3(b) depicts the jet multiplicity distributions after this extra requirement: most of the top events are removed, while the amount of Z-events is reduced by only $\sim 1/3$. Extrapolating this to a first data sample of 50 pb^{-1} would give us ~ 500 Z-events to measure the b-tagging efficiency.

Extracting ε_l^W from ε_l^Z

For the measurement of the b-tagging efficiency we only use the average of the two- and three-jet samples. In Fig. 6.4(a) and 6.4(b) the results are shown for respectively the combined IP3D+SV1 b-tagger and the JetProb b-tagger. The black distribution is the efficiency on the selected W-events (that is with the one lepton and $\not{E}_T$ cut). This is the efficiency needed in our analysis. The 'stars'-distribution is the efficiency for all events with exactly two leptons.[5)] For both b-taggers, and especially IP3D+SV1, the b-tagging efficiency is higher on the two-lepton sample. This is caused by the many top events present, as shown with Fig. 6.3(a).

With the extra requirement of $|M_{ll} - M_Z| < 5.0$ GeV on the two-lepton sample most of the top events are removed. In Fig. 6.4(a) and 6.4(b) the gray distributions (with error-bars) show the results after this extra requirement on samples with integrated luminosity of 50 pb^{-1}; the uncertainties shown are statistical. The conclusion is that even with not more than approximately 500 Z+jets events with two leptons a meaningful b-tagging efficiency can be extrapolated. In Fig. 6.5 the exact b-tagging efficiency for only the Z+jets sample is again shown and we see that it is almost a perfect match with the ε_l^W.

Uncertainty on the b-tagging efficiency

One problem remains, that is the possibility of contamination of the Z+jets events with Z+$b\bar{b}$. In Section 1.1.4 we listed the cross sections of W- and Z+$b\bar{b}$ with leptonic decay. From the same section we can deduce that the ratio of Z+$b\bar{b}$ to Z+jets is approximately four times larger than the ratio W+$b\bar{b}$ to W+jets. Unfortunately ATLAS has not produced a Z+$b\bar{b}$ sample at 10 TeV at the time of writing of this thesis; to measure the possible offset for ε_l^W we have therefore calculated the b-tagging efficiency on a sample of W+jets including a sample of W+$b\bar{b}$ four times too large or four times too small. The result is depicted in Fig. 6.6, where the offset of the gray distributions compared to the upper/lower error-bars is the offset caused by too many/few W+$b\bar{b}$ events. These two outer distributions will be used in Section 6.4.2 to determine the uncertainty on the fit results as a consequence of the uncertainty on ε_l^W due to b-jets in the Z+jets sample.

At a later stage the ratios of W+$b\bar{b}$ to W+jets and Z+$b\bar{b}$ to Z+jets will probably be measured by ATLAS. These measurements should be used to validate the analysis presented in this chapter.

The study presented in this section has shown that ε_l^W can be extracted from two-lepton events. In the remaining studies in this chapter the true number of tagged jets in the W+jets events is used to define ε_l^W.

---

5) Both the black and the stars-distributions are measured on all available events to increase the number of selected events.

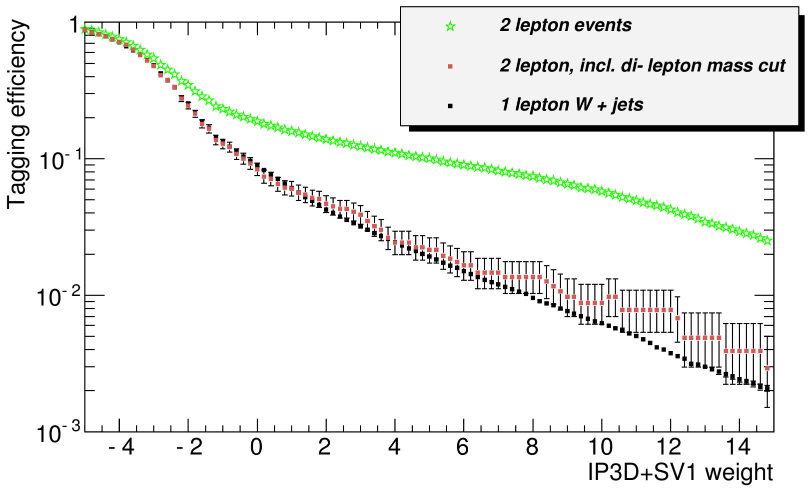

(a)

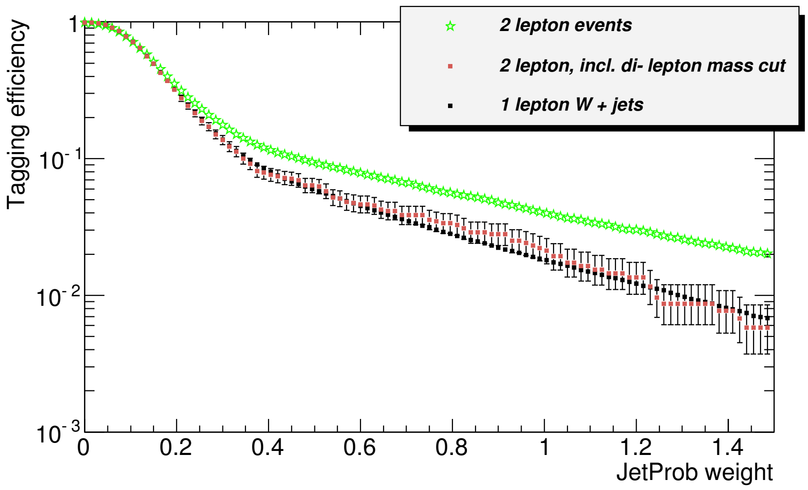

(b)

Figure 6.4: *B-tagging efficiencies with the IP3D+SV1 b-tagger (a) and the JetProb b-tagger (b). Black: IP3D+SV1 efficiency on the W + light quark jets, i.e. one-lepton events. Stars: IP3D+SV1 efficiency on all events with two leptons. Gray with error-bars: same as stars, with extra requirement* $|M_{ll} - M_Z| < 5.0$ *GeV, sample of* 50 pb^{-1}. *The figures show how in the two-lepton channel a simple requirement on the di-lepton invariant mass reduces the b-tagging efficiency on the present jets to the b-tagging efficiency on the one-lepton W+jets events.*

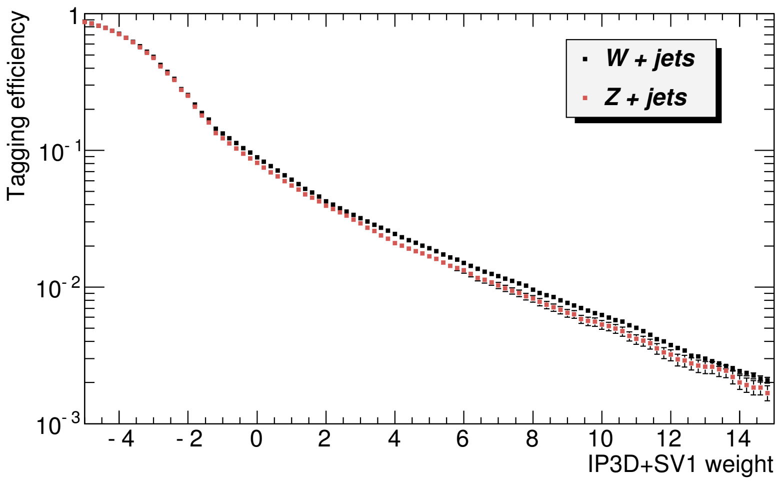

Figure 6.5: *Black: IP3D+SV1 efficiency on the W + light quark jets events with one lepton (the errors are too small to see). Gray: IP3D+SV1 efficiency on Z + light quark jets events with two leptons. Both are calculated on a sample of* 150 pb^{-1}. *No background channels are included. The results show how the b-tagging efficiency on the pure W- and Z+jets samples almost coincide; the difference is less than the statistical uncertainty at* 50 pb^{-1} *in Fig. 6.4(a).*

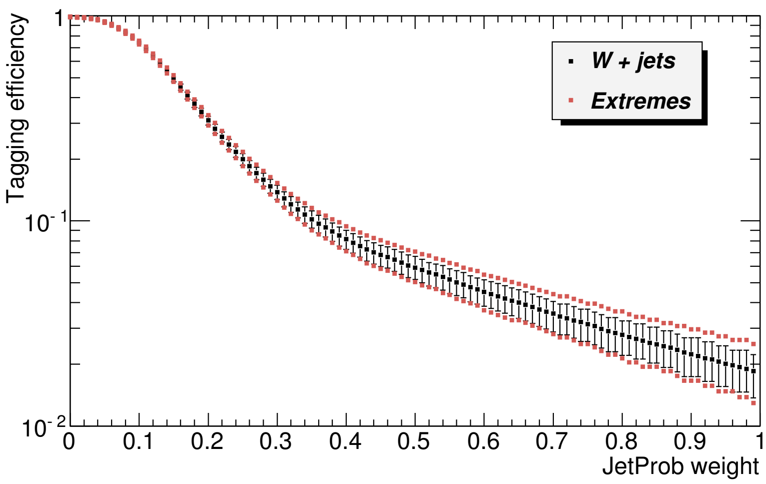

Figure 6.6: *B-tagging efficiency on the W+jets sample with the JetProb b-tagger. The black distribution is the efficiency on W+jets events (incl. $W+b\bar{b}$). The uncertainty of this black distribution is calculated from a sample of $5 \cdot 10^2$ events to estimate the statistical error to be expected from an analysis on* 50 pb^{-1} *Z+jets sample with two leptons. The upper/lower gray distribution is again the efficiency on the W+jets sample. This is calculated with the $W+b\bar{b}$ contribution scaled up/down by a factor of 4, <u>and also includes</u> the upper/lower fluctuation of the statistical uncertainty shown in black. These two extreme distributions will be used later on in this chapter.*

6.1.5 Results on a large sample

In this section we show how a set of solutions is extracted. A large sample of events with $L = 500$ pb^{-1} is used to reduce the statistical uncertainty, except for the W+jets sample, for which the results have been scaled up from approximately 150 pb^{-1}. Performing a scan over a large range of the IP3D+SV1 b-tagger weights, the results are the five distributions as shown in Fig. 6.7.

Definition: The #top is defined as the sum of $t\bar{t}$ and single top events and will be used as such throughout this chapter.

In the results for the #top/#total fits in Fig. 6.7 we see a clear plateau over a large range in the b-tag weight, corresponding to a large range in ε_b. As the same sample is used in each of the 100 fits at different weights, the results in each of the five distributions are correlated. To extract one value from these fits, we must therefore chose one specific weight. Throughout this chapter we state the results at a IP3D+SV1 weight of 4.0, as this is usually the point halfway the plateau.

At this weight the ε_l^{top} is 0.05, while ε_b is still at 0.64. Higher weights reduce the ε_b faster than the ε_l^{top}, reducing the discriminating power of the b-tagger and effectively decreasing the degree of freedom in the maximization of the likelihood. This effect is visible for weights above ~ 10, for which the results are less accurate. At lower weights the plateau can extend down to a weight of ~ -2.0, below which the ε_l^{top} increases rapidly. With more and more jets tagged, the number of events with one tag reaches zero, effectively again decreasing the degree of freedom in the analysis. Below a weight of ~ -2.0 the analysis therefore does not result in sensible measurements.

The conclusion is that over a large range of the b-tagger weight the analysis finds a stable solution and the analysis is thus almost independent of the choice of b-tagging efficiency.

Table 6.4 lists the number of events of each of the sub-samples selected and the #top/#total ratios that should be expected. The fitted #top/#total stated in the Table are extracted from Fig. 6.7 at a IP3D+SV1 weight of 4.0. Here we see that the single top events are fitted as tops: the fitted #tops corresponds to the true #tops, defined as the sum of $t\bar{t}$ plus single top events. The conclusion can thus be drawn that the differences between the $R_{nj}^{i\ bJet}$ fractions for the single top sample and those for the $t\bar{t}$ sample, as mentioned in Section 6.1.3, are of little importance.

	$t\bar{t}$ (MC@NLO)	Single top	W+jets (incl. W+$b\bar{b}$)	True #top/#total	Fitted #top/#total
2 jet sample	$1.20 \cdot 10^4$	$3.05 \cdot 10^3$	$7.07 \cdot 10^4$	0.17	0.17 ± 0.005
3 jet sample	$1.10 \cdot 10^4$	$1.31 \cdot 10^3$	$1.23 \cdot 10^4$	0.50	0.51 ± 0.01
4 jet sample	$4.81 \cdot 10^3$	313	$2.25 \cdot 10^3$	0.70	0.70 ± 0.02

Table 6.4: *The number of events with 2,3 or 4 jets passing the selection cuts. An integrated luminosity of* 500 pb^{-1} *is used for each sub-sample. The fitted #top/#total are extracted from Fig. 6.7 at a IP3D+SV1 weight of 4.0.*

	True efficiency	Fitted efficiency
ε_b	0.630 ± 0.003	0.638 ± 0.011
ε_l^{top}	0.053 ± 0.001	0.037 ± 0.004
ε_l^{W}	0.027 ± 0.0004	-

Table 6.5: *The b-tagging efficiencies on the b-jets in the $t\bar{t}$ sample, on the light quark jets in the $t\bar{t}$ sample and on the jets in the W+jets sample. The latter is shown for comparison only. The fitted efficiencies are extracted from Fig. 6.7 at a IP3D+SV1 weight of 4.0. The fitted ε_b agrees with the true value within the statistical uncertainty, the fitted ε_l^{top} is too low. See text for more details.*

In Table 6.5 the fit results for ε_b and ε_l^{top} at a IP3D+SV1 weight of 4.0 can be compared to the true values for the efficiencies. The fitted ε_b agrees with the true value within the statistical uncertainty. As can also be seen in Fig. 6.7(a), the fitted ε_l^{top} is significantly lower than the true value. During this research we have not found any specific observable which has an influence on the ε_l^{top} only, nor have we found any sign that the offset propagates in a mis-measurement of the #top/#total ratios.

As the other measurements do correspond with the expected values, the small offset of ε_l^{top} might imply that the likelihood functions as constructed in Section 6.1.1 are not completely accurate: in Section 4.4.3 it was discussed how the b-tagging efficiencies depend on the jet transverse momentum, yet in the likelihood functions this is not taken into account. Although this negligence might be the reason for the offset of ε_l^{top}, it is not important. The offset is small, and all other measurements work well.

The overall conclusion is that, within the statistical uncertainty on the fit, the results are a non-biased match of the values for #top/#total with the true ratios and an accurate measurement of the b-tagging efficiency on b-jets, over a large range of the efficiencies.

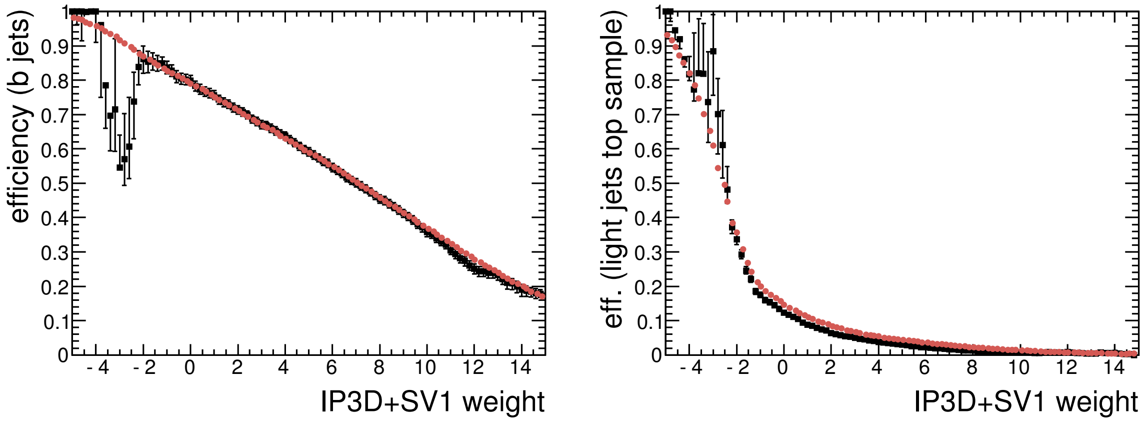

(a) Left: results for ε_b. Right: results for ε_l^{top}. The distribution with error-bars is the fit result, the distribution without is the true efficiency for the used sample.

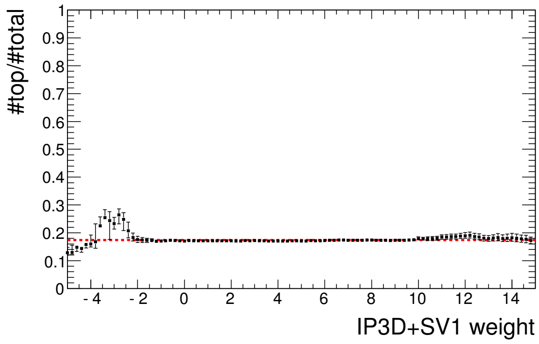

(b) Ratio of $top/total$ for events with 2 jets.

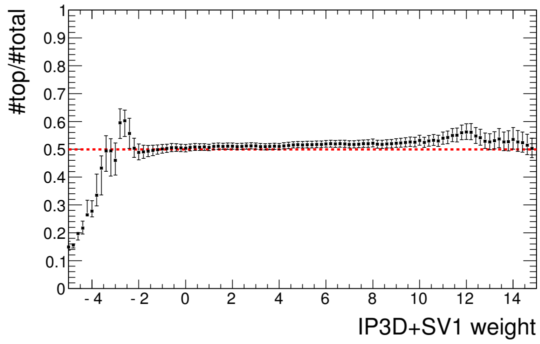

(c) Ratio of $top/total$ for events with 3 jets.

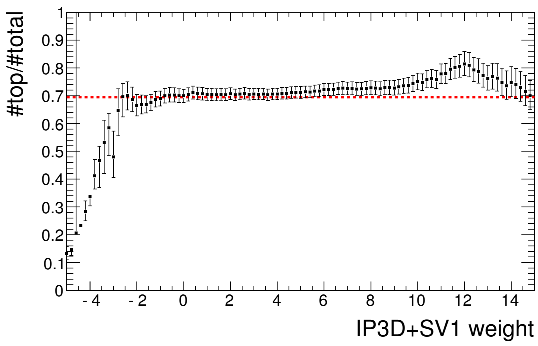

(d) Ratio of $top/total$ for events with 4 jets.

Figure 6.7: *Fit result for a sample with integrated luminosity of* 500 pb^{-1}, *where IP3D+SV1 is used as b-tagger. All results correspond with the expected values, except for a small offset in the fit of* ε_l^{top}. *The correct values for the ratio fits are depicted by dotted lines.*

6.2 Systematic uncertainties

In this section we discuss the systematic uncertainties present in our analysis. The best performing b-tagger is used in order to get a good estimate of the size of the uncertainties.

6.2.1 The expected fraction of b-jets

In Section 6.1.3 we explained the $R_{nj}^{i\ bJet}$ fractions and showed their values in top samples from different MC generators. For a study of the systematic uncertainty due to variations in these values we have chosen to apply the fractions obtained from the AcerMC sample on a 500 pb^{-1} sample containing $t\bar{t}$ events from MC@NLO, and vice-versa.

	True #top/#total	Fitted #top/#total $R_{nj}^{i\ bJet}$ from AcerMC	Fitted #top/#total $R_{nj}^{i\ bJet}$ from MC@NLO
2 jet sample	0.17	0.17 ± 0.005	0.17 ± 0.005
3 jet sample	0.50	0.50 ± 0.01	0.51 ± 0.01
4 jet sample	0.70	0.71 ± 0.02	0.70 ± 0.02

Table 6.6: *The fitted #top/#total ratios with the $R_{nj}^{i\ bJet}$ fractions from two different $t\bar{t}$ samples applied on a sample containing $t\bar{t}$ events from MC@NLO.*

	True #top/#total	Fitted #top/#total $R_{nj}^{i\ bJet}$ from AcerMC	Fitted #top/#total $R_{nj}^{i\ bJet}$ from MC@NLO
2 jet sample	0.17	0.17 ± 0.005	0.17 ± 0.005
3 jet sample	0.52	0.53 ± 0.01	0.54 ± 0.01
4 jet sample	0.74	0.75 ± 0.02	0.75 ± 0.02

Table 6.7: *The fitted #top/#total ratios with the $R_{nj}^{i\ bJet}$ fractions from two different $t\bar{t}$ samples applied on a sample containing $t\bar{t}$ events from AcerMC.*

The results are summarized in Table 6.6 and 6.7, where we observe that the effect is minimal: *within* each table the differences between AcerMC and MC@NLO are not more than 1% in the three- and four-jet samples. No effect is visible for the results in the two-jet sample. The differences *between* the two tables listed are another systematic effect, which is discussed in Section 6.2.3.

The results for the fitted values of the b-tagging efficiencies ε_b and ε_l^{top} show no systematic effect and are in agreement with the results stated in section 6.1.5.

We note that the systematic uncertainty due to variations in values of the $R_{nj}^{i\ bJet}$ fractions does not have to be identical when a different b-tagging algorithm is used. Yet we will use these results when applying the JetProb algorithm, for the simple reason that a similar study to obtain the uncertainty with the JetProb b-tagger remains inconclusive. The performance of JetProb is worse and the small uncertainty is not measurable.

6.2.2 Energy scale variations

We have studied independently two energy scales subject to mis-calibration: the Jet Energy Scale (*JES*) and the $\not{E}_T$ scale. The two are however correlated. If for example we select an event with only one jet, with the direction of the $\not{E}_T$ opposite to the jet direction, and the jet energy is measured with an offset of +10%, the missing transverse energy is also measured with an offset of approximately +10%. The correlation is not exactly 100%, as there are some out-of-cluster effects, see Section 4.5.1, but to first approximation the correlation is very high.

In our studies of the *JES* we have adjusted the jet energies with +10% and -10%, while at the same time adjusting the $\not{E}_T$ such that the vectorial sum of all jets+$\not{E}_T$ stays constant. These steps are of course taken before the event selection. In our studies of the $\not{E}_T$ scale we only adjust the $\not{E}_T$, again with +10% and -10%. [6] The changes have no effect on the stability of the fits. Although the $R^{i\ bJet}_{nj}$ fractions used are slightly off in the mis-calibrated samples, see Table 6.1, we know from Section 6.2.1 that this effect is negligible.

In Table 6.8 we state the effect of *JES* offsets on the fitted #tops and #W, in Table 6.9 the results are listed with $\not{E}_T$ scale offsets. For clarity: with a $JES = 1.1$ we mean that the jet energies have been scaled up. As the selection of jets stays at $p_T > 40$ GeV, this results in more jets passing the cut. A similar reasoning goes for $\not{E}_T$ scale = 1.1, etc... As the energy scale offsets alter the absolute number of events selected, the tables list the absolute number of tops and W fitted; the total number of events is of course the sum of both. The changes compared to the fitted number of events in Table 6.4 are given in percentages. The fitted number of events agree well with the true values of the selected events in each channel.

	Fitted #tops ($JES = 1.1$)	Fitted #W ($JES = 1.1$)	Fitted #tops ($JES = 0.9$)	Fitted #W ($JES = 0.9$)
2 jet sample	14.1(−4.3%)	83.8(+18.1%)	15.3(+3.6%)	58.9(−17.0%)
3 jet sample	13.8(+10.1%)	14.9(+24.2%)	10.9(−12.7%)	8.93(−25.7%)
4 jet sample	6.45(+25.0%)	2.76(+25.6%)	3.96(−23.2%)	1.54(−30.0%)

Table 6.8: *Results for the fitted #tops and #W* ($\times 10^3$) *with jet energy over-calibrated (JES=1.1) and under-calibrated (JES=0.9). The changes compared to the fitted number of events in Table 6.4 are given in percentages.*

	Fitted #tops ($\not{E}_T$ scale = 1.1)	Fitted #W ($\not{E}_T$ scale = 1.1)	Fitted #tops ($\not{E}_T$ scale = 0.9)	Fitted #W ($\not{E}_T$ scale = 0.9)
2 jet sample	15.0(+1.4%)	73.0(+2.8%)	14.4(−2.1%)	68.1(−4.1%)
3 jet sample	12.8(+1.9%)	12.3(+2.0%)	12.1(−3.0%)	11.6(−3.0%)
4 jet sample	5.32(+3.0%)	2.22(+1.0%)	5.12(−1.0%)	2.09(−5.1%)

Table 6.9: *Results for the fitted #tops and #W* ($\times 10^3$) *with* $\not{E}_T$ *over-calibrated* ($\not{E}_T$ *scale=1.1) and under-calibrated* ($\not{E}_T$ *scale=0.9).*

[6] This is in fact an overestimation, as the $\not{E}_T$ scale is correlated to the *JES*.

In Table 6.10 the results are listed for the b-tagging efficiencies with JES- and $\not{E}_T$ scale offsets. Although the absolute number of events selected showed large changes with the energy scale offsets, the efficiencies are almost not affected. Within the statistical uncertainties the results correspond with those in Table 6.5.

	True efficiency ($JES = 1.1$)	Fitted efficiency ($JES = 1.1$)	True efficiency ($JES = 0.9$)	Fitted efficiency ($JES = 0.9$)
ε_b	0.626 ± 0.002	0.627 ± 0.011	0.635 ± 0.003	0.626 ± 0.013
ε_l^{top}	0.052 ± 0.001	0.039 ± 0.004	0.056 ± 0.002	0.040 ± 0.005
ε_l^W	0.026 ± 0.0003	-	0.028 ± 0.0004	-

	True efficiency ($\not{E}_T$ scale $= 1.1$)	Fitted efficiency ($\not{E}_T$ scale $= 1.1$)	True efficiency ($\not{E}_T$ scale $= 0.9$)	Fitted efficiency ($\not{E}_T$ scale $= 0.9$)
ε_b	0.630 ± 0.003	0.637 ± 0.011	0.629 ± 0.003	0.635 ± 0.011
ε_l^{top}	0.053 ± 0.001	0.037 ± 0.004	0.054 ± 0.001	0.038 ± 0.004
ε_l^W	0.027 ± 0.0004	-	0.027 ± 0.0004	-

Table 6.10: *Results for the b-tagging efficiencies with jet energy over-calibrated (JES=1.1) and under-calibrated (JES=0.9), and with $\not{E}_T$ over-calibrated ($\not{E}_T$ scale=1.1) and under-calibrated ($\not{E}_T$ scale=0.9).*

6.2.3 The expected total number of events

In Table 6.4 results are given with the $t\bar{t}$ events generated by MC@NLO. The change which occurs in the number of $t\bar{t}$ events selected when an AcerMC sample is used, is shown in Table 6.11. In fact it is not the difference in generators which results in the discrepancies, it is the showering procedure after the generation which is the cause: the same effect was measured in [93]. For more details we refer to [122], with the comment that this work was performed on MC samples generated in an earlier version of Athena (version 12). Similar studies on newer MC samples are in progress. For the final measurement of the number of top and the number of W events in Section 6.4.3 we will use the average of the measurements in Table 6.11, and assign half of the differences as systematic uncertainties.

The uncertainty expected on the total number of events also depends on the uncertainty on the measurement of the luminosity. In [29] it is explained that the luminosity initially can be measured to an accuracy of $\sim 20\%$, which ultimately should improve to $\sim 5\%$.

	AcerMC	MC@NLO
2 jet sample	11.8	12.0
3 jet sample	12.2	11.0
4 jet sample	6.08	4.81

Table 6.11: *The number of $t\bar{t}$ events ($\times 10^3$) selected from an AcerMC and from a MC@NLO sample, both normalized to an integrated luminosity of* $500\ \text{pb}^{-1}$.

6.2.4 Discussion

We have studied most of the systematic uncertainties important for our analysis. One uncertainty we could not quantify: the uncertainty on the expected number of W+jets events, which has been calculated so far only by looking at Alpgen samples. Unfortunately we do not have immediate access to enough events from other generators to check systematic effects on W+jets events, but the effect could be as high as 50% on the expected number of events in the four-jet sample, see [116]. The uncertainty on the expected number of single top events is also not accounted for, although its low value compared to the expected number of $t\bar{t}$ events makes this uncertainty less important.

With a good overview of the performance of the analysis we now first show how it can be applied to measure the cross sections for $t\bar{t}$, single top and W+jets in a sample with known sub-samples, yet unknown cross sections. In Section 6.4 we continue with a small sample of 50 pb^{-1} and we implement the systematic uncertainties.

6.3 Analysis of a 'blind' mixed sample

As to check that the analysis presented does not run into problems if for example the yield of the W+jets events is varied without changing the $t\bar{t}$ normalization, we apply the analysis to a 'blind' mixed sample.

This Mixed sample was generated into a Egamma-, Muon- and a Jet-stream for the ATLAS collaboration, see also 2.6.3. In this section only the Muon-stream is used, i.e. events triggered by the muon trigger. The sample has an integrated luminosity of 146 pb^{-1}. Before starting the exercise, the list of sub-samples in the mix is:

- $t\bar{t}$ generated with AcerMC, in combination with the Pythia showering algorithm.
- W+jets generated with Alpgen, with between two and five additional partons.
- Single top generated with AcerMC; only the Wt- and t-channel.

This resembles closely the samples mentioned in Section 6.1.2, except that no $W+b\bar{b}$ is used. We have applied our analysis to this Mixed sample, as if it were the real unknown data from ATLAS. To make a sensible comparison with MC-results, we cannot compare these to the results in the previous sections, as these did contain the $W+b\bar{b}$. We therefore have rerun the analysis on a new MC-sample, with the same sub-samples as present in the Mixed sample. Throughout the rest of this section we refer to this sample as the MC08 sample. As a test, we do compare the results on MC08 containing $t\bar{t}$ from MC@NLO, and on MC08 containing $t\bar{t}$ from AcerMC.

6.3.1 Mixed sample results

Figure 6.8 shows the fit results of the analysis on the Mixed muon-stream using the IP3D+SV1 b-tagger and using the $R^{i\ bJet}_{nj}$ fractions from MC@NLO in the maximization of the likelihood functions. As in Fig. 6.7(a) the ε^{top}_{l} has a visible offset. From the discussion on the results in Section 6.1.5 we conclude that this is no reason for concern and that the measured #top/#total ratios are unbiased.

Measuring the ratios again at a weight of 4.0, we obtain for the number of tops and the number of W's the results as listed in Table 6.12. Performing the same steps on MC08, with the

	Total # events	Fitted #tops	Fitted #W
2 jet sample	17.2	2.49 ± 0.17	14.7 ± 0.17
3 jet sample	4.78	2.32 ± 0.12	2.46 ± 0.12
4 jet sample	1.52	1.07 ± 0.08	0.46 ± 0.08
TOTAL	23.5	5.87 ± 0.22	17.6 ± 0.22

Table 6.12: *The results* $(\times 10^3)$ *for the fitted #tops and #W on the selected events in the Mixed sample muon-stream. The* $R^{i\ bJet}_{nj}$ *fractions from MC@NLO are used in the likelihood functions.*

	Total # events	Fitted #tops	Fitted #W
2 jet sample	15.0	2.53 ± 0.08	12.4 ± 0.08
3 jet sample	4.23	2.14 ± 0.04	2.10 ± 0.04
4 jet sample	1.28	0.90 ± 0.03	0.39 ± 0.03
TOTAL	20.5	5.57 ± 0.09	14.9 ± 0.09

Table 6.13: *The results* $(\times 10^3)$ *for the fitted #tops and #W on MC08, containing* $t\bar{t}$ *generated by MC@NLO. These values are obtained by using all available events and scaling the samples to* 146 pb^{-1}*; the statistical uncertainties are thus smaller compared to those in Table 6.12. The* $R^{i\ bJet}_{nj}$ *fractions from MC@NLO are used in the likelihood functions.*

$t\bar{t}$ events generated by MC@NLO, the results in Table 6.13 are obtained. For an extraction of the cross section of the W+jets we can now simply compare the total number of measured W events in the Mixed sample to the number of W events in MC08, resulting in

$$\sigma^W_{Mix} = \frac{(1.76 \pm 0.02) \cdot 10^4}{1.49 \cdot 10^4} \cdot \sigma^W_{MC} = (1.18 \pm 0.02) \cdot \sigma^W_{MC} \tag{6.8}$$

For the calculation of the cross sections of the $t\bar{t}$ and of the single top events we use the measurements of the fitted number of tops in the two- and three-jet samples. Defining the factors

$$\begin{aligned} f_{t\bar{t}} &= \sigma^{t\bar{t}}_{Mix} / \sigma^{t\bar{t}}_{MC} \\ f_{sT} &= \sigma^{singleTop}_{Mix} / \sigma^{singleTop}_{MC} \end{aligned} \tag{6.9}$$

we can solve these two factors from the two equations

$$f_{t\bar{t}}(N^{tops}_{MC,2j} - N^{singleTops}_{2j}) + f_{sT}(N^{tops}_{MC,2j} - N^{t\bar{t}}_{2j}) = N^{tops}_{Mix,2j} \tag{6.10}$$

$$f_{t\bar{t}}(N^{tops}_{MC,3j} - N^{singleTops}_{3j}) + f_{sT}(N^{tops}_{MC,2j} - N^{t\bar{t}}_{2j}) = N^{tops}_{Mix,3j}. \tag{6.11}$$

The variables $N^{tops}_{Mix,XX}$ are the fitted number of tops in the Mixed sample, in the two- or three jet sample. $N^{t\bar{t}}_{XX}$ is the *true* number of $t\bar{t}$ in MC08 (the same holds for $N^{singleTops}_{XX}$), while $N^{tops}_{MC,XX}$ is the *fitted* number of tops in MC08. Although no bias is measured in the fitted ratios so far, this setup ensures that any possible bias is accounted for when measuring on real data. The end result is:

$$\begin{aligned} \sigma^{t\bar{t}}_{Mix} &= (1.24 \pm 0.13) \cdot \sigma^{t\bar{t}}_{MC} \\ \sigma^{singleTops}_{Mix} &= (0.00 \pm 0.60) \cdot \sigma^{singleTops}_{MC}. \end{aligned} \tag{6.12}$$

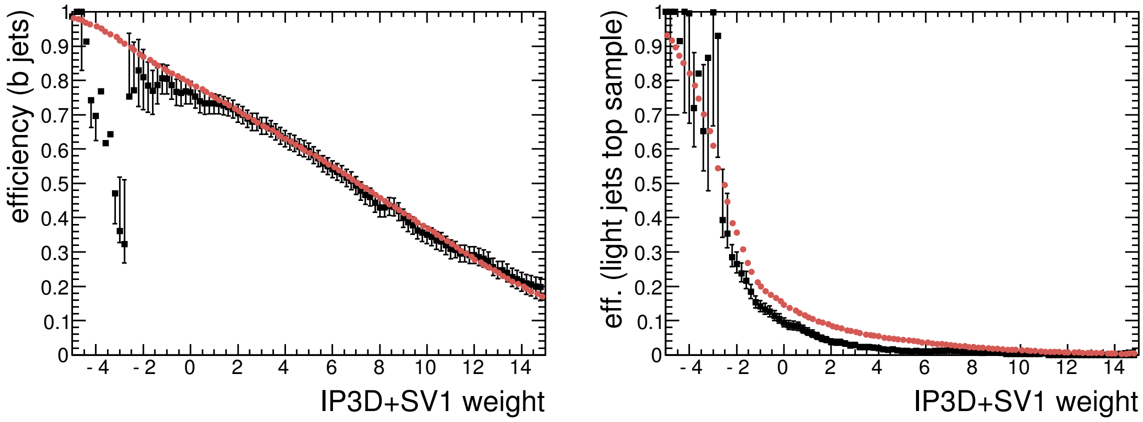

(a) Left: results for ε_b. Right: results for ε_l^{top}. The distribution with error-bars is the fit result, the distribution without is the true efficiency when using $t\bar{t}$ events generated by MC@NLO.

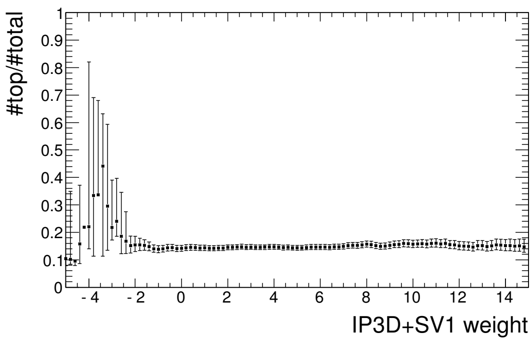

(b) Ratio of $top/total$ for events with 2 jets.

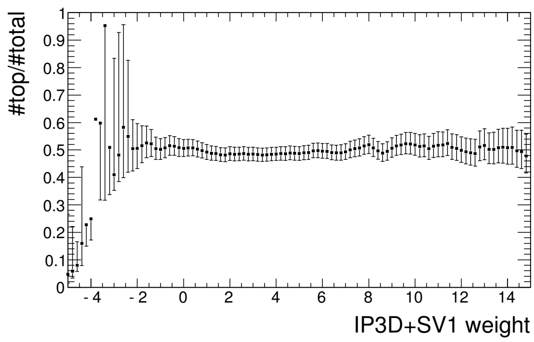

(c) Ratio of $top/total$ for events with 3 jets.

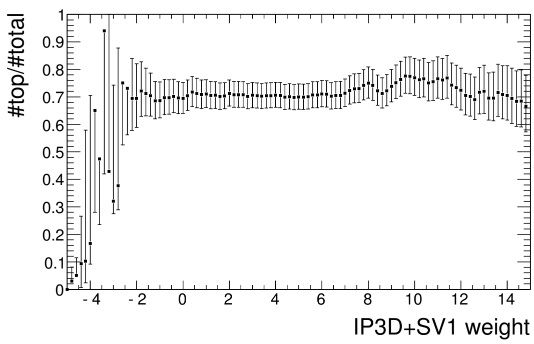

(d) Ratio of $top/total$ for events with 4 jets.

Figure 6.8: *Fit results for the Mixed sample (muon stream) with* $L = 146$ pb^{-1}. *The IP3D+SV1 is used as b-tagger, and the* $R_{nj}^{i\ bJet}$ *fractions are extracted from the MC@NLO sample.*

	Total # events	Fitted #tops	Fitted #W
2 jet sample	14.9	2.52 ± 0.08	12.4 ± 0.08
3 jet sample	4.42	2.37 ± 0.04	2.06 ± 0.04
4 jet sample	1.49	1.10 ± 0.03	0.39 ± 0.03
TOTAL	20.8	5.99 ± 0.10	14.8 ± 0.10

Table 6.14: *The results* $(\times 10^3)$ *for the fitted #tops and #W on MC08, containing $t\bar{t}$ generated by AcerMC. These values are obtained by using all available events and scaling the samples to* 146 pb^{-1}*; the statistical uncertainties are thus negligible compared to those in Table 6.12. The $R_{nj}^{i\,bJet}$ fractions from MC@NLO are used in the likelihood functions.*

For a determination of the cross sections in the Mixed sample we do not have to take into account any of the systematic uncertainties mentioned in Section 6.2, as we have used the same sub-samples in the Mixed sample and in MC08, except for the $t\bar{t}$ events: we used the $t\bar{t}$ from MC@NLO instead of the $t\bar{t}$ from AcerMC.

If we apply the analysis on MC08 with $t\bar{t}$ events from AcerMC, while keeping the $R_{nj}^{i\,bJet}$ fractions from the MC@NLO sample, we can immediately compare the new results (summarized in Table 6.14) with Table 6.12. The end result is

$$\begin{aligned} \sigma_{Mix}^{W} &= (1.19 \pm 0.02) \cdot \sigma_{MC}^{W} \\ \sigma_{Mix}^{t\bar{t}} &= (1.00 \pm 0.10) \cdot \sigma_{MC}^{t\bar{t}} \\ \sigma_{Mix}^{singleTops} &= (0.90 \pm 0.47) \cdot \sigma_{MC}^{singleTops}. \end{aligned} \tag{6.13}$$

The b-tagging efficiencies

The fit results for the b-tagging efficiencies in Fig. 6.8 are as expected: the ε_b is fitted as 0.63 ± 0.02 and corresponds with the true value of 0.63 obtained from MC@NLO $t\bar{t}$ events, see Table 6.5. The ε_l^{top} is fitted as 0.02 ± 0.01 and is lower than the true value of 0.05 obtained from MC@NLO $t\bar{t}$ events. This last discrepancy is not the result of using different MC generators, but a bias we observed earlier.

6.3.2 Discussion

To emphasize the importance of accurate MC predictions, we performed the analysis with MC@NLO $t\bar{t}$ events and with Alpgen $t\bar{t}$ events. The results in eq. (6.12) and eq. (6.13) show a large difference, in effect resulting in a significant systematic uncertainty in the analysis. In the next section we will quantify this more accurately.

The correct values for the cross sections in this 'blind' sample study are obtained with the Alpgen sample, that is the values in eq. (6.13). The study shows that a variation of the cross sections can be measured; the W cross section is measured with the highest accuracy.

6.4 Early data analysis

In this section we study the possible results on a first data sample of 50 pb^{-1}. For clarity, the selection of events with electrons is again applied and the $W+b\bar{b}$ sample is again included in our MC set of samples.

JetProb is the recommended b-tagger for first data. It is a much simpler and more robust algorithm, with the drawback that its performance is worse compared to a (calibrated) IP3D+SV1, see Fig. 4.12. We observe this again in Fig. 6.9 which shows the results of the analysis performed on a sample of 500 pb^{-1}. On the horizontal axis $-\log_{10} P$ is plotted, where P is the probability output of the b-tagger. The probability range is chosen such that the same ε_b range is covered as was the case with the IP3D+SV1 b-tagger. Compared to Fig. 6.7 where the latter is used, the results are worse: the efficiencies show more fluctuation and the distributions for the ratios have less clear plateaus.

Looking at the results for the four-jet events, which have the largest uncertainties, we conclude that with the JetProb b-tagger the best weight to use is in the range $\sim 0.4 - 0.7$. Within the given fit uncertainties the results are in agreement with the expected values from Table 6.4 (depicted with the dotted lines); only the results in the four jet sample in Fig. 6.9(d) are more than '1-sigma' off. Figure 6.10 depicts the results on a sample of no more than 50 pb^{-1}. These results do show a correct fit for the ratio in the four jet sample.

6.4.1 Excluding the four-jet sample

In Fig. 6.9(d) the results in the four jet sample show a more than '1 sigma' offset compared with the expected value from Table 6.4, and in Fig. 6.10(d) the results in the four jet sample show a large uncertainty; it is worth checking whether the measurements in the four jet sample improve the analysis, or worse, whether the measurements do not bias the results in the two and three jet sample. As the latter are more important, the analysis can be repeated excluding the measurements on the four jet sample. This implies only five measurements are used in the likelihood discussed in Section 6.1.1 to solve four unknowns: the two efficiencies, and the number of top events in the two- and three jet samples.

We performed such an analysis on a 50 pb^{-1} sample and the conclusion is that no difference is visible with the previous results; using larger samples or the IP3D+SV1 b-tagger does not alter this conclusion. The three extra measurements in the four jet sample thus give too little information to influence the fit results in the two and three jet sample, yet can be used to estimate the number of tops and W's in the four jet sample.

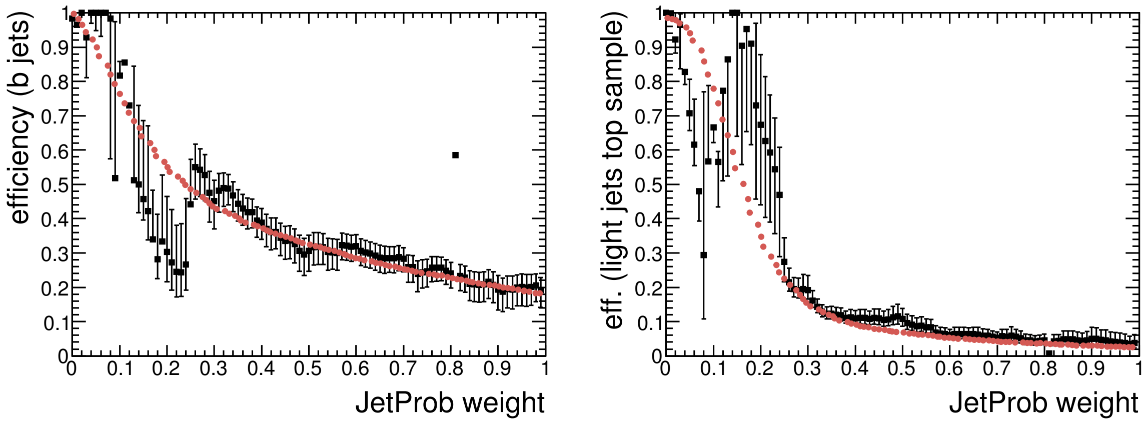

(a) Left: results for ε_b. Right: results for ε_l^{top}. The distribution with error-bars is the fit result, the distribution without is the true efficiency for the used sample.

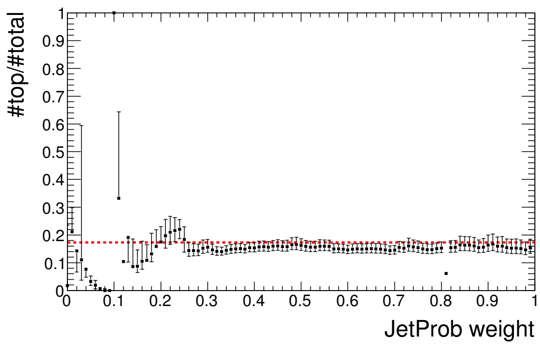

(b) Ratio of $top/total$ for events with 2 jets.

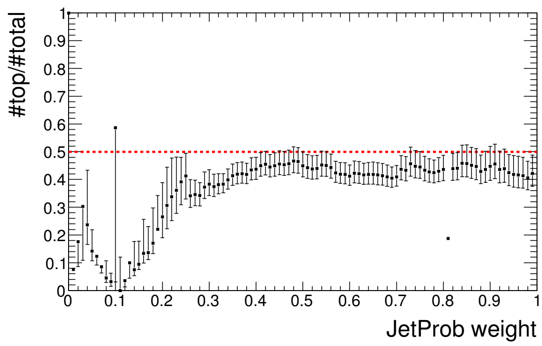

(c) Ratio of $top/total$ for events with 3 jets.

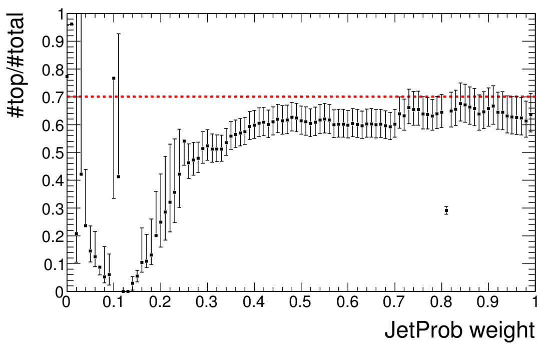

(d) Ratio of $top/total$ for events with 4 jets.

Figure 6.9: *Fit result for a sample with* $L = 500$ pb^{-1}. *JetProb is used as b-tagger. Compared to the results in Fig. 6.7 with IP3D+SV1 as b-tagger, these results show more fluctuations. Also, the fitted ratios show larger deviations from the true values (from Table 6.4), depicted by the dotted lines.*

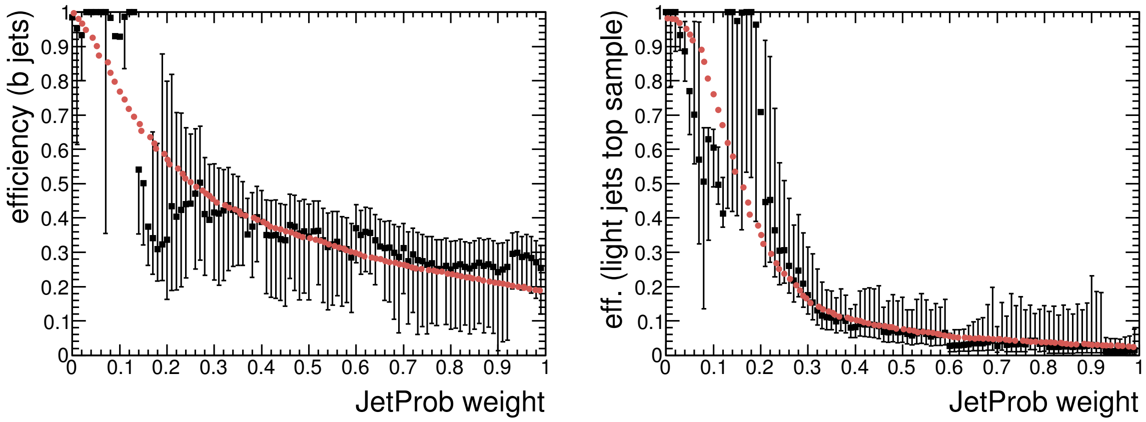

(a) Left: results for ε_b. Right: results for ε_l^{top}. The distribution with error-bars is the fit result, the distribution without is the true efficiency for the used sample.

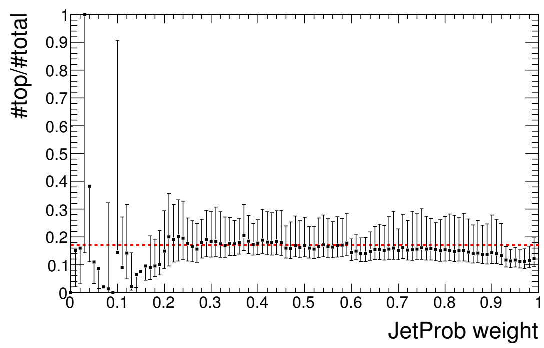

(b) Ratio of $top/total$ for events with 2 jets.

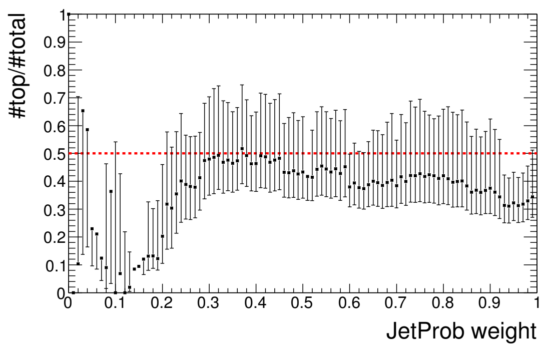

(c) Ratio of $top/total$ for events with 3 jets.

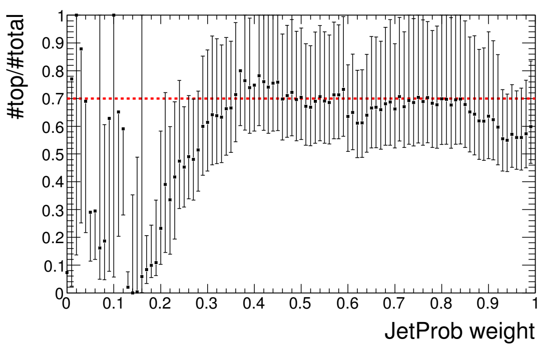

(d) Ratio of $top/total$ for events with 4 jets.

Figure 6.10: *Fit result for a sample with integrated luminosity of* 50 pb^{-1}. *JetProb is used as b-tagger. The correct values for the ratio fits are depicted by dotted lines.*

6.4.2 Uncertainty on the b-tagging efficiency on W+jets

Before extracting the cross sections from the results on the 50 pb^{-1} sample, the uncertainty on the b-tagging efficiency on W+jets still has to be taken into account. In Section 6.1.4 an upper and lower limit on ε_l^W was estimated by taking into account the difference between the W- and Z+jets cross sections, plus the statistical fluctuations expected from a 50 pb^{-1} sample of Z+jets events. The results for the upper and lower limits were shown in Fig. 6.6.

Repeating the analysis on a first data sample of 50 pb^{-1} with these extreme distributions for ε_l^W the fit results at a JetProb weight of 0.5 in Table 6.15 are obtained. We observe that compared to the 'nominal' results in the distributions in Fig. 6.10 a too low value for ε_l^W increases the fitted number of top events, while at the same time decreases the ε_b and increases the ε_l^{top}. A too high value for ε_l^W has the opposite effect.

We conclude that the uncertainty on ε_l^W results in errors on the fitted #top/#total with sizes of 9%, 12% and 13%, respectively for the two, three and four jet sample. For the b-tagging efficiencies the systematic uncertainty is ± 0.05 for ε_l^b and ± 0.01 for ε_l^{top}.

	With lower limit ε_l^W	With correct ε_l^W	With upper limit ε_l^W
Fitted #top/#total:			
2 jet sample	0.25 ± 0.13	0.17 ± 0.10	0.09 ± 0.05
3 jet sample	0.55 ± 0.20	0.44 ± 0.18	0.32 ± 0.15
4 jet sample	0.84 ± 0.16	0.71 ± 0.24	0.59 ± 0.21
Fitted efficiencies:			
ε_b (true = 0.36)	0.30 ± 0.15	0.36 ± 0.15	0.40 ± 0.15
ε_l^{top} (true = 0.07)	0.07 ± 0.10	0.06 ± 0.06	0.05 ± 0.06

Table 6.15: *The fit results from the analyses with different distributions of the efficiency ε_l^W on a sample of 50 pb^{-1}, at a JetProb weight of 0.5.*

6.4.3 Measurement of the cross sections

In Section 6.3 the cross section for W+jets, single tops and $t\bar{t}$ is calculated with the use of six values: the measured number of top events in the two- and three jet sample, N_{2j}^{top} and N_{3j}^{top}, plus the total number of W events measured, N^W. These are compared with the three expected values $N_{MC,2j}^{top}$, $N_{MC,2j}^{top}$ and N_{MC}^W from a MC sample.

From Section 6.2.3 we conclude that the measurements for $N_{MC,2j}^{top}$ and $N_{MC,3j}^{top}$ can be made to respectively 1% and 5%. To stay on the safe side, we also assume an uncertainty of 5% on N_{MC}^W. Adding the uncertainties on the lepton trigger and reconstruction[7)], we summarize the uncertainty on the MC predictions as in Table 6.16. As for the results obtained from the fits, Table 6.17 gives an overview of the uncertainties measured, and their uncorrelated total sum per variable. The uncertainty on the luminosity is listed with its lower and upper limit.

With the maximum uncertainties on N_{MC}^W and N^W in Table 6.17 we conclude that the cross section for the W+jets can be measured up to 32% with first data. The total cross section for

[7)] In Section 4.6.1 we stated these uncertainties, which were gained from studies performed on a sample of 100 pb^{-1} 14 TeV collisions. As we study the performance on a smaller sample at lower center-of-mass energy, these quoted uncertainties are not entirely correct. Yet these uncertainties are almost negligible compared to the total; we will therefore leave them unchanged.

	Parton showering	Trigger Efficiency	Lepton reconstruction	TOTAL
N^W_{MC}	5%	1%	1%	5.2%
$N^{top}_{MC,2j}$	1%	1%	1%	1.7%
$N^{top}_{MC,3j}$	5%	1%	1%	5.2%

Table 6.16: *Uncertainties on the three predictions from MC samples for the number of top events in the two- and three jet sample, and for the total number of W events.*

	Luminosity	JES	$\not{E}_T$ scale	$R^{i\ bJet}_{nj}$	ε^W_l	Statistical	TOTAL
N^W	5-20%	19%	3.3%	1%	9.7%	11.5%	25-32%
N^{top}_{2j}	5-20%	4%	2.1%	–	53%	59%	80-82%
N^{top}_{3j}	5-20%	13%	3.0%	2%	24%	36%	46-50%

Table 6.17: *Uncertainties on the three measurements for the number of top events in the two- and three jet sample, and for the total number of W events.*

top quark pairs plus single tops can be measured to 50% combining the results in the two and three jet sample; if we were to follow similar steps as taken in Section 6.3 to obtain the cross sections in eq.(6.13) for the individual channels, the uncertainties on the cross sections for $t\bar{t}$ and for single top would be 110% and 580% respectively.

6.4.4 Conclusion

We have shown that for a first data sample of 50 pb^{-1} a measurement up to 32% accuracy can be made for the W+jets background cross section to the top channels in the lower jet multiplicities. An individual cross section measurement for the top quark pair and for the single top events results in large uncertainties, respectively 110% and 580%, yet a total cross section for the top quark pair plus single top events can be determined up to 50% accuracy.

Compared to a dedicated W or top cross section analysis the advantage is that the presented analysis is independent of the b-tagging efficiency, which is in fact determined simultaneously with the cross sections. The JetProb efficiency ε_b on b-jets is measured with a statistical uncertainty of ± 0.15 and a systematic uncertainty of ± 0.05, both of which are correlated to the uncertainties on the cross section measurements.

The uncertainty on the measurement of the b-tagging efficiency on W+jets events was estimated from the higher expected value for the cross section ratio of Z+$b\bar{b}$ to Z+jets compared to that of W+$b\bar{b}$ to W+jets. If the first ratio is truly higher, we can expect a positive offset in the measurement of the efficiency ε^W_l, biasing our end results. Further research using simulated Z+$b\bar{b}$ events is needed to investigate the exact offset and to explore possibilities to compensate for the bias. The same conclusion can be drawn on the subject of QCD events. With only a small fraction of $b\bar{b}$ in QCD events, we expect these events to be W+jets like. Using simulated multi-jet events the expected number of QCD events passing the selection requirements, and their effect on the analysis presented, should be investigated.

6.5 The effect of supersymmetry on the top/W ratio

In this section we study the effect of the presence of supersymmetric particles on the analysis set up in this chapter. As in section 5.9 we study the SU3 (bulk) and SU4 (low mass) models.

6.5.1 Event selection

We first study the effect of the presence of SU4 with the standard event selection listed in Section 6.1.2. We then perform the analysis with higher requirements on the $\not{E}_T$ and transverse momentum of the jets as to increase the signal to background ratio, where the signal in this case is the events with supersymmetric particles. We have not performed any research to define the best requirements, yet based on the work done in [60] we have chosen for:

- Missing transverse energy $\not{E}_T > 100$ GeV.
- Exactly one isolated lepton, be it electron or muon, with $p_T > 20$ GeV. At the same time, the Event Filter trigger EF_e25i_medium1 must have passed if the lepton is an electron, or the trigger EF_mu20 must have passed if it is a muon.
- At least one jet with $p_T > 100$ GeV. Any additional jet must have $p_T > 50$ GeV.

With these new criteria we analyze the effect of two supersymmetric models. The samples analyzed are reconstructed with a center-of-mass energy of 10 TeV and are the SU3 and SU4 samples generated with Isajet [118] plus HERWIG, see Section 4.2. We note that for the SU4 sample we only had access to a sample corresponding to 169 pb^{-1} and we normalized the results in this section to 500 pb^{-1}.

6.5.2 Results

The requirements mentioned above on the missing transverse energy and the jet p_T could affect the results of the fit procedure and introduce biases in the events selected. Before including the supersymmetric channels we checked the results of the scan procedure on the Standard Model events with these requirements. The fit results are still correct: the distributions for the fitted number of top events are flat and at the correct values. Also the fitted efficiencies correspond to the 'true' values.

The SU4 model is one of the models with the lowest masses for the supersymmetric particles and its cross section is relatively high: 402 pb [60]. Table 6.18 lists the results for the fitted number of top and W events using the standard selection requirements from Section 6.1.2 on a sample of 500 pb^{-1} including the SU4 supersymmetric events. The columns to the left in the Table list the number of events for each channel passing the selection; the number of events for the Standard Model channels are the same as in Table 6.4. The values for the fitted number of tops and number of W's are extracted from the results in Fig. 6.11 at a IP3D+SV1 weight of 4.0.

Within the statistical uncertainty the measured number of W events corresponds to the actual number of W events present; only in the two jet sample is the measured number of W events slightly too high. The measured number of tops actually equals the sum of top and supersymmetry events. In Section 6.4.2 a too high number of W's was correlated with a too high fit result for ε_b. This is not the case here: the fitted b-tagging efficiency ε_b is too low.

With the flat distributions for the ratios in Fig. 6.11 and the efficiencies having only a small offset from the true distributions we can conclude that the SU4 events resemble the top events in their b-jet contents. This is as we might expect from the phenomenology of SU4 events, see [124]:

- 63% of the SU4 events produced contain at least one gluino. The gluino is dominantly decaying to the third generation $\widetilde{q}q$, with
  - $\widetilde{g} \to \widetilde{b}_1 b$ (branching ratio = 47%),
  - $\widetilde{g} \to \widetilde{t}_1 t$ (branching ratio = 42%),
  - $\widetilde{g} \to \widetilde{b}_2 b$ (branching ratio = 4%).

  The squarks $\widetilde{b}_1$ and $\widetilde{b}_2$ decay to $\widetilde{t}_1 W$ with a probability of about 50%. The lightest scalar top $\widetilde{t}_1$ is only 30 GeV heavier than its Standard Model partner ($m_{\widetilde{t}_1} = 206$ GeV) and decays to final states similar to those of the top quark:
  $\widetilde{t}_1 \to \widetilde{\chi}_1^{\pm} b$ (branching ratio = 100%). The $\widetilde{\chi}_1^{\pm}$ decays through a virtual $W^{\pm}$ and a $\widetilde{\chi}_1^0$.
- 11% of the SU4 events produced in the hard scattering result in a scalar top pair $\widetilde{t}_1\bar{\widetilde{t}}_1$.

All in all, a large fraction of SU4 events (53%) is characterized by a decay through at least two (virtual) W-bosons and two b-quarks, with as result a $t\bar{t}$ -like final state.

In Table 6.19 we summarize the results after the selection requirements mentioned in Section 6.5.1. The results for all five distributions are shown in Fig. 6.12. We can almost draw the same conclusion as before: for the three- and four-jet samples the measured number of W events is correct and all supersymmetry events are measured as top events. In the two-jet sample the number of W's is too high however.

Repeating the last analysis with the high energetic requirements on a sample containing SU3 instead of SU4 we obtain the results from Table 6.20 and Fig. 6.13. These measurements are inconclusive: the small amount of supersymmetry events does not make it possible to see any significant effect on the results.

6.5.3 Conclusion

Combining the results of this section with those of Section 5.9 from the previous chapter we can conclude that the SU4 events resemble the top events in their b-jet contents, while at the same time they do not satisfy a complete semi-leptonic $t\bar{t}$ hypothesis. In the analysis in Section 5.9 on SU3 events an excess of events was visible after the tight selection cuts. With the low jet multiplicity demanded in this section the excess is not clear.

With the large parameter space available, supersymmetric models with other b-jet contents than those in the SU3 and SU4 models analyzed in this section are possible; we cannot assume that all models will be easily identified as $t\bar{t}$ like, as was the case for the SU4 model, or W+jets like. We can only conclude that if supersymmetry exists, with some luck, the b-tagging analysis presented in this chapter might give a hint of the composition of the supersymmetric events.

	$t\bar{t}$ + single tops	W+jets (incl $b\bar{b}$)	SU4	Fitted #top	Fitted #W
2 jet sample	14.9	70.7	3.98	18.4 ± 0.45	71.3 ± 0.45
3 jet sample	12.3	12.3	4.74	17.3 ± 0.30	12.0 ± 0.30
4 jet sample	5.23	2.23	4.05	9.20 ± 0.23	2.30 ± 0.23

Table 6.18: *Results for the fitted number of top and W events ($\times 10^3$) using the standard selection requirements from Section 6.1.2 on a sample of* 500 pb^{-1} *including the supersymmetric SU4 model. To the left the number of events are listed for the different samples present. Within the statistical uncertainty the fitted number of W events corresponds to the actual number of W events present; the fitted number of tops equals the sum of top and supersymmetry events.*

	$t\bar{t}$ + single tops	W+jets (incl $b\bar{b}$)	SU4	Fitted #top	Fitted #W
2 jet sample	1.60	4.43	3.21	4.16 ± 0.23	5.08 ± 0.23
3 jet sample	1.23	1.19	3.11	4.31 ± 0.22	1.22 ± 0.22
4 jet sample	0.47	0.21	1.86	2.23 ± 0.13	0.31 ± 0.13

Table 6.19: *Results ($\times 10^3$) using the supersymmetry selection requirements on a sample of* 500 pb^{-1} *including SU4 events. Almost the same conclusion can be drawn as in Table 6.18: the fitted number of W events is correct in the three- and four-jet sample and all supersymmetry events are measured as top events. Yet in the two-jet sample the fitted number of W events is too high.*

	$t\bar{t}$ + single tops	W+jets (incl $b\bar{b}$)	SU3	Fitted #top	Fitted #W
2 jet sample	1.60	4.43	0.21	1.62 ± 0.12	4.62 ± 0.12
3 jet sample	1.23	1.19	0.27	1.40 ± 0.09	1.29 ± 0.09
4 jet sample	0.47	0.21	0.20	0.57 ± 0.05	0.31 ± 0.05

Table 6.20: *Results ($\times 10^3$) using the supersymmetry selection requirements on a sample of* 500 pb^{-1} *including SU3 events. Compared to the results with SU4 events, it is unclear whether the supersymmetry events are fitted as top or as W events. The small amount of supersymmetry events does not make it possible to see any significant effect on the results.*

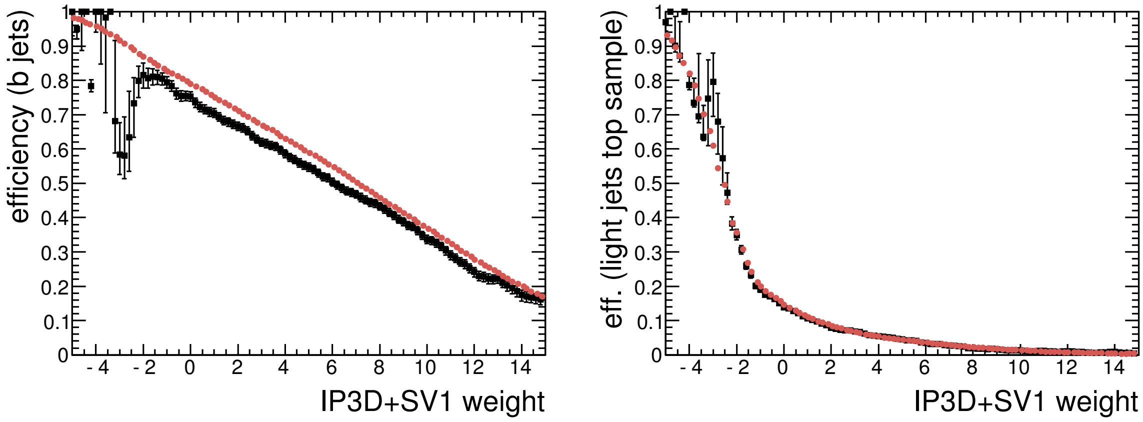

(a) Left: results for ε_b. Right: results for ε_l^{top}. The distribution with error-bars is the fit result, the distribution without is the true efficiency when using $t\bar{t}$ events generated by MC@NLO.

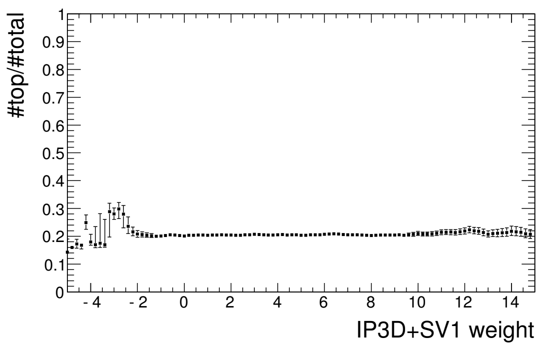

(b) Ratio of $top/total$ for events with 2 jets.

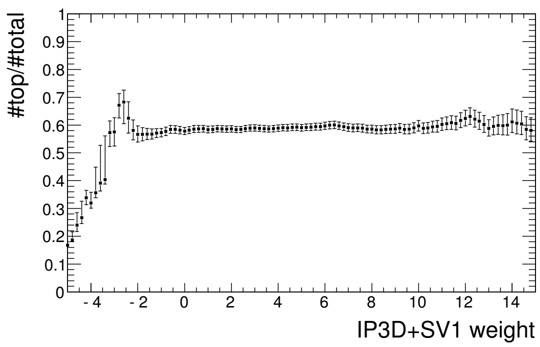

(c) Ratio of $top/total$ for events with 3 jets.

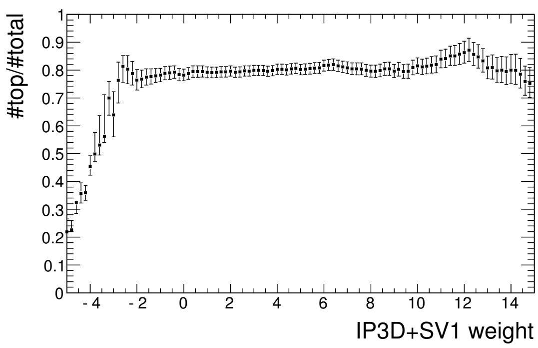

(d) Ratio of $top/total$ for events with 4 jets.

Figure 6.11: *Fit result for a sample containing the supersymmetry events SU4, with luminosity of* $500\ \text{pb}^{-1}$. *The standard event selections from Section 6.1.2 are used, while IP3D+SV1 is used as b-tagger.*

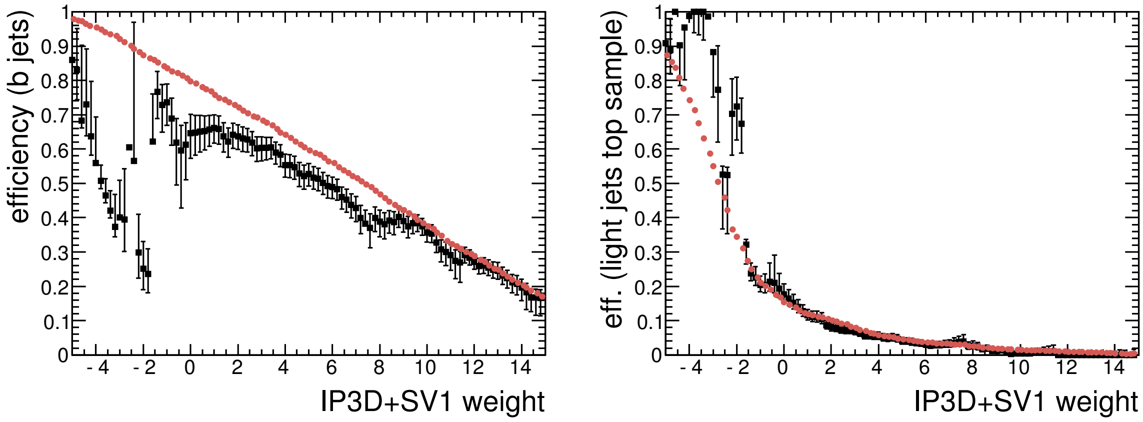

(a) Left: results for ε_b. Right: results for ε_l^{top}. The distribution with error-bars is the fit result, the distribution without is the true efficiency when using $t\bar{t}$ events generated by MC@NLO.

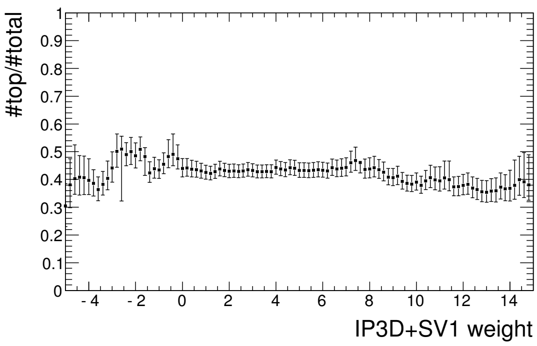

(b) Ratio of $top/total$ for events with 2 jets.

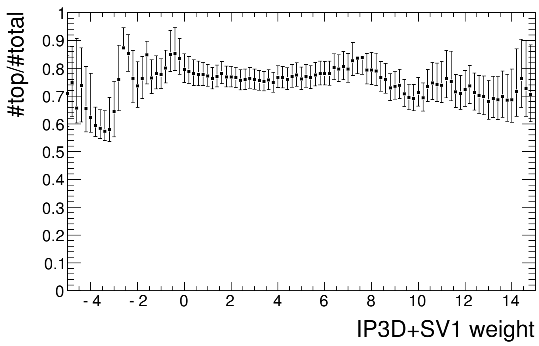

(c) Ratio of $top/total$ for events with 3 jets.

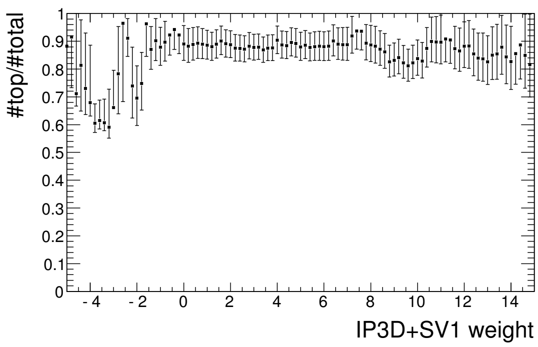

(d) Ratio of $top/total$ for events with 4 jets.

Figure 6.12: *Fit result for a sample containing the supersymmetry events SU4, with luminosity of* 500 pb^{-1}. *The supersymmetry requirements mentioned in Section 6.5.1 are used, while IP3D+SV1 is used as b-tagger. The* $R_{nj}^{i\ bJet}$ *fractions are extracted from the MC@NLO* $t\bar{t}$ *events,* after *the event selection.*

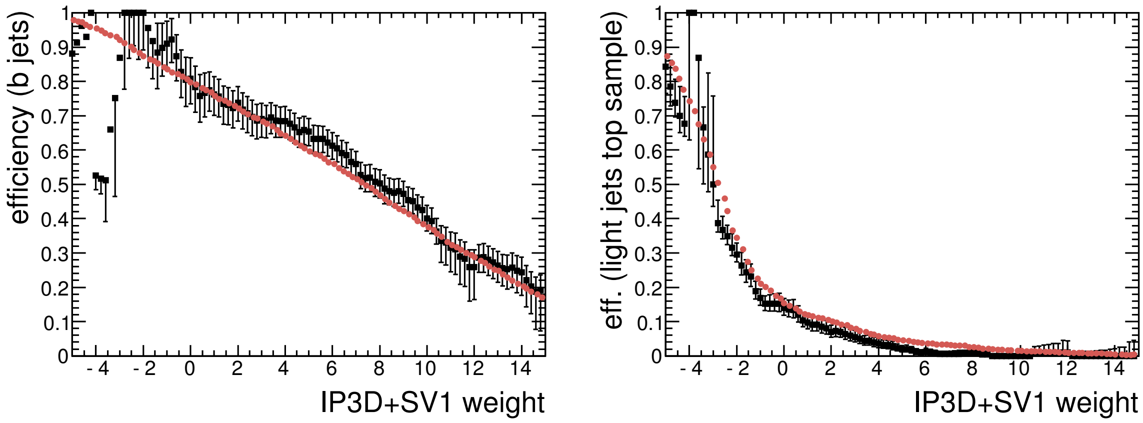

(a) Left: results for ε_b. Right: results for ε_l^{top}. The distribution with error-bars is the fit result, the distribution without is the true efficiency when using $t\bar{t}$ events generated by MC@NLO.

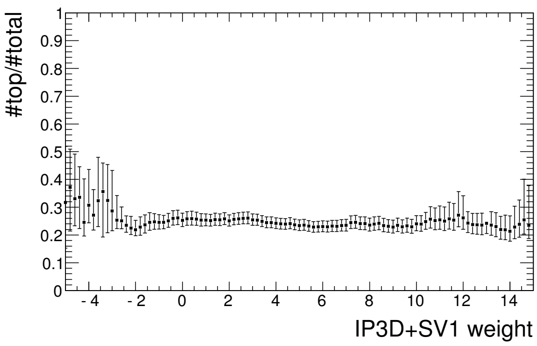

(b) Ratio of $top/total$ for events with 2 jets.

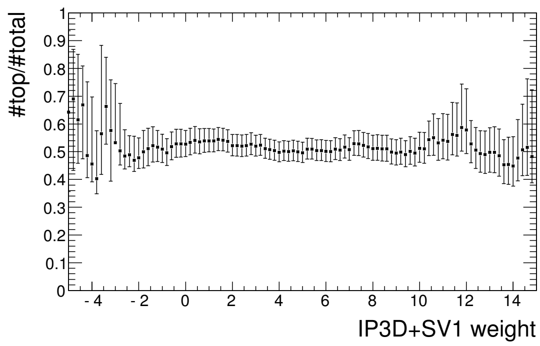

(c) Ratio of $top/total$ for events with 3 jets.

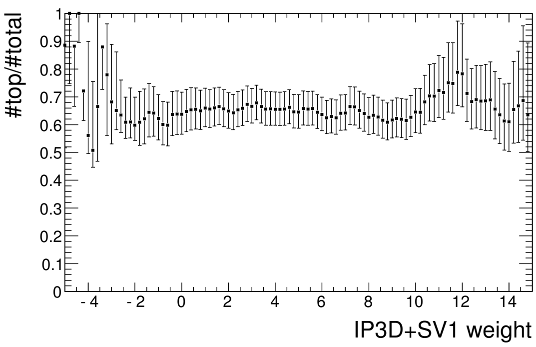

(d) Ratio of $top/total$ for events with 4 jets.

Figure 6.13: *Fit result for a sample containing the supersymmetry events SU3, with luminosity of* 500 pb^{-1}. *The susy requirements mentioned in Section 6.5.1 are used, while IP3D+SV1 is used as b-tagger. The* $R_{nj}^{i\ bJet}$ *fractions are extracted from the MC@NLO* $t\bar{t}$ *events,* after *the event selection.*

Appendix A

Likelihood functions

In Section 6.1.1 the likelihood functions used in the analysis for the top quark pair and W boson production cross section measurements are discussed by going into detail on the functions for the expected number of tagged jets in the two-jet sample. This appendix states the functions needed for the three- and four-jet samples. The complete definition for the negative log-likelihood (NLL) to be minimized is:

$$-\ln L = -\ln \prod_{x,n} P(N_{nj}^{x\ tag,meas}, N_{nj}^{x\ tag}) \equiv -\ln \prod_{x,n} \frac{e^{-N_{nj}^{x\ tag}} \left(N_{nj}^{x\ tag}\right)^{N_{nj}^{x\ tag,meas}}}{N_{nj}^{x\ tag,meas}!}, \quad \text{(A.1)}$$

where $P(N_{nj}^{x\ tag,meas}, N_{nj}^{x\ tag})$ is the Poisson Likelihood of measuring $N_{nj}^{x\ tag,meas}$, that is the number of events with x jets b-tagged in the n-jet sample, when $N_{nj}^{x\ tag}$ events are expected.

The functions N_{2j}^{1tag} and N_{2j}^{2tag} have been given in Section 6.1.1. For the expected number of events with one, two or three jets tagged in the three-jet sample we have

$$N_{3j}^{1tag} = \varepsilon_1^W N_{3j}^W + \varepsilon_1^{top} N_{3j}^{top} \quad \text{(A.2)}$$

$$N_{3j}^{2tag} = \varepsilon_2^W N_{3j}^W + \varepsilon_2^{top} N_{3j}^{top} \quad \text{(A.3)}$$

$$N_{3j}^{3tag} = \varepsilon_3^W N_{3j}^W + \varepsilon_3^{top} N_{3j}^{top} \quad \text{(A.4)}$$

$$\varepsilon_1^W = 3\varepsilon_l^W (1-\varepsilon_l^W)^2 \quad \text{(A.5)}$$

$$\varepsilon_2^W = 3(\varepsilon_l^W)^2 (1-\varepsilon_l^W) \quad \text{(A.6)}$$

$$\varepsilon_3^W = (\varepsilon_l^W)^3 \quad \text{(A.7)}$$

$$\begin{aligned} \varepsilon_1^{top} &= 3\varepsilon_l^{top}(1-\varepsilon_l^{top})^2 R_{3j}^{0\ bJet} \\ &+ \left(\varepsilon_b \left(1-\varepsilon_l^{top}\right)^2 + 2\varepsilon_l^{top}\left(1-\varepsilon_l^{top}\right)\left(1-\varepsilon_b\right)\right) R_{3j}^{1\ bJet} \\ &+ \left(\varepsilon_l^{top}\left(1-\varepsilon_b\right)^2 + 2\varepsilon_b\left(1-\varepsilon_b\right)\left(1-\varepsilon_l^{top}\right)\right) R_{3j}^{2\ bJet} \end{aligned} \quad \text{(A.8)}$$

$$\begin{aligned} \varepsilon_2^{top} &= 3\left(\varepsilon_l^{top}\right)^2\left(1-\varepsilon_l^{top}\right) R_{3j}^{0\ bJet} + \left(2\varepsilon_b\varepsilon_l^{top}\left(1-\varepsilon_l^{top}\right) + \left(1-\varepsilon_b\right)\left(\varepsilon_l^{top}\right)^2\right) R_{3j}^{1\ bJet} \\ &+ \left(\varepsilon_b^2\left(1-\varepsilon_l^{top}\right) + 2\varepsilon_l^{top}\varepsilon_b\left(1-\varepsilon_b\right)\right) R_{3j}^{2\ bJet} \end{aligned} \quad \text{(A.9)}$$

$$\varepsilon_3^{top} = \left(\varepsilon_l^{top}\right)^3 R_{3j}^{0\ bJet} + \varepsilon_b\left(\varepsilon_l^{top}\right)^2 R_{3j}^{1\ bJet} + \varepsilon_b^2\varepsilon_l^{top} R_{3j}^{2\ bJet}. \quad \text{(A.10)}$$

For the expected number of events with one, two or three jets tagged in the four-jet sample we have

$$N_{4j}^{1tag} = \varepsilon_1^W N_{4j}^W + \varepsilon_1^{top} N_{4j}^{top} \tag{A.11}$$

$$N_{4j}^{2tag} = \varepsilon_2^W N_{4j}^W + \varepsilon_2^{top} N_{4j}^{top} \tag{A.12}$$

$$N_{4j}^{3tag} = \varepsilon_3^W N_{4j}^W + \varepsilon_3^{top} N_{4j}^{top} \tag{A.13}$$

$$\varepsilon_1^W = 4\varepsilon_l^W (1-\varepsilon_l^W)^3 \tag{A.14}$$

$$\varepsilon_2^W = 6(\varepsilon_l^W)^2 (1-\varepsilon_l^W)^2 \tag{A.15}$$

$$\varepsilon_3^W = 4(\varepsilon_l^W)^3 (1-\varepsilon_l^W) \tag{A.16}$$

$$\begin{aligned}\varepsilon_1^{top} &= 4\varepsilon_l^{top}(1-\varepsilon_l^{top})^3 R_{4j}^{0\ bJet} \\ &+ \left(\varepsilon_b\left(1-\varepsilon_l^{top}\right)^3 + 3\varepsilon_l^{top}\left(1-\varepsilon_l^{top}\right)^2(1-\varepsilon_b)\right) R_{4j}^{1\ bJet} \\ &+ \left(2\varepsilon_l^{top}\left(1-\varepsilon_l^{top}\right)(1-\varepsilon_b)^2 + 2\varepsilon_b(1-\varepsilon_b)\left(1-\varepsilon_l^{top}\right)^2\right) R_{4j}^{2\ bJet}\end{aligned} \tag{A.17}$$

$$\begin{aligned}\varepsilon_2^{top} &= 6(\varepsilon_l^{top})^2\left(1-\varepsilon_l^{top}\right)^2 R_{4j}^{0\ bJet} + \left(3\varepsilon_b\varepsilon_l^{top}\left(1-\varepsilon_l^{top}\right)^2 + 3(1-\varepsilon_b)\left(1-\varepsilon_l^{top}\right)(\varepsilon_l^{top})^2\right) R_{4j}^{1\ bJet} \\ &+ \left(\varepsilon_b^2\left(1-\varepsilon_l^{top}\right)^2 + 4\varepsilon_l^{top}\varepsilon_b(1-\varepsilon_b)\left(1-\varepsilon_l^{top}\right) + \left(\varepsilon_l^{top}\right)^2(1-\varepsilon_b)^2\right) R_{4j}^{2\ bJet}\end{aligned} \tag{A.18}$$

$$\begin{aligned}\varepsilon_3^{top} &= 4\left(\varepsilon_l^{top}\right)^3\left(1-\varepsilon_l^{top}\right) R_{4j}^{0\ bJet} \\ &+ \left(3\varepsilon_b\left(\varepsilon_l^{top}\right)^2\left(1-\varepsilon_l^{top}\right) + (1-\varepsilon_b)\left(\varepsilon_l^{top}\right)^3\right) R_{4j}^{1\ bJet} \\ &+ \left(2\varepsilon_b^2\varepsilon_l^{top}\left(1-\varepsilon_l^{top}\right) + 2\left(\varepsilon_l^{top}\right)^2\varepsilon_b(1-\varepsilon_b)\right) R_{4j}^{2\ bJet}.\end{aligned} \tag{A.19}$$

Bibliography

[1] Michael Edward Peskin and Daniel V. Schroeder. *An Introduction to quantum field theory.* Addison-Wesley, USA, 1995.

[2] R. Keith Ellis, W. James Stirling, and B. R. Webber. *QCD and collider physics.* Cambridge Univ. Pr., UK, 1996.

[3] Francis Halzen and Alan D. Martin. *Quarks and Leptons: An Introductory Course in Modern Particle Physics.* Wiley, February 2001.

[4] S. L. Glashow. Partial Symmetries of Weak Interactions. *Nucl. Phys.*, 22:579–588, 1961.

[5] Jeffrey Goldstone, Abdus Salam, and Steven Weinberg. Broken Symmetries. *Phys. Rev.*, 127:965–970, 1962.

[6] Steven Weinberg. A Model of Leptons. *Phys. Rev. Lett.*, 19:1264–1266, 1967.

[7] Peter W. Higgs. Broken symmetries and the masses of gauge bosons. *Phys. Rev. Lett.*, 13:508–509, 1964.

[8] Peter W. Higgs. Broken symmetries, massless particles and gauge fields. *Phys. Lett.*, 12:132–133, 1964.

[9] Peter W. Higgs. Spontaneous symmetry breakdown without massless bosons. *Phys. Rev.*, 145:1156–1163, 1966.

[10] Y. Ashie et al. Evidence for an oscillatory signature in atmospheric neutrino oscillation. *Phys. Rev. Lett.*, 93:101801, 2004. arXiv:hep-ex/0404034.

[11] Y. Ashie et al. A measurement of atmospheric neutrino oscillation parameters by Super-Kamiokande I. *Phys. Rev.*, D71:112005, 2005. arXiv:hep-ex/0501064.

[12] M. L. Mangano and T. J. Stelzer. Tools for the simulation of hard hadronic collisions. *Ann. Rev. Nucl. Part. Sci.*, 55:555–588, 2005.

[13] Gerard 't Hooft and M. J. G. Veltman. Regularization and Renormalization of Gauge Fields. *Nucl. Phys.*, B44:189–213, 1972.

[14] John M. Campbell, J. W. Huston, and W. J. Stirling. Hard Interactions of Quarks and Gluons: A Primer for LHC Physics. *Rept. Prog. Phys.*, 70:89, 2007. arXiv:hep-ph/0611148.

[15] F. Abe et al. Observation of top quark production in $\bar{p}p$ collisions with the Collider Detector at Fermilab. *Phys. Rev. Lett.*, 74:2626–2631, 1995. arXiv:hep-ex/9503002.

[16] Tevatron Electroweak Working Group. Combination of CDF and D0 Results on the Mass of the Top Quark. 2009. arXiv:0903.2503.

[17] Stuart Raby, Savas Dimopoulos, and Leonard Susskind. Tumbling Gauge Theories. *Nucl. Phys.*, B169:373, 1980.

[18] Zack Sullivan. Understanding single-top-quark production and jets at hadron colliders. *Phys. Rev.*, D70:114012, 2004. arXiv:hep-ph/0408049.

[19] John Campbell and Francesco Tramontano. Next-to-leading order corrections to W t production and decay. *Nucl. Phys.*, B726:109–130, 2005. arXiv:hep-ph/0506289.

[20] J.M. Campbell and R.K. Ellis, A Monte Carlo for FeMtobarn processes at Hadron Colliders, 2007.
`http://mcfm.fnal.gov`.

[21] Jeroen Hegeman. Measurement of the top quark pair production cross section in proton-antiproton collisions at $\sqrt{s} = 1.96$ TeV, hadronic top decays with the D0 detector. 2009. FERMILAB-THESIS-2009-07.

[22] W. K. Tung et al. Heavy quark mass effects in deep inelastic scattering and global QCD analysis. *JHEP*, 02:053, 2007. arXiv:hep-ph/0611254.

[23] C. Amsler et al. Review of particle physics. *Phys. Lett.*, B667:1, 2008.

[24] UA1 Collaboration. Experimental observation of isolated large transverse energy electrons with associated missing energy at $\sqrt{s} = 540$ GeV. *Phys. Lett.*, B122:103–116, 1983.

[25] UA1 Collaboration. Experimental observation of lepton pairs of invariant mass around 95 GeV/c^2 at the CERN SPS collider. *Phys. Lett.*, B126:398–410, 1983.

[26] UA2 Collaboration. Evidence for $Z^0 \to e^+e^-$ at the CERN $\overline{p}p$ collider. *Phys. Lett.*, B129:130–140, 1983.

[27] ATLAS Collaboration, Expected Performance of the ATLAS Experiment, Detector, Trigger and Physics, ch. Cross sections, Monte Carlo simulations and systematic uncertainties. CERN-OPEN-2008-020, Geneva, 2008.

[28] John M. Campbell, R. Keith Ellis, and David L. Rainwater. Next-to-leading order QCD predictions for W + 2jet and Z + 2jet production at the CERN LHC. *Phys. Rev.*, D68:094021, 2003. arXiv:hep-ph/0308195.

[29] ATLAS Collaboration, Expected Performance of the ATLAS Experiment, Detector, Trigger and Physics, ch. Top Quark Physics. CERN-OPEN-2008-020, Geneva, 2008.

[30] Christopher Neu. W/Z + Light Flavor Jets and W/Z + Heavy Flavor Jets at the Tevatron. 2008. arXiv:0809.1407.

[31] Alan D. Martin, R. G. Roberts, W. James Stirling, and R. S. Thorne. Parton distributions and the LHC: W and Z production. *Eur. Phys. J.*, C14:133–145, 2000. arXiv:hep-ph/9907231.

[32] A. D. Martin, R. G. Roberts, W. J. Stirling, and R. S. Thorne. Uncertainties of predictions from parton distributions. I: Experimental errors. ((T)). *Eur. Phys. J.*, C28:455–473, 2003. arXiv:hep-ph/0211080.

[33] Daniel Stump et al. Inclusive jet production, parton distributions, and the search for new physics. *JHEP*, 10:046, 2003. arXiv:hep-ph/0303013.

[34] Daniel Stump. Uncertainties of parton distribution functions. 2003. Prepared for PHYSTAT2003: Statistical Problems in Particle Physics, Astrophysics, and Cosmology, Menlo Park, California.

[35] Matteo Cacciari, Stefano Frixione, Michelangelo L. Mangano, Paolo Nason, and Giovanni Ridolfi. Updated predictions for the total production cross sections of top and of heavier quark pairs at the Tevatron and at the LHC. *JHEP*, 09:127, 2008. arXiv:0804.2800.

[36] M. Cacciari, S. Frixione, M. L. Mangano, P. Nason, and G. Ridolfi. The $t\bar{t}$ cross section at 1.8 TeV and 1.96 TeV: A study of the systematics due to parton densities and scale dependence. *JHEP*, 04:068, 2004. arXiv:hep-ph/0303085.

[37] Stefano Frixione and Bryan R. Webber. Matching NLO QCD computations and parton shower simulations. *JHEP*, 06:029, 2002. arXiv:hep-ph/0204244.

[38] Stefano Frixione, Paolo Nason, and Bryan R. Webber. Matching NLO QCD and parton showers in heavy flavour production. *JHEP*, 08:007, 2003. arXiv:hep-ph/0305252.

[39] M. R. Whalley, D. Bourilkov, and R. C. Group. The Les Houches Accord PDFs (LHAPDF) and Lhaglue. 2005. arXiv:hep-ph/0508110.

[40] Roberto Bonciani, Stefano Catani, Michelangelo L. Mangano, and Paolo Nason. NLL resummation of the heavy-quark hadroproduction cross- section. *Nucl. Phys.*, B529:424–450, 1998. arXiv:hep-ph/9801375.

[41] A. D. Martin, W. J. Stirling, R. S. Thorne, and G. Watt. Update of parton distributions at NNLO. *Phys. Lett.*, B652:292–299, 2007. arXiv:0706.0459.

[42] Ian J. R. Aitchison. Supersymmetry and the MSSM: An elementary introduction. 2005. arXiv:hep-ph/0505105.

[43] M. Drees, R. Godbole, and P. Roy. *Theory and phenomenology of sparticles: An account of four-dimensional N=1 supersymmetry in high energy physics*. World Scientific, USA, 2004.

[44] M. Dine. *Supersymmetry and string theory: Beyond the standard model*. Cambridge Univ. Pr., UK, 2007.

[45] Jerzy Szwed. The 'square root' of the Dirac equation and solutions on superspace. *Acta Phys. Polon.*, B37:455–462, 2006. arXiv:hep-th/0403036.

[46] Adam Bzdak and Leszek Hadasz. The square root of the Dirac operator on the superspace and the Maxwell equations. *Phys. Lett.*, B582:113–116, 2004. arXiv:hep-th/0312179.

[47] Gordon L. Kane and Mikhail A. Shifman. *The supersymmetric world: The beginnings of the theory*. World Scientific, Singapore, 2000.

[48] Daniel Z. Freedman, P. van Nieuwenhuizen, and S. Ferrara. Progress Toward a Theory of Supergravity. *Phys. Rev.*, D13:3214–3218, 1976.

[49] Stanley Deser and B. Zumino. Consistent Supergravity. *Phys. Lett.*, B62:335, 1976.

[50] R. Barate et al. Search for the standard model Higgs boson at LEP. *Phys. Lett.*, B565:61–75, 2003. arXiv:hep-ex/0306033.

[51] Ugo Amaldi, Wim de Boer, and Hermann Furstenau. Comparison of grand unified theories with electroweak and strong coupling constants measured at LEP. *Phys. Lett.*, B260:447–455, 1991.

[52] E. J. Buis. *Detecting R-parity violation in the ATLAS inner detector*. PhD thesis, Nikhef, 2002.

[53] J. Dunkley et al. Five-Year Wilkinson Microwave Anisotropy Probe (WMAP) Observations: Likelihoods and Parameters from the WMAP data. *Astrophys. J. Suppl.*, 180:306–329, 2009. arXiv:0803.0586.

[54] Pierre Fayet and J. Iliopoulos. Spontaneously Broken Supergauge Symmetries and Goldstone Spinors. *Phys. Lett.*, B51:461–464, 1974.

[55] L. O'Raifeartaigh. Spontaneous Symmetry Breaking for Chiral Scalar Superfields. *Nucl. Phys.*, B96:331, 1975.

[56] S. Heinemeyer, W. Hollik, and G. Weiglein. The Masses of the neutral CP - even Higgs bosons in the MSSM: Accurate analysis at the two loop level. *Eur. Phys. J.*, C9:343–366, 1999. arXiv:hep-ph/9812472.

[57] Tao Han, Paul Langacker, and Bob McElrath. The Higgs sector in a U(1) -prime extension of the MSSM. *Phys. Rev.*, D70:115006, 2004. arXiv:hep-ph/0405244.

[58] `http://www.linearcollider.ca/vic04/abstracts/physics/newphysics/bob_mcelrath.pdf` .

[59] G. F. Giudice and R. Rattazzi. Theories with gauge-mediated supersymmetry breaking. *Phys. Rept.*, 322:419–499, 1999. arXiv:hep-ph/9801271.

[60] ATLAS Collaboration, Expected Performance of the ATLAS Experiment, Detector, Trigger and Physics, ch. Supersymmetry. CERN-OPEN-2008-020, Geneva, 2008.

[61] Irene Niessen. Supersymmetric Phenomenology in the mSUGRA Parameter Space. 2008. arXiv:0809.1748.

[62] Gabriel Caceres and Dan Hooper. Neutralino Dark Matter as the Source of the WMAP Haze. *Phys. Rev.*, D78:123512, 2008. arXiv:0808.0508.

[63] Kim Griest and David Seckel. Three exceptions in the calculation of relic abundances. *Phys. Rev.*, D43:3191–3203, 1991.

[64] Evans, Lyndon, (ed.) and Bryant, Philip, (ed.). LHC Machine. *JINST*, 3:S08001, 2008.

[65] G. Aad et al. The ATLAS Experiment at the CERN Large Hadron Collider. *JINST*, 3:S08003, 2008.

[66] ATLAS Collaboration, Expected Performance of the ATLAS Experiment, Detector, Trigger and Physics, ch. The expected performance of the ATLAS Inner Detector. CERN-OPEN-2008-020, Geneva, 2008.

[67] Budagov, J. and others, Study of TileCal Sampling Fraction for Improvement of Monte-Carlo Data Reconstruction, tilecal-pub-2006-006, CERN .

[68] ATLAS. ATLAS high-level trigger, data acquisition and controls: Technical design report. 2003. CERN-LHCC-2003-022.

[69] T. Kono for the ATLAS Collaboration, The ATLAS trigger menu for early data-taking, arXiv.org:0808.4102v1, 2008.

[70] ATLAS collaboration. ATLAS Inner Detector Technical Design Report. Technical report, CERN, 1997. CERN-LHCC/97-16.

[71] A. Abdesselam et al. Engineering for the ATLAS SemiConductor Tracker (SCT) end-cap. *JINST*, 3:P05002, 2008.

[72] Peeters, Simon J. M., The ATLAS semiconductor tracker endcap, CERN-THESIS-2003-013, 2003.

[73] C.A. Magrath. *The Heart of ATLAS*. PhD thesis, Nikhef, 2009.

[74] D. Ferrere. The ATLAS SCT endcap: From module production to commissioning. *Nucl. Instrum. Meth.*, A570:225–229, 2007.

[75] A. Abdesselam et al. The ATLAS semiconductor tracker end-cap module. *Nucl. Instrum. Meth.*, A575:353–389, 2007.

[76] Proceedings of the Topical Workshop on Electronics for Particle Physics, TWEPP-08, Naxos, Greece, 15-19 September 2008.

[77] E. Abat et al. Combined performance tests before installation of the ATLAS Semiconductor and Transition Radiation Tracking Detectors. *JINST*, 3:P08003, 2008.

[78] P. Bruckman et al., Global χ^2 approach to the Alignment of the ATLAS Silicon Tracking Detectors, ATL-INDET-PUB-2005-002.

[79] D. Attree et al. The evaporative cooling system for the ATLAS inner detector. *JINST*, 3:P07003, 2008.

[80] Olcese M. Engineering Overview of the ATLAS Inner Detector. *IEEE Nucl. Sci. Symp. Conf. Rec.*, 2:895–901, 2006.

[81] Verlaat B., CO2 cooling for HEP experiments, talk given at TWEPP-08 Topical Workshop on Electronics for Particle Physics; Delil A.A.M., Woering A.A and Verlaat B., Development of a Mechanically Pumped Two-Phase CO2 Cooling Loop for the AMS-2 Tracker Experiment,NLR-TP-2002-271 published by NLR (the National Aerospace Laboratory of the Netherlands), 2002.

[82] ATLAS Computing Group. ATLAS Computing Technical Design Report. Technical report, CERN, 2005. CERN-LHCC-2005-022.

[83] G. Barrand et al. GAUDI - A software architecture and framework for building HEP data processing applications. *Comput. Phys. Commun.*, 140:45–55, 2001.

[84] S. Agostinelli et al. GEANT4 - A Simulation Toolkit. *Nuclear Instruments and Methods*, A506:250–303, 2003.

[85] R. Brun and F. Rademakers. ROOT: An object oriented data analysis framework. *Nucl. Instrum. Meth.*, A389:81–86, 1997.

[86] Borut Paul Kersevan and Elzbieta Richter-Was. The Monte Carlo event generator AcerMC version 1.0 with interfaces to PYTHIA 6.2 and HERWIG 6.3. *Comput. Phys. Commun.*, 149:142–194, 2003. arXiv:hep-ph/0201302.

[87] Borut Paul Kersevan and Elzbieta Richter-Was. The Monte Carlo event generator AcerMC version 2.0 with interfaces to PYTHIA 6.2 and HERWIG 6.5. 2004. hep-ph/0405247.

[88] Torbjorn Sjöstrand, Stephen Mrenna, and Peter Skands. PYTHIA 6.4 physics and manual. *JHEP*, 05:026, 2006. arXiv:hep-ph/0603175.

[89] G. Corcella et al. HERWIG 6.5: an event generator for Hadron Emission Reactions With Interfering Gluons (including supersymmetric processes). *JHEP*, 01:010, 2001. arXiv:hep-ph/0011363.

[90] G. Corcella et al. HERWIG 6.5 release note. 2002. arXiv:hep-ph/0210213.

[91] Michelangelo L. Mangano, Mauro Moretti, Fulvio Piccinini, Roberto Pittau, and Antonio D. Polosa. ALPGEN, a generator for hard multiparton processes in hadronic collisions. *JHEP*, 07:001, 2003. arXiv:hep-ph/0206293.

[92] S. Catani, F. Krauss, R. Kuhn, and B. R. Webber. QCD Matrix Elements + Parton Showers. *JHEP*, 11:063, 2001. arXiv:hep-ph/0109231.

[93] M Gosselink, A P Colijn, and E N Koffeman. Measurement of the ttbar + n-jet spectrum in atlas. Technical Report ATL-COM-PHYS-2008-046, CERN, Geneva, Apr 2008.

[94] S. Catani, Yuri L. Dokshitzer, M. H. Seymour, and B. R. Webber. Longitudinally invariant K_t clustering algorithms for hadron hadron collisions. *Nucl. Phys.*, B406:187–224, 1993.

[95] ATLAS Collaboration, Expected Performance of the ATLAS Experiment, Detector, Trigger and Physics, ch. Jet Reconstruction Performance. CERN-OPEN-2008-020, Geneva, 2008.

[96] Gerald C. Blazey and others, Run II Jet Physics: Proceedings of the Run II QCD and Weak Boson Physics Workshop, 2000
`http://www.citebase.org/abstract?id=oai:arXiv.org:hep-ex/0005012`.

[97] J. M. Butterworth, J. P. Couchman, B. E. Cox, and B. M. Waugh. KtJet: A C++ implementation of the K(T) clustering algorithm. *Comput. Phys. Commun.*, 153:85–96, 2003. arXiv:hep-ph/0210022.

[98] Gavin P. Salam and Gregory Soyez. A Practical Seedless Infrared-Safe Cone jet algorithm. *JHEP*, 05:086, 2007. arXiv:0704.0292.

[99] Matteo Cacciari, Gavin P. Salam, and Gregory Soyez. The anti-k_t jet clustering algorithm. *JHEP*, 04:063, 2008. arXiv:0802.1189.

[100] ATLAS Collaboration, Expected Performance of the ATLAS Experiment, Detector, Trigger and Physics, ch. Detector Level Jet Corrections. CERN-OPEN-2008-020, Geneva, 2008.

[101] ATLAS Collaboration, Expected Performance of the ATLAS Experiment, Detector, Trigger and Physics, ch. b-Tagging performance. CERN-OPEN-2008-020, Geneva, 2008.

[102] Paul W. Balm. Measurement of the B_d^0 lifetime using $B_d^0 \to J/\psi K_S^0$ decays at Dzero. 2004. FERMILAB-THESIS-2004-16.

[103] ATLAS Collaboration, Expected Performance of the ATLAS Experiment, Detector, Trigger and Physics, ch. Soft muon b-tagging. CERN-OPEN-2008-020, Geneva, 2008.

[104] ATLAS Collaboration, Expected Performance of the ATLAS Experiment, Detector, Trigger and Physics, ch. Soft electron b-tagging. CERN-OPEN-2008-020, Geneva, 2008.

[105] ATLAS Collaboration, Expected Performance of the ATLAS Experiment, Detector, Trigger and Physics, ch. Vertex reconstruction for b-tagging. CERN-OPEN-2008-020, Geneva, 2008.

[106] ATLAS Collaboration, Expected Performance of the ATLAS Experiment, Detector, Trigger and Physics, ch. Measurement of missing transverse energy. CERN-OPEN-2008-020, Geneva, 2008.

[107] ATLAS Collaboration, Expected Performance of the ATLAS Experiment, Detector, Trigger and Physics, ch. Reconstruction and Identification of Electrons. CERN-OPEN-2008-020, Geneva, 2008.

[108] S. Hassani et al. A muon identification and combined reconstruction procedure for the ATLAS detector at the LHC using the (MUONBOY, STACO, MuTag) reconstruction packages. *Nucl. Instrum. Meth.*, A572:77–79, 2007.

[109] Th. Lagouri et al. A muon identification and combined reconstruction procedure for the ATLAS detector at the LHC at CERN. *IEEE Trans. Nucl. Sci.*, 51:3030–3033, 2004.

[110] ATLAS Collaboration, Expected Performance of the ATLAS Experiment, Detector, Trigger and Physics, ch. Jet Energy Scale: In-situ Calibration Strategies. CERN-OPEN-2008-020, Geneva, 2008.

[111] ATLAS Collaboration, Expected Performance of the ATLAS Experiment, Detector, Trigger and Physics, ch. Jets from light quarks in $t\bar{t}$ events. CERN-OPEN-2008-020, Geneva, 2008.

[112] ATLAS Collaboration, Expected Performance of the ATLAS Experiment, Detector, Trigger and Physics, ch. Measurement of missing transverse energy. CERN-OPEN-2008-020, Geneva, 2008.

[113] Snyder, S. S., Measurement of the top quark mass at D0, FERMILAB-THESIS-1995-27, 1995.

[114] F. James and M. Roos. Minuit: A System for Function Minimization and Analysis of the Parameter Errors and Correlations. *Comput. Phys. Commun.*, 10:343–367, 1975.

[115] F. James. Minuit reference manual. 1994. CERN Program Library Long Writeup D506, v94.1.

[116] ATLAS Collaboration, Expected Performance of the ATLAS Experiment, Detector, Trigger and Physics, ch. Determination of the top quark pair production cross-section. CERN-OPEN-2008-020, Geneva, 2008.

[117] ATLAS Collaboration, Expected Performance of the ATLAS Experiment, Detector, Trigger and Physics, ch. Top quark mass measurements. CERN-OPEN-2008-020, Geneva, 2008.

[118] Frank E. Paige, Serban D. Protopopescu, Howard Baer, and Xerxes Tata. ISAJET 7.69: A Monte Carlo event generator for p p, anti-p p, and e+ e- reactions. 2003. arXiv:hep-ph/0312045.

[119] Wouter Verkerke and David Kirkby. The RooFit toolkit for data modeling. 2003. arXiv:physics/0306116.

[120] S. Moch and P. Uwer. Heavy-quark pair production at two loops in QCD. *Nucl. Phys. Proc. Suppl.*, 183:75–80, 2008. arXiv:0807.2794.

[121] `https://twiki.cern.ch/twiki/bin/viewauth/AtlasProtected/TopReferences10TeV`.

[122] L. Mijovic, private communication. See also `http://indico.cern.ch/getFile.py/access?contribId=2&resId=1&materialId=slides&confId=10127`.

[123] ATLAS Collaboration, Expected Performance of the ATLAS Experiment, Detector, Trigger and Physics, ch. Production of jets in association with Z bosons. CERN-OPEN-2008-020, Geneva, 2008.

[124] J. Krstic, M. Milosavljevic, and D. Popovic. Studies of a low mass SUSY model at ATLAS with full simulation. *Acta Phys. Polon.*, B38:627–634, 2007. ATL-PHYS-PUB-2006-028.

Summary

At the CERN laboratory, located on the border between France and Switzerland, the LHC is soon to become operational. This accelerator will be the largest and most energetic hadron collider ever constructed. In an underground circular tunnel it will collide protons on protons at a maximum center-of-mass energy of 14 TeV. Detectors at four different locations will study the collisions, which are also known as “events”. One of the two general purpose detectors is the ATLAS experiment.

The purpose of the ATLAS detector is, among other things, to search for particles with masses up to several TeV. The greatest expectations lie in the discovery of the Higgs boson, the last of the fundamental particles in the Standard Model to remain undiscovered. Also, in different theorized extensions of the Standard Model new particles are predicted which might be produced at the LHC. The searches for these particles are far from easy: in the collisions they are swamped by the production of ‘uninteresting’ low mass particles. Furthermore, even before the searches can begin, the detector has to be commissioned and calibrated.

This thesis covers three subjects: the commissioning of the Inner Detector of ATLAS, a calibration scheme for the energy scales of the detector and finally an experimental setup for the measurement of the rate of production of W bosons and top quarks in first data.

First, the final steps of the installation and commissioning of the ATLAS detector are described. The data collected during the cosmic ray runs in the fall of 2008 have been used to study the performance of the SCT detector, the second most inner sub-detector in ATLAS. The SCT has been shown to perform in agreement with the design specifications. Extra attention is given to the commissioning of the evaporative cooling system of the SCT, which is to keep the temperature of the sensors at around -7°C. The system also cools the pixel detector, the most inner sub-detector in ATLAS, to around 0°C. Several problems occurred during the installation and commissioning of the system, notably with the heaters responsible for the evaporation of the remaining cooling fluid in the last steps of the cooling cycle. The problems are solved partly by adjusting the controls and partly by redesigning the cooling system.

As a second subject, an analysis is presented for the energy scale calibration of the detector, fine-tuned for the study of the top quark. The top quark is the heaviest of all six quarks known in the Standard Model and its large mass gives it a special role in the interaction between the Standard Model particles. Also the properties of undiscovered particles predicted by (yet) unproven theories such as supersymmetry are dependent on the top quark mass.

Using a kinematic fit with constraints for a semi-leptonic top quark pair decay, the jet energy scale and the missing transverse energy scale are determined on events simulated with Monte Carlo generators. A sample with integrated luminosity of $L = 160$ pb^{-1} at a center-of-mass energy of 14 TeV is used to show the feasibility of this procedure for first data calibration. Scanning over large ranges of the energy scales, with offsets up to 20%, it is shown that the

two correlated energy scales can be determined independently: first the jet energy scale by minimization of the χ^2 function and subsequently the missing transverse energy scale by using as estimator the transverse momentum difference between the two top quarks, as reconstructed with the kinematic fit.

Finally, an analysis is described to measure the rate of production of top quarks and W bosons in proton-proton collisions with ATLAS. The signal of a W boson production event can resemble the signal of a top quark pair event; for the study of the latter, W boson production thus constitute a background channel. A second background channel to top quark pair events is single top quark production. A first step in the identification of these backgrounds is the determination of their rate of production.

Events with between two and four jets are studied; jets are the observable objects in the ATLAS detector originating from either quarks or gluons. Using b-tagging algorithms, i.e. special reconstruction tools for the identification of b-quarks, the number of jets tagged as originating from a b-quark is measured as a function of the total number of jets in the event. A likelihood method is applied to fit the composition of a sample of top quark and W boson events. The method is shown not only to be independent of the cuts applied in the b-tagging algorithm, but also to be able to determine its efficiency on data. Applying the JetProb b-tagging algorithm on a simulated sample of events with integrated luminosity of 50 pb^{-1} at a center-of-mass energy of 10 TeV, the W boson production rate can be measured, together with the combined production rate of the single and pair produced top quark events.

With both of these analyses the impact of supersymmetric events as predicted by two models is studied. The kinematic fit is shown to possibly result in information on the mass scale of the supersymmetric events. The likelihood method is shown to be sensitive to the b-quark content in one of the supersymmetric models.

Samenvatting

Op het CERN laboratorium te Genève zal binnenkort de LHC in gebruik genomen worden. Deze deeltjesversneller zal de meeste energetische hadron botsingen opleveren ooit door de mens tot stand gebracht. Gebouwd in een tunnel onder de grens van Frankrijk en Zwitserland zal de versneller protonen met elkaar laten botsen bij een maximum zwaartepuntsenergie van 14 TeV. Op vier verschillende locaties zullen de botsingen worden waargenomen door experimenten; één van de vier is de ATLAS detector.

De detector heeft onder andere als doel het zoeken naar tot nu toe niet-waargenomen deeltjes. Het Higgs deeltje is een zeer begeerde: het is het laatste niet-waargenomen deeltje in het Standaard Model, de theorie die tot op de dag van vandaag het beste de fundamentele deeltjes en hun interacties beschrijft. Andere gezochte deeltjes zijn de voorspelde deeltjes in nieuwe theorieën. Het Standaard Model kent namelijk verschillende uitbreidingen: nieuwe, onbewezen theorieën die oplossingen bieden voor de verschillende problemen die nog open staan in de deeltjesfysica. Een mogelijkheid om deze theorieën te toetsen is te zoeken naar het bestaan van voorspelde deeltjes met de ATLAS detector.

De ingebruikname van de ATLAS detector is een uiterst minutieus proces. De eerste twee onderwerpen van dit proefschrift betreffen twee stappen in dit proces: het gereedmaken van de Inner Detector, de sub-detector van ATLAS het dichtst op de botsingen, en het kalibreren van de energieschalen voor de reconstructie van de botsingen. Het derde onderwerp van dit proefschrift is een analyse om de doorsnede te meten van W bosonen en van top quarks met de eerste verzameling aan botsingen.

Voor het eerste onderwerp, het gereedmaken van de Inner Detector, zijn de data gebruikt uit de herfst van 2008. In deze periode werden de kosmische stralen die doordringen tot het experiment waargenomen. Met deze data is de werking van de SCT, de op-één-na binnenste sub-detector van de Inner Detector, bestudeerd. Uit de studie blijkt dat de SCT volgens specificaties functioneert. In de studie is extra aandacht besteed aan de werking van het koelsysteem van de SCT. Gedurende de installatie en de ingebruikname traden verschillende problemen op, met name met de elementen die in de laatste fase van het koelen de overblijvende vloeistof dienen te verdampen. De problemen zijn opgelost, deels door herontwerp en deels door controleparameters aan te passen.

Het tweede onderwerp, de kalibratie van de energieschalen, betreft een specifieke kalibratie van de detector voor de waarneming van top quarks. De top quark is het zwaarste van alle quarks in het Standaard Model. Deze grote massa heeft invloed op de interacties tussen alle deeltjes in het Standaard Model en op de eigenschappen van voorspelde deeltjes in nieuwe theorieën, zoals de theorie van supersymmetrie.

Gebruikmakend van gesimuleerde botsingen bij een zwaartepuntsenergie van 14 TeV worden de schalen van de jet energie en van de ongedetecteerde transversale energie gekalibreerd met een kinematische fit voor semi-leptonisch verval van top quark paren. De studie toont dat met een verzameling gesimuleerde botsingen met geïntegreerde luminositeit van $L = 160$ pb^{-1} de twee gecorreleerde schalen onafhankelijk gekalibreerd kunnen worden: eerst de jet energie schaal door minimalisatie van de χ^2 functie en vervolgens de ongedetecteerde transversale energie schaal met behulp van het transversale momentum verschil tussen de twee gereconstrueerde top quarks.

Als laatste onderwerp van het proefschrift wordt een analyse gepresenteerd voor de meting van de doorsnede van W bosonen en top quark paren. Het signaal waargenomen met de ATLAS detector van een W boson kan op dat van een top quark paar lijken. Wanneer het laatste bestudeerd wordt, dan zal de achtergrond die de W bosonen vormen geïdentificeerd moeten worden. Een eerste stap in dit proces is de bepaling van diens doorsnede.

Voor deze studie worden botsingen gebruikt met twee, drie of vier jets; een jet is het waarneembare object ontstaan uit een quark of een gluon. Met behulp van b-algoritmes speciaal bedoeld voor de identificatie van jets ontstaan uit b-quarks, zogenaamde b-jets, wordt het aantal geïdentificeerde b-jets als functie van het aantal jets in een botsing bepaald. Vervolgens wordt via een 'likelihood methode' de meest waarschijnlijke samenstelling van top quarks en W bosonen bepaald. De analyse is onafhankelijk van de snede gebruikt in de b-algoritme en tegelijkertijd geschikt om de efficiëntie van de identificatie te bepalen. De studie toont dat op een verzameling gesimuleerde botsingen met geïntegreerde luminositeit van $L = 50$ pb^{-1}, bij een zwaartepuntsenergie van 10 TeV, de doorsnede van het W boson bepaald kan worden tegelijkertijd met die van top quarks, geproduceerd in paren of individueel.

Zowel de functionering van de kalibratie analyse als die van de laatste analyse zijn getoetst op de aanwezigheid van deeltjes voorspeld door twee verschillende supersymmetrische theorieën. De kinematische fit kan mogelijkerwijs informatie opleveren over de massa-schaal van de supersymmetrische botsingen. In de studie van de doorsnede van W bosonen en top quarks is de meting gevoelig voor de b-quarks in één van de twee supersymmetrische modellen.

Acknowledgements

The Acknowledgements! Finally, my last few words. Reaching this point is quite an achievement, if I may say so myself. Looking back at where I started four years ago, the office next door, I can say I've come a long way. Yet I couldn't have done this on my own and want to thank here all those who helped.

Four years ago I even said I would quit physics. I had no idea, but apparently my parents always knew that was nonsense and that I'd continue. I want to thank them first for always knowing me better than myself and for their support.

I want to thank Stan Bentvelsen. During my application he probably realized that I didn't actually know what I was starting. I hardly knew the difference between ATLAS and ANTARES, and yet he took me in. Luckily I could always turn to him and Paul de Jong for questions and discussions. To Paul I am especially grateful. Without his patience and him always (truly) knowing better I'd probably still be at a lost. Chapeau to the one who can still find mistakes in this thesis after his careful reading. Especially sentences without verbs.

For the work on the energy calibration I often walked over to the office of Marcel Vreeswijk. The analysis, the note, none of these would ever have finished without him. Working together was a great pleasure, both the serious and the non-serious parts. I doubt he can look at Fig. 1.1 without getting a smile on his face.

The beautiful work I got to do would not have been the same without all the fellow PhD students. Starting on day one, which was at the BND school at Texel. Realizing there I would be doing my PhD at the same time as Jan, I thought: "as long as I get some work done. Tomorrow." It's good that this never changed in Geneva. At CERN I shared the office with Maaike and Manuel. Reminiscing, it is incredible that we survived all our frustrations in that small office without any problems. To Maaike and Jacopo: I'll never forget your wedding! To Manuel: really, you still look like you need one more laatste biertje.

With Eduard, Nicola and Jacopo I had my brief career as a boxer. It is too bad we didn't find a place to continue the club back in Amsterdam. With Folkert I enjoyed the French Impro. Speaking of comedians: Tristan, you really know how to put the fun into the fundamental... Luckily for all of us we had Gossie and Manouk to compensate for that! Bad Honnef, Geneva, (Hungary) they wouldn't have been the same without them.

Some of my best time I had at CERN, where I also got to learn another side of the detector in its cooling. Different from what I worked on before, Steve, Koichi and Alex were the best at introducing me to the system. Thanks guys! I enjoyed all of it, along with the night shifts together, the shooting pool, the drinks. Their best tip: in case of a powercut, go skiing!

Anton, I want to thank you for your no-nonsense approach to science. It helped in keeping an eye on the finish-line. And at that finish-line, Irene, I hope you'll take good care of your broertje the 4$^{\text{th}}$ December... I'll need it.

Sometimes, when I'm overconfident, it feels like it was easy to reach this point. Probably the only person who can exactly tell you how difficult it was, is Karolina. After my master's thesis she had to again bare with all my ups and downs, my "sure, everything is fine..." and my (mental) absences. Luckily she always knew how to pull me back into the real world. And in return, my eternal attempts to learn Polish have gotten me no further than three words. The first is kabanosy; delicious sausages, but out of place in this text. The two others are those that matter: *Kocham cie.*